Systematic studies of crystal structures under non-ambient conditions

Smith, Philip S.

Systematic Studies of Crystal Structures Under Non-Ambient Conditions

Philip S. Smith

Thesis submitted in part fulfilment of the requirements for the degree of

Doctor of Philosophy

at the

University of Durham

Department of Chemistry
May 2004

Systematic Studies of Crystal Structures Under Non-Ambient Conditions

Submitted for the degree of Doctor of Philosophy, May 2004,

by Philip S. Smith, Chemistry Department, University of Durham

Abstract

Variable temperature single crystal X-ray diffraction analysis has been used to study four molecular systems: 4-(p-trifluoromethyl phenylethynyl) prefluorotoluene (1), 2-methyl-4-(4-trifluoromethyl-phenyl) but-3-yn-2-ol (2), phenylethynyl perfluorotoluene (3) and Zinc Pyromellitate. In the case of the systems (1) – (3), the aim was to analyse the extent of the dynamic disorder in the CF_3 groups that are contained in these systems. To this end, segmented rigid body analysis has been employed to estimate forces constants and barriers to rotation of the relevant groups. Complimentary computational methods have been used to obtain further estimates of this barrier to rotation in these systems for both the isolated (gas phase) molecules and for the condensed matter phases for compounds (1) and (3).

For Zinc Pyromellitate, variable temperature single crystal X-ray and neutron analysis have been used to probe the behaviour of a proton that sits in a short, strong intramolecular hydrogen bond. The aim here was to discover whether the system exhibits proton migration along the hydrogen bond as a function of temperature and thus gain insights into the energy potential well in which the proton sits. To this end, both computational methods have been used to study the pyromellitate fragment, and variable temperature full crystal structure data so as to gain direct access to information regarding this potential well.

Declaration

The work described in this thesis was carried out in the Department of Chemistry at the University of Durham between October 2000 and September 2003, under the supervision of Prof. Judith A.K. Howard. All the work is my own, unless otherwise stated, and has not been previously submitted for a degree at this, or any other university.

Philip Smith

Acknowledgments

Firstly, I must thank my supervisor, Judith Howard, for not only being more than helpful and patient beyond the call of duty during my time of study, but also having the temperament to put up with my occasionally offensive and certainly over the top, sense of humour. Few others would have...

The computational aspects of this work would not have been possible with out the input of Dr. Stewart Clark of the Physics Department. Having had to put up with answering my many elementary questions about density functional theory over the past two years, I find it rather surprising that that he continues to remain cheerful as I pop into his office 'for a chat'.

Many of my crystals were synthesised and grown in the laboratory of Prof. Todd Marder – without this work, there would have been no crystallographic study! Thanks guys. Our Indian collaborators, especially V.R. Vangala and B.R. Bhogala must also be thanked on the crystal front: it has been *fun*.

Thanks to Prof. Chick Wilson at ISIS and Dr. Sax Mason at the ILL who have made my trips to these facilities both scientifically productive and socially entertaining.

Hat tip to everyone in the CG72 lab crew, especially Dr. Andrei "Batsie" Batsanov for the sound grounding in crystallography some 4 years ago and Dr. Dima Yufit for help with some really nasty crystal structures... and those delightful vodka parties.

At Home, Dr. Horst Puschmann's skills as a sound engineer, photographer and computing technician have been invaluable. Just drink the whisky, if you like, and don't bother to ask me!

For many a fun evening at the card table, I'll like to thank the past and present members of Durham University Bridge Club: especially Bryony Youngs, and my regular tournament partners over the years: David Nolland, Mike Scanlon, Luke Porter & Geraint Harker: I'll be happy to punt 3NT if *your* playing it...

And finally I would like to thank my family:

Edwin, Frieda and Martin Smith

and

Christ Jesus *et al.*

"*For everything you know, there is a time before you knew it. That's important, and I'm going to repeat it. For every single thing that someone else is stupid for not knowing, there was a muffled moment in your own life when you didn't know it, either. And there are definable instants in our lives before which we are ignorant and after which we are informed.*" - Mick Caro

TABLE OF CONTENTS

1 Introduction

1.1 *Opening Remarks*

Surprisingly few variable temperature single crystal X-ray studies have been carried out on molecular systems. Historically this can be put down to the fact that collecting high quality data sets over a range of temperatures would require weeks of diffractometer time – time that was at a premium. In addition, the ability to carry out low temperature studies at anything other than large-scale facilities has not existed for so many years. In fact there are many countries in the world today where carrying out low temperature work, standard practice in the 1st world, is simply out of the question on the grounds of cost. For those who have the means, technology has changed the field, however; liquid nitrogen temperature has been attainable as a part of standard crystallography labs for around the past 15 years, and the advent of area detectors in the mid 1990's has dramatically reduced the time taken to collect data.

In light of these changes, and the opportunities available, it may seem odd that so little work has been carried out at variable temperatures on molecular systems. This stems from the fact that crystallographic experiments are often carried out for a chemist who wants to have his (or her) reaction product analysed with a view to publication and more recently simply to confirm that a reaction step has taken place in the anticipated way. This being the case, experiments tend to be carried out at low temperature (involving flash freezing) so as to attain the best possible data in the shortest possible time. The increase in data collection capacity due to area detectors becoming more commonly available, has been compensated for by an increase in the number of samples submitted for study and a reduction in the required crystal quality.

The literature does contain some examples of the use of variable temperature crystallography to solve various problems, and to give insight into various solid-state phenomenon such as phase changes and internal motion. A selection of these cases will be discussed in this chapter with a view to evaluating the state of play in the field, and gathering insight into the possibilities that exist when using variable temperature crystallography.

1.2 *Areas of Interest*

We aim to use the crystallographic technique, combined with theoretical methods to investigate, primarily, two areas of interest: the nature of motion in the solid state and hydrogen bonding. With regards to hydrogen bonding, both weak intermolecular interactions and investigations into crystal structure anticipation, and short, strong hydrogen bonding are considered. In the former case we examine disorder in crystal structures and consider what (if anything) can be derived from establishing the nature of said disorder.

In the following discussion, a basic understanding of the crystallographic technique and particularly single crystal X-ray diffraction shall be assumed. There are many texts available that deal with crystallographic concepts such as diffraction, unit cells, space group symmetry, the phase problem, structure solution, structure refinement and the like [1, 2], so we shall restrict ourselves here to aspects of experimentation that are directly relevant to our studies.

1.2.1 Atomic Displacement Parameters (ADPs)

Fundamentally, ADPs have meaning only as the approximation of the smearing out of electron density from the mean atomic position [3]. That is: X-rays are diffracted by electrons, and the diffraction from an atom is the convolution of the scattering from its stationary electrons (its form factor) with a probability density function (p.d.f.) that defines the smearing out of said electron density. This p.d.f. can be approximated by a Gaussian distribution such that the displacement of an atom from its mean position is [4]:

$$D(\mathbf{x}) = \frac{(\det \mathbf{U}^{-1})^{1/2}}{(2\pi)^{3/2}} \exp(-x^T U^{-1} x/2) \qquad \text{Equation 1.2-1}$$

Where $\mathbf{x}$ is the instantaneous displacement vector and $\mathbf{U}^{-1}$ is the inverse of the matrix of second moments $\mathbf{U} = \langle \mathbf{x}\mathbf{x}^T \rangle$. This 2nd order symmetric matrix, **U**, has six independent components and these are called the anisotropic displacement parameters (ADPs)[i]. To be clear on this point: the p.d.f. – and hence **U** – does *not* describe the electron density of the stationary atom, rather it approximates further the smearing out of electron density, and thus provides a probability surface that describes the diffuseness in the 'electron cloud' about the nuclear position of the atom. When U is a positive definite, the equiprobability surface of the p.d.f. can be illustrated by an ellipsoid of probability:

---

[i] In principle it is possible to approximate the smearing of the electron density with additional terms, for the description of non-Gaussian p.d.f.s. In addition to the six parameters describing the second moments, ten cubic terms, fifteen quartic terms (and so on) could be added. However, this is seldom sensible as in the absence of disorder there is little point, and in the presence of disorder the diffraction power of the atom(s) in question falls off sharply and so high angle data is impossible to obtain.

$$\mathbf{x}^T\mathbf{U}^{-1}\mathbf{x} = c^2$$ Equation 1.2-2

For c = 1.538, the probability of finding an atom in the volume enclosed by the ellipsoid is 50%, the standard value used for plots of ADPs which adorn so much of the crystallographic literature [4].

A Gaussian p.d.f. corresponds to motion (of the atom) in a quadratic potential and has the advantage that the Fourier transform of a Gaussian is also a Gaussian. Consequently the Fourier transform of Equation 1.2-3 leads to [3]:

$$T(\mathbf{h}) = \exp(-2\pi^2\mathbf{h}^T\mathbf{U}\mathbf{h})$$ Equation 1.2-4

Here $\mathbf{h}(h_1, h_2, h_3)$ is the scattering vector of length $2\sin\theta/\lambda$ and **U** is the aforementioned matrix of second moments. It is therefore possible to measure the elements of **U** directly from the angle dependence of Bragg diffraction intensities. T(**h**) is anisotropic as it has different values in different directions.

Of course, while the smearing out of electron density (and hence the enlarging of the ADPs) *may* be due to atomic motion, there is nothing to ensure that this is the case. There are other factors that could influence the size and shape of ADPs. For example, systematic errors such as a lack of a proper absorption or extinction correction, may cause inaccuracies. More obviously, perhaps, is the fact that poor sample quality – imperfect or cracked crystals - will yield poor data and thus erroneous conclusions. Finally the crystal may be randomly disordered from unit cell to unit cell, such that the atoms throughout the crystal are distributed across a number of discrete positions. With these

problems in mind it should be obvious that some caution is required when interpreting the results of diffraction experiments in terms of physical properties.

Some of these problems can be overcome by use of variable temperature experiments: especially when it comes to distinguishing between dynamic disorder and static disorder. If T(h) in Equation 1.2-5, and therefore the elements of $\mathbb{U}$, show undue temperature dependence, then this p.d.f. can be attributed to dynamic disorder. Conversely, if there is little change in the elements of $\mathbb{U}$ as temperature is varied then the p.d.f. is due mainly to static disorder. The other problems may be circumvented to some extent by: a) being especially careful when collecting data and b) collecting data on different crystals, since defective crystal may be the root cause of unexpectedly large ADPs. Obviously, as there is no way of measuring the quality of a crystal quantitatively (and many samples look perfectly reasonable under preliminary optical inspection) - one simply has to use sound judgment.

1.2.2 Modeling Thermal Motion

Cruickshank, in 1956, [5-7] used rigid body motion to model anisotropic thermal motion of atoms in crystals. He treated the atomic displacement as having two components - libration about some point in the molecule, and translation – each being represented by a tensor. This treatment was extended by Schomaker and Trueblood [8] when it became clear that Cruickshank's original work only held true when a molecular centre is imposed by space group symmetry. In the later work molecular motion was considered in terms of three tensors representing libration (Libration tensor L), translations (translation tensor T), and the correlation between the two (tensor S, a "screw" motion). This approach

to the analysis of thermal displacement parameters is known as the TLS method and has been widely used.

The central assumption that leads to the TLS analysis is fairly severe: we are treating the molecules as rigid bodies. That is, all molecular deformations require infinite energy and thus one can consider the motion of molecules as a whole – the motion of the atoms within the molecule are completely correlated [4]. This being the case, the elements of T, L and S can be found by least-squares fit to the ADPs. Obviously, the assertion that a molecule will behave as a rigid body may or may not be reasonable, while a phenyl ring might well be rigid to a first approximation, other molecular features such as a hydrocarbon chain would not be reasonably considered so. Over the years, the TLS analysis has been applied widely, and where the assumption of rigidity seems reasonable the model has given a good account of itself for calculating both ADPs [9 - 10] and correcting interatomic distances. [11 - 13]

An extension of the rigid body model is the segmented rigid body approach that has been developed by various authors [14 - 17]. The basic idea is that the internal motion as a whole is considered in terms of a network of coupled rigid bodies, the motions of which correlate in a predictable way. A CF_3 group, for example, could be considered to rotate about the C-C bond that attaches it to the rest of the molecule – see Figure 1.2-1. To model this, a rotation parameter for torsional motion about the bond can be added [15]. The upshot of this treatment is that it provides a semi-quantitative description of molecular motion, and has been used to good effect in estimating torsional amplitudes and corresponding quadratic force constants in librating groups [16].

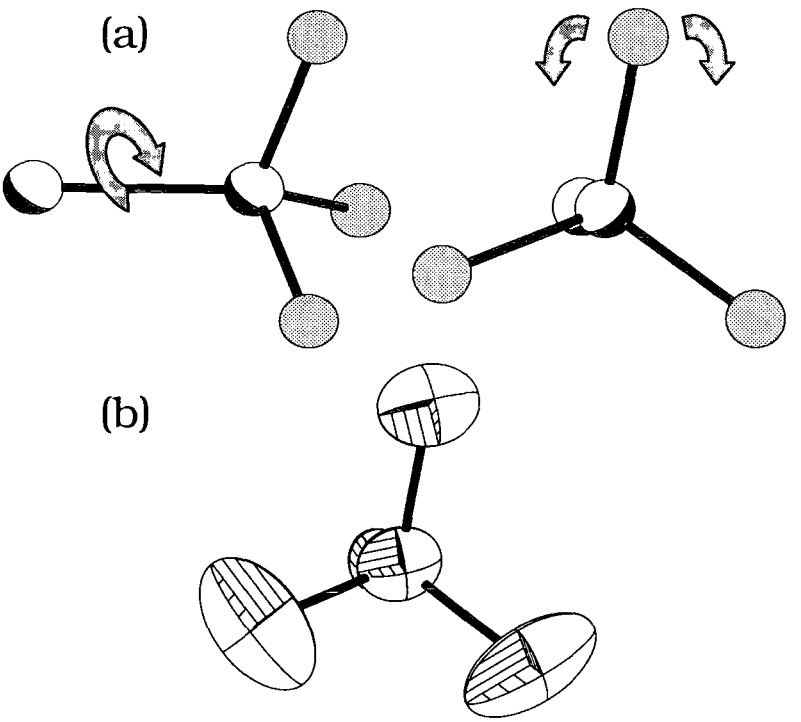

Figure 1.2-1 (a) A CF_3 group is expected to librate about the C-C bond. The result, (b), is large ADPs in the direction of circular motion about the C-C bond.

The simple one parameter model has been used to good effect to calculate [15, 16] force constants and potential barriers for the torsional motion of various groups. By assuming that the terminal group behaves as a simple harmonic oscillator, the barrier to rotation per mole, B, is related to the potential by:

$$V(\phi) = \frac{B(1-\cos n\phi)}{2} \qquad \text{Equation 1.2-6}$$

Where n is the periodicity and Φ is the librational amplitude. Providing Φ represents a small deviation from the equilibrium (i.e. $\Phi \approx 0$) and the potential

in which the atoms reside is quadratic, then the energy barrier is, in the classical approximation[ii]:

$$B = \frac{2RT}{n^2\phi^2} \qquad \text{Equation 1.2-7}$$

There are, however, a number of problems with this simple treatment [17]: ADPs provide no direct information on the nature and amplitudes of individual modes of motion and correlations among various motions are ignored. Additionally the vectors about which rotational motions occur must be chosen by chemical intuition – this is not a problem with CF_3 groups; however, a relevant consideration when more complicated systems are considered. A third problem with this simple model is that it does not take into account correlations among differing types of motion; extra correlations can be added. However, it has been shown that only when $< \Phi^2 >$ is large compared with the parallel component of L is the value meaningful. In spite of some objections to the simplifications inherent in this method [17], reasonable agreement with values of other, mostly gas phase, techniques has been achieved. [16, 18]

[ii] Classical Boltzmann distribution for a quadratic potential yields a Gaussian with second moment $<x^2>$ such that $<x^2> = kT/f$, where f is the force constant. As a temperature T=0 would give an infinitly sharp p.d.f. this is clearly invalid as T approaches 0K.

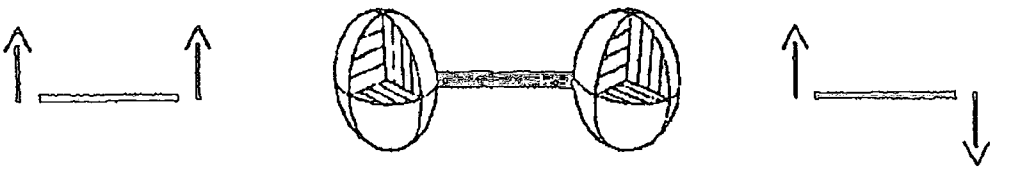

Figure 1.2-2 The motion of this diatomic, represented by the two ADPs could be the result of translational motion, left, librational motion, right, or both. With data collected at only one temperature it is impossible to tell. Consideration of the limiting behaviours, however, that is the behaviour (close to) zero K, and the behaviour at high temperature where classical relationships apply, should yield this information [19].

To overcome some of the difficulties in ascribing specific molecular and atomic motions to ADPs, Burgi and Capelli [19] have suggested analysing displacements in terms of temperature dependent and temperature independent normal modes. By studying crystal structures at various temperatures, the temperature dependence of the ADPs can be analysed and so information about the correlation between atomic motion can be determined. In their model, high frequency modes are considered as being temperature independent, and so are present as part of zero point motion, while the low frequency modes are considered temperature dependent. When used in conjunction with a molecular mean field model [20], a model that considers atoms in molecules to be tied more strongly to one another than atoms that are not in the same molecule, they report success in reproducing the results of vibrational spectroscopy in deuterated benzene and urea [21]. They note, however, that in order to obtain satisfactory results, it is necessary to use neutron data or high quality X-ray data such as those obtained in charge density studies, as 'ADPs tend to absorb features of valence – electron density if spherical atomic form factors are used in standard structure refinements. [19]

1.2.3 Recent Variable Temperature Experiments

1.2.3.1 Rotation of CH_3 and CF_3 Groups

Variable temperature experiments have recently been carried out by C.C. Wilson to probe the librational motion of various terminal CH_3 groups using neutron diffraction and the TLS approach [22 - 27]. The advantage of using a variable temperature approach is that it provides additional information on the behaviour of the hydrogen atoms and the potentials in which they sit. The extent of temperature dependence can also give insight into the effects of chemical environment on the motion of molecules in crystals.

Variable temperature experiments on dimethylnaphthalene [24, 27] (Figure 1.2-3) show that the extent of the CH_3 group librations is largely temperature independent. This is explained as being due to steric hindrance around the CH_3 group, locking it into one conformation. Interestingly, even at temperatures close to its melting point (340K), the CH_3 group is seen to remain in its low temperature conformation [23]. This behaviour can be contrasted with that of aspirin [25] and paracetamol [22], where the extent of libration of their respective terminal CH_3 groups has a far greater temperature dependence (Figure 1.2-3), which is due to a lack of intramolecular steric hindrance. Equally interesting is that in all four systems the zero point motion is approximately equal, suggesting that the apparent thermal motion of hydrogen atoms in a crystal structure cooled close to absolute zero may be of a fairly constant magnitude. [25]

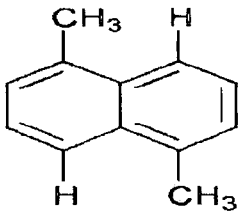

1 (1,5-dimethylnaphthalene)

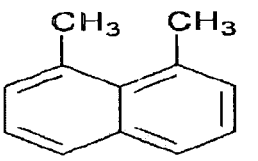

2 (1,8-dimethylnaphthalene)

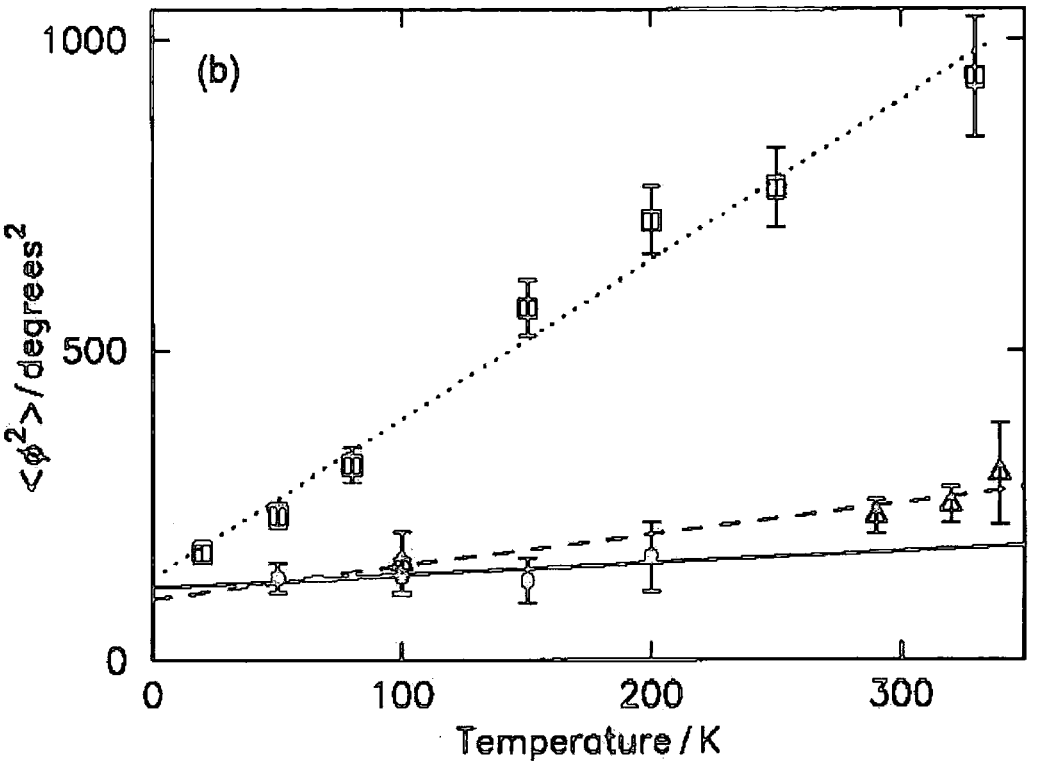

Figure 1.2-3 Two isomers of dimethylnaphalene studied at variable temperature, top 1 and 2, and below: the extent of libration at various temperatures for the two dimethylnaphalene systems (circles and triangles) and, for comparison, those found in paracetamol. Note that the three plots converge to approximately the same value at zero temperature.

There have been a number of variable temperature studies of CF_3 rotation via NMR. [28 - 31] The energy barriers to CF_3 rotation derived in these studies is in the 5 – 25 $kJmol^{-1}$ range. What is most interesting about these studies is that while the energy barrier of CF_3SO_3Cs is temperature dependent [28], the barriers of the other three systems, $Cu_4(CF_3COO)_4.2C_6H_6$, CF_3COOAg and CF_3SO_3Li, are temperature independent [29 - 31]. No explanation is given for this anomaly.

1.2.3.2 Crystal Cell Dimensions

The study of crystal cell dimensions at variable temperature has, for the most part been restricted to powder diffraction work on continuous solids. In these systems phase transitions are often identified by monitoring the change in cell dimensions as a function of temperature. Molecular systems, however, have not been considered in great detail. From those studies that have been carried out, [32 - 35] there seem to be two trends that exist. Firstly, thermal expansion – that is, the expansion of the lattice parameters as temperature rises – tends to be anisotropic. Secondly, this thermal expansion is linear as a function of temperature; at least over a temperature range which excludes quantum effects that arise due to zero point energy.

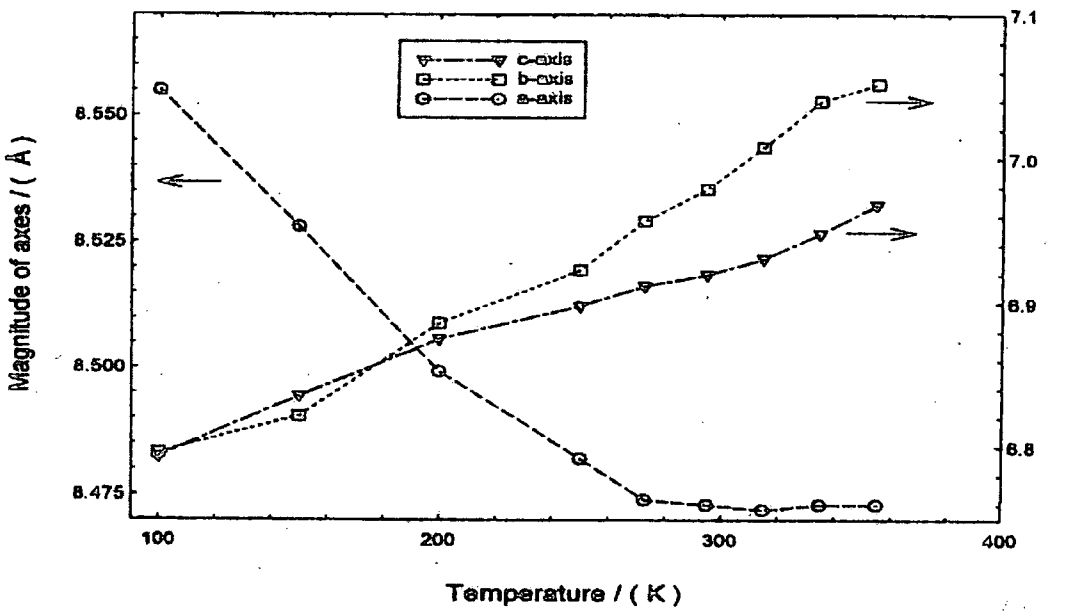

Figure 1.2-4 Variation of the magnitude of the cell dimensions with temperature in N-methylurea. [35] There is negative thermal expansion along the c-axis from 100K until around 273K. All the cell parameter changes are linear as a function of temperature.

Perhaps most interesting in these studies is the report in negative thermal expansion in two nonlinear optical crystals [33, 35] in one direction, coupled with positive thermal expansion in the other two directions. That is, as the

temperature increases one of the crystallographic axes contracts, while the others expand (Figure 1.2-4). No explanation is given by the authors for this behaviour, presumably for the simple reason that such behaviour is not well understood. It is interesting that very little is suggested in the way of explanation as to why this might be the case in any of these systems.

1.2.3.3 Phase Transitions

Anthony West, in his book "Solid State Chemistry and its Applications" [36], wrote an excellent chapter on the basics of phase transitions. If a crystalline material is capable of existing in two or more polymorphic forms the process of transformation from one polymorph to another is a phase transition. One can use a thermodynamic approach to consider the behaviour of the derivatives of the free energy. This approach partitions phase transitions into 1st and 2nd order by defining:

A 1st order transition as showing a change in the 1st derivative of the free energy:

$$\frac{\delta V}{\delta T} = -S \qquad \frac{\delta P}{\delta P} = V \qquad H = U + PV$$

so

$$\Delta S = \frac{\Delta H}{T}$$

i.e. there is a discontinuity in the volume, and hence density, of the crystal at a 1st order phase transition.

A 2nd order transition shows a change in the 2nd derivative of the free energy, so that there is a different rate of change of unit cell volume as a function of temperature. By studying the unit cells of crystal systems at variable temperature, it is generally straight forward to follow phase transitions – one simply plots the volume of the unit cell against temperature.

The kinetics of phase transitions are harder to define; however, the rate of conversion between two polymorphs should be considered as a balance between the kinetic and thermodynamic factors. The Arrhenius equation:

$$\text{Rate } (k_1) = A\exp(-E/RT)$$

Where E is the activation energy, shows us that the rate of reaction will increase rapidly with increasing temperature, and fall rapidly with increasing activation energy. One must also consider the difference in free energy between the two polymorphs, as this will be the driving force behind the transformation. At the transition temperature (T_c) there is no difference in the free energy, but in the idealized case (H and S are temperature independent) the change in free energy on transition will simply be:

$$\Delta G_{I\text{-}II} = ((T_c\text{-}T)/T)\Delta H_{I\text{-}II}$$

Combining the two factors, we get an expected rate of transition, which will be of the form of Figure 1.2-5. Notice that there is a maximum that exists as the temperature is reduced below the equilibrium transition temperature (T_c). Once the temperature falls to well below the T_c, the rate of transformation will be zero, even if there is a good thermodynamic driving force behind it. For example consider diamond and graphite: the latter is the thermodynamically stable form

at room temperature. This is of importance when considering low temperature XRD, as it means we cannot expect large changes in the structure, as at low temperature the activation energy must be small, or the kinetics will dictate that no phase change occurs. Secondly, at very low temperatures it will be easy to super-cool a crystal and so miss a phase transition altogether.

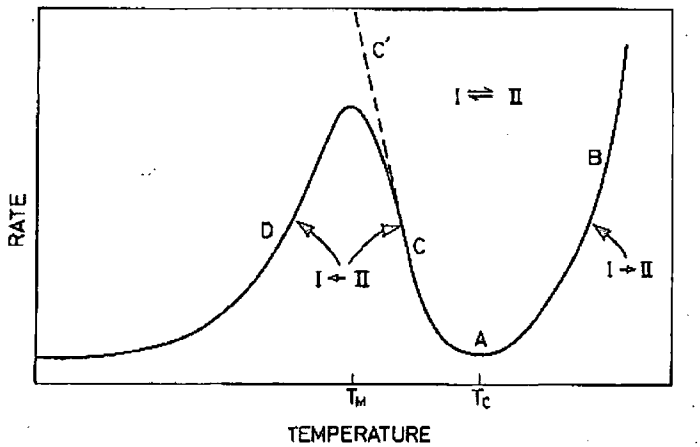

Figure 1.2-5 Temperature dependence of a phase transition. [36] Notice that while there is a maximum for the rate of transition below the critical temperature, there is no such maximum above the critical temperature.

In the wider literature there is no shortage of examples of phase transitions in continuous solids, mostly studied by powder methods. The reporting of low temperature phase transitions in molecular systems is far less common. This is probably due to the fact that they don't happen very often, and when they do, it is usually simply a small displacive move that leads to a change in symmetry or cell parameters. In comparison with studying the super ionic conducting phases of, say, silver iodide, or the super conducting phases of perovskites, these changes may not seem particularly glamorous; however, they are in fact of great importance if we wish to consider the fundamental interactions that lead to crystal structure.

Looking at the literature, there are a number of common features of low temperature phase changes [37 - 40]. Firstly, low temperature phases tend to be ordered, or more ordered than their high temperature counter parts. Secondly, in a phase change involving unit cell doubling, the low temperature form will have the doubled cell. These points are illustrated by the work of Prout *et al.* on various thiourea pyridinium halides [38]. These systems were studied over a temperature range and various phases were discovered - interesting (and unique, to the best of my knowledge) as they systematically studied the effect of substituting chloride, bromide and iodide on the phase behaviour. These systems show three phases: at low temperatures the bromide and iodide versions are ordered and it is anticipated that the chloride system will be ordered at sufficiently low temperature, and disordered at room temperature. The ADPs at high temperature do not correspond to TLS motion and were treated as static disorder. All the crystal systems were orthorhombic though the chloride experienced doubling of the a-axis when it changed from space group Cmcm to Pbca (265K and 110K structures respectively, Figure 1.2-6).

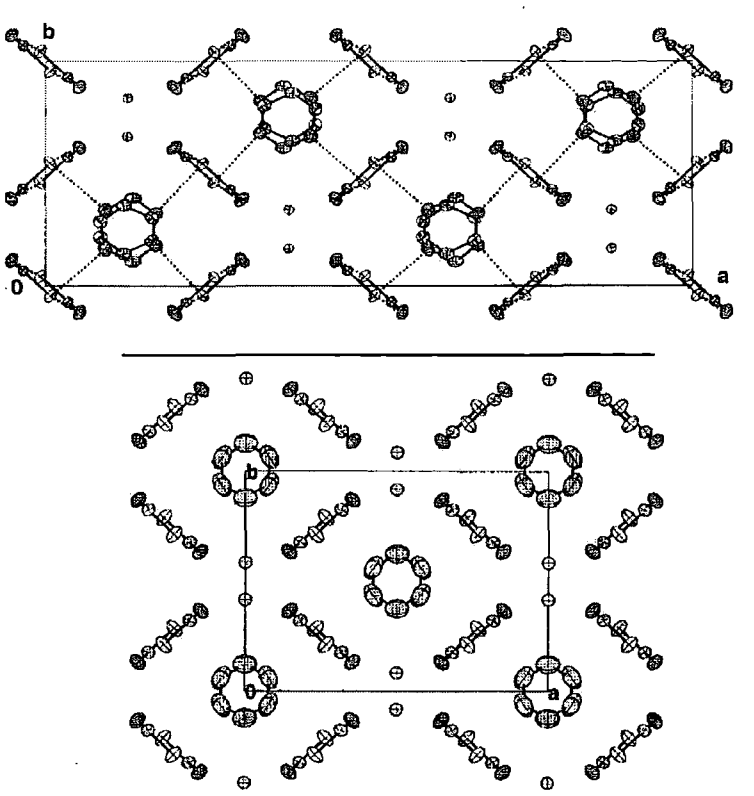

Figure 1.2-6 Packing diagram of Bis(thiourea) pyridinium chloride and 110K (top) and 295K (bottom) viewed along the c-axis. Notice that the a-axis is doubled in the low temperature phase.

1.2.4 Hydrogen Bonding

Hydrogen bonding has received a huge amount of attention over the decades [41]. The interest in the study of hydrogen bonds lies in their importance in fields as diverse as mineralogy, general organic and inorganic chemistry, supramolecular chemistry, molecular medicine and pharmacy. Clearly this is a gigantic field of research, and so to limit the scope of the review contained here, only areas directly related to work carried out and reported within this document are included. This falls into two categories: work involving the probing of short-strong hydrogen bonding and work involving the study of weak intermolecular interactions, as a general contribution to the field of crystal structure anticipation (or 'crystal engineering').

What is a hydrogen bond exactly?

The 'hydrogen bond' is a very broad phenomenon and consequently only a very flexible, wide-ranging definition of the term must be used. In general, the interaction X-H···A is a hydrogen bond when: (i) X-H acts as a proton donor to A; and (ii) it constitutes a local bond [42]. X and A can in principle be any atom provided the system satisfies these two criteria. Consequently one has a huge variety of interactions involving a very wide range of chemical constituents. As a result, the dissociation energies of this class of interaction vary from around 1 kJ mol^{-1} to around 160 kJ mol^{-1}.

For weak and conventional hydrogen bonds, those with dissociation energy of less than around 60 $KJmol^{-1}$, the interaction is primarily electrostatic [41]. In the classical view the proton is attached to an electron withdrawing atom, thus becoming electron deficient. The proton acceptor is electron rich and thus there is an electrostatic interaction. If one considers the most famous hydrogen bonded system, water, this should be apparent:

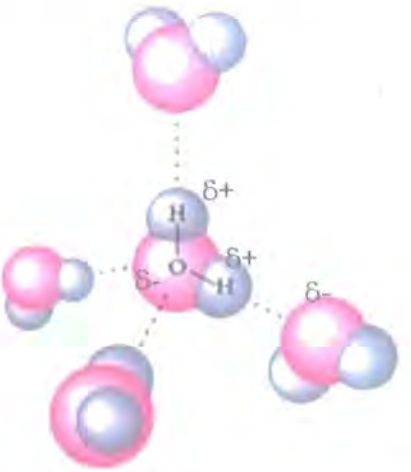

Figure 1.2-7 Diagram of hydrogen bonding in water. The partially charged hydrogen atoms point directly at the partially negative lone pairs of adjacent oxygen atoms. Diagram from: http://www.sc.chula.ac.th/courseware/2303105/life/77.jpg]

The hydrogen atom is partially charged (δ+) and points directly at an oxygen's electron lone pair of the filled p orbitals. As the partial charge on the hydrogen and acceptor oxygen atom increase (increasingly positive and negative respectively), the electrostatic attraction increases and so, consequently, does the strength of the hydrogen bond. For the water O-H...O interaction, this is in the region of 20 KJ mol^{-1}. [43]

As the electronegativity of the donor atom falls, so the partial charge on the proton falls, and so does the strength of the overall interaction. For example, one can tune the strength of the C-H hydrogen bond 'donor' group by altering the hybridization around the carbon: the interaction energy decreases as $C(sp)>C(sp^2)>C(sp^3)$. This holds true regardless of whether the proton acceptor is oxygen or a π electron system [44]. Thus the strength of $HC{\equiv}CH...OH_2$, $H_2C{=}CH_2...OH_2$ and $CH_4...OH_2$ are 9.2, 4.2 and 2.1 $KJmol^{-1}$. [45 - 46].

Our interest in these weak and conventional hydrogen bonds is in the field of structure anticipation ("crystal engineering"). The ability to predict crystal structure successfully from molecular structure is of obvious importance: the physical properties of a material, such as non-linear optics, ferromagnetism and conductivity, are directly related to crystal structure. Crystal structure, in turn, is the consequence of molecular packing on condensation to the solid (crystalline) state, which is governed by intermolecular interactions. Simply put, if one could anticipate how molecules would pack simply from their molecular structure, it would be possible to create crystals with designer properties [47].

There are many factors that govern crystal structure – a competition, if you like, of interactions of varying strengths and directionalities. Thus, while it would seem obvious that a full understanding of strong, highly directional forces such as 'conventional' hydrogen bonds is necessary if there is to be any hope of

reaching our goal of crystal structure design, it is also absolutely essential to understand the effect that more subtle interactions, such as weak hydrogen bonds, have on crystal structure [48]. While the stronger interactions have received much attention over the years, there is still a great deal to be learned from the weaker interactions, the importance of which were for many years overlooked. In part, this may have been due to initial scepticism as to their importance [49] and in part due to the greater difficulties in their study: when both strong and weak interactions are present, the stronger interactions will tend to dominate the crystal structure.

For study of weaker interactions, it is therefore desirable to choose systems that only have weaker directional interactions in them. One approach is to synthesise systematically systems that have similar molecular structure and then to characterise and monitor the changes in crystal structure. For example, one could substitute a fluorine atom for a chlorine atom and compare the structures of the two systems. While this method certainly probes the effect of subtle molecular changes it is obviously extremely time consuming. In an alternative approach, database searches of previously solved crystal structures, can be used to seek out all known instances of a given interaction and the resulting crystal structures noted. This suffers from the fact that one is left to the mercy of what others have chosen to study in the past, though with over 260,000 structures in the Cambridge Structural Database [50] and thousands being continually added, this is becoming an evermore profitable and satisfactory method. Computational (theoretical) methods too are improving, principally because increases in computing power allow for the study of more complicated systems and the use of improved levels of theory in these calculations. With these tools at our disposal, the study of many subtle

intermolecular interactions is possible and, over time, will lead to a far greater understanding of crystal structure prediction.

Before ascending into a state of Utopia based upon our soon to be discovered abilities of accurate crystal structure prediction, a word of warning should be raised as to just how many factors there are the affect crystal structures. This warning can be summed up by one word: polymorphism [51, 52]. Sometimes, the same molecules crystallise in different solid state forms. Crystallisation conditions play a significant factor, especially the solvent used, and in general it must be noted that as the condensed phase of the material forms, it is the interactions in the liquid / solution state that govern the crystallisation, rather than the resultant packing and intermolecular contacts found in a crystallographic experiment. If there are multiple possible crystal structures for a given system, each of which has a similar energy, the resultant crystal structure will certainly be dependent on the kinetics governing the crystallisation rather than the thermodynamics governing the lowest energy resultant crystal structure. All this having been said, it is clear that the greater our general understanding of all the factors that affect crystal structure, the greater our ability will be to anticipate the likely crystal structure of any given molecule.

1.2.5 Short Strong Hydrogen Bonds

Short strong hydrogen bonds (SSHB) have recently received a great deal of attention, not least because of their role in enzymatic catalysis [53, 54]. Special attention has been paid to low barrier hydrogen bonds and possible mechanisms for proton transfer. For example, it has been shown that the catalysis of serine proteases can be mediated by Low Barrier Hydrogen Bonds

(LBHB), a class of SSHB. [55]. Short-strong hydrogen bonds are characterised as having bond energies greater than ~ 60 KJmol^{-1} and are the result of a combination of covalent and electrostatic interations, [56] with donor-acceptor atoms separated by less than about 2.55 Å in the solid state, donor-hydrogen bond lengthening of more than 0.08 Å and NMR ^{1}H downfield shifts of more than 14 ppm [41].

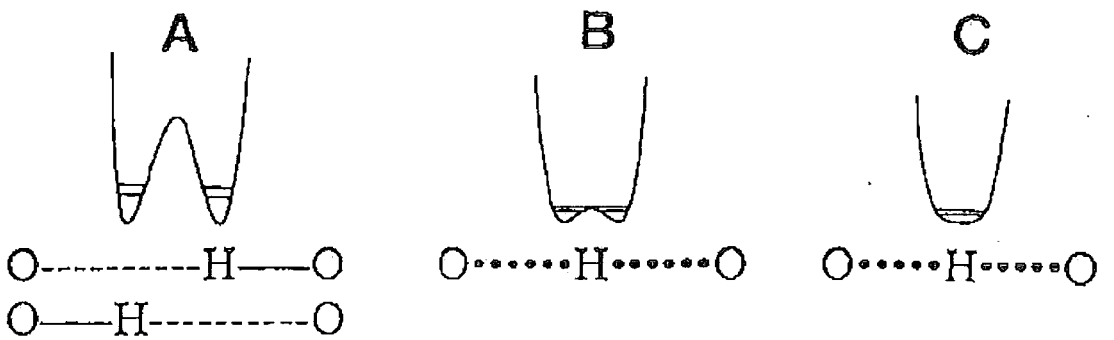

Figure 1.2-8 schematic showing the change in the shape of the potential well in which the proton sits, going from weak hydrogen bonds of the left to strong hydrogen bonds on the right. The upper line in the well is for hydrogen, the lower line is for deuterium [54].

In practice the situation is less clear-cut than that presented in Figure 1.2-8. After all, if the O...O contact is not entirely symmetrical then, apart from the fact that it would be unreasonable to expect a symmetrical well, there are forces present that could disrupt the potential well/hydrogen bonding [57]. A charge density study of benzoylacetone carried out by Larsen et al. [58] at very low temperature, illustrates well this point. Using neutron and X-ray data it is clear that the proton is smeared out in the direction between the two oxygen atoms, which are 2.502(4)Å apart (Figure 1.2-9, top). When we look at the electrostatic potential (Figure 1.2-9, bottom), we see that the proton sits in an electrostatic potential perpendicular to the line between the two oxygen atoms. On the basis of this interaction, one would expect the proton to be smeared out

perpendicular to the line connecting the two oxygen atoms. The fact that it is not, confirms the covalent contribution to the hydrogen bond in this case.

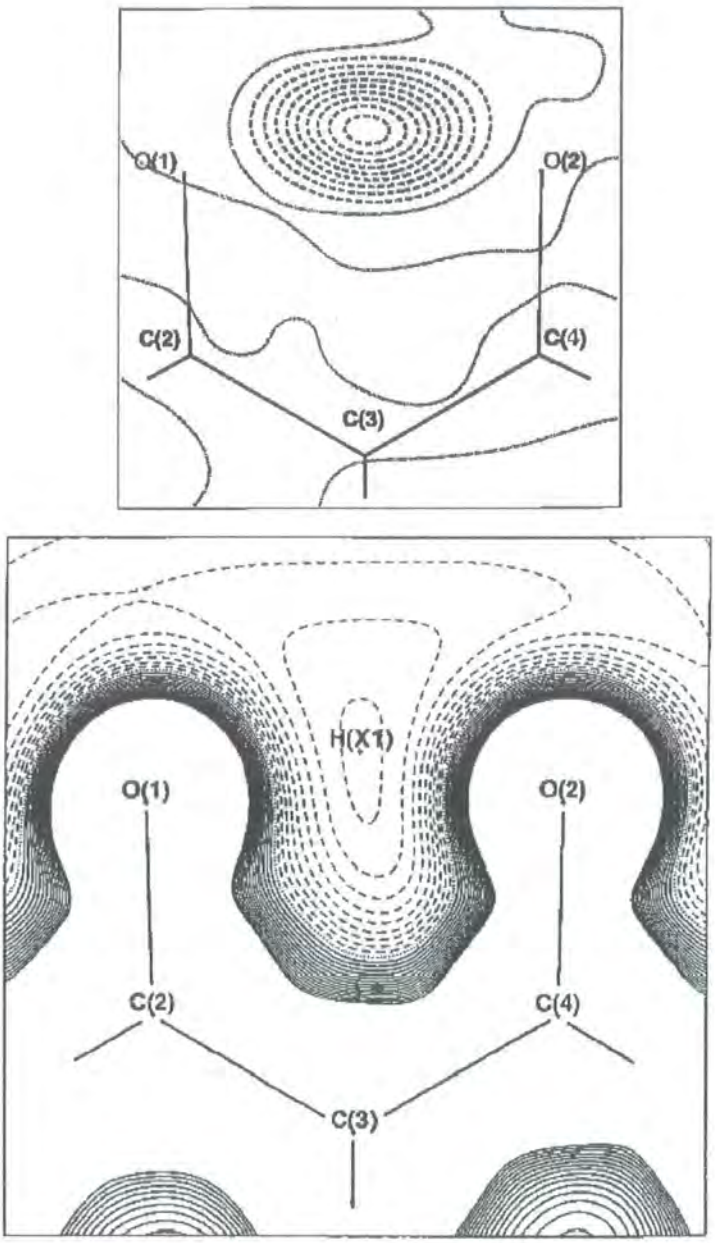

Figure 1.2-9: Difference map from the neutron refinement with the enol hydrogen atom omitted from the model, top, and a close up of the electrostatic potential in the enol region calculated after the removal of the contribution of the enol hydrogen, bottom. [58]

Variable temperature neutron diffraction studies carried out on short O...O contacts, log the change in the shape of hydrogen atom ADPs [24, 26, 59, 60]. In a study of aspirin, Wilson [60] showed that the shape of the proton ADP involved in short hydrogen bonding changes with temperature. Below 200K, the ADP is well defined and fairly symmetric whereas above 200K it is seen to be asymmetric and less well defined (Figure 1.2-10). As the O...O contact distance is 2.635Å, the potential well is not expected to be a shallow single well. Instead it is postulated that it is a double well, where the barrier between the two minima is too great to be explored by the proton at temperatures below 200K. If this were the case, one might expect there to be two independent sites which the proton can occupy. The data does not support this[iii], and it is suggested that the proton is simply able to "explore to a significant extent the anharmonicity in the bonding potential above 200K." This is in contrast to work carried out on the benzoic acid dimer [59] where a dual site model was supported by variable temperature neutron data at all temperatures. Similar work carried out on a 1:1 urea-phosphoric acid complex [24] shows a different phenomenon. In this system the proton migrates across the strong O-H...O hydrogen bond. At low temperatures (150K) the O...O separation is 2.400(5)Å and the proton is closer to the urea oxygen (1.178Å). However, at 335K the proton has become more or less centred between the two oxygen atoms. In each of the three variable temperature studies we see subtle differences in the behaviour of the protons in short strong hydrogen bonds. This should be evidence enough that further work is required in the area.

[iii] To allow data to be collected at many different temperatures under the time restrictions that inevitably exist on neutron experiments, rather short data sets were collected. As a result there was a low data to parameter ratio and a loss of resolution.

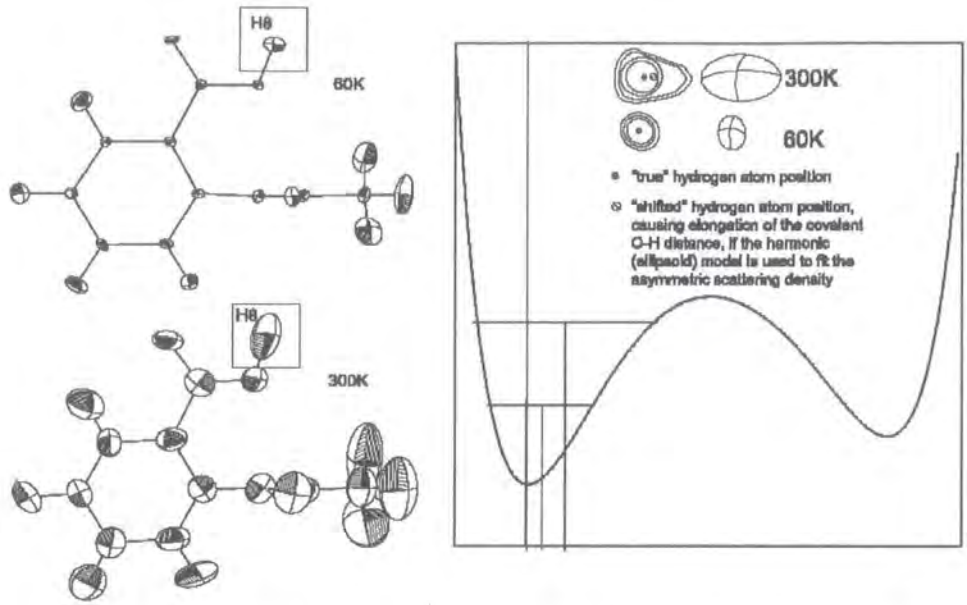

Figure 1.2-10 The proton that forms part of the carboxylic acid dimers in aspirin (boxed in, left) at 60 and 300K as determined by neutron diffraction studies [60]. There is a clear change in the shape and size of the ADP. The proposed potential well in which the proton sites is shown on the right. The solid horizontal lines show the energy level of the proton at the two temperatures and the vertical lines show where the apparent centre of the atomic scattering will lie.

It may be instructive here to consider what it is about certain systems that results in the formation of a SSHB, while others yield weaker, conventional hydrogen bonds. For the most part the answer appears to lie in the matching of proton affinities (PAs) and the pK_as of the partner donor and acceptor atoms. [61] As pKa values are a solution property, it is not possible to transfer this directly into the solid state. However, the formation of SSHB between acids and their conjugate bases – when pKa values are identical – is well known. [62] The difference in pKa values need not be precisely zero for a SSHB to exist; [63, 64] as the difference in proton affinity increases, the orbital mixing of the donor and acceptor atomic orbitals becomes weaker and the strength of the interaction falls off [65]. This is why most of the SSHB investigated to date are of systems where the donor and acceptor atoms are of the same atomic species.

An excellent study by Gilli et al. [66] on β-diketones and related systems, sheds light on the extent that N-H...O contacts can be low barrier hydrogen bonds. The energy of the nitrogen and oxygen atomic orbitals are not the same and this causes difficulties in orbital mixing, making the formation of a low barrier hydrogen bond more difficult. The proton affinity (PA) of the two atoms can be modified chemically to become more equal e.g. by the substitution of electron withdrawing groups adjacent to the nitrogen atom. When this is carried out, the hydrogen bond becomes stronger and the interaction acquires covalent characteristics. This is seen in the IR stretching frequencies of various N-H...O hydrogen bonds found, Figure 1.2-11 [66]. This is an illustration of the two effects that are involved in the SSHB, and their relationship with the donor – acceptor contact distance. When this distance is above ca. 2.60Å there is only an electrostatic contribution; at distances of less then 2.60Å there is a covalent contribution that increases in importance as the contact distance becomes shorter.

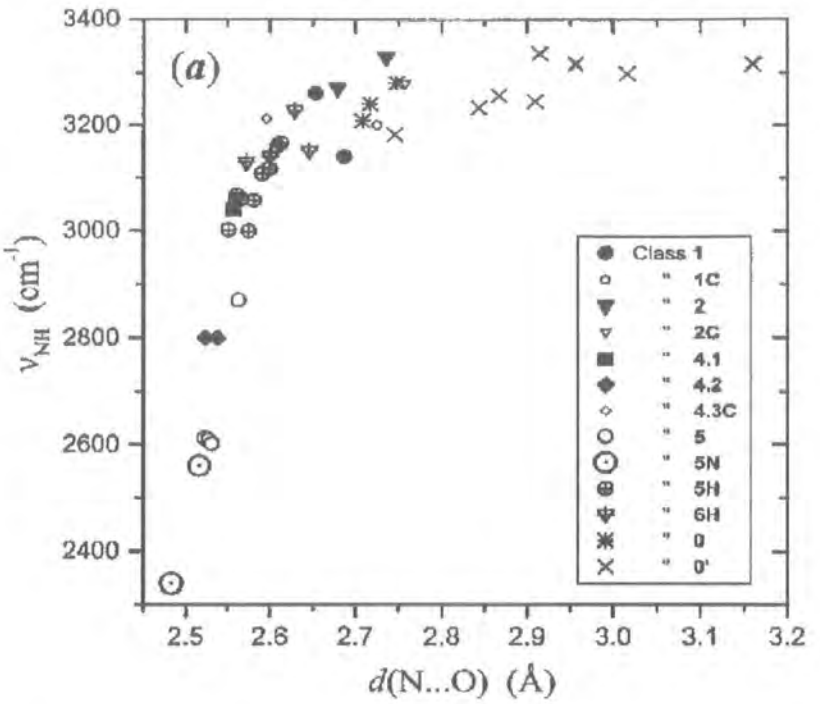

Figure 1.2-11 IR VNH-stretching frequencies (cm-1) versus H-bond contact distances, from Gilli et al [66]. The classes refer to various substituents around the enaminone. There is a rapid, linear fall in the stretching frequency as the contact distance falls, staring at around 2.60Å. This reflects the onset of covalency in the hydrogen bond.

1.3 *Techniques*

1.3.1 Single Crystal X-Ray Diffraction

XRD experiments were carried out employing a variety of machinery which are catalogued and referenced here.

1.3.1.1 Diffractometers in Durham[iv]

Bruker SMART-1000: Siemens SMART Version 4.050 (Siemens Analytical X-ray Instruments, 1995 [67]

SMART-6000 Siemens SMART Version 5.625 [68]

Fddd four-circle diffractometer [69]

The SMART 1K and 6K machines are fitted with area detectors and molybdenum X-ray tubes producing monochromatic radiation of wavelength 0.71073Å. Figure 1.3-1, below, shows the experimental set up of the machines used for all standard experiments. The Fddd is a four circle machine that is fitted with: (i) a Siemens rotating-anode generator; (ii) a Huber goniometer with offset Φ circle; (iii) a Siemens Fast Scintillation Detector; and (iv) an APD '202' Displex cryogenic refrigerator [69].

[iv] At time of writing, information on all equipment in the Durham University Crystallography group can be found at: http://www.dur.ac.uk/crystallography.group/

Figure 1.3-1 The SMART 1000 as found in the Durham crystallography laboratory. In this diagram, the Oxford Cryosystems' 'HeliX' is being used.

1.3.1.2 Temperature Regulation

All standard experiments were carried out using an Oxford Cryosystems Ltd. Cryostream [70]. This operates using an open flow of N_2 gas that can be used to regulate a stable experimentation temperature of between 90 and 400K. A continuous stream of dry nitrogen gas, of initial temperature 77K, is heated to the desired temperature and then blown onto the sample, thus providing a stable temperature. There is the added bonus that this provides a oxygen and water-free environment for the sample, thus helping to reduce sample degradation should the sample be air or water sensitive[v]. For this reason even experiments carried out under ambient temperatures have been done under nitrogen flow.

[v] Since the advent of area detectors, the data collection phase of a standard experiment has fallen to only a fraction of what it was just 10 years ago. While this has reduced problems associated with crystals becoming damaged due to their experimental environment, it is obviously advantageous to reduce all potential sources of error.

For lower temperatures (on the SMART-1K) a He gas open flow "HELIX" cryostream was used. [71] This equipment works in the same way as the N_2 cryostream of the previous paragraph, excepting that as Helium gas is being used, the lowest temperature available is in the region of 28(0.3) K. As He gas is rather more expensive than N_2 gas, only experiments below around 100K are carried out using this equipment; though higher temperatures are possible, they may as well be carried out under nitrogen.

1.3.1.3 Processing, Interpretation and Presentation of data

The intensities of the Bragg reflections were calculated using the SAINT+ software package [72], and prepared for analysis using XPREP. [73] The initial structure solution was derived using SHELXS-97 and structure refinement carried out using SHELXL-97 [73]. The molecular graphics used within this document were generated from either XP within the SHELXL software suite or Materials Studio [74]. Where it has been applied, analytical correction for absorption has been carried out using SADABS [72].

1.3.2 Neutron Diffraction Experiments

The general principles of single crystal neutron diffraction are discussed fully by C.C. Wilson in "Single Crystal Neutron Diffraction From Molecular Materials" [75]: any reader who is interested in the basic principles, applications, strengths and weaknesses of such an experiment are encouraged to read this, or other suitable texts. We shall restrict ourselves here to aspects of neutron diffraction that are directly relevant to our studies, and details of experimental equipment used.

Why use neutrons at all?

X-rays are diffracted from the electrons while neutrons are diffracted by the nuclei of atoms. As the nuclei of different atoms - and different isotopes - diffract very differently, it is possible to distinguish between atoms with similar numbers of electrons in a neutron experiment. This simple isotropic differentiation is not possible using X-rays. In our studies, neutron diffraction is of most importance when considering hydrogen atoms. Since protons have only one electron associated with them, and this electron is always involved in bonding, it is very difficult to locate the proton position – impossible to do so with great accuracy or certainty using X-ray diffraction techniques. This problem is overcome in neutron diffraction as: (i) it is the proton *itself* that does the diffracting and, (ii) the scattering power of said proton is comparatively high when compared to X-ray heavy atoms. Thus, when the position and atomic displacement parameters of hydrogen atoms are central to the study, neutron diffraction has been sought as the technique of choice.

1.3.2.1 Experiments at the ILL

The Institute Max von Laue-Paul Langevin (ILL) is a high flux neutron source dedicated to scientific research. Comprehensive information about the Institute can be found at http://www.ill.fr/. The thermal neutron four-circle diffractometer 'D19' at the ILL has been used for various experiments reported within this work. This diffractometer has its own web pages at: http://www.ill.fr/YellowBook/D19/ which cover all fundamental aspects of experimentation on this machine.

1.3.2.2 Experiments at ISIS

The Rutherford Appleton Laboratory is home to ISIS, a high intensity spallation neutron source. Rather than producing a steady state of neutrons, as is the case with reactor based neutron sources (such as the ILL), a spallation source generates neutrons by firing high energy charged particles at a heavy metal target. At ISIS this process involves accelerating H^- ions in a linear particle accelerator, and then in a synchrotron, until they have an energy of 800MeV, at which point they are shot at a tantalum target. This procedure is repeated 50 times a second and the result is a pulse of neutrons. Complete information about ISIS can be found at: http://www.isis.rl.ac.uk/index.htm. The SXD Single Crystal Diffractometer has been used at ISIS. It uses the time of flight Laue technique to access large 3-D volumes of reciprocal space in a single measurement. A good introduction to this machine can be found at http://www.isis.rl.ac.uk/crystallography/sxd/

1.4 *Computational Chemistry*

Throughout this work, plane wave density functional theory (DFT) has been used via the Cambridge Serial Total Energy Package (CASTEP) [76]. CASTEP was used because one of its authors, Dr. Stewart Clark, has some links with the chemical crystallography group in Durham, and was therefore on hand to advise and assist with the calculations presented here. Here follows a summary of the basic principles of DFT and CASTEP, along with some basic details of the experimental set up.

1.4.1 Density Functional theory (DFT)

When carrying out calculations of solid state materials (or gas phase molecules or even atoms) from first principles, one is immediately faced with the "many body problem": electrons interact with one another. Thus, while the behaviour of the electron in an isolated hydrogen atom is a trivial problem with an exact answer, the behaviour of the two electrons of an isolated helium atom has no exact solution. The coupled equations can, in a simulation, be solved by numerical methods – though there will be millions of variables that need to be satisfied. Density Functional theory (DFT hereafter) is an exact theory for interacting electrons [77]. It is based on two seemingly simple principles, namely:

1. It is impossible that two different potentials give rise to the same ground-state electron density distribution, ρ(r).
2. The variational minimum of the energy is exactly equivalent to the true ground-state energy

Simply put, (1) states that the density of electrons determines the potential acting on the electrons and vice-versa. Therefore the energy of the system is a function of the electron density rather than the many body wavefunctions. From this starting point, Kohn and Sham derived their Kohn-Sham equation that is at the centre of the practical application of DFT. [78]:

$$E = E[\rho(r)] = \int \delta r V_{ext}(r)\rho(r) + E_{KE}[\rho(r)] + E_{H}[\rho(r)] + E_{XC}[\rho(r)] \qquad \text{Equation 1.4-1}$$

Or if you prefer: the energy of the electron density functional, E[ρ(**r**)], is the sum of four components (in the order of Equation 1.4-1, above): the electron-nuclear interaction (external potential), the kinetic energy of the electrons, the Hartree energy (coulomb e-e) and the exchange correlation of the electrons. The first three terms are formal and correct and we can know them exactly: the fourth

term is not known. In fact, the exchange correlation functional encompasses all the complexity of interacting electrons that were the cause of our many body problem, above.

This problem is overcome by using a very simple approximation that works very well over a range of systems. The exchange correlation of a uniform electron gas (jellium) can be calculated. We assume that for an infinitesimal element of density $\rho(r)\delta r$, the exchange-correlation energy is that of jellium with a density of $\rho = \rho(r)$. This is called the Local Density Approximation (LDA) [78], and while it is patently wrong – the charge density is highly non-uniform around atoms – its success has become its justification. For some systems LDA is poor, particularly with respect to binding and dissociation energies. This is no doubt a result of ignoring spatial variations in the density and so a functional has been developed that includes the gradient of the density, known as the Generalised-Gradient Approximation (GGA) [79]. The GGA scheme has been used exclusively in the work presented here.

1.4.2 The Plane Wave Pseudopotential Approach (PWP)

CASTEP uses plane waves as its basis set. The periodic plane waves are used to find the single practical solution of the Kohn-Sham equation – that is the ground state electron density. The plane wave basis sets' advantages and disadvantages can be summarized thus [76]:

- It is unbiased, so all space is treated equally
- It is complete (i.e. it spans all space)
- There is a single convergence criterion
- Plane waves are mathematically simple and their derivatives are products in k-space
- Plane waves do not depend on atomic positions

Although it has disadvantages:

- The number of plane waves needed is determined by the greatest curvature of the wavefunction
- Empty space has the same quality of representation (and cost) as regions of interest.

The advantages are significant and, from the point of view of the end user, it is especially useful to have a single parameter that defines the quality of the experiment: the energy cut-off, E_c. All plane waves of energy less than the energy cut off parameter are used in the expansion of the Fourier series that describes the overall wavefunction. For a more accurate simulation, one simply has to increase this energy cut-off until the practical results (total energy, bond length, cell parameters and so on) stop changing as the basis set size increases.

The problems with the method are also significant, and lead to the introduction of pseudopotentials[vi]. Since the number of plane waves required is dependent on the greatest curvature of the wavefunction, the tightly bound core electrons would require perhaps 10^{20} plane waves to represent the electronic states accurately. To side step this, an effective potential is constructed that replaces the nucleus and the core electrons. [80] This step is a further source of approximation in the simulation; however, as the core electrons do not take part in the chemistry of the system (by definition) and are usually environment independent, this turns out to be a reasonable indulgence. [81] Pseudopotentials have the additional advantage of reducing the number of electrons in the simulation [76]. The overall result is that one requires a far lower energy cut off of the basis set to achieve comparable quality of calculation.

[vi] Sometimes called 'effective core potentials'

1.4.3 Running CASTEP (PWP in practice)

A fundamental problem for any simulation is the compromise that must be reached between including all of the chemistry and physics of a system and the computational limits that are imposed as the model system becomes larger. While it would be nice to work with condensed matter systems with unit cells of, say, 2000Å^3, high quality simulations of such systems are extremely expensive. One must therefore work with model systems that cover the essentials of the system in question. As computing power becomes ever greater this problem eases: the calculations presented in this work were carried out on a desk top PC – just five years ago this would not have been possible.

With this in mind, calculations are carried out on isolated molecules rather than condensed matter (crystal structure) when (i) the crystal structure is unsuitable for calculations (basically, too large) and (ii) the molecule on its own is a reasonable representation of the system in question. To study an isolated molecule in CASTEP one places the molecule into a large unit cell to create a super cell. For condensed matter simulations one can simply feed crystallographic data into the code – although the diffraction derived geometry may not be identical to the optimized geometry within the particular basis set. Apart from anything else, the calculation refers to the 0K structure: experimentation is generally carried out at higher temperatures.

The quality of the simulation will affect how long the calculation will take. Time constraints are an important issue, and there is thus a compromise that has to be made as to quality verses time taken. The adjustable parameters that affect this trade off are energy cut off, E_c, the self consistent field tolerance, SCF, and the k point-sampling. Energy cut off (E_c) dictates the size of the basis set: all

plane waves of 'energy' less than this cut off are used. Depending on the atoms involved in the model system (and the type of pseudopotentials used), this value will vary as to what can be considered a high quality calculation. For a hydrocarbon C_xH_y, a E_c of 280 eV would be high quality while 240 eV would represent moderate quality[vii]. If one were to add a fluorine atom to the system then these values would rise to 330 eV for a high quality calculation and 300 eV for moderated quality.

The SCF tolerance defines when the calculation is 'finished', that is, when the changes in energy from cycle to cycle are sufficiently small to consider the calculation converged. Clearly there is a balance to be struck here as a value that reflects the overall quality of the simulation must be chosen. In general, a value of $1x10^{-6}$ eV has been chosen to give values that are expected to converge to about a milli electron volt.

k-point sampling arises from the application of Bloch's theorem: instead of having an infinite number of electrons in a crystal we have only the electrons of the unit cell, and a periodic potential which we describe with our plane-waves. This generates an infinite number of reciprocal space vectors within the first Brillouin zone and we *do* have an infinite number of electrons. However, when the k-points are close together, the differences when calculating the wavefunctions become negligible so we only have to calculate at a finite number of k-points. The upshot of all this is that as the k points are in reciprocal space, the larger the unit cell dimensions, the fewer k points need be sampled.

[vii] Convergence and validation notes for pseudopotentials used in this work can be found at the beginning of the pseudopotential files in Folder 'Chapter 1', Appendix C (on CD)

Needless to say, this is an extremely fortunate result. When considering the quality of the experiments and how many k-points to sample, one must consider what it is that is being calculated and the unit cell dimensions. A unit cell axis length of greater than 15Å probably need only be sampled once. This is because convergence of the results will be in the milli electron volt region when using a single k point in these cases.

Computational methods have the great advantage that in principle any system can be studied. While experimentalists have to be concerned with factors such as 'how easy is it to synthesis that compound' or 'will it crystalise' , the theorist can simply make things appear on the computer screen. A point of caution, however, is that not everything the theorist dreams up will be physically reasonable: the computer will, however, produce an answer to his question – regardless of the reasonableness of that question. Another great advantage of the computer simulation is that it provides direct access to properties such as the energy of a system, which can only be inferred from experimental techniques. The only question marks that hang over these results are the validity of the simulation itself – level of theory, basic set, approximations – and the aforementioned credibility of the model system used.

1.5 Concluding remarks

A variety of complimentary techniques have been employed here to probe various aspects of crystal structure. The detailed consideration of crystal structure under variable thermodynamic conditions is of great interest, primarily because there is a great deal to be learned from such studies that can not be discovered from single environment-condition experiments. There is still a great deal to be learned about crystal structures themselves, not least because it is still not possible to predict a crystal structure accurately or to predict features of molecular systems, such as the melting point of a system and its likely willingness to crystallise, a priori.

Computational methods are becoming ever more reliable and ever more accessible to the non-expert, a direct result of the increasing speed and memory of desk top computers. For the practical scientist this presents an enormous opportunity: the results of experiment can be compared with those of theory such that accurate insight into the subtleties of crystal structure can be fathomed. Presented here are some calculations that I hope provide some insight into the systems under closest scrutiny.

1.6 *References*

[1] W. Clegg, *Crystal Structure Determination*, OUP, Oxford, **1998**.

[2] J. P. Glusker, K. N. Trueblood, *Crystal Structure Analysis - A Primer*, 2 ed., OUP, New York, **1985**.

[3] J. D. Dunitz, E. F. Maverick, K. N. Trueblood, *Angew. Chem. Int. Ed. Engl.* **1988**, *27*, 880.

[4] H. B. Burgi, *Annu. Rev. Phys. Chem.* **2000**, *52*, 275.

[5] D. W. J. Cruickshank, *Acta Crystallogr.* **1956**, *9*, 747.

[6] D. W. J. Cruickshank, *Acta Crystallogr.* **1956**, *9*, 754.

[7] D. W. J. Cruickshank, *Acta Crystallogr.* **1957**, *10*, 504.

[8] V. Schomaker, K. N. Trueblood, *Acta Crystallogr.* **1968**, *B24*, 63.

[9] J. P. Chesick, J. D. Dunitz, U. v. Gizycki, H. Musso, *Chem. Ber.* **1973**, *106*, 150.

[10] K. L. Brown, G. J. Down, J. D. Dunitz, P. Seiler, *Acta Crystallogr.* **1982**, *B38*, 1241.

[11] W. R. Busing, H. A. Levy, *Acta Crystallogr.* **1964**, *17*, 142.

[12] C. P. Brock, J. D. Dunitz, *Acta Crystallogr.* **1982**, *B38*, 2218.

[13] P. Seiler, J. D. Dunitz, *Acta Crystallogr.* **1979**, *B35*, 2020.

[14] C. K. Johnson, *Thermal Neutron Diffraction*, OUP, Oxford, **1970**.

[15] J. D. Dunitz, D. N. J. White, *Acta Crystallogr.* **1973**, *A29*, 93.

[16] K. N. Trueblood, J. D. Dunitz, *Acta Crystallogr.* **1983**, *B39*, 120.

[17] V. Schomaker, K. N. Trueblood, *Acta Crystallogr.* **1998**, *B54*, 507.

[18] E. Maverick, J. D. Dunitz, *Mol. Phys.* **1987**, *62(2)*, 451.

[19] H. B. Burgi, S. C. Capelli, *Acta Crystallogr.* **2000**, *A56*, 403.

[20] H. B. Burgi, *Acta Crystallogr.* **1995**, *B51*, 571.

[21] S. C. Capelli, M. Fortsch, H. B. Burgi, *Acta Crystallogr.* **2000**, *A56*, 413.

[22] C. C. Wilson, *Chem. Phys. Lett.* **1997**, *280*, 531.

[23] C. C. Wilson, *Chem. Commun.* **1997**, 1281.

[24] C. C. Wilson, H. Nowell, *New J. Chem.* **2000**, *24*, 1063.

[25] C. C. Wilson, *Chem. Phys. Lett.* **2001**, *335*, 57.

[26] C. C. Wilson, *New J. Chem.* **2002**, *26*, 1733.

[27] C. C. Wilson, *Chem. Phys. Lett.* **2002**, *362*, 249.

[28] C. I. Ratcliffe, B. A. Dunell, *J. Chem. Soc. Faraday Trans.* **1980**, *77*, 2169.

[29] A. Kubo, R. Ikeda, J. A. Sampedro, M. Inoue, D. Nakamura, *Bull. Chem. Soc. Japan* **1985**, *58*, 2947.

[30] M. Punkkinen, L. Ingham, D. Taylor, P. Allen, *J. Phys. Chem.* **1975**, *8*, 2159.

[31] M. Mortimer, E. A. Moore, M. A. K. Williams, *J. Chem. Soc. Faraday Trans.* **1996**, *92*, 2871.

[32] J. M. Cole, C. C. Wilson, J. A. K. Howard, F. R. Cruickshank, *Acta Crystallogr.* **2000**, *B56*, 1085.

[33] P. Kerkoc, V. Venkataramenen, S. Lochran, R. T. Bailry, F. R. Cruickshank, D. Pugh, J. N. Sherwood, R. Moseley, A. E. Goeta, C. W. Lehmann, J. A. K. Howard, *J. Appl. Phys.* **1996**, *80*, 6666.

[34] W. B. Connick, L. M. Henling, R. E. Marsh, H. B. Gray, *Inorg. Chem.* **1996**, *35*, 6261.

[35] R. T. Bailey, F. R. Cruickshank, P. Kerkoc, S. Lochran, D. Pugh, J. N. Sherwood, A. J. Blake, S. Parsons, *J. Appl. Phys.* **1995**, *78*, 3102.

[36] A. R. West, *Solid State Chemistry and its Applications*, John Wiley & Sons, New York, **1984**.

[37] N. K. Solanki, M. A. Leech, E.J.L. McInnes, J.P. Zhao, F.E. Mabbs, N. Fedder, J. A. K. Howard, J.E. Davies, J.M. Rawson, M. A. Halcrow; *J. Chem. Soc: Dalton Tarns.* **2001,** *14*, 2083-2088.

[38] K. Prout, S. J. Heyes, C. M. Dobson, A. McDaid, T. Maris, M. Muller, M. J. Seaman, *Chem. Mater.* **2000**, *12*, 3561.

[39] F. Grepioni, G. Cojazzi, S. M. Draper, M. Scully, D. Braga, *Organometallics* **1998**, *17*, 297.

[40] L. J. Farrugia, A. M. Senior, D. Braga, F. Grepioni, A. g. Orpen, J. G. Crossley, *J. Chem. Soc. Dalton Trans.* **1996**, 631.

[41] G. A. Jeffrey, *An Introduction to Hydrogen Bonding*, OUP, New York, **1997**.

[42] T. Steiner, *Angew. Chem. Int. Ed. Engl.* **2002**, *41*, 48.

[43] M. W. Feyereison, D. Feller, D. A. Dixon, *J. Phys. Chem.* **1996**, *100*, 2993.

[44] J. J. Novoa, F. Mota, *Chem. Phys. Lett.* **2000**, *318*, 345.

[45] L. Turi, J. J. Dannenberg, *J. Phys. Chem.* **1993**, *97*, 7899.

[46] T. v. Mourik, F. B. v. Duijnevekdt, *J. Mol. Struct.* **1995**, *341*, 63.

[47] G. R. Desiraju, *Angew. Chem. Int. Ed. Engl.* **1995**, *34*, 2311.

[48] G. R. Desiraju, *Acc. Chem. Res.* **1996**, *29*, 441.

[49] F. A. Cotton, L. M. Daniels, G. T. Jordan, C. A. Murillo, *Chem. Commun.* **1997**, 1673.

[50] F. H. Allen, *Acta Crystallogr.* **2002**, *B58*, 380.

[51] G. R. Desiraju, *Science* **1997**, *278*, 404.

[52] J. Bernstein, J. Henck, *Mat. Res. Bull.* **1998**, 119.

[53] W. W. Cleland, P. A. Frey, J. A. Gerlt, *J. Biol. Chem.* **1998**, *273*, 25529.

[54] W. W. Cleland, *Arch. Biochem. Biophys.* **2000**, *382*, 1.

[55] P. A. Frey, S. Whitt, J. Tobin, *Science* **1994**, *264*, 1927.

[56] H. B. Burgi, J. D. Dunitz, *Acc. Chem. Res.* **1983**, *16*, 153.
[57] G. K. H. Madsen, C. Wilson, T. M. Mymand, G. J. McIntyre, F. K. Larsen, *J. Phys. Chem. A* **1999**, *103*, 8684.
[58] G. K. G. Madsen, B. B. Iversen, F. K. Larsen, M. Kepon, G. M. Reisner, F. H. Herbstein, *J. Am. Chem. Soc.* **1998**, *120*, 10040.
[59] C. C. Wilson, N. Shankland, A. J. Florence, *Chem. Phys. Lett.* **1996**, *253*, 103.
[60] C. C. Wilson, *Acta Crystallogr.* **2001**, *B57*, 435.
[61] Z. Malarski, M. Rospenk, L. Sobczyk, E. Greech, *J. Phys. Chem.* **1982**, *86*, 401.
[62] F. Hibbert, J. Emsley, *Adv. Phys. Org. Chem.* **1990**, *26*, 255.
[63] G. Zundel, *Adv. Phys. Org. Chem.* **2000**, *111*, 1.
[64] T. Steiner, C. C. Wilson, I. Majerz, *Chem. Commun.* **2000**, 1231.
[65] S. Humbel, *J. Phys. Chem.* **2002**, *A106*, 5517.
[66] P. Gilli, V. Bertolasi, V. Ferretti, G. Gilli, *J. Am. Chem. Soc.* **2000**, *122*, 10405.
[67] Bruker AXS, Madison, Wisconsin, U.S.A. **1995**. http://www.bruker-axs.de/
[68] Bruker AXS, Madison, Wisconsin, U.S.A. **2000**. http://www.bruker-axs.de/
[69] R. C. B. Copley, A.E.Goeta, C. W. Lehmann, J. C. Cole, D. S. Yufit, J. A. K. Howard, J. M. Archer, *J. Appl. Cryst.* **1997**, *30*, 413.
[70] Oxford Cryosystems Ltd, Oxford, UK. http://www.oxfordcryosystems.co.uk/
[71] Oxford Cryosystems Ltd, Oxford, U.K. http://www.oxfordcryosystems.co.uk/
[72] Saint+ Version 6.02., Bruker AXS, Madison, Wisconsin, U.S.A., **1998**.
[73] G. M. Sheldrick, Version 5.1 ed., Bruker AXS, University of Göttingen, Germany., **1997**.
[74] Accelrys Inc, **2004**. www.accelrys.com
[75] C. C. Wilson, *Single Crystal Neutron Diffraction From Molecular Materials*, World Scientific Publishing Co. Pte. Ltd., London, **2000**.
[76] M. D. Segall, P. J. D. Lindan, M. J. Probert, C. J. Pickard, P. J. Hasnip, S. J. Clark, M. C. Payne, *J. Phys.: Condens. Matter.* **2002**, *14*, 2717.
[77] P. Hohenberg, W. Kohn, *Phys. Rev.* **1964**, *136*, B864.
[78] W. Kohn, L. J. Sham, *Phys. Rev.* **1965**, *140*, A1133.
[79] J. P. Perdew, J. A. Chevary, S. H. Vosko, K. A. Jackson, D. J. Singh, C. Fiolhais, *Phys. Rev.* **1992**, *B46*, 6671.
[80] M. T. Yin, M. L. Cohen, *Phys. Rev.* **1982**, *B26*, 3510.
[81] D. Vanderbilt, *Phys. Rev.* **1990**, *B41*, 7892.

2 4-(p-trifluoromethyl phenylethynyl) Fluorotoluene

2.1 *Introduction*

Various rod-like molecules have been characterised via single crystal X-ray diffraction as part of the collaboration with Professor Todd Marder and co-workers (see chapter 6.5). On considering one of these systems, it became obvious that the terminal CF_3 groups were disordered and investigation into the nature of this disorder began. As the crystals of this compound were not of the highest quality, a request was made to the good synthetic chemists to prepare crystals of a similar molecular system, namely the tolan 4-(p-trifluoromethyl phenylethynyl) prefluorotoluene of Figure 2.1-1, Tolan 1 hereafter, and this was duly supplied.

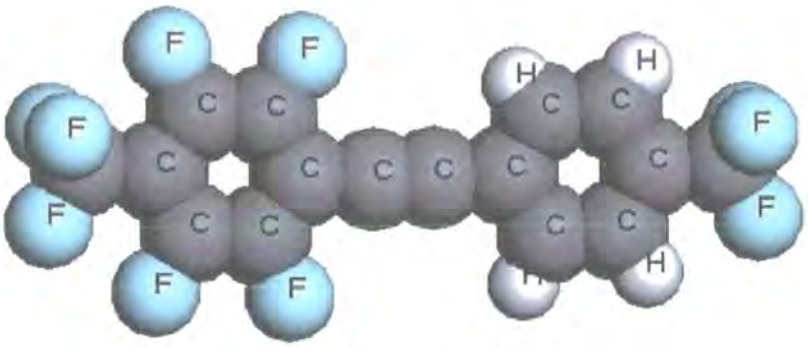

Figure 2.1-1 Sketch of the molecular system being studied. CF_3 groups are attached to the para position of the phenyl ring. One ring is perfluorinated (left) and the other perhydrogenated.

Of course there was no way of guaranteeing that this system would have disordered terminal CF_3 groups, however, there was good reason to believe that it would have. None the less, CF_3 groups are often disordered: a search of the

Cambridge Structural Database (CSD[1]) using a CF_3 group attached to a phenyl ring with any substitution as the fragment yielded 919 hits. Of these, 446 contained some disorder. In addition, there are no obvious strong intermolecular interactions expected for this system; nothing that would suggest the terminal triflouromethane group would be 'locked' into a definite conformation.

This particular system has two CF_3 groups that are in slightly different local environments: one is attached to a perfluorinated phenyl ring, while the other is attached to a hydrogenated phenyl ring (Figure 2.1-1). The main advantage of this is that we get 'two for the price of one' in the experimental phase. The similarities of the molecular environments are such that comparisons can be made between the two terminal groups in terms of the fluorination or hydrogenation of the phenyl rings and what effect that has on the behaviour of those terminal groups.

2.2 280K Structure of $C_{16}F_{10}H_4$

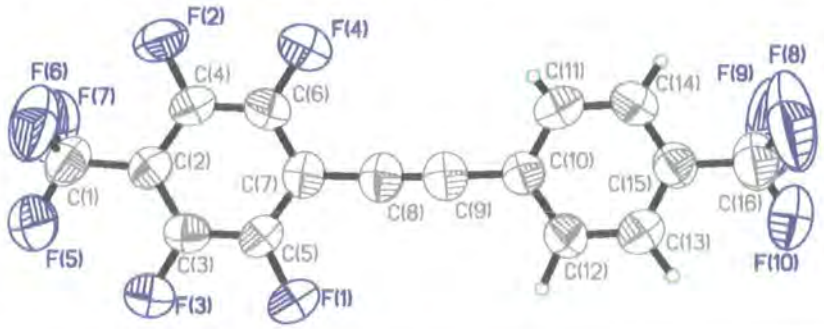

***2-2-1: $C_{16}F_{10}H_4$ at 280K**: monoclinic, $P2_1/n$ and $Z = 4$, $R_1 = 7.84\%$, $R_2 = 29.67\%$, Rint = 0.0570, $a = 5.5687(3)$ Å, $b = 14.6960(7)$ Å, $c = 18.5503(9)$ Å, $\beta = 91.999°(2)$, $V = 1517.19(13)$ Å^3*

[1] Conquest V 1.6 (2003), CCDC

Description of Structure: As this (above) is an ambient temperature crystal structure, the ADPs of all the atoms are substantial. This is especially true of the terminal CF_3 groups, whose ADPs are significantly bigger than those of the rest of the molecule, as can be seen from Table 2.2-1. This suggests that there is disorder in the terminal CF_3 groups over and above the thermally induced vibration motion that the rest of the molecule experiences. Note that the hydrogen atoms positions have been found using the difference map rather than geometric positioning. Since there is very little high angle scattering from this crystal at ambient temperature, and hydrogen atoms are difficult to place due to their inherent lack of scattering power, the derived carbon – hydrogen bond lengths are inconsistent. The lengths here are 0.808(57), 0.926(57), 0.971(55) and 1.072(49) Å and should, of course, be similar; the fact that they are not, emphasises the difficulties that X-ray diffraction has when dealing with hydrogen atoms. The expected value, found in the International Tables, is 1.083(11) Å.[ii]

	F1-F4				F5-F7			F8-F10		
U_{eq}	.0897	.0956	.0914	.0973	.1622	.1444	.1482	.2502	.2390	.2283
mean	0.0935				0.1516			0.2392		

Table 2.2-1The size of the ADPs of the three groups of fluorine atoms expressed as the volume that they would encompass were they spherical

2.2.1 Crystal Packing and Intermolecular Interactions

There are four molecules in the unit cell. As expected, there are no short contacts indicating that there are no strong intermolecular interactions. The only even remotely short contact is between F2 and H12, that being 2.531 Å

[ii] International Tables for Crystallography; Vol C, Part 9.5 pp 691-707, IUCr - Kluwer Academic publishers (1992)

(3.248(3) Å F2 – C12). It should be stressed that this in not likely to be anything more that a marginally attractive force, as (i) it is between a phenyl fluorine and a phenyl hydrogen atom and (ii) 2.531 Å is not especially close. Diagrams of both the unit cell and the close intermolecular contact are shown in Figure 2.2-1.

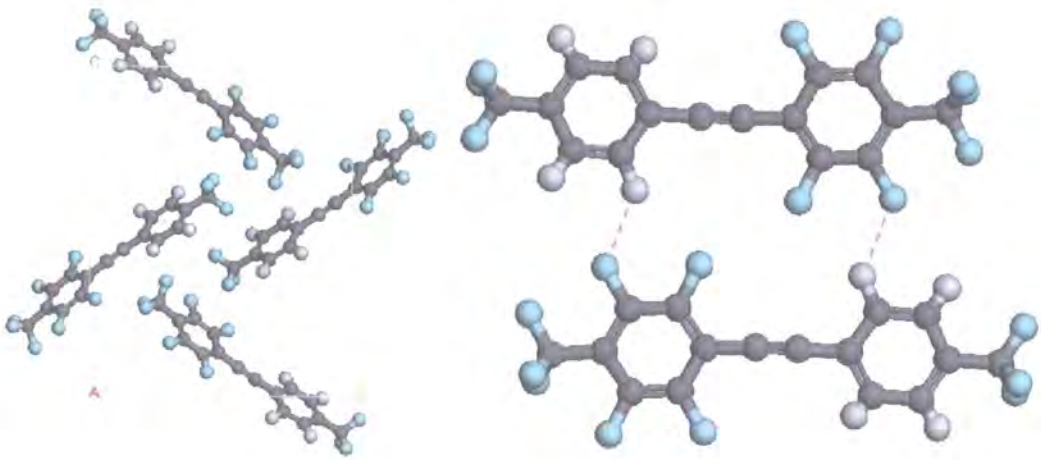

Figure 2.2-1 The unit cell viewed down the a-axis (left), and the 'close contact' between F3 and H2 (right)

From the point of view of the study of the terminal CF_3 groups it is instructive to consider the crystal environment in which they lie. The closest contact here is between F8 and H4 – they are 2.769 Å apart. Otherwise all contacts are in excess of 3 Å: F9 and F2 are 3.046(3) Å apart, F8 and F6 are 3.090(3) Å apart. The van der Waals radii of fluorine and hydrogen are 1.47 and 1.20 Å respectively[iii]. Thus none of these contacts are particularly short: the two groups are not likely to impact heavily on one another. The importance of this should be clear, that motion of the two groups, and the hindrance thereof, should be primarily due to molecular considerations rather than crystal packing effects.

[iii] A. Bondi, *J. Phys. Chem.*, (1964), **68**, 441.

2.2.2 Refinement Details

Although the quality of the data recorded is reasonable – R_{int} is 0.0570 – the refinement statistics are depressingly poor, R_1 is 7.48% and R_2 is 29.67%. Close inspection of the residual Fourier maps indicate that there are 8 peaks in electron density that are above 0.25, and all these peaks are around the trifluoromethyl groups. This unaccounted for electron density, coupled with the fact that the ADPs of these terminal fluorine atoms are abnormally large, indicates that there is disorder of these groups.

2.2.3 Modelling Disorder

A cursory study of the Fourier maps immediately shows the problem with using a non-disordered model for the CF_3 groups (Figure 2.2-2): while there are three main sites where the fluorine atoms are situated, there is some electron density found in a full circle. This is especially true of the F8-F10 group where one can see that there is a 1.5 eÅ^{-3} bridge running in a circle, while the highest region of electron density is 3.98 eÅ^{-3}. The F5-F7 group is certainly more ordered, although there is still a bridge of 0.5 eÅ^{-3} between the fluorine atoms; the maximum electron density is 5.98 eÅ^{-3} in this case.

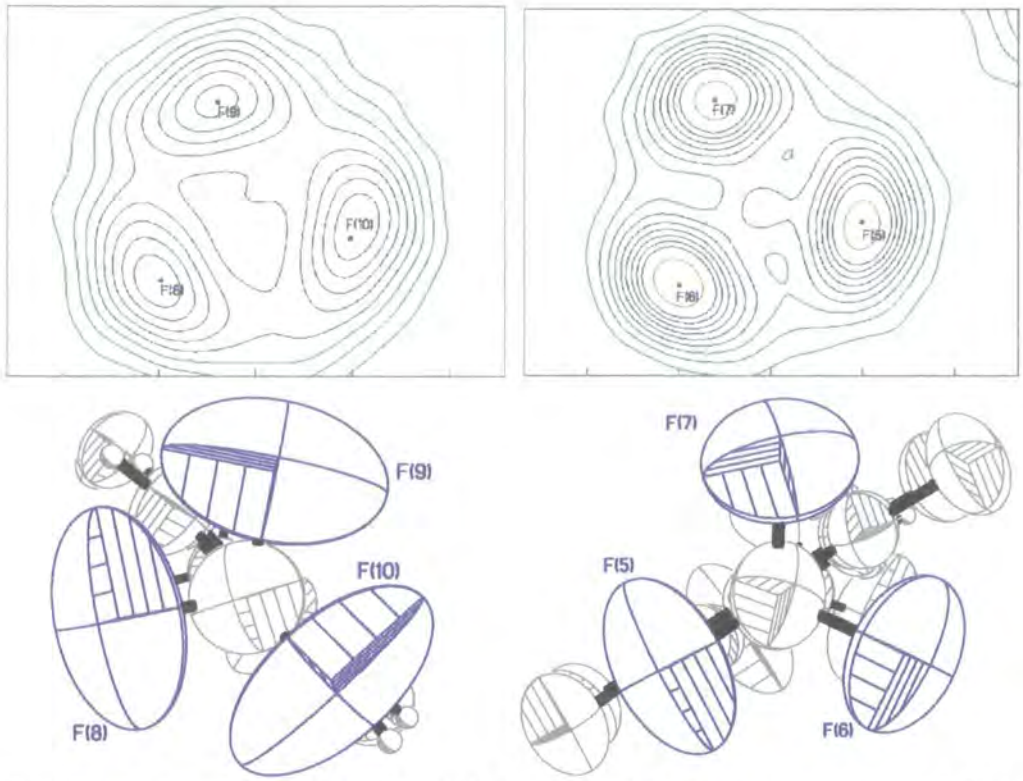

Figure 2.2-2 Fourier maps of the electron density in the plane of the three fluorine atoms plotted, top, and the corresponding ADPs (bottom). Contours of the Fourier maps are: 0, 0.5 and 1 $eÅ^{-3}$ (green); 1.5, 2.0, 2.5, 3.0, 3.5 and 4 $eÅ^{-3}$ (blue); 5 $eÅ^{-3}$ (brown).

In view of this a disordered model was used to refine the crystal structure, firstly when only the F8 – F10 group was considered to be disordered, and secondly when both the F8 – F10 *and* F5 – F7 groups were considered to be disordered. This was done by adding a second CF_3 group and introducing a partial occupancy of both the new group and the existing group such that the summation of the occupancy of the two groups was unity. The carbon – fluorine bond lengths were restrained to be approximately 1.30 Å in all cases (the expected value from the International Tables[11]). This method of modelling the disorder, in all its detail, was used in all experiments throughout this chapter.

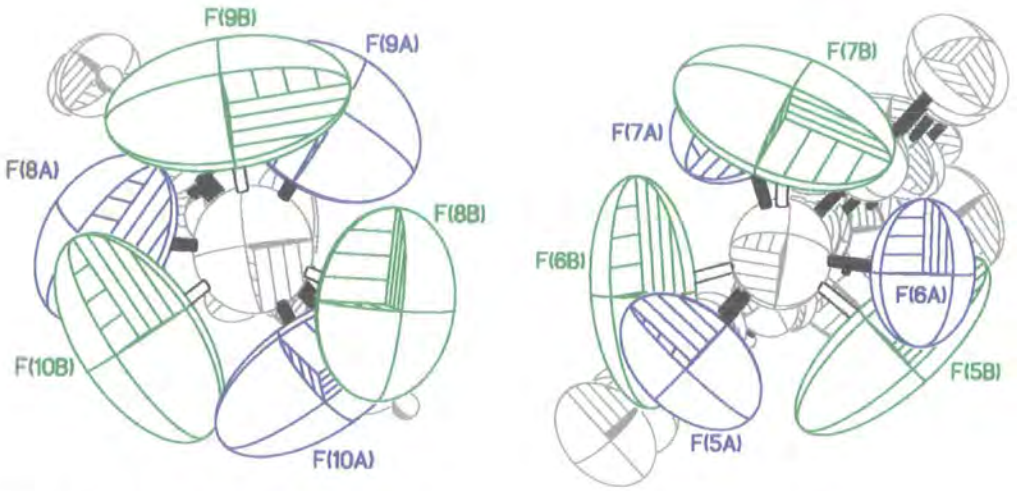

Figure 2.2-3 ADPs of the terminal CF_3 groups when a disordered model is used. Note that the ADPs of the minor component of the F5 – F7 group are not well behaved, and are indicative of a flawed model. (e.g. the disordered model is not appropriate)

When a disordered model is added to F8-F10 group, that is, the more diffusely distributed electron density, the six ADPs that now represent the electron density cover a far greater volume than when just three are used, although each ADP individually becomes smaller, Figure 2.2-3, left. The ADP sizes are summarised in Table 2.2-2. In this refinement the partial occupation of each of the two sets of atoms are 0.56057 : 0.43943 in favour of the F8a – F10a group. Given this, is seems reasonable to conclude that this is a reasonable model, rather than the artefact of a refinement that has been cynically engineered to improve the refinement statistics. The inclusion of this disorder has a dramatic effect on the refinement statistics: R_1 falls from 7.84% to 5.58% and R_2 falls from 29.67% to 18.37%! That is to say that most of the problem with the refinement is due to disorder in this CF_3 group.

	F8-F10			F8a-F10a			F8b-F10b		
U_{eq}	.2502	.2390	.2283	0.1489	0.1621	0.1830	0.1643	0.2158	0.2165
mean	0.2392			0.1647			0.1989		
	F5-F7			**F5a-F7a**			**F5b-F7b**		
U_{eq}	.1622	.1444	.1482	.1106	.1200	.1245	.1976	.2044	.2197
mean	0.2392			0.1185			0.2072		

Table 2.2-2 The ADP magnitude of the terminal fluorine atoms, without a disordered model (F8-10) and with a disordered model (F8a,b-F10a,b).

The second trifluoromethyl group, F5-F7 shows far less disorder in the Fourier maps and thus has smaller ADPs to start with. When a disordered model is used to describe this part of the crystal structure, the effect on the refinement statistics is not nearly so pronounced. R_1 falls to 4.38% (from 5.58%) and R_2 falls to 12.78% (from 18.37) on the addition of the second disordered group. This time the partial occupancy of the two CF_3 groups F5a-F7a and F5b-F7b are not approximately equal, rather the split is 0.713 : 0.287 in favour of the major group (suffix A). The secondary group's ADPs are also much larger than their major group counterparts and there is a great deal of overlap between the two sets of ADPs. In short, while the disordered model improves the refinement statistics – and it could hardly fail to do so – the improvement is small and the plausibility of the resulting ADPs is questionable. This model has therefore been rejected and in all experiments in this chapter, only the F8-F10 group has been modelled as disordered.

2.3 *Variable Temperature Experiments*

Data from the Tolan 1 crystals have been recorded at 10 different temperatures ranging from 293 K to 40 K, using various crystals and both the 1K and 6K SMART diffractometers.

A summary of the experiments is given in Table 2.3-1 The experiment number refers to the number of the experiment that was given within the lab (all documentation refers to this number). There were 4 different crystals used throughout these standard experiments, with dimensions:

- Crystal 1: 0.30 x 0.26 x 0.16 mm.
- Crystal 2: 0.38 x 0.28 x 0.15 mm.
- Crystal 3: 0.15 x 0.15 x 0.1 mm.
- Crystal 4: 0.20 x 0.15 x 0.08 mm.

These crystals were mounted on a glass pin with epoxy glue and reused over several experiments as indicated in Table 2.3-1.

Temp/K	Exp No.	Machine	Crystal	Selected Diagrams:
293	2-3-1	6K	2	
280	2-2-1	1K	1	
230	2-3-2	1K	4	
200	2-3-3	1K	2	
160	2-3-4	1K	4	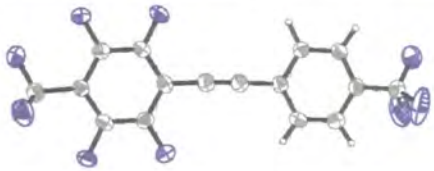
140	2-3-5	6K	4	
120	2-3-6	6K	2	
105	2-3-7	1K	4	
90	2-3-8	6K	4	
40	2-3-9	1K	3	

Table 2.3-1 A Summary of the experiments undertaken. Molecular structure diagrams at 280, 200, 140, 105 and 40 K (top to bottom) included.

Unit cell parameters for the full length experiments are tabulated in Table 2.3-2 and these results are shown plotted in Figure 2.3-1. In addition, the cell volume was found from short matrix determination experiments over the temperature range 30 – 320 K (Table 2.3-3). The difference between these long and short experiments is that while the full data collection yields thousands of data, for example 3391 data for structure 2-3-3 these matrix determinations typically have 40-60 reflections. As a result the errors in the latter are far greater: indeed the error figures generated by XL (the least squares refinement program) are optimistic for all the data reported as they do not take into account systematic errors.

Inspection of the data shows that the change in the unit cell volume is significant: -5.68% going from 293 to 40K (long experiments) and -6.74% going from 320 to 40K (short experiments). This indicates that the crystal is not tightly packed at room temperature. The changes in the unit cell parameters as a function of temperature are more or less isotropic: that is the a, b, and c axis lengths vary by about the same percentage over the temperature range. As expected, there is a linear relationship between the temperature and the cell volume, except as the experimental temperatures approached 0 K, where the ground-state structure is reached. The 230K structure appears to be an outlier in terms of the unit cell size, however, there is no indication from the refinement statistics that there is anything wrong or unusual about the structure refinement.

Temp (K)	a-axis (Å)	b-axis (Å)	c-axis (Å)	Beta (°)	Volume (Å^3)
40	5.4397(2)	14.4418(4)	18.2014(4)	92.894(2)	1428.1(1)
90	5.4604(2)	14.4488(4)	18.2045(5)	92.651(1)	1434.7(1)
105	5.4668(2)	14.4864(4)	18.2012(6)	92.655(2)	1439.9(1)
120	5.4768(2)	14.4959(4)	18.2324(6)	92.596(1)	1446.0(1)
140	5.4790(2)	14.5124(4)	18.2710(5)	92.611(1)	1451.3(1)
160	5.4891(5)	14.5691(13)	18.3097(16)	92.567(2)	1462.8(3)
200	5.5155(3)	14.5937(8)	18.3502(10)	92.468(2)	1475.7(2)
230	5.5140(3)	14.6068(8)	18.3845(8)	92.393(3)	1479.4(2)
280	5.5687(3)	14.6960(7)	18.5503(9)	91.999(2)	1517.2(2)
293	5.5675(10)	14.6667(25)	18.5528(33)	91.933(20)	1514.2(6)

Table 2.3-2 Unit cell parameters of the 10 structure refinements, with the estimated errors.

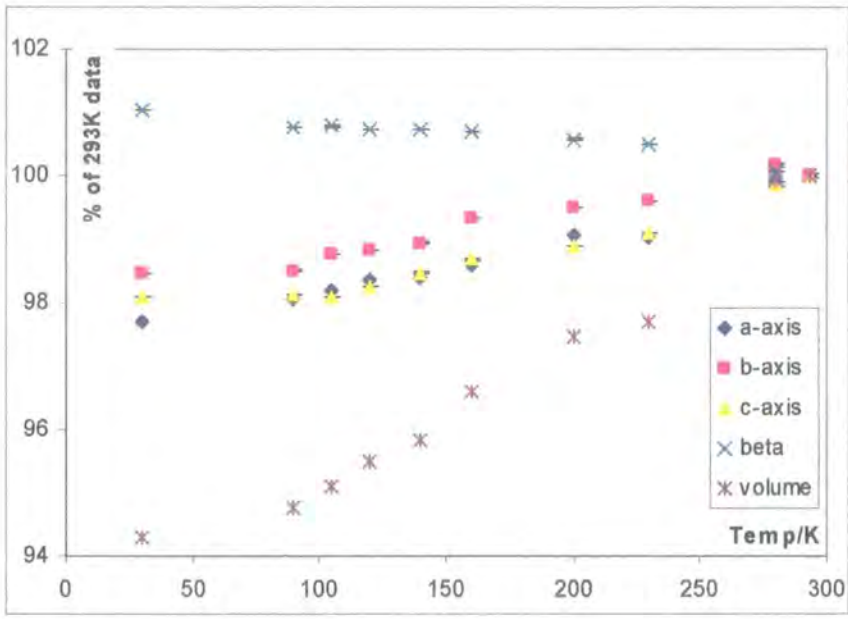

Figure 2.3-1 Plot of the unit cell parameters expressed as a percentage of the 293K data. Note that the error bars have been added, they are simply so small that they are not visible.

Temp (K)	Volume (Å^3)	Temp (K)	Volume (Å^3)
40	1428.22(25)	210	1479.47(97)
90	1435.14(32)	220	1484.12(80)
120	1448.52(8)	240	1494.25(73)
120	1448.56(10)	260	1499.81(80)
140	1454.38(74)	280	1513.24(70)
140	1451.19(52)	293	1514.17(58)
150	1457.9(1.5)	295	1513.97(87)
160	1462.18(70)	300	1515.9(1.1)
180	1468.69(74)	320	1530.3(2.1)
200	1474.97(64)		

Table 2.3-3 Unit cell volumes from matrix determinations and the estimated errors. At temperatures above room temperature the diffraction power of the crystals falls off dramatically – hence the errors rise sharply. This is also the reason that full length datasets were not collected above room temperature.

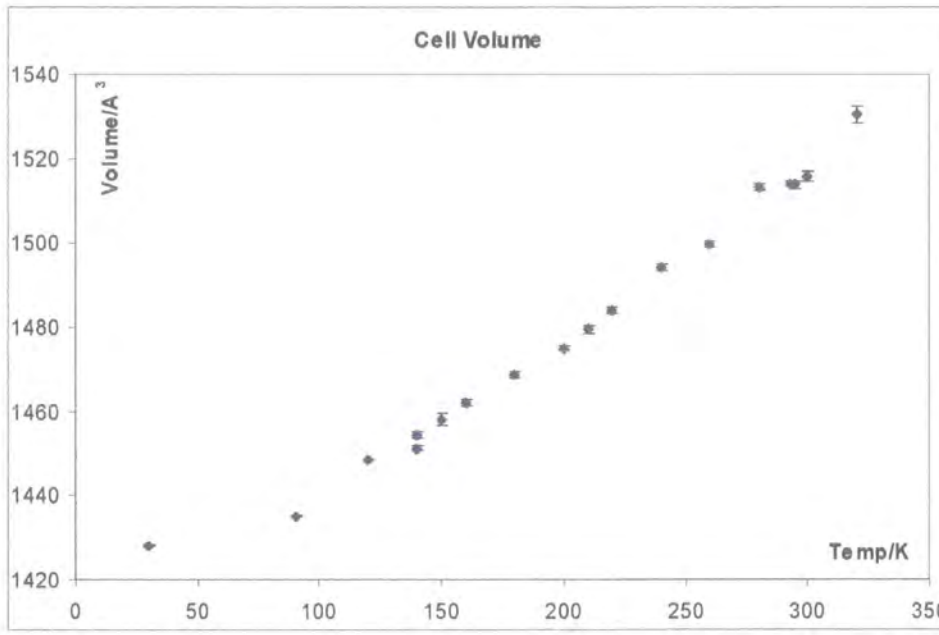

Figure 2.3-2 Plot of the unit cell volumes found from unit cell determinations. Note that the R^2 value of the line of best fit through the data, excluding the 40K experiment, is an excellent 0.994.[iv]

[iv] $R^2 = 1 - \text{sum}((\text{data} - \text{regression})^2 / \text{sum}(\text{data} - \text{datamean})^2)$

2.3.1 Atomic Displacement Parameters (ADPs)

The size of the ADPs reflects the smearing out of electron density from the mean position. Clearly at ambient temperatures the smearing out of electron density will be greater that at low temperatures. That is not to say, of course, that the smearing out will vary uniformly as a function of temperature: rather the difference in this variation yields insight into the flexibility of various parts of the molecule. Our title compound has three chemically distinct types of fluorine atoms: the phenyl fluorine atoms: F1-F4, the CF_3 group attached to the perfluorinated phenyl ring, F5 – F7, and the CF_3 group attached to the perhydrogenated phenyl ring, F8 to F10. The mean sizes of the ADPs of these three groups at all temperatures are tabulated in Table 2.3-4 and plotted in Figure 2.3-3.

Temp (K)	F1-F4	F5-F7	F8-F10
40	0.01538	0.01909	0.02268
90	0.02969	0.04167	0.05830
105	0.03094	0.04533	0.06903
120	0.03896	0.05593	0.08688
140	0.04445	0.06526	0.10569
160	0.04623	0.07159	0.12632
200	0.05917	0.09199	0.16493
230	0.07012	0.11279	0.19526
280	0.09350	0.15160	0.23917

Table 2.3-4 ADPs of the three groups of fluorine atoms.

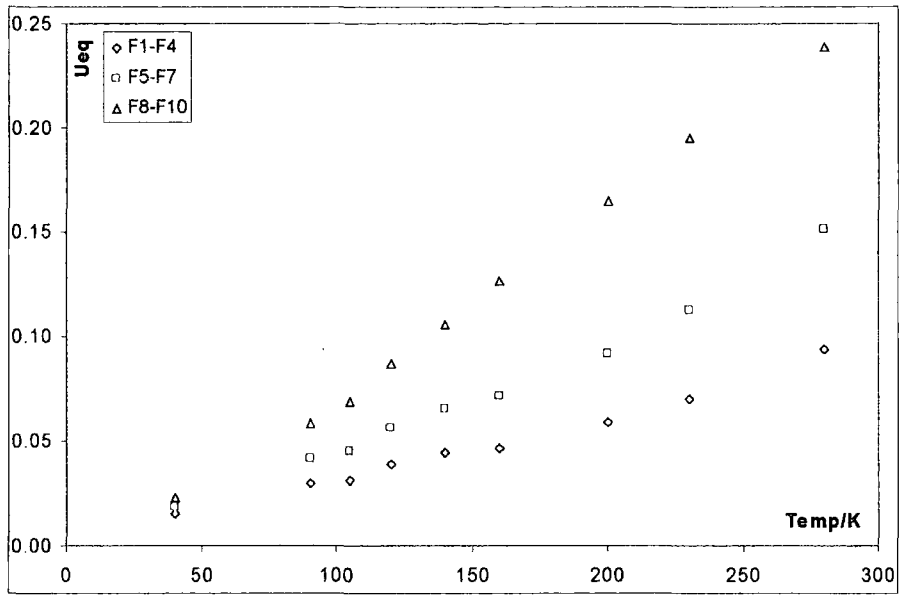

Figure 2.3-3 Plot of the mean size of the ADPs of the three groups of fluorine atoms. While at higher temperatures the mean sizes are different for the three groups, at 40K the values converge to approximately the same size.

As temperature approaches 0 K, the size of the ADPs of the three groups converge to a similar size. Away from the zero point structure, the size of the ADPs of the three groups increases, however those of F5 – F7 do so to a greater extent than those of F1-4, and those of F8 – F10 do so to an even greater extent. Were the experiment carried out at merely one temperature, this additional ADP size between the three fluorine atom groups could be due to static disorder – that is, frozen in positional disorder of the CF_3 group throughout the crystal. However, with the multiple temperature experiments one sees the variation in the ADP size, and hence this explanation cannot hold true. Therefore the explanation is that the additional size of the ADPs is the result of additional dynamic disorder. That is, the ADPs of atoms F5 – F10 are the result of motion that is in addition to that which one would expect were there only thermal motion present.

If one excludes the 40K data, where the results are expected to be anomalous due to quantum effects on approaching 0 K, the size of the ADPs varies with the equations:

$$F1\text{-}F4: y = 0.00033T - 0.0022, R^2 = 0.9795$$

$$F5\text{-}F7: y = 0.00056T - 0.0139, R^2 = 0.9833$$

$$F8\text{-}F10: y = 0.00097T - 0.0298, R^2 = 0.9992$$

Where R^2 is the linear regression and y is the mean size of the ADPs. The gradient of the line of best fit through the three sets of data is three times as steep in the case of F8-F10 as compared to F1-F4. The question then becomes,, what are the properties of this additional motion and why does it come about?

2.3.2 Fourier Maps, ADPs and Modelling Disorder

As the ADPs are the approximation of the smearing of the electron density, it is instructive to look at the Fourier maps that lead to them. In Figure 2.3-4, the Fourier maps of the electron density in the plane of atoms F8 – F10 are shown. In all electron density diagrams, the contours are 0, 0.5 and 1 eÅ^3 (green); 1.5, 2.0, 2.5, 3.0, 3.5 and 4 eÅ^{-3} (blue); 5, 6, 7, 8, 9 and 10 eÅ^{-3} (brown); 12, 14, 16, 18, 20 eÅ^{-3} (red). Their F5 – F7 counterpart diagrams are plotted in Figure 2.3-5, all plotting parameters are the same to those in Figure 2.3-4. For comparison a selection of Fourier maps of the perfluorinated phenyl ring are included in Figure 2.3-6.

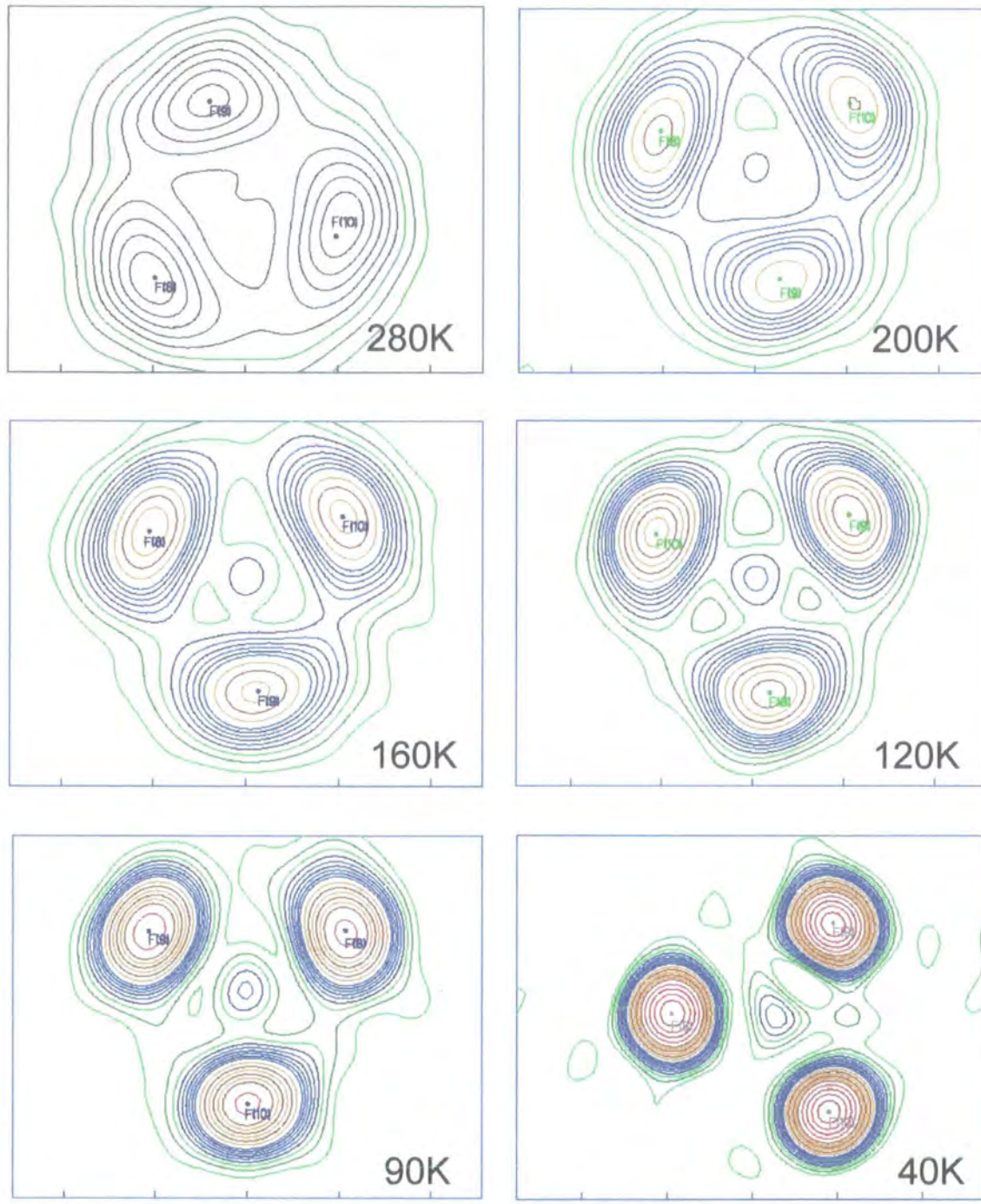

Figure 2.3-4 The Fourier Maps in the plane of atoms F8 – F10 across the 40 – 280K temperature region. While the 40K maps are almost fully ordered, even in the 120K maps there is significant electron density all around the plane. The electron density peaks are also becoming less circular going from 40K to 120K and beyond).

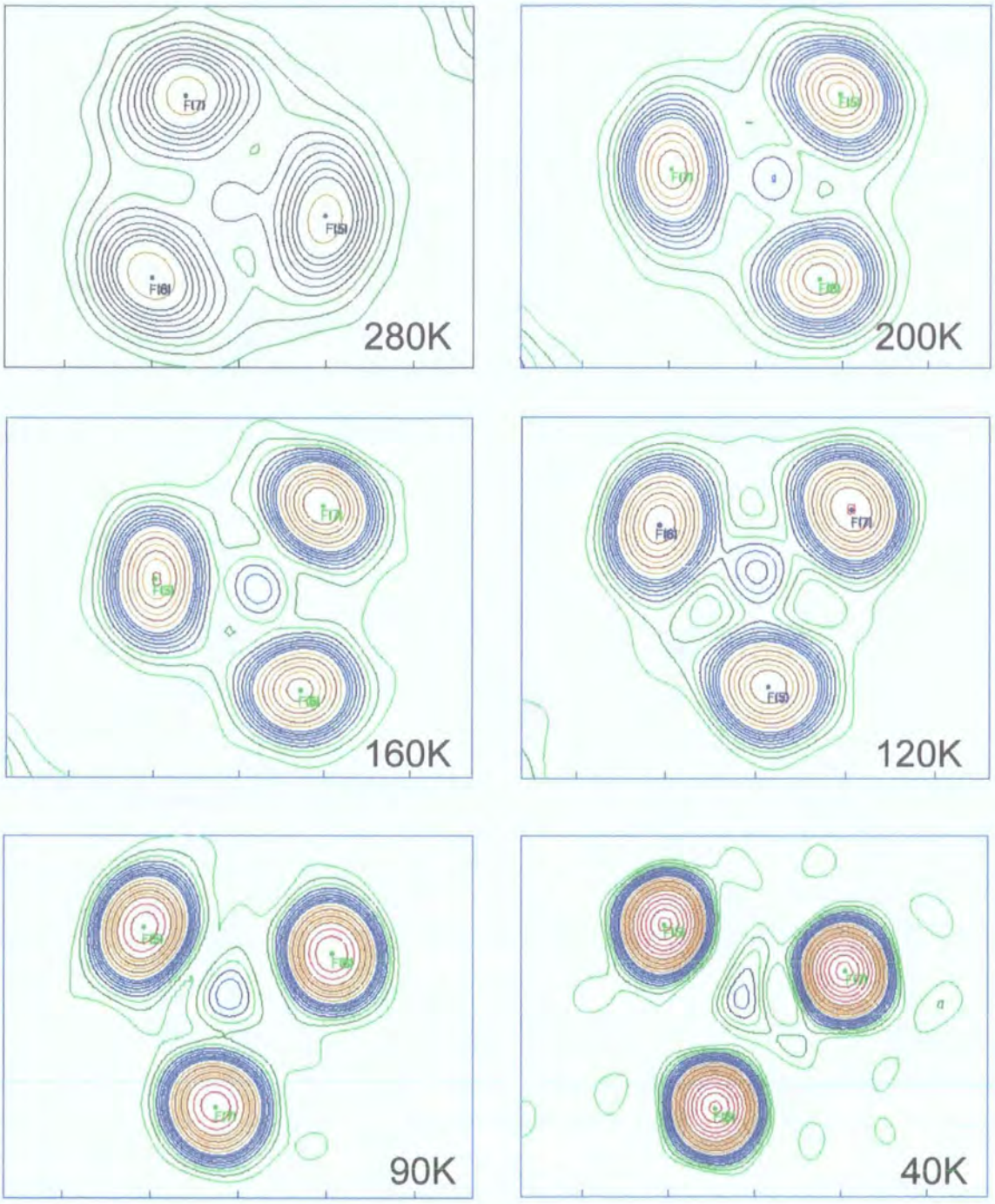

Figure 2.3-5 The Fourier Maps in the plane of F5 – F7 across the 40 – 280K temperature region. This group is more ordered than the F8 – F10 group at all temperatures. This is perhaps best illustrated with a close look at the 200K maps. While in the present figure, there is a 'bridge' of 0.5 $eÅ^{-3}$ in a circle around the group, in the F8 – F10 group this 'bridge' is 1.5 $eÅ^{-3}$.

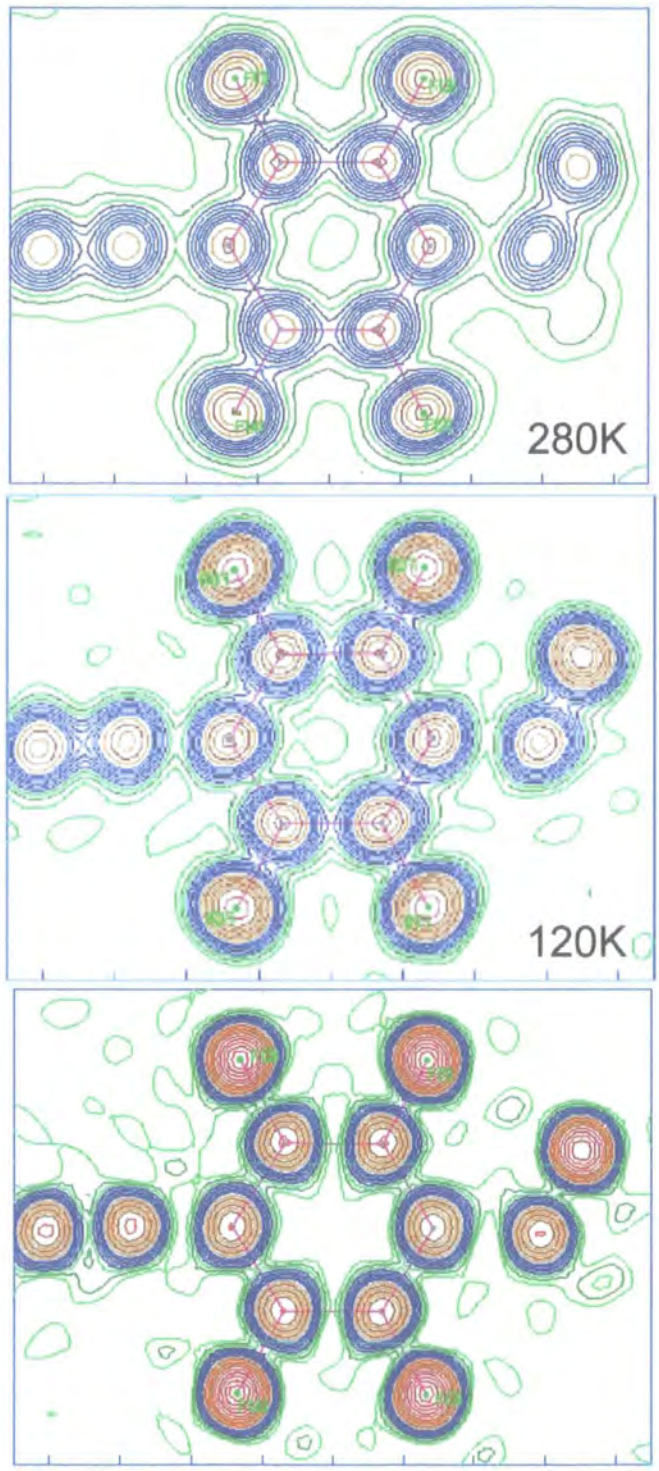

Figure 2.3-6 For comparison, the Fourier maps of F1 – F4 and the phenyl ring to which they are attached. Note that the peaks in electron density that represent the position of the atoms are well defined, even those at 280K.

The higher temperatures experiments confirm that there is a circular smearing of the electron density, and given that it is *known* that this disorder is dynamic, this represents a circular motion of the CF_3 group. At lower temperatures the system, as expected from the plots of the mean size of the ADPs, is ordered.

In terms of the structure refinement, it was shown (above) that employing a disordered model using a split set of fluorine atom positions improved the refinement statistics. To explore the effect of this kind of refinement on the refinement statistics, the F8 – F10 group was modelled at each temperature. The results are plotted in Figure 2.3-7. At 40K it was not possible to produce a stable refinement using a disordered model – this is due to there being no disorder to model at the lowest temperatures, as shown in the Fourier map of the 40K structure in Figure 2.3-4.

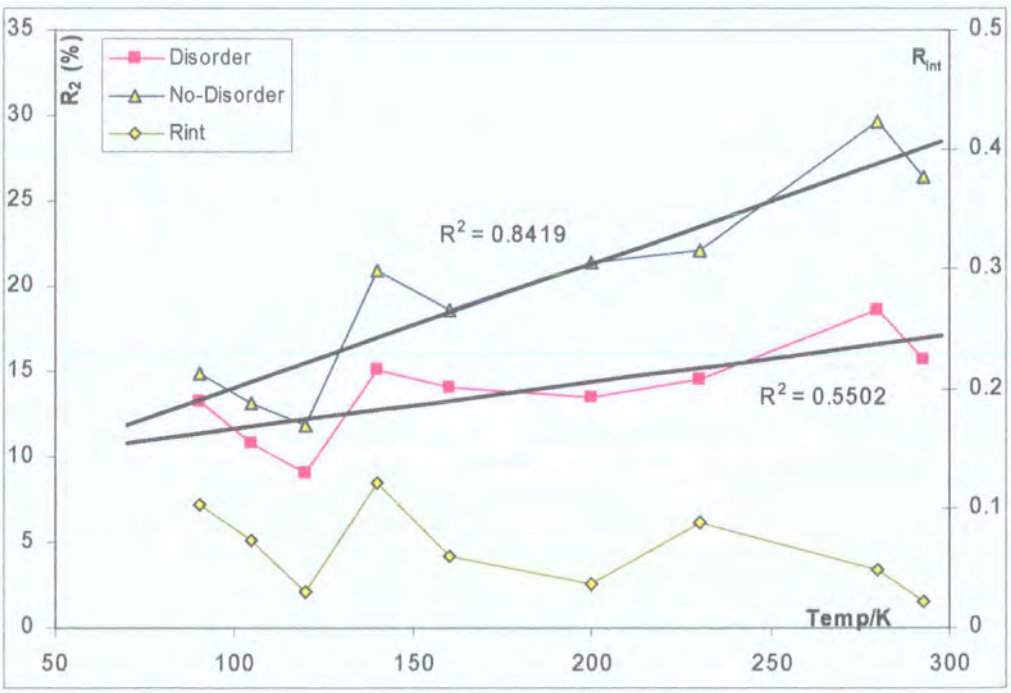

Figure 2.3-7 Plot of the R_2 values (blue and pink; scale on left axis) and the R_{int} (yellow; scale on right axis). While the refinement statistics tend to get better as experimental temperatures becomes lower, a major factor is the R_{int} value. Also note that the difference between the ordered and disordered structure reduces with temperature. R^2 of the trend line included: the temperature dependence of the refinement statistics is not entirely convincing.

As might be expected, the improvement in the refinement statistics becomes less significant at lower temperatures. Clearly, as there is less diffusely smeared electron density at lower temperatures, the non-disordered model describes the system better and better: The difference between the R_2 values at 280K is 11.05% [29.67% vs. 18.62%), while at 90K the difference was a meagre 1.7% (14.93% vs. 13.23%). At the lower temperatures the ADPs of the disordered model begin to become less stable and their shapes less reasonable. Perhaps more interesting is the fact the quality of the data, R_{int}, while having a significant effect on the refinement statistics (Figure 2.3-7), didn't seem to have a significant effect on the size of the ADPs and unit cell parameters (Figure 2.3-3 and Figure 2.3-1 respectively).

2.3.3 TLS Analysis

Segmented rigid body analysis was carried out on all structure refinements using THMA11 version 20-04-91, within the WinGX software suite[v]. In each case the molecule was split up such that the terminal CF_3 groups were considered as separate rigid segments with an axis of rotation about the carbon – carbon bond that attaches the CF_3 group to the phenyl ring included (i.e. C2 – C1 in the case of group F5 – F7 and C15 – C16 in the case of the F8 – F10 group). A summary of the results is given in Table 2.3-5. These include the mean squared amplitude (MSA), force constant (FC) assuming harmonic motion, and a barrier to rotation (Barrier) assuming that the CF_3 group is sitting in a three fold potential.

---

[v] L.J. Farrugia (1991) *J. Appl. Cryst.* **32** 837-838

F5 - F7			
Temp	**MSA Deg^2**	**FC $J\ mol^{-1}\ deg^{-2}$**	**Barrier $kJ\ mol^{-1}$**
40	20.5 (2.5)	19.6(2.5)	14.3
90	61.9 (5.8)	12.4(1.1)	9.1
105	72.0 (6.2)	12.4(1.0)	9
120	88.1 (7.1)	11.5(0.9)	8.4
140	107.3 (8.8)	11(0.8)	8
160	133.6 (10.2)	10(0.7)	7.2
200	178.4 (14.2)	9.4(0.7)	6.8
230	231.5 (17)	8.3(0.6)	6
280	313.7 (24.1)	7.4(0.5)	5.4
F8 - F10			
Temp (K)	**MSA (Deg^2)**	**FC ($J\ mol^{-1}\ deg^{-2}$)**	**Barrier ($kJ\ mol^{-1}$)**
40	33.2 (2.9)	11.2 (1.0)	8.2
90	129.5 (6.2)	5.9 (0.3)	4.3
105	179.6 (9.5)	4.9 (0.2)	3.6
120	228.7 (11.4)	4.4 (0.2)	3.2
140	301.0 (9.7)	3.9 (0.1)	2.8
160	423.1 (20.4)	3.2 (0.1)	2.3
200	591.8 (31.9)	2.8 (0.1)	2.1
230	733.1 (39.3)	2.6 (0.1)	1.9
280	889.6 (56.1)	2.6 (0.2)	1.9

Table 2.3-5 Summary of the segmented-rigid body analysis: Mean Square Amplitude (MSA), Force Constant (FC) and Barrier to Rotation in a 3-fold potential (Barrier).

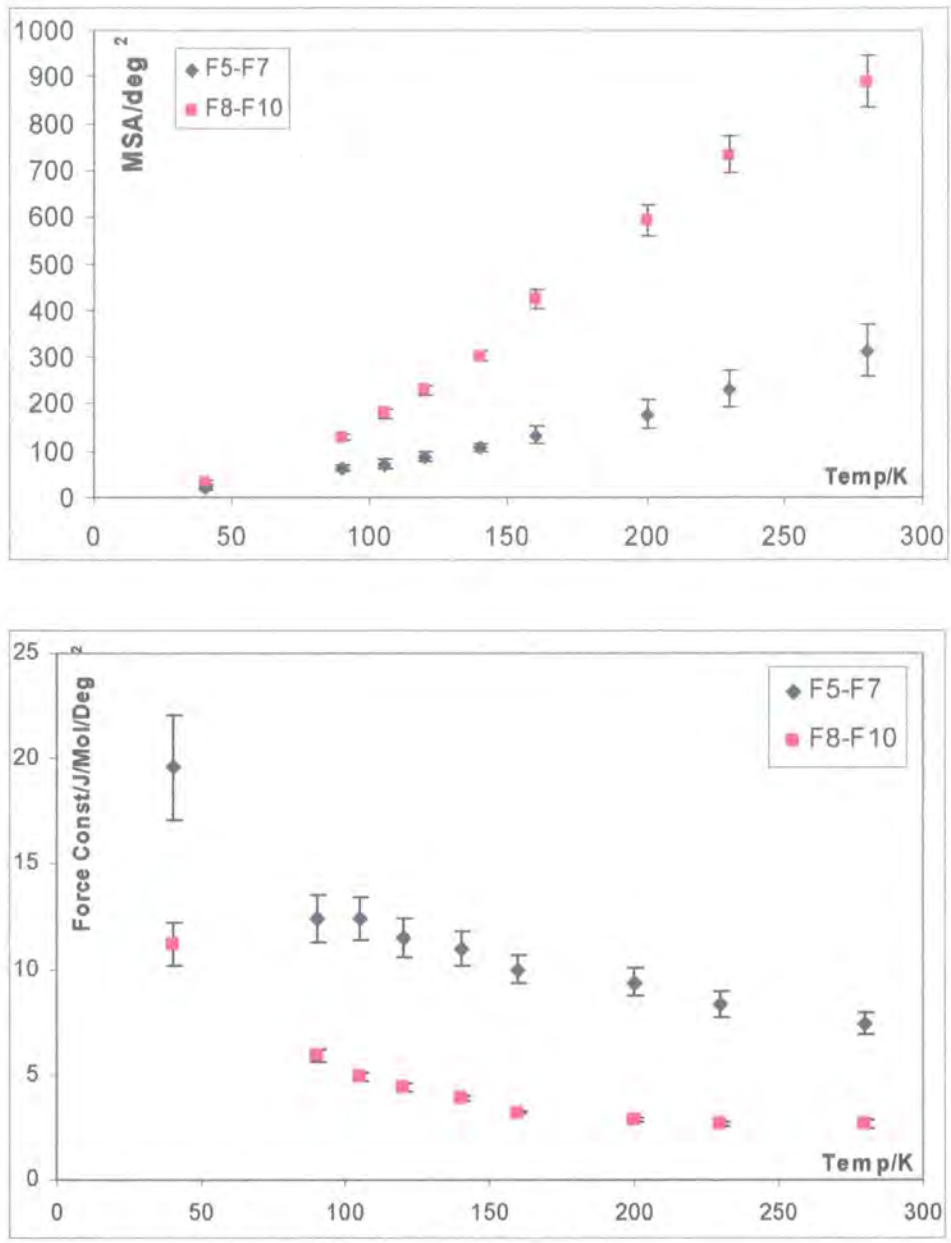

Figure 2.3-8 Plots of the mean square amplitude (top) and the corresponding force constants (bottom). The barrier to rotation mirrors the force constant values. Note that although the mean square amplitude values are subject to the smallest errors at 40K, the errors in the force constant (and hence rotation barrier) are greatest at the lowest temperatures.

The barrier to rotation is found to be between 1.9 and 4.3 kJ mol^{-1} for F8-F10 and 5.4 and 9.1 kJ mol^{-1} for group F5 to F7 depending on the temperature used. In principle this result should be temperature independent, and it is worth considering why there seems to be temperature dependence and why the 40 K result is so out of kilter with the other results. The latter question is in fact quite straight forward: the segmented rigid body analysis analyses the additional motion in the terminal CF_3 groups as against the rest of the molecule - even a cursory look at Figure 2.3-8 reveals that there isn't a great deal of additional motion at 40K. Hence the result is subject to massive errors and is not reliable.

At the higher temperatures there are a number of factors that will affect the results, none of which can be readily quantified. Firstly the assumption that there is simple harmonic motion within the CF_3 groups at higher temperatures breaks down. Secondly, the assumption that the crystal field is constant over a full range of temperatures is flawed: the volume of the unit cell varies by over 5% across the temperature range studied in this system, so it is unreasonable to make this assumption. Quite the opposite: as the crystal expands it would seem reasonable to believe that the motion of all parts of the molecules becomes less rigid. For a loosely packed molecular system, such as we have here, the assumption that the *rest* of the molecule is rigid (apart from the two CF_3 groups) may be poor.

2.4 *Neutron Structure*

Large crystals of Tolan 1 were taken to the Institute Laue-Langevin, Grenoble, France, and subjected to single crystal neutron diffraction analysis. A summary of the data is given below. The main difference between the low temperature neutron and X-ray structure is that the positions of the atomic nuclei are found accurately, in the former. This is especially true of the protons, for which it is possible to derive anisotropic ADPs from the neutron diffraction data (see below).

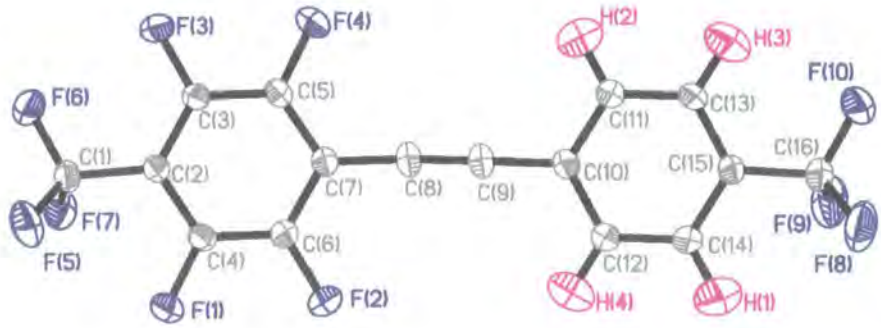

***2-4-1: $C_{16}F_{10}H_4$ at 40K (neutrons)**: monoclinic, $P2_1/n$ and $Z = 4$, $R_1 = 2.64\%$, $R_2 = 5.16\%$, $R_{int} = 0.0197$, $a = 5.4452(2)$ Å, $b = 14.4926(4)$ Å, $c = 18.2226(6)$ Å, $\beta = 92.9193°(1)$, volume = 1436.17(8) Å^3*

The ADPs (above) are drawn with 90% probability (rather than the 50% used for the X-ray structures), and shows the hydrogen atom's ADPs as being larger then those of the fluorine and carbon counterparts. Indeed, the mean size of the hydrogen ADPs is 0.0293(4), while the three groups of fluorine atoms are 0.0137(2), 0.0175(2) and 0.0224(2) (F1-3, F5-7 & F8-10 respectively), and are thus larger than any of the terminal fluorine atoms. The results of the segmented body TLS analysis shown in Table 2.4-1, along with the values for the 40K X-ray structure. The neutron values are significantly lower than those derived from X-rays, and consequently more in line with the TLS analysis derived over a large range of temperatures. However, it must be stressed that

the very low temperature structures are *not* ideal for this type of analysis as there is not a great deal of motion of any kind.

F5 – F7				
Temp	**Mean ADP size**	**MSA (Deg^2)**	**FC ($J\ mol^{-1}\ deg^{-2}$)**	**Barrier ($kJ\ mol^{-1}$)**
40	0.01262	25.9 (4.9)	15.0 (2.7)	10.9
40	*0.01909*	*20.5(2.5)*	*19.6(2.5)*	*14.3*
F8 – F10				
Temp	**Mean ADP size**	**MSA (Deg^2)**	**FC ($J\ mol^{-1}\ deg^{-2}$)**	**Barrier ($kJ\ mol^{-1}$)**
40	0.017	40.4 (5.6)	9.0 (1.2)	6.6
40	*0.02268*	*33.2 (2.9)*	*11.2 (1.0)*	*8.2*

Table 2.4-1 The results of TLS analysis on the 40K neutron structure, and the 40K X-ray structures (italics). The lower values of force constant (FC) and energy barrier to rotation (Barrier) are more in line with the X-ray values derived at higher temperatures. That is not to suggest that a variable temperature neutron diffraction study would not generate lower values across all temperatures: this is unknown.

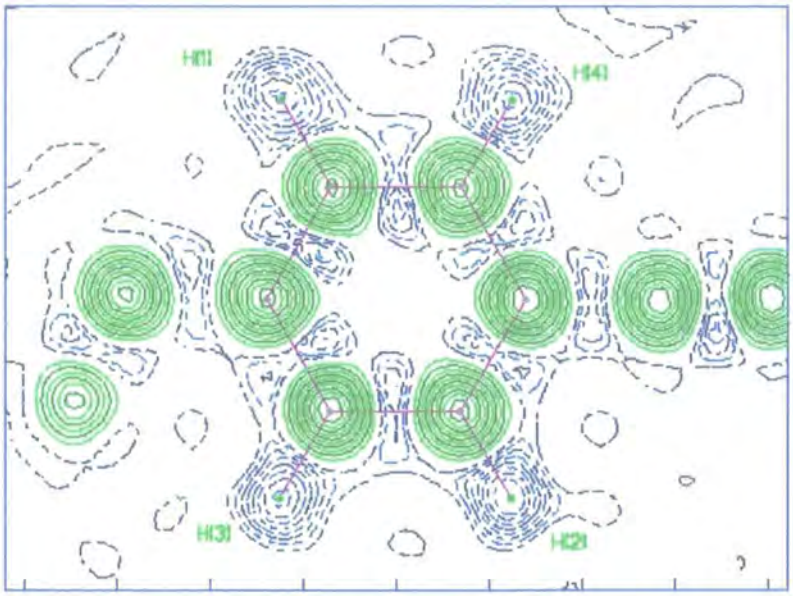

Figure 2.4-1 The Fourier map in the plane of the four hydrogen atoms. Contours: -2, -4, -6... barns (blue, dashed) are the result of the hydrogen atoms (^1H has a negative neutron scattering length); 4, 8, 12... barns (green, solid) are the result of carbon atoms; Zero contour omitted for clarity. The peaks at the carbon atom positions reach +40, while the same at the hydrogen atoms are around –18 barns.

More interesting, perhaps, is a comparison between this structure and its 40K X-ray counterpart. The carbon – hydrogen bond lengths are now 1.088(2) Å in

three cases and 1.086(2) Å in the fourth (C11 – H2) while they are 0.92(2), 0.94(2), 0.96(2), 0.97(2) Å in the 40K X-ray structure. Note that even at 40 K, and an organic system (no heavy metals) X-rays have difficulty in pinpointing the position of hydrogen atoms. Their more accurate positioning yields a better evaluation of the intermolecular contacts. The 'close contact' between F3 and H2 is 2.355(2) Å (2.41(2) Å with X-rays). Additionally it would appear that there are several contacts that are shorter than the sum of the Van der Waals radii around the terminal CF_3 groups: F7-H4, F9-H1 and F5-F2 have contact distances of 2.530(2), 2.508(2) and 2.859(1) Å respectively.

2.5 *A Second Polymorph*

A second flask containing a sample of $C_{13}F_{10}H_4$ was *found* in the synthesis lab and subsequently studied by single crystal X-ray diffraction. There was no anticipation *a priori* that this sample would be any different from the previous sample, however when the crystals were found to explode on flash freezing, the ambient temperature experiment revealed that this was in fact a different polymorph. The basic experimental data are:

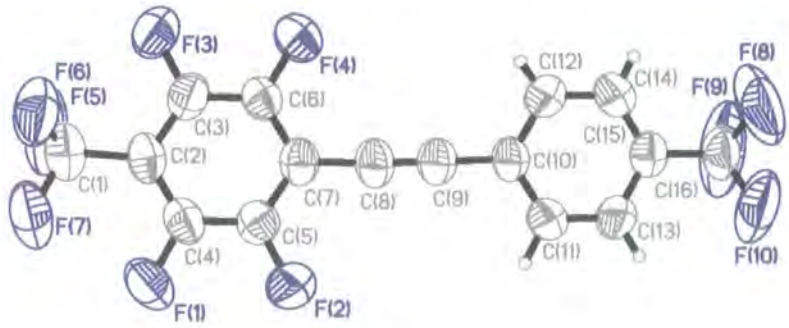

2-5-1: $C_{16}F_{10}H_4$ at 280K: *triclinic, P-1 and Z = 2, R_1 = 7.94%, R_2 = 25.18%, R_{int} = 0.0486, a = 8.6672(3) Å, b = 8.8327(3) Å, c = 10.2460(4) Å, α = 90.614(1)°, β = 96.044°(1), γ = 105.553(2)° Volume = 750.83(5) Å³*

Even with slow cooling this crystal system goes through a destructive phase transition between 240 and 220 K. Unit cell data have been collected below this temperature, albeit from cracked crystals, and hence they were unsuitable for full data collection. Indeed the lower temperature results are derived from very poor data and certainly a unit cell would be impossible to index without the prior knowledge of the approximate dimensions. The unit cell volumes and axis lengths are plotted in Figure 2.5-1 as a percentage of the 280 K data.

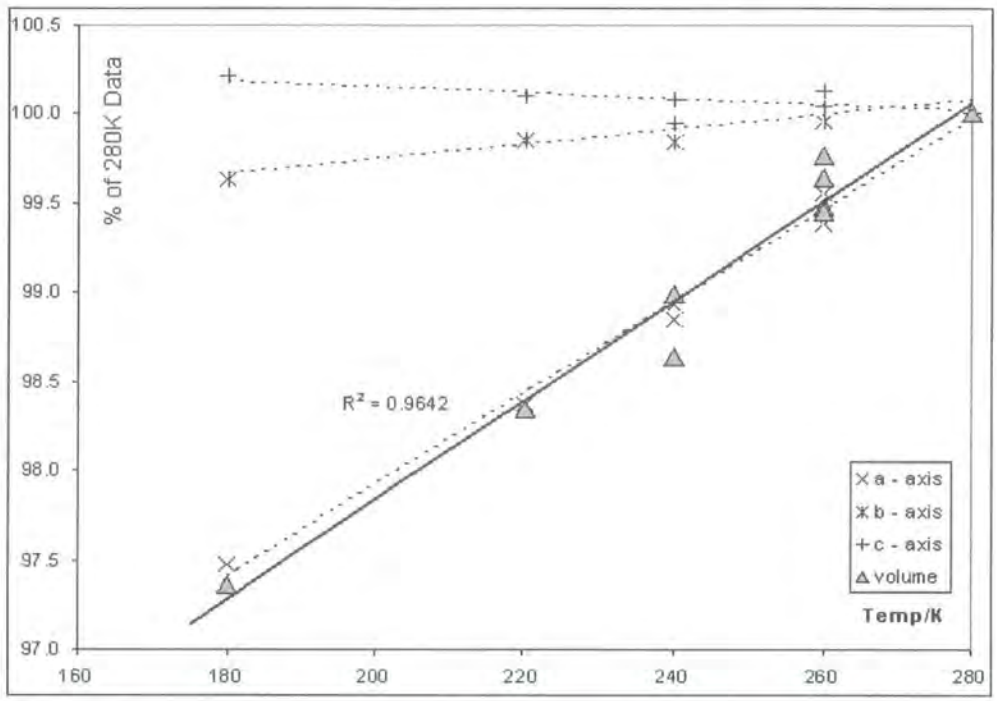

Figure 2.5-1 Lengths of the unit cell axis and the overall volume. The temperature dependence of the volume of the unit cell is due almost entirely to the temperature dependence of the a-axis.

In contrast to the $P2_1/n$ polymorph, the changes in the unit cell parameters are anisotropic in this case: change in the volume of the unit cell being mostly due to the temperature dependence of the a-axis. It should be noted that the temperature dependence of the cell volume here is 0.2085 Å^3 per degree. This is proportionally greater than the 0.3974 Å^3 per degree that its $P2_1/n$ counterpart exhibits, as the unit cell contains half the number of molecules in this case.

2.5.1 ADPs and TLS analysis

Full structure solution and refinement have been carried out at 280 and 240 K (structures 2-5-1 and 2-5-2 respectively) on this polymorph and the same procedures for disorder / order investigation and segmented rigid-body analysis were followed. The differences in the two crystal structures are significant - the packing is face to face with respect to the phenyl rings (see Figure 2.5-2), rather than the herringbone type packing of the $P2_1/n$ polymorph (cf. Figure 2.2-1). That having been said, given the lack of close contacts around either CF_3 group (none below the Van der Waals radii), it would be reasonable to imagine that the ADPs and TLS analysis would be fairly unaffected by this difference. This isn't exactly the case; the ADPs of F1 - F4 are slightly larger in the present case while those for F5 – F10 are significantly smaller. Consequently the results of the TLS analysis yield mean square amplitudes for rotation that are smaller and corresponding force constants and rotation barrier energies are greater for the P-1 polymorph. The results are tabulated in Table 2.5-1, along with the comparable data from the $P2_1/n$ polymorph.

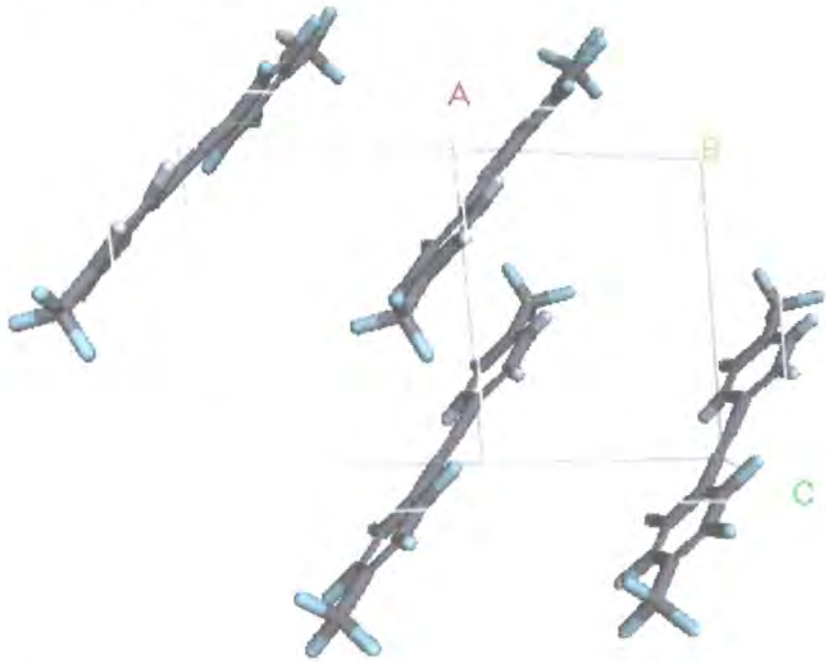

Figure 2.5-2 Unit cell viewed down the b-axis. Compare this motif with that of the $P2_1/n$ structure, Figure 2.2-1. While this packing is face to face with respect to the phenyl rings, the $P2_1/n$ structure shows the herringbone motif.

F5 – F7				
Temp	**Mean ADP**	**MSA (Deg^2)**	**FC ($J\ mol^{-1}\ deg^{-2}$)**	**Barrier ($kJ\ mol^{-1}$)**
280	0.1428	193.4 (28.3)	12.1 (1.5)	8.8
280	*0.1516*	*313.7 (24.1)*	*7.4 (0.5)*	*5.4*
240	0.1075	141.7 (14.2)	14.1 (1.3)	10.3
230	*0.1128*	*231.5 (17.0)*	*8.3 (0.6)*	*6.0*
F8 – F10				
Temp	**Mean ADP**	**MSA (Deg^2)**	**FC ($J\ mol^{-1}\ deg^{-2}$)**	**Barrier ($kJ\ mol^{-1}$)**
280	0.2040	636.5 (64.7)	3.7 (0.3)	2.7
280	*0.2392*	*889.6 (56.1)*	*2.6 (0.2)*	*1.9*
240	0.1620	493.0 (25.4)	4.1 (0.2)	3.0
230	*0.1953*	*733.1 (39.3)*	*2.6 (0.1)*	*1.9*

Table 2.5-1 Summary of the results of the segmented-rigid body analysis of the P-1 polymorph at 280 and 240K and, for comparison the values for the $P2_1/n$ polymorph at 280 and 230K (in italics).

2.6 *Computational Chemistry*

Plane wave density functional theory (PW-DFT) has been used to carry out a theoretical study of this system using the CASTEP[vi] code that was outlined in the introductory chapter. The main thrust of this computational study is to consider the geometry of the molecule and the energetics involved in the rotation of the CF_3 groups. Selected CASTEP input and output files can be found on the accompanying CD.

2.6.1 Geometry Optimisation of the Bulk Crystal Structure

The starting atomic co-ordinates and unit cell of the second polymorph (space group P-1) were used to optimise the crystal structure. The second polymorph

[vi] M.D. Segall, P.L.D. Lindan, M.J. Probert, C.J. Pickard, P.J. Hasnip, S.J. Clark, M.C. Payne; *J. Phys.: Cond. Matt.* **14**(11) pp 2717-2743 (2002)

was used purely for computational expediency: the unit cell is half the size of the $P2_1/n$ polymorph and thus the calculation is far smaller and hence faster – this calculation required 172 hours to converge. Input parameters chosen represent convergence criteria which will yield values which are accurate to about a milli-electron volt.

Calculation Summary (input):

Files: 2-6-1

Exchange Functional: PW91; Plane wave cut off: 330 eV;

Energy Tolerance: $1x10^{-6}$ eV; K-point sampling: 2x1x1 (coarse);

Geometry Optimisation:

Energy Tolerance: 0.000040 eV/atom; Force Tolerance: 0.0500 eV/Å;

Stress Tolerance: 0.100 eVÅ^{-3}; Dispersion Tolerance: 0.0020 Å;

Method: BFGS

Calculation Summary (output):

Unit Cell: $a = 8.5561$ Å, $b = 8.6513$ Å, $c = 9.6732$ Å, $\alpha = 90.9629°$, $\beta = 94.8322°$, $\gamma = 106.2191°$, Volume = 684.472 Å^3 Energy = -18394.11787 eV, Enthalpy = $-1.8394x10^4$

The first question to consider is whether or not the calculation results make sense. This is best achieved by looking at the optimised parameters and considering how they compare with the experimental crystal structure, or by comparing the bond lengths with those in the International Tables for Cyrstallography[vii]. In the present case it was not possible to obtain a very low temperature crystal structure by crystallographic means – the calculation is for

[vii] International Tables for Crystallography; Vol C, Part 9.5 pp 691-707, IUCr - Kluwer Academic Publishers (1992)

the 0 K structure, but a comparison with the 240 K structure still has some merit.

The unit cell volume from the simulation is 684.5 $Å^3$, as compared to 740.6 $Å^3$ in the 240K experiment. If one were to extrapolate the cell volume from the variable temperature experiments then the ground state (0 K) structure would have a volume of 692.92 $Å^3$, if effects relating to zero point motion are discarded (i.e. linear extrapolation of the experimentally derived unit cell volumes to 0 K gives a cell volume of 692.92 $Å^3$). As a result, the calculated structure has a greater number of intermolecular contacts that are significantly shorter than the sum of the Van der Waals radii. The four shortest calculated contacts are between F1...H4, F3...H2, F6...H1 and F5...F6, with lengths of 2.192, 2.422, 2.402 and 2.625 Å respectively. The equivalent contacts in the 240 K X-ray structure are 2.64, 2.69, 2.71 and 3.15 Å respectively. The (calculated) contacts are illustrated in Figure 2.6-1.

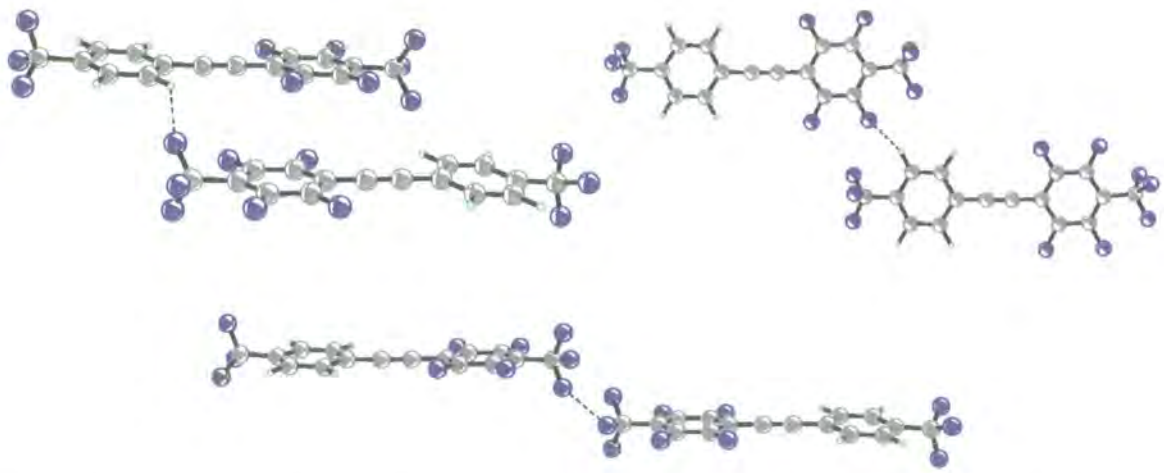

Figure 2.6-1 Illustration of the close contacts in the calculated structure: F6 – H1 top left, F1 – H4 top right and F5 – F6 bottom. Note that while in the calculated structure these contacts are significantly shorter than the sum of the Van der Waals radii, the X-ray structure (ambient temperature) does not show these values as notably short.

2.6.2 Geometry Optimisation of the Isolated Molecule

The starting molecular geometry of the 40K X-ray structure was used to optimise the geometry of the isolated molecule. To isolate the molecule, a large unit cell was constructed (a super-cell) of dimensions a = 8.240 Å, b = 14.442 Å, c = 11.001 Å, $\alpha = \beta = \gamma = 90°$, Volume = 1309.12 $Å^3$ and the molecule placed within. The aim is to make the cell big enough that the molecules in one cell don't interact with those in the next cell, while avoiding unnecessary computational expense by creating a unit cell that is pointlessly large. The simulation input was similar to that of the bulk geometry optimisation calculation, except that only the gamma k-point was sampled and a total energy convergence tolerance of 0.2000E-04 eV/atom was used. It is reasonable to use only one k-point as the molecules are not interacting with one another from one cell to the next.

The output, of course, yields nothing about intermolecular contacts or unit cell parameters; however, the molecular geometry and bond lengths are of interest and are tabulated, along with those for the bulk calculation, 240K X-ray structure and 40K neutron structure. The torsion angles between the adjoining phenyl ring and the CF_3 groups are illustrated in the Figure 2.6-2.

	Mean Bond Lengths (Å)				Torsion Angle (°)	
Structure	**$C_{ar} - H_{1-4}$**	**$C_{ar} - F_{1-4}$**	**$C - F_{5-7}$**	**$C - F_{8-10}$**	**$C\text{-}C\text{-}C\text{-}F_{5-7}$**	**$C\text{-}C\text{-}C\text{-}F_{8-10}$**
Bulk (calc)	1.107	1.376	1.402	1.406	10.304	26.441
Isolated	1.082	1.340	1.355	1.361	4.324	10.339
40K Neutron	1.088	1.336	1.340	1.343	6.125	10.988
240K X-ray	0.884	1.336	1.312	1.283	6.908	28.524
Tables	1.083	1.363	1.336	1.336	n/a	n/a

Table 2.6-1 The mean vales of the bond lengths found from CASTEP in the bulk structure and isolated molecule, 40K neutron structure ($P2_1/n$ polymorph), 240K X-ray structure (P-1 polymorph) and the values found in the international tables. The torsion angles of the CF_3 groups with the phenyl ring are also given. Note that this value is expected to be crystal environment sensitive to a greater extent than the bond lengths and so the direct comparison between, say, the 40K $P2_1/n$ neutron structure and the calculated geometry optimisation of the P-1 structure may be fanciful.

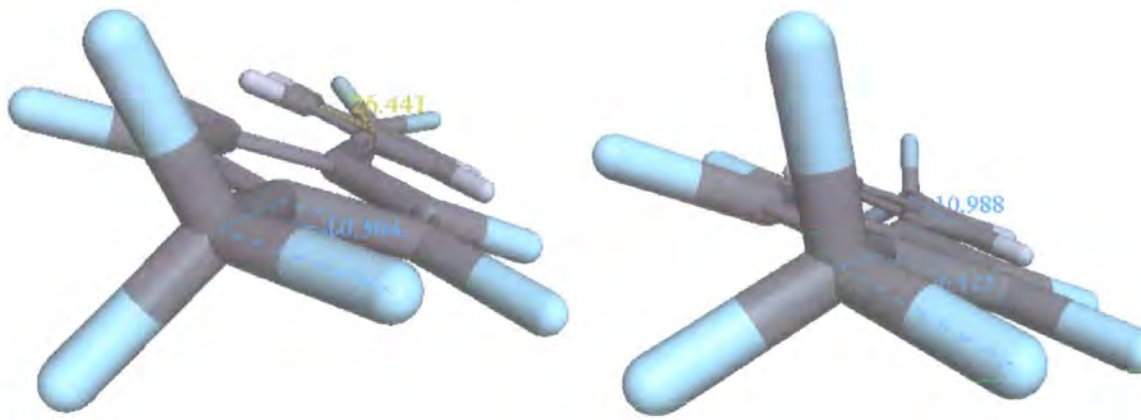

Figure 2.6-2 Illustration of the torsion angles (from Table 2.5-1), the calculated bulk molecular structure on the left and the 40K neutron structure on the right.

The calculations have over-estimated the bond lengths by a couple of percent, though the calculated structure appears reasonable. This provides validation for the further calculations that consider the energy barrier to rotation of the CF_3 groups – the simulation quality used here will be good enough to furnish us with credible, if approximate, results.

2.6.3 Barrier to Rotation and the Energy Potential

A series of studies into the shape of the potential well in which the CF_3 group sits, with respect to librational motion and for both the bulk material and the isolated molecule are presented. In each case the geometry optimised structure from CASTEP has been used for the calculation. Two methods have been employed: A rigid body approach to the librational displacements from the groud state geometry of the CF_3 group and a transition state search. In the first method, the CF_3 group is rotated about the C – C bond that attaches it to the phenyl ring, as a rigid group. The energy of the system is calculated every few degrees, such that an energy profile for the rotation is obtained. Using this profile one can gain a crude estimate of the barrier to rotation. A major drawback to this method is that one is using (a rotated version of) the ground state geometry at all points in the series of calculations. While this is reasonable for torsion angles that are close to the optimised geometry, it is not necessarily a valid representation of the transition state geometry.

The second method involves a search for a transition state between a 'reactant' and a 'product' – in this case the structure found from the geometry optimisation is the reactant and the structure when the CF_3 group is rotated by +/- 120° is the product. This involves employing the Linear Synchronous Transit (LST) method[viii] to generate a reaction pathway, by linearly interpolating the distances between the pairs of atoms in the reactant and product. The LST path is defined by determining the molecular geometry with inter-nuclear distances as close as possible to the idealized values. This interpolation is purely geometrical, it involves no calculation of energy. The energy of the

---

[viii] Halgren, T.A.; Lipscomb, W.N. *Chem. Phys. Lett.*, **49**, 225 (1977)

system is calculated at various points along the reaction profile and the energy maximum found by bracketing the maximum between the reactant and product. The maximum thus found is the transition state of the reaction. This very crude energy barrier is then improved by performing an energy minimization in directions conjugate to the reaction pathway at the transition state.

Both methods suffer from the fact that one does not know how moving one atom will affect other atoms; this is especially a problem when looking at the bulk structures, where the many intermolecular interactions in the crystal cannot be taken into account. After all, as one moves the fluorine atoms to their transition state positions, the surrounding atoms will no longer be in energy minimum geometries, but rather would be shifted to compensate. It is not possible to calculate these 'better' positions so this is simply ignored. Clearly, the energy barrier so calculated will be greater than the actual energy barrier.

In the work presented here, the energy barriers to rotation of both the bulk and isolated molecule structures are considered. Using statistical thermodynamics, the populations of energy states that deviate from the ground state geometry (torsion angle) are calculated for a range of temperatures.

2.6.3.1 Rigid CF_3 Rotation of F5-F7, Isolated Molecule

Using the molecular structure calculated for CASTEP discussed in section 2.6.2, the CF_3 group containing atoms F5-F7 was rotated about the C1-C2 bond. The torsion angle F5-C1-C2-C4 was varied from +90 to -90 ^{o} in 5 degree intervals, with the energy of each structure calculated. In all calculations the basis set used is: 330 eV plane wave cut-off, with 1.0×10^{-6} SCF tolerance, using

the GGA-PW91 functional. The unit cell size is that used in 2.6.2. The resulting energy profile is shown in Figure 2.6-3 along with diagrams of the molecular conformation at the energy minima and maxima.

Figure 2.6-3 Energy profile of the system as the CF_3 is rotated as a rigid body about the C1-C2 bond. The

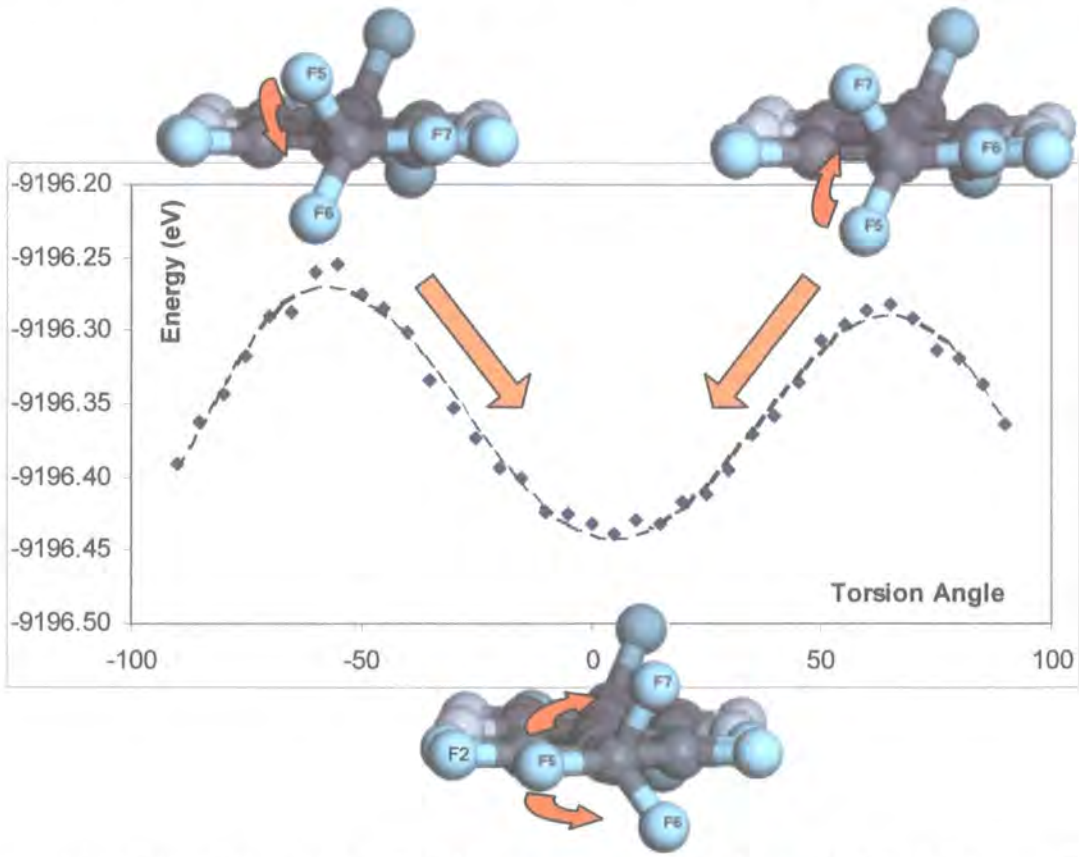

energy minima occurs when atom F5 (and by symmetry, F6 and F7) pass F2. The line of best fit is superimposed as a dashed black line. Note that the maxima occur when the same atoms pass F1 (see main text)

The minimum energy conformation is at 5° with an energy of –9196.439 eV, the maximum values are at –55° and 65° with energy of –9196.254 and –9196.281 eV respectively. The generates an energy barrier of 0.184 or 0.158 eV, depending on which direction one moves the CF_3 group. The energy profile is not entirely smooth, especially around the energy minimum (ground state) where, for example, a torsion angle of 15° produced a lower energy then that of 10°, even though it is the 5° structure that has the lowest energy. This highlights the limitations of the model system used and the fact that the

differences are less that a hundredth of an electron volt between 0, 5, 10 and 15° torsion angles.

Statistical thermodynamics was used to get an idea of how these energy values translate into populations of various energy states - that is the probability of the molecule adopting a particular torsion angle at a given temperature. This is done by employing the following equations:

$$Z(t) = \sum e^{\frac{-\Delta E}{k_b T}}$$

so

$$P(\theta) = \frac{e^{\frac{-\Delta E}{k_b T}}}{Z(t)}$$

Where Z is the partition function, ΔE is the increase in energy from the ground state, k_b is the Boltzmann constant and P(θ) is the probability of angle (θ) being populated by any one molecule. From these equations the probability function at T (temperature) = 40, 120 and 280K was calculated, using angles of between -80 and 80° and these results are plotted in Figure 2.6-4.

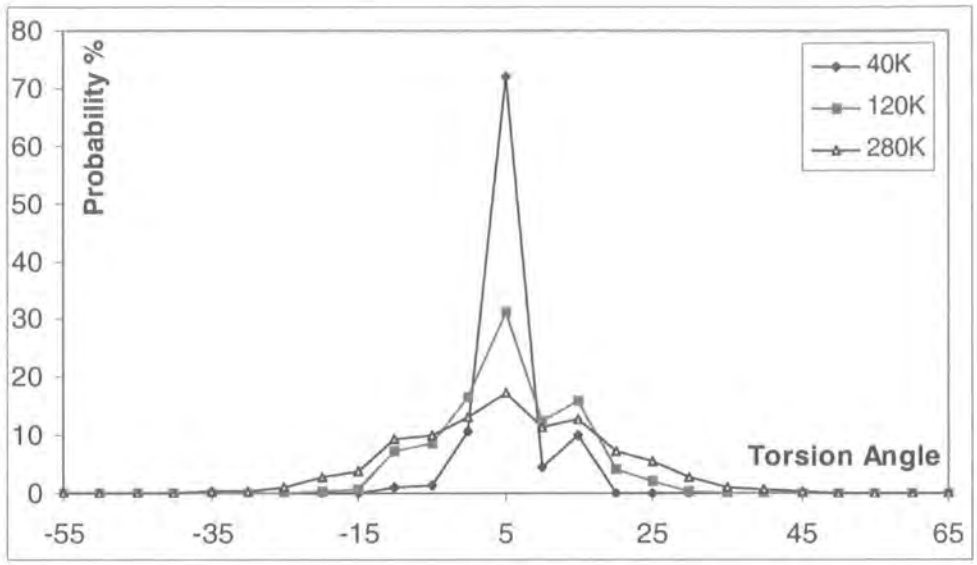

Figure 2.6-4 The expected populations of the various torsion angles at 40, 120 and 280K. Even at 40K there is significant population of four energy levels (angles).

As expected, at 40K the ground state structure dominated the probability function, though it should be noted that even at this very low temperature there is a significant probability that other torsion angles are populated. At higher temperatures the distribution of the CF_3 group is widely spread suggesting that, were the energy values presented here representative of the actual crystal structure, the diffraction pattern would show a high degree of disorder.

The results are slightly erratic close to the minima, probably a result of inaccuracies in the physical model used. To combat this, a line of best fit was calculated for the data and the population probabilities calculated for this fit line close to the energy minima. Using the equation found for a polynomial line of best fit limited to terms involving $x \leq 6$:

$$y = 8x^{6}.10^{-13}. - 2x^{5}.10^{-11} - 2x^{4}.10^{-08}. + 3\,x^{3}.10^{-07} + x^{2}.10^{-04} - 0.001x - 9196.4$$

A 2.5° energy grid from 45 to –35 was created. The results are plotted in Figure 2.6-5. The bottom five energy states carry 87.3% of the population at 40K. That is to say that 12.7% of the population *at 40K* are expected to be in energy levels that represent torsion angles of 7.5°, or greater, from the minimum.

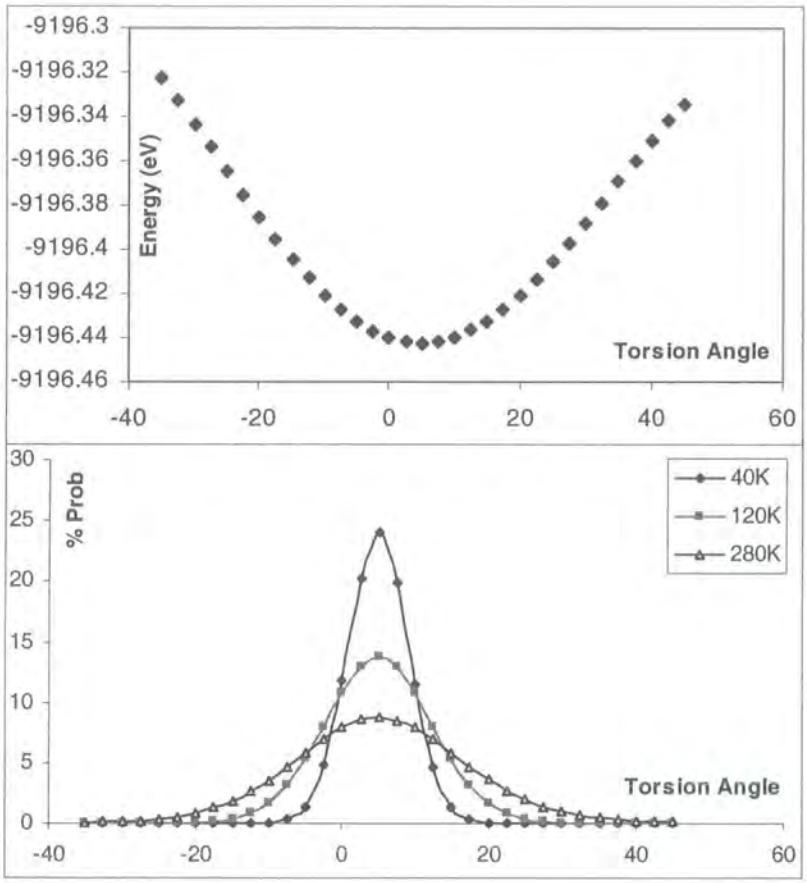

Figure 2.6-5 The energy profile close to the energy minima according to the line of best fit through the raw data (top) and the resulting expected populations at 40, 120 and 280K. At 280K there is a huge spread in the populated energy levels.

A cursory look at the molecular diagram leads one to suspect that the energy profile ought to be six-fold rather than three-fold in its maxima and minima. After all, if the molecule is approximately symmetrical, apart from the CF_3 groups themselves, the molecule has mirror symmetry: is there any difference between the maximum and minimum presented in Figure 2.6-3? Were the labels F5, F6 and F7 to be removed the only visible sign that the two structures

are different is the CF_3 at the *other* end of the molecule, and that will not make a significant difference.

The answer to this problem comes from the geometry of the optimised structure. Figure 2.6-6 shows the geometry of the CF_3 group in relation to the perfluorinated phenyl ring. The angles formed by atoms C4-C2-C1 and C3-C2-C1 are 124.0 and 118.7° respectively, and as such the C1-C2 bond does not protrude straight out of the phenyl ring (see Figure 2.6-6). No doubt this is to minimise the interaction between F5 and F1 (on the phenyl ring). As the group is rotated about the C1-C2 bond, a maximum is reached when either F7 or F6 eclipse F1. While this is at best a questionable measurement of the barrier to rotation, the rigid model should still be valid close to the optimised structure.

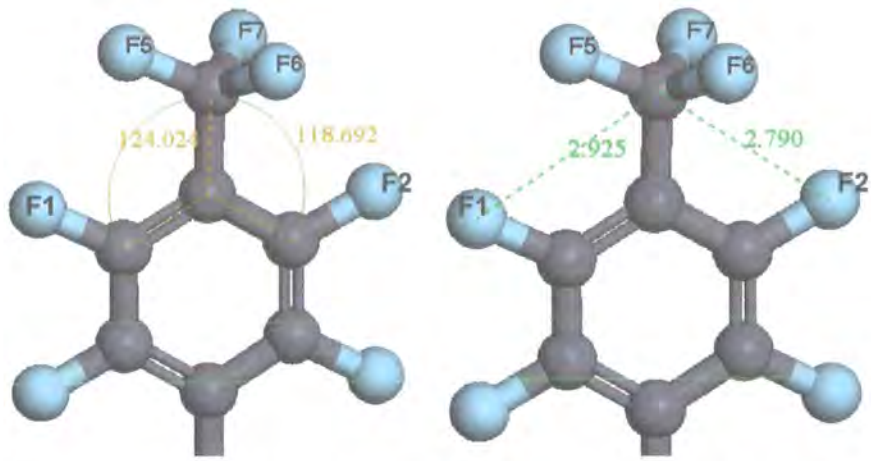

Figure 2.6-6 The molecular geometry about the F5-F7 group. In the ground state structure the C1-C2 bond does not come 'straight' out of the phenyl ring; rather it points slightly away from F1 – no doubt to minimise the steric interaction between F5 and F1. The result is that as the group is rotated about the C1-C2 bond, an energy minimum occurs as the atoms F5-7 approach F1, and a maximum occurs when the same atoms approach F2.

2.6.3.2 Barrier to Rotation via TS search

Using the LST/optimisation method outlined in section 2.6.3, the barrier to rotation was calculated. Starting geometry ("reactant") of 4.32° and finishing geometry of 124.32° ("product") were used. The basis set used was 330 eV plane

wave cut-off, with $1.0x10^{-6}$ SCF tolerance, and the GGA-PW91 functional. The convergence criteria for the transition state search was 0.25 eV/Å. Figure 2.6-7 is a plot of the calculated energies as the calculation progressed. The simple LST calculation is plotted in green, and the energy minimisation from the conjugate path is plotted in orange.

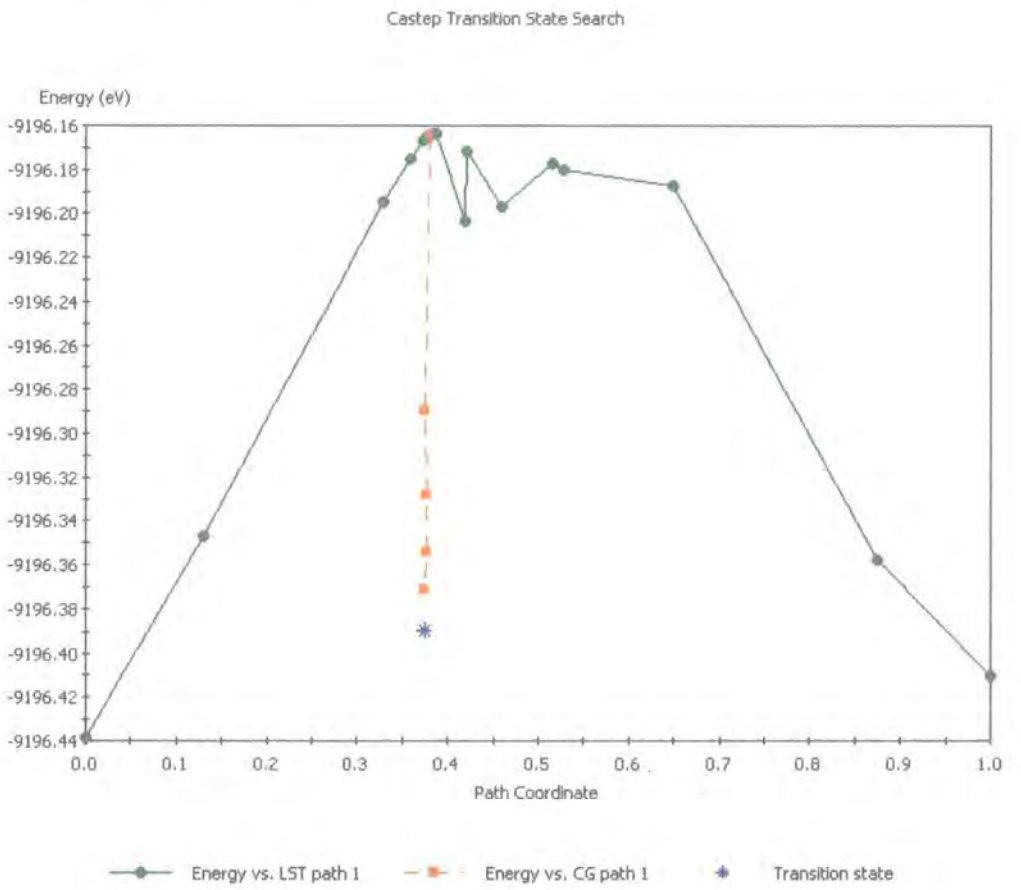

Figure 2.6-7 The energy of the LST/optimisation as the calculation proceeds. The green solid line represents the LST part of the calculation: a geometry based approach to finding the energy maximum between the 'reactant' and 'product' (starting geometry and ending geometry in this case). Once the maximum is found the optimisation attempts to find the saddle point in the energy between the 'product' and 'reactant' (orange dashed line). The final energy barrier is 0.04917 eV.

The key results from the calculations are as follows (input and output files 2-6-3):

LST Maximum

Energy of reactant/product: -9196.439 / -9196.411 eV

Energy of LST maximum: -9196.164 eV

Barrier from reactant/product: 0.275 / 0.246 eV

Optimized Transition State

Energy of reactant/product: -9196.439 / -9196.411 eV

Energy of transition state: -9196.390 eV

Barrier from reactant/product: 0.049 / 0.021 eV

The results of the crude LST calculation are in the same region of the results that came from the rigid rotation model: in fact, the calculated barrier is bigger in this case. On optimisation, the energy of the system falls sharply to 0.0492 eV. Needless to say this is a very small energy barrier. However, this should be the best estimate of the barrier to rotation in these systems.

The values generated here and in section 2.6.3.1 suggest a barrier to rotation of 17.77 (rigid), 26.49 (LST) and 4.74 $kJmol^{-1}$ (LST/optimisation). The values derived from the X-ray diffraction data varied from 5.4 to 9.1 $kJmol^{-1}$. Of course, this is the isolated molecule rather than the bulk structure, where there are intermolecular effects to consider: the problems associated with it not possible being to know how moving one atom will affect the position of other atoms will be greater in the bulk structure. The simple models used here will therefore overestimate the energy barriers of these systems when applied to the bulk structure as the barrier geometry of the rest of the crystal structure will be as it was when the rotated CF_3 group was at its energy minimum. That said, as we have a crystal system that does have a unit cell which is small enough to be easily explored computationally (P-1 polymorph, cell volume 749.06 Å), the

energy barrier for the rotation about C1-C2 has been calculated in the bulk structure.

2.6.3.3 *Bulk Structure Calculations*

Using the geometry optimised structure found in section 2.6.1, the barrier to rotation was calculated using the methods outlined in sections 2.6.3.1 and 2.6.3.2. In the first instance the CF_3 group was rotated from –80 to 30° about the C3-C2-C1-F5 torsion angle. Once again a plane wave energy cut off of 330 eV, 6 x 10^{-6} SCF tolerance were used, though this time a 2x2x2 k-point grid was employed. The results are plotted in Figure 2.6-8, with minimum and maximum energies of –18372.497 and 18371.922 eV respectively. This leads to a barrier to rotation of 0.533 eV, or 51.40 $kJmol^{-1}$. This barrier is far larger than those found from the X-ray diffraction experiments, or those calculated for the isolated molecule (section 2.6.3.1). While it is clear that the crystal structure imposes further restrictions on the rotation of the CF_3 group, this value is known to be an overestimate of the barrier as it fails to take into account any correlation of motion as the group is rotated. The expected populations of the energy levels at 40, 120 and 280 K are plotted in Figure 2.6-8. At 40 K the calculations yielding the lowest two energies account for over 98% of the population, while at 280 K a similar coverage requires the lowest 6 energy points to be summed.

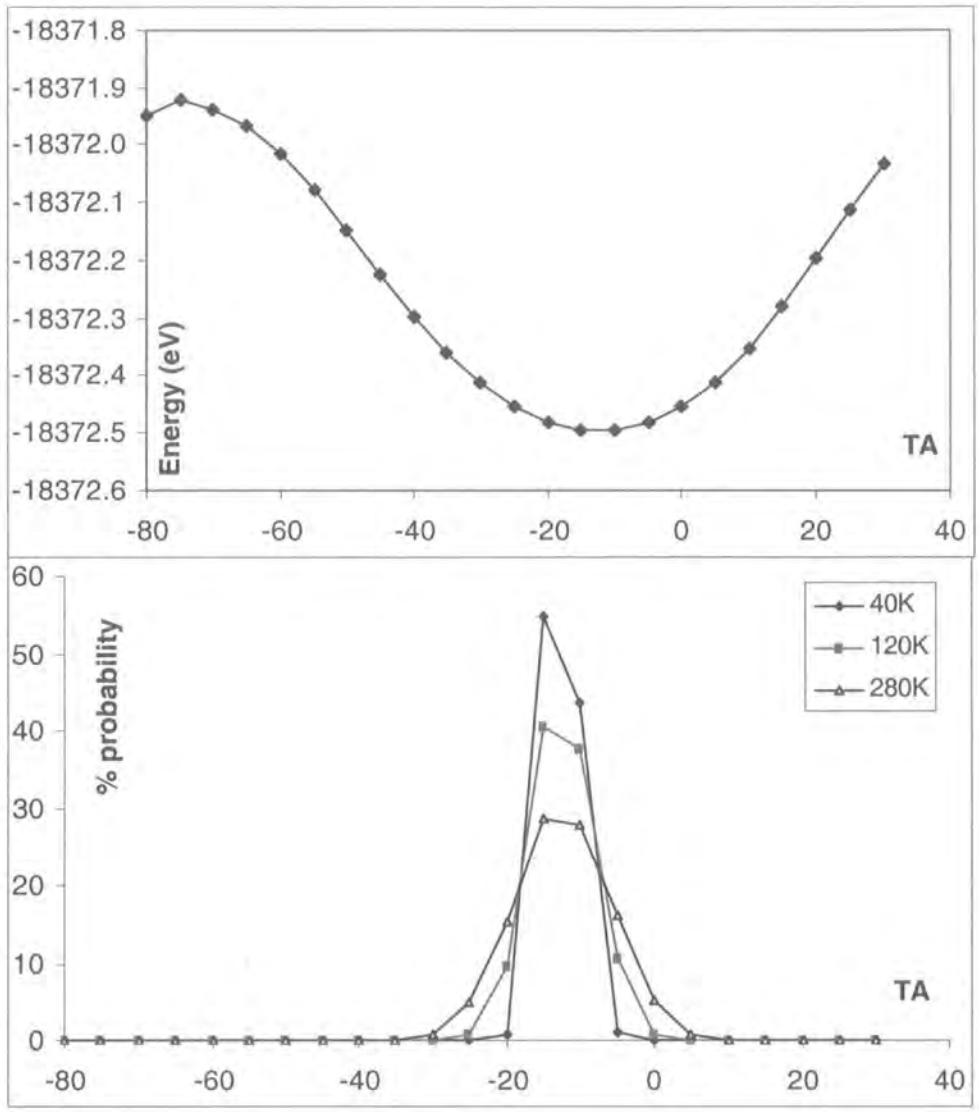

Figure 2.6-8 The energy profile for moving the CF_3 group about the C1-C2 bond in bulk (crystal) structure, top, and the resulting expected populations at 40, 120 and 280K (bottom). Notice that although the energy barrier is far higher here than was the case with the isolated molecule, the energy differences between the lowest four energies are comparable (cf. Figure 2.6-3). That is to say, for small deviations from the minimum there is little difference between the two cases, while at large deviations the energy of the bulk structure becomes far larger.

The LST/optimisation was carried out with the same calculation parameters as those above, using a starting torsion angle of –10.214 and ending at –130.214°. The results are as follows (input and output files 2-6-4):

Energy of reactant/product: -18392.822 / -18392.777 eV

Energy of LST maximum: -18381.900 eV

Barrier from reactant/product: 11.021 / 10.977 eV

Energy of transition state: -18392.102 eV

Barrier from reactant/product: 0.720 / 0.675 eV

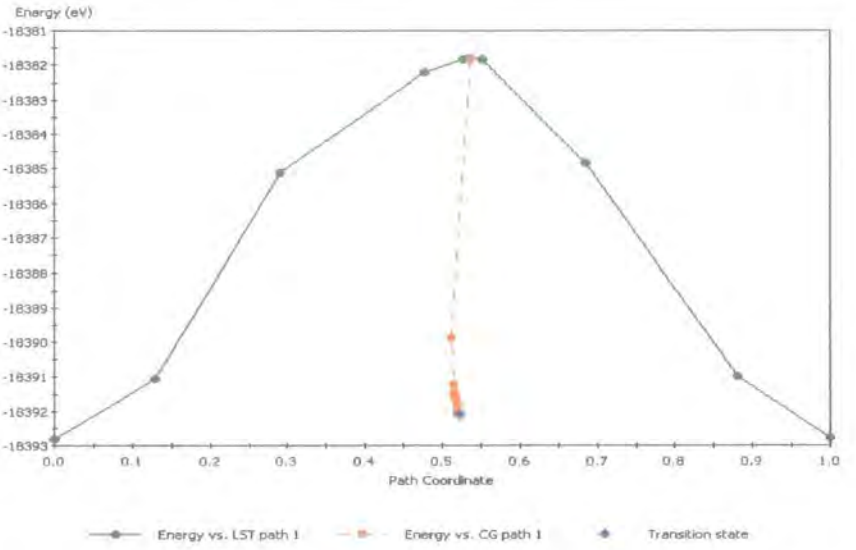

Figure 2.6-9 The energy of the LST/optimisation as the calculation proceeds, the green line being the LST part.

The energy of the 'reaction' pathway is plotted in Figure 2.6-9, the green solid line being the LST maximization and the orange dotted line is the optimization. A barrier of 0.720 eV or 69.43 $kJmol^{-1}$ is found and is far larger than that found from the diffraction data. To some extent this may be due to the fact that the geometry optimization produces a smaller unit cell than that found by the diffraction experiments. As a result it would seem reasonable that moving the

CF_3 group without any other compensatorary movement of other atoms would induce a greater energy penalty.

To test this aspect of the calculation the CF_3 group (F5-F7) was rotated about the C3-C2-C1-F5 torsion angle, from -40 to 80° using the unit cell and molecular geometry of the 240 K X-ray diffraction experiment. The resulting energy profile is plotted in Figure 2.6-10; an energy barrier of 0.214 eV (20.63 $kJmol^{-1}$) is calculated. While this is still a factor of 2-3 times larger than the values found from the diffraction experiments, it is far closer to the diffraction derived values than the value generated from the geometry optimised structure. Of course, in this case the crystal packing is unrealistically loose, and so the value is expected to be an underestimate of the barrier height. As the system was not in its geometry optimised state, a transition state search via LST/optimisation is of minimal value[ix].

[ix] That is to say the calculation was carried out, however, the energy of the transition state energy was *lower* than its supposed starting point. This is to be expected, as without the initial geometry optimisation, the starting point is not the energy minimum, but rather the diffraction-found co-ordinates.

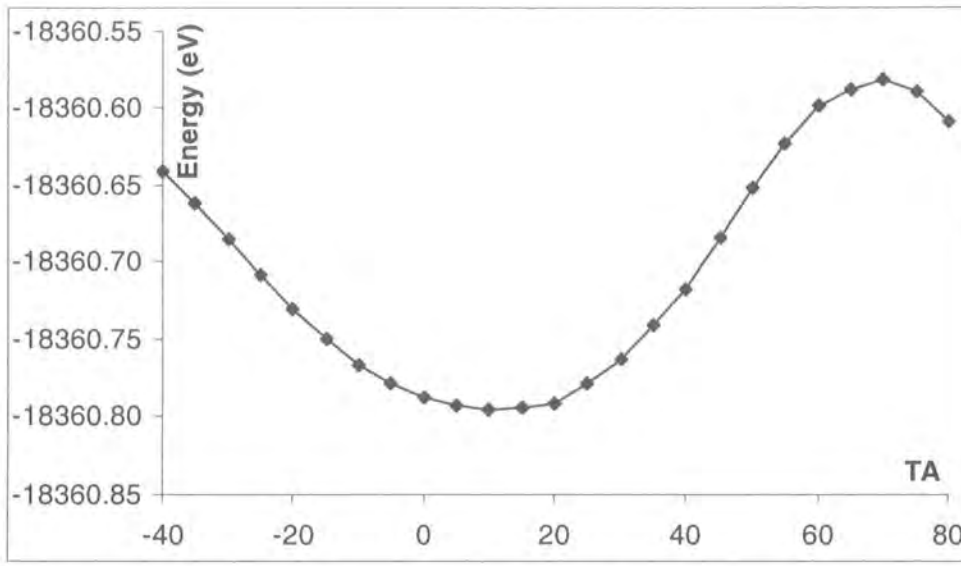

Figure 2.6-10 The energy profile for moving the CF_3 group about the C1-C2 bond in bulk (crystal) structure. In this case the co-ordinates from the 240 K diffraction experiment have been used. The results show a lower barrier to rotation and a shallower energy profile close to the energy minimum.

2.6.3.4 Barrier of CF_3 Rotation: F8-F10

Employing the same methods as were used for the F5-F7, the barrier to rotation of the second CF_3 group has been probed. As before, the input parameters at all stages were: 330 eV plane wave cut-off, with 1.0×10^{-6} SCF tolerance, using the GGA-PW91 functional. For the isolated molecule, only the gamma k-point has been used, while for the bulk calculation, a 2x2x2 k-point grid has been used.

The results for the rigid rotation of the CF_3 group over a 180° torsion angle in the isolated molecule model system (cf. Section 2.6.3.1) show that there is very little difference in energy between the various conformations of the molecule (Figure 2.6-11). The difference between the highest and lowest energy entry, those for 50 and −10° respectively, is 0.030 eV (2.20 $kJmol^{-1}$), though given the scattering of results this value must be subject to significant error. Essentially, the magnitude of this effect (i.e. the energy of the system as a function of CF_3 group rotation) is smaller than can be studied from this kind of calculation.

From the estimated trend line through the data, the expected populations of the various torsion angles have been generated and also plotted in Figure 2.6-11. It is clear that, except at the very lowest temperatures, this energy profile predicts significant populations at all angles.

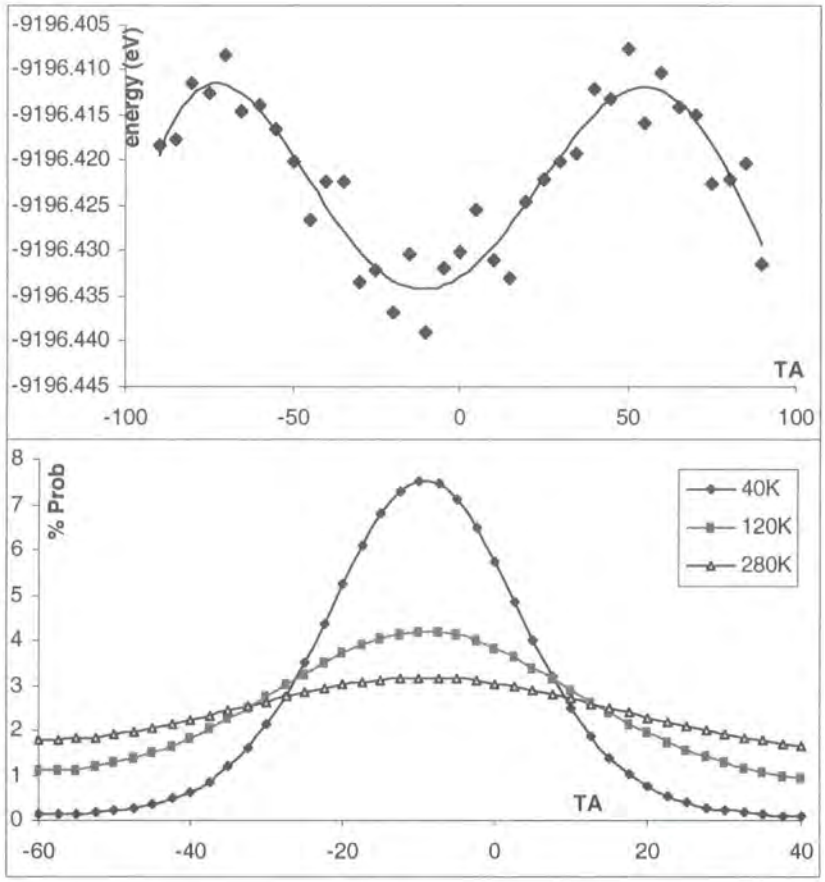

Figure 2.6-11 The energy profile for moving the CF_3 group about the C15-C16 bond in isolated molecule, top, and the resulting expected populations at 40, 120 and 280 K (bottom). The difference in energy between the energy minimum and maximum is very small – this is close to free rotation about the C15-C16 bond.

So where, one might ask, does this small energy barrier come from? Once again it is important to look at the geometry of the molecule around the CF_3 group that is being rotated to see what is actually happening to the atoms as the torsion angle is varied. The geometry around the CF_3 group is shown in Figure 2.6-12. One should contrast this with the similar diagram, Figure 2.6-6 (section

2.6.3.1). The CF_3 group is not nearly as distorted this time – no doubt a result of the phenyl ring being hydrogen substituted in this case, and thus less bulky. The distance, for example, between the atoms H3, H4 and C16 is 2.717 and 2.681 Å compared with 2.925 and 2.790 Å for F2 – C1 and F1 – C1 respectively. As a result, the minimum distance between the fluorine atoms F9 and F10 and the hydrogen atoms H3 and H4 varies less as a function of torsion angle. Obviously, the additional size of fluorine atoms as against hydrogen atoms will also make this difference more important; however, it is worth bearing in mind that part of the effect is inevitably due to the structure that is produced by the optimisation geometry.

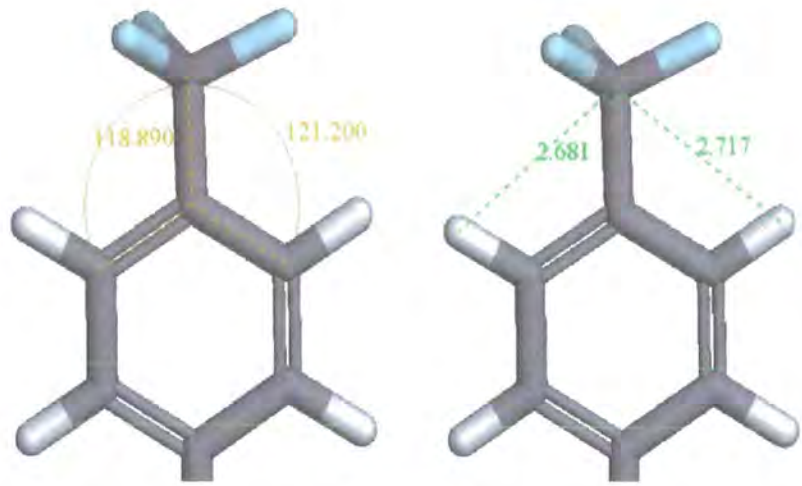

Figure 2.6-12 The molecular geometry about the F8-F10 group. In contrast to the F5-F7 group (Figure 2.6-6), the C15-C16 bond points approximately 'straight' out of the phenyl ring, resulting in roughly equal distances between H1, H2 and C16. This partly explains the very low calculated barrier to rotation in this case.

A transition state search via a LST/optimisation has been carried out, with 'product' and 'reactant' geometries of (torsion angle equals) –10.89 and 108.66°. The summary of the results is as follows (input and output files 2-6-5):

Energy of reactant/product: -9196.439 / -9196.434 eV

Energy of LST maximum: -9196.129 eV

Barrier from reactant/product: 0.310 / 0.305 eV

Energy of transition state: -9196.437 eV

Barrier from reactant/product: 0.0015 / -0.0035 eV

The energy of the 'reaction' pathway is plotted in Figure 2.6-13, the green solid line being the LST maximization and the orange dotted line is the optimization. By this calculation, the energy of the 'product' – that is the energy minimum at +120° – is higher than the transition state. A barrier of 0.148 $kJmol^{-1}$ is, needless to say, nominal. This essentially represents free rotation about the C15-C16 bond.

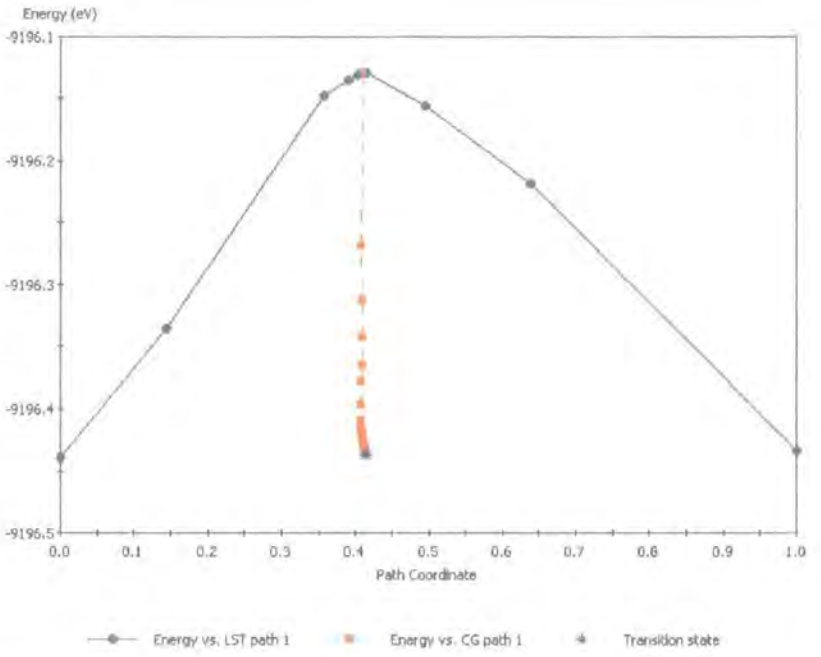

Figure 2.6-13 The energy of the LST/optimisation as the calculation proceeds, the green line being the LST optimisation. Obviously the calculated barrier here is minimal.

Using the geometry optimised crystal structure; the barrier to rotation of the F8-F10 CF_3 group was probed via a rigid body rotation. Torsion angles of between 100 and –35° were used and the results are plotted in Figure 2.6-14. The energy minima and maxima are at 25 and 80°: -18372.497 and –18372.262 eV respectively; the energy barrier is thus 0.234 eV (22.567 $kJmol^{-1}$). This is ca. 5-10 times greater than the values of 2-4 $kJmol^{-1}$ obtained from diffraction experiments. As there is very little difference in the ground state molecular geometry - the distances H3-C16 and H4-C16 are 2.669 and 2.703 respectively – this massive increase in energy barrier is due to the presence of the other molecules in the crystal structure being included in the calculation.

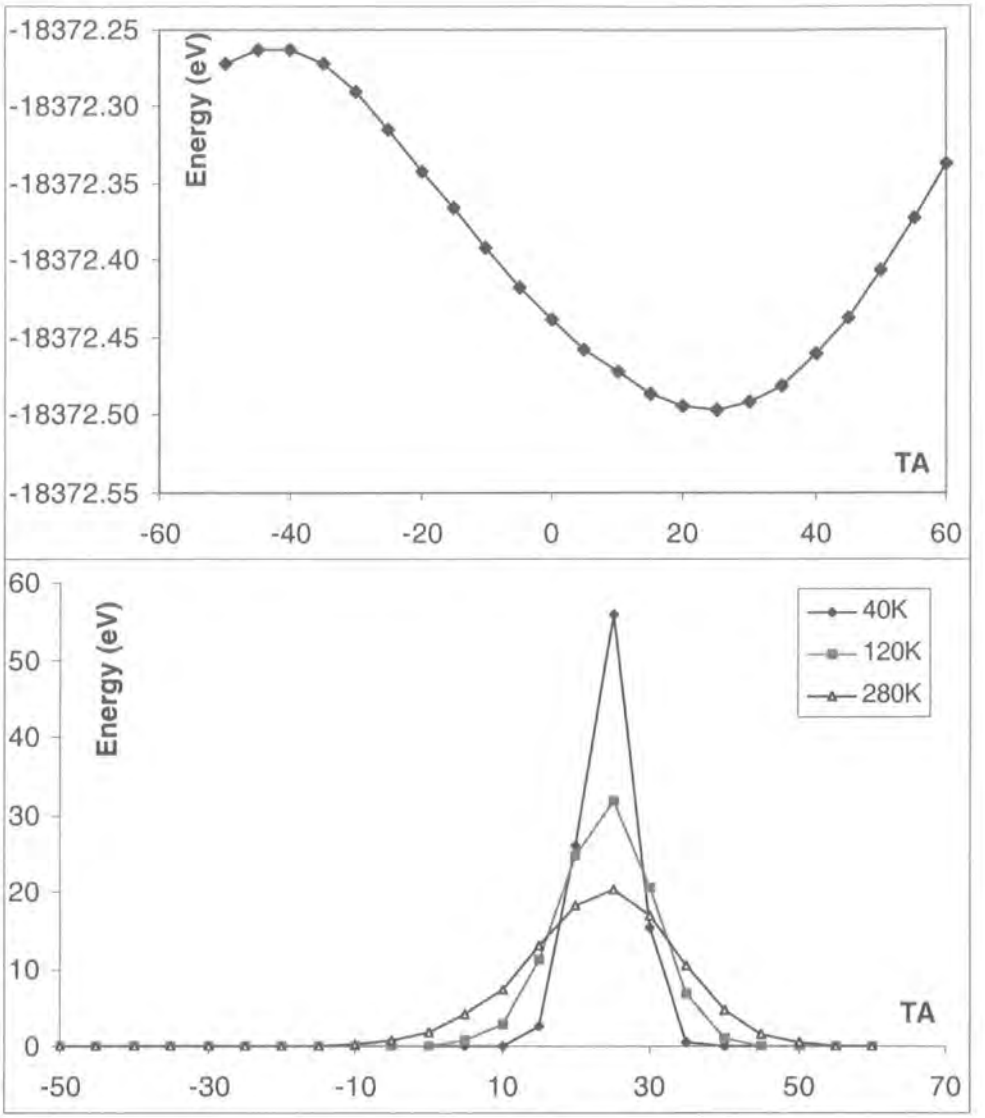

Figure 2.6-14 The energy profile for rotating the CF_3 group about the C15-C15 bond in bulk (crystal) structure, top, and the resulting expected populations at 40, 120 and 280K (bottom).

2.7 *Summary and Comments*

4-(p-trifluoromethyl phenylethynyl) perfluorotoluene has been studied by variable temperature X-ray diffraction, and computational techniques. In the former case, the aim was to understand the extent of the disorder on the terminal CF_3 groups and why it might arise, along with harvesting information about physical properties, such as the barrier to rotation of the CF_3 groups, once it was established that that is what they were doing. Additionally,

information about the effect of temperature on the unit cell sizes and sizes of atomic displacement parameters has been gained.

The computational aspects, while originally an attempt to cross check the barriers derived from the X-ray experiments, have opened up fascinating opportunities in the study of molecular crystal structure. Gaining a direct view of the energy potential in which atoms in a crystal structure sit is inherently interesting – though in the present case there have been problems when considering the correlations of motion. Perhaps this work has been a little over ambitious in this respect: the use of time averaged and theoretical techniques to study dynamic effects is not ideal.

With the above in mind, these samples have been passed on to the solid state NMR group to obtain further estimates of the barriers of rotation, the results of which shall be published elsewhere. We shall conclude, then, with a summary table of the energy barriers to rotation found for the two CF_3 groups using the various experimental and theoretical data. All values are quoted in kJ mol^{-1}.

Crystal Structure					Isolated Molecule	
Group	**Diffraction data**	**Rigid**	**LST/opt**	**X-240**	**Rigid**	**LST/opt**
F5-F7	5.4-9.1	55.46	69.43	20.63	17.77	4.74
F8-F10	1.9-4.3	22.57	- - - -	- - - - -	2.91	0.15

3 Studies of 2-methyl-4-(4-trifluoromethyl-phenyl) but-3-yn-2-ol

A precursor to the Tolan 1 of Chapter 2, 2-methyl-4-(4-trifluoromethyl-phenyl) but-3-yn-2-ol, formula $C_{12}F_3H_{11}O$, Tolan 2 hereafter, was crystallised by Professor Todd Marder and co-workers and duly studied by both variable temperature X-ray crystallography and plane wave DFT. Once again, the central consideration of the study was to look at the terminal CF_3 group

3.1 *100K Crystal Structure of $C_{12}F_3H_{11}O$*

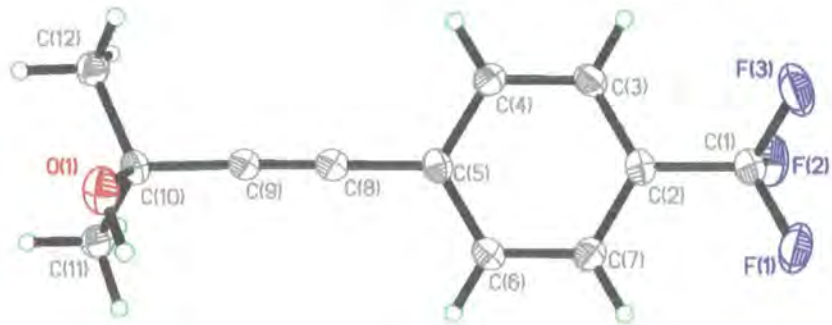

***3-1-1: $C_{12}F_3H_{11}O$ at 100K**: Orthorhombic, Pbca and Z = 8, R_1 = 4.07%, R_2 = 11.24%, Rint = 0.1032, a = 16.4745(6) Å, b = 5.6043(2) Å, c = 23.3685(9) Å, V = 2157.57(14) Å^3*

Description of the molecular structure: the ADPs of the fluorine atoms are a little larger that those of the other atoms, the mean size of F1-F3 is (average of U_{eq} =) 0.0441(3). At 105 K, Tolan 1 ($C_{16}F_{10}H_4$ Chapter 2.3.1) had fluorine atom ADPs of 0.0453 and 0.0690 for groups F5-F7 and F8-F10 respectively. The initial indication, therefore, is that this terminal CF_3 group is similar in the extent of its disorder to the F5-F7 group in the $C_{16}F_{10}H_4$ compound. This is interesting as in the present case, the CF_3 group is attached to a hydrogenated

phenyl ring, while in the previous example it was the CF_3 group that was attached to the perfluorinated ring.

The crystal structure refinement was straight forward and the hydrogen atom positions were found from the difference map. Perfectly acceptable refinement statistics of R_1 = 4.07% and R_2 = 11.24% were recorded, although the quality of the data recorded is not especially good – R_{int} is 0.1032. On application of an absorption correction, the R_{int} value falls to 0.0378 – though the values for R_1 and R_2 improve only slightly to 3.82 and 10.77% respectively. The crystals did not diffract well and even at 100 K there was very little high angle diffraction.

3.1.1 Crystal Packing and Intermolecular Interactions

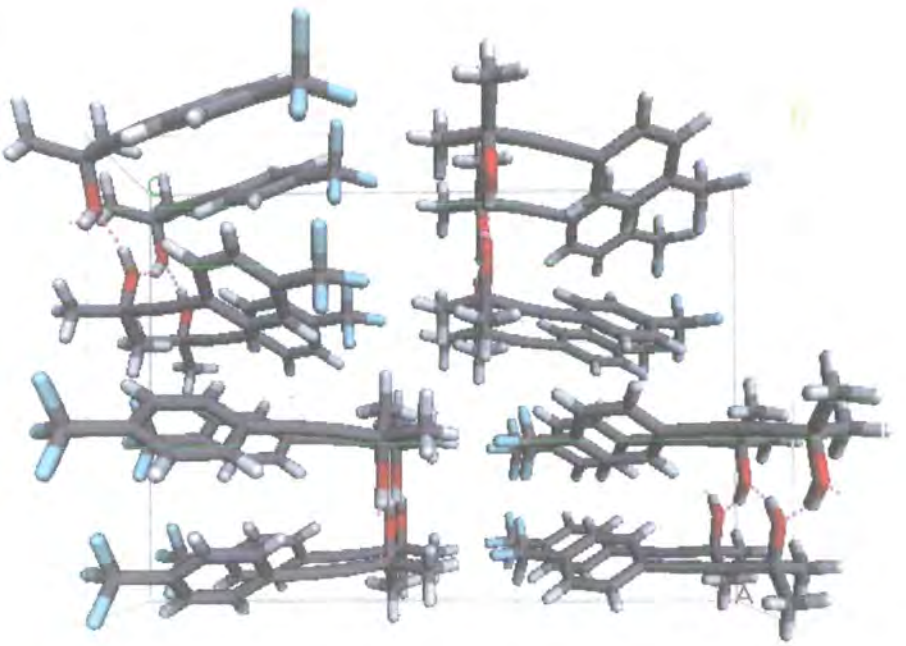

Figure 3.1-1 The unit cell viewed down the b-axis. Two unit cells are included to illustrate better the crystal packing: an OH...O chain is the main feature of the crystal structure. The phenyl rings are packed at right angles to one another.

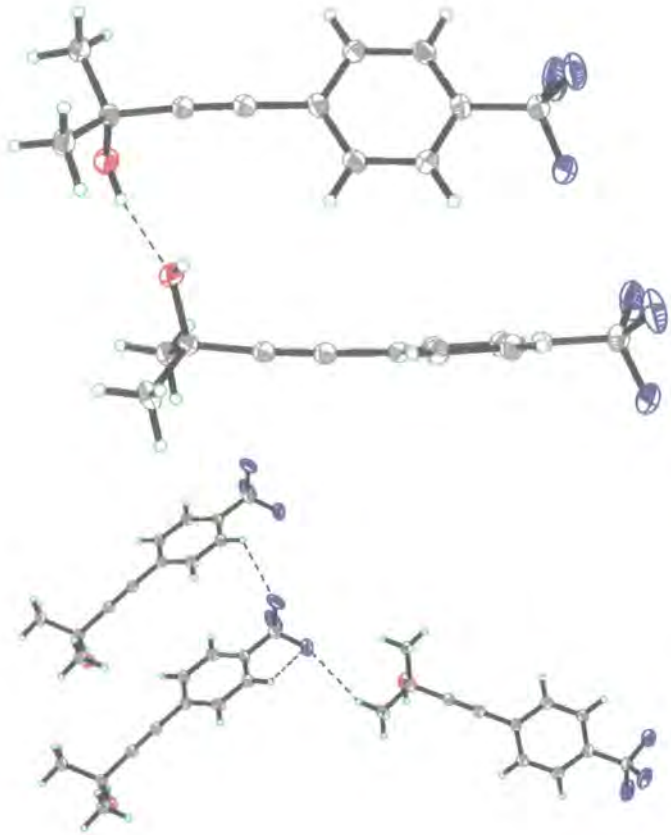

Figure 3.1-2 The hydrogen bonding is illustrated (top), along with the closest contacts around the CF_3 group. Note that of these three F...H contacts, the shortest is the intramolecular one (2.56 Å).

As one might expect, the OH group forms an O-H...O hydrogen bond with O...H contact distance of 2.26(2) Å (an O...O separation of 3.065(2) Å, Figure 3.1-1). Other than this conventional hydrogen bond there are no intermolecular contacts that would be considered as particularly short, and therefore indicative of significant attractive interaction. The packing around atoms F1-F3 is no exception in this respect, the intermolecular contact distances illustrated in Figure 3.1-2 being 2.66(2) for F2...H1 and 2.84(2) Å for F3...H6, the intermolecular contact distance of 2.47(2) Å being the shortest of the three illustrated (F3...H1). While these contact distances are overestimates of the actual contact distances, since X-ray experiments underestimate the lengths of X-H bonds, and the van der Waals radii of fluorine and hydrogen are 1.47 and 1.20 Å respectively, these contacts are unlikely to be significant.

3.2 *Variable Temperature Experiments*

The system was studied at 9 temperatures ranging from 280 to 100 K using both the Bruker 1K and 6K SMART diffractometers. A summary of the experiments is given in Table 3.2-1. Two crystals were used for four temperatures each, mounted on a hair and flash cooled in oil. A third crystal was mounted on a glass fibre with epoxy glue for the 280 K data collection. The crystal dimensions were as follows:

(1) Crystal 1: 0.20 x 0.14 x 0.12 mm

(2) Crystal 2: 0.30 x 0.14 x 0.10 mm

(3) Crystal 3: 0.38 x 0.20 x 0.08 mm

Due to the fact that the crystals were known to diffract poorly, a large crystal was deliberately selected for the room temperature experiment in an attempt to obtain diffraction data of reasonable intensity.

Temp/K	Exp No.	Machine	Crystal	Selected diagrams:
280	3-2-8	1K	3	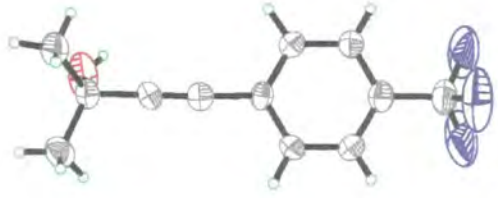
250	3-2-7	1K	1	
220	3-2-6	6K	2	
200	3-2-5	1K	1	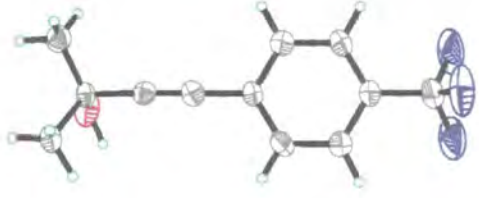
180	3-2-4	6K	2	
160	3-2-3	1K	1	
140	3-2-2	6K	2	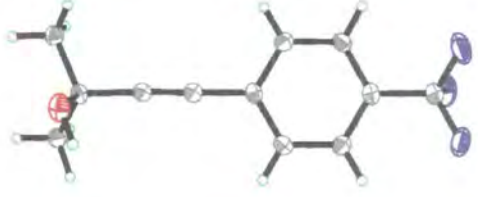
120	3-2-1	1K	1	
100	3-1-1	6K	2	

Table 3.2-1 A summary of the experiments undertaken. Molecular structure diagrams at 280, 200 and 100K (top to bottom) included.

3.2.1 Unit Cell Parameters

Unit cell parameters for the experiments are tabulated in Table 3.2-2 and these results are plotted in Figure 3.2-1 as a percentage of the 280 K data. Over the temperature range studied the length of the c-axis remains approximately constant while the length of the a and b-axis each reduce by almost exactly the same percentage (2.46 and 2.40% respectively). The result on the unit cell volume is a reduction in size by 5.2% over the 180 K temperature range.

Temp (K)	a-axis (Å)	b-axis (Å)	c-axis (Å)	Volume (Å^3)
100	16.4745(6)	5.6043(2)	23.3685(9)	2157.6(1)
120	16.559(3)	5.6291(8)	23.426(4)	2183.6(6)
140	16.5436(8)	5.6267(3)	23.394(1)	2177.6(2)
160	16.606(2)	5.6465(7)	23.414(3)	2195.4(5)
180	16.6125(7)	5.6492(2)	23.398(1)	2195.9(2)
200	16.665(3)	5.671(1)	23.424(4)	2213.6(7)
220	16.710(1)	5.6817(3)	23.426(2)	2224.1(2)
250	16.8037(9)	5.7104(3)	23.455(1)	2250.6(2)
280	16.867(3)	5.733(1)	23.453(5)	2267.9(8)

Table 3.2-2 Unit cell parameters of the 9 structure refinements, with the estimated errors.

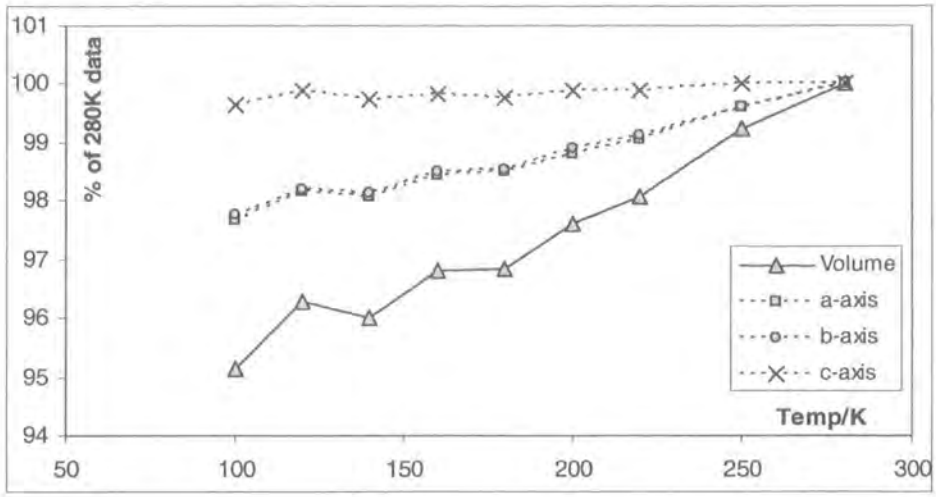

Figure 3.2-1 Plot of the unit cell parameters expressed as a percentage of the 280 K structure. Experiments at 120, 160, 200 and 250 K were carried out on a different crystal and diffractometer (SMART 1K) than those carried out at 100, 140, 180 and 220 K (SMART 6K).

Somewhat concerning are the erratic jumps in the unit cell volumes at lower temperatures. There are two reasonable explanations as to why this is the case: firstly as two different crystals were used it may be that they had unit cells of different sizes, or that the errors inherent from crystal to crystal make these differences within the boundaries of error. As there is no evidence that the two crystals were different polymorphs, the errors from the experiment would have to be huge to give such conflicting results, crystal to crystal. Alternatively, as the crystals were run on different machines it is possible that miscellaneous machine errors are the cause of the differences observed. It has in fact been found that the SMART 1000 in Durham does produce unit cells in the region of 0.3-0.9% larger than other Durham diffractometers[i]. The precise increase depends on the quality of crystal, space group and whether or not positive 2θ data was used in the cell determination.

[i] Dr. A. S. Batsanov. Private communication.

3.2.2 Atomic Displacement Parameters ADPs

The mean sizes of the fluorine ADPs, F1-F3 are tabulated in Table 3.2-3 and plotted in Figure 3.2-2, along with those of C2 and the oxygen, over the full range of temperatures. The oxygen and carbon atom were chosen arbitrarily for comparison with the fluorine atoms. A close look at the results suggests that: (i) while the problems with the unit cells are mirrored to some extent by the size of the carbon and oxygen ADPs, the bigger unit cells producing smaller ADPs, the fluorine atoms' ADPs are not significantly affected; and (ii) at temperatures in excess of 220 K the results seem to be out of line when compared to the lower temperature data. It should be pointed out that any relationship with unit cell size and ADP size from one temperature to the next is likely to be an artefact of the data refinement. One would expect a linear relationship of the ADPs size with temperature, and this seems not to be the case at the higher temperatures.

Temp (K)	F1 – F3 Mean	C2	O
100	0.04414	0.02119	0.02762
120	0.05193	0.02081	0.03096
140	0.06274	0.02734	0.03752
160	0.07193	0.02557	0.04006
180	0.08633	0.03496	0.04976
200	0.10194	0.03477	0.05398
220	0.12028	0.04569	0.06924
250	0.13477	0.04181	0.06918
280	0.15392	0.04499	0.07710

Table 3.2-3 The size of the ADPs of the atoms F1-F3 along with the size of the ADPs of C2 and oxygen over the temperature range studied.

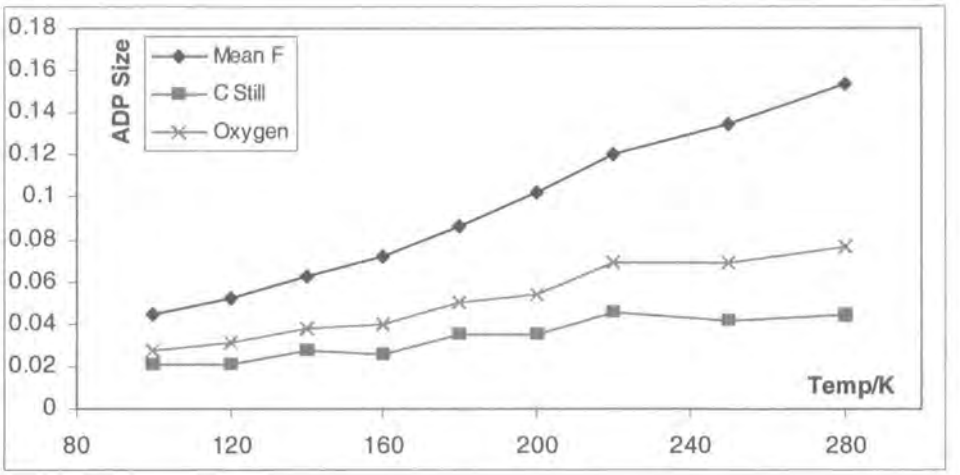

Figure 3.2-2 Plot of the mean size of the ADPs of fluorine atoms along with atoms C2 and oxygen for comparison. While the fluorine atom ADPs appear robust to the problems with the unit cells (Figure 3.1-1), the carbon and oxygen atoms display similar problems.

With this in mind one can make the case that the unit cell data also points to an anomaly at temperatures above 220 K. With the differences in the unit cell volumes between the two crystals/diffractometers it is hard to be certain; however, close inspection of Figure 3.2-1 might lead one to suspect that there is a linear relationship of volume with temperature over the 220 K to 280 K region, and a different (linear) relationship of volume with temperature below 220 K.

The above values have been taken from non-absorption corrected data. On the application of SADABS, the results vary only marginally; the correction results in a typical reduction in the ADP sizes of between 1 and 3%. Nonetheless, the results post SADABS treatment were rather inconsistent, especially at higher temperatures where the data quality is lower. Additionally, some of the data collections were relatively short and so the SADABS correction may not be totally reliable as it must work with fewer equivalents in these cases. Because of this – and the fact that this is a small organic molecular system which will display very little absorption – all values quoted in the main text of this chapter are for the uncorrected data.

3.2.3 Fourier Maps, ADPs and Modelling Disorder

Figure 3.2-3 shows the Fourier maps of the electron density in the plane of atoms F1-F3 at 280, 200 and 100 K, along with the ADPs that result from them. In all electron density diagrams, the contours are 0, 0.5 and 1 eÅ^{-3} (green); 1.5, 2.0, 2.5, 3.0, 3.5 and 4 eÅ^{-3} (blue); 5, 6, 7, 8, 9 and 10 eÅ^{-3} (brown); and 12, 14, 16 eÅ^{-3} (red). A cursory look at the maps suggests that the CF_3 group is ordered at 100 K and 200 K, while at 280 K there would appear to be very significant disorder around the group.

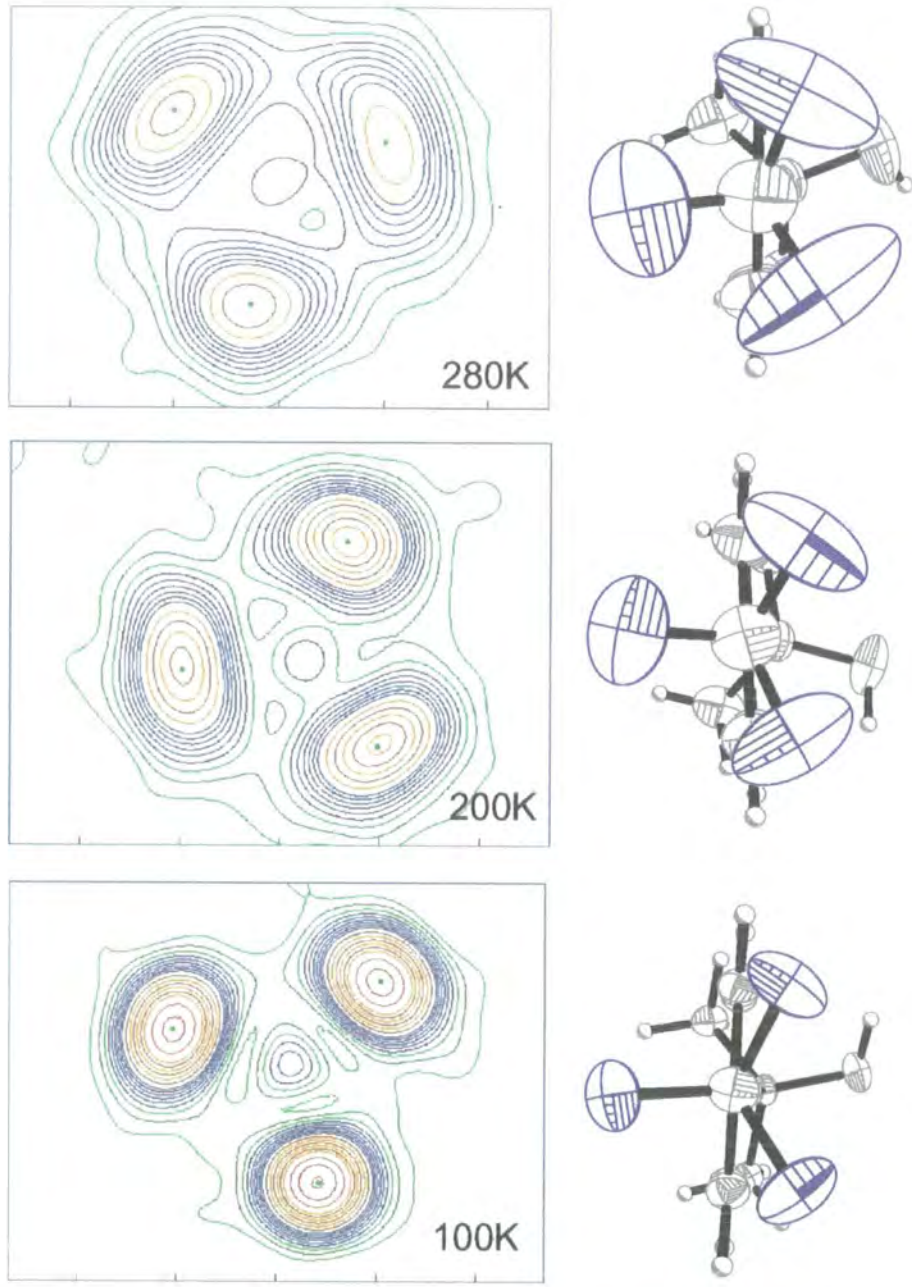

Figure 3.2-3 The Fourier maps in the plane of atoms F1-F3 at 100, 200 and 280K. In all electron density diagrams, the contours are 0, 0.5 and 1 eÅ^{-3} (green); 1.5, 2.0, 2.5, 3.0, 3.5 and 4 eÅ^{-3} (blue); 5, 6, 7, 8, 9 and 10 eÅ^{-3} (brown); and 12, 14, 16 eÅ^{-3} (red). As expected, the 100K map appears are well ordered as, for the most part is the 200K map. What is surprising is the very disordered 280 K map.

From consideration of the Fourier maps and the size of the resulting ADPs, it is not anticipated that a disordered model for the CF_3 group will make a significant improvement in the structure refinement. It is clear, however, that there is a serious problem with the 280 K data, in so far as the structure solves but fails to refine properly. Interestingly, a disordered model fails to improve the refinement statistics in any significant way (see Figure 3.2-4), even at 280 K where the Fourier maps would suggest such a treatment would pay dividends. Again this is offered as corroborating evidence that there are more serious problems with the data.

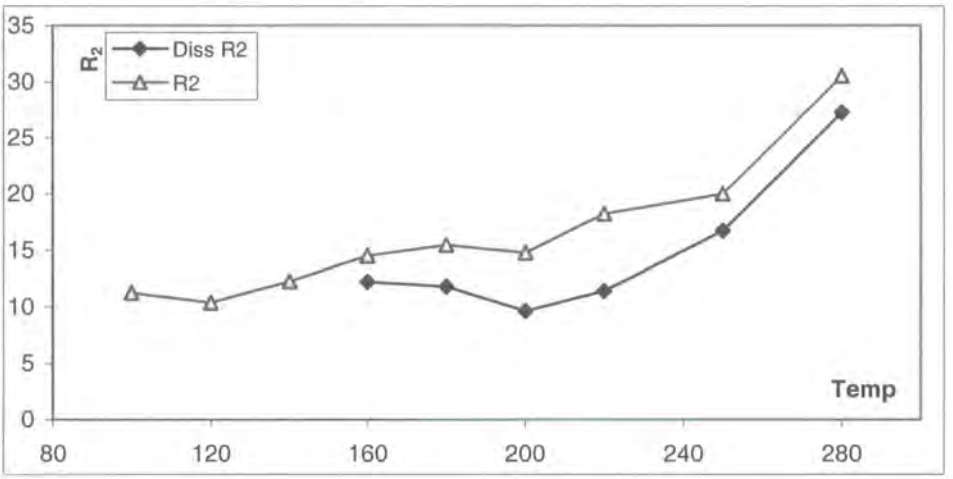

Figure 3.2-4 Plot of the R_2 values for a ordered (triangles) and disordered model (squares). What is obvious is that the 280 K refinement is very poor, and that the use of a disordered model does not improve this.

3.2.4 TLS analysis

Segmented rigid body analysis was carried out on all structure refinements using THMA11 version 20-04-91, within the WinGX software suite[ii]. In each case the molecule was split up such that the terminal CF_3 group was considered as a separate rigid segment, with an axis of libration about the carbon – carbon bond that attaches the group to the phenyl ring. A summary of the results is given in Table 3.2-4. These include the mean squared amplitude (MSA), force constant (FC) assuming harmonic motion, and a barrier to rotation (Barrier), assuming that the CF_3 group is sitting in a three fold potential. These values are plotted in Figure 3.2-5. The values for the barrier to rotation derived from the SADABS corrected data were 0.1-0.3 $kJmol^{-1}$ higher than the values quoted here, except at 250 K, where the value found was 3.6 $kJmol^{-1}$.

F5 - F7			
Temp	**MSA Deg^2**	**FC $J\ mol^{-1}\ deg^{-2}$**	**Barrier $kJ\ mol^{-1}$**
100	84.1 (4.0)	10.1 (0.5)	7.3
120	111 (5)	9.1 (0.4)	6.6
140	133 (5)	8.9 (0.3)	6.5
160	173 (7)	7.7 (0.3)	5.6
180	196 (7)	7.7 (0.3)	5.6
200	245 (9)	6.8 (0.2)	5
220	289 (10)	6.4 (0.2)	4.6
250	384 (20)	5.4 (0.3)	4.0
280	463 (25)	5.0 (0.3)	3.7

Table 3.2-4 Summary of the segmented-rigid body analysis: Mean Square Amplitude (MSA), Force Constant (FC) and barrier to rotation assuming a 3-fold potential (Barrier)

[ii] L.J. Farrugia (1991) *J. Appl. Cryst.* **32** 837-838

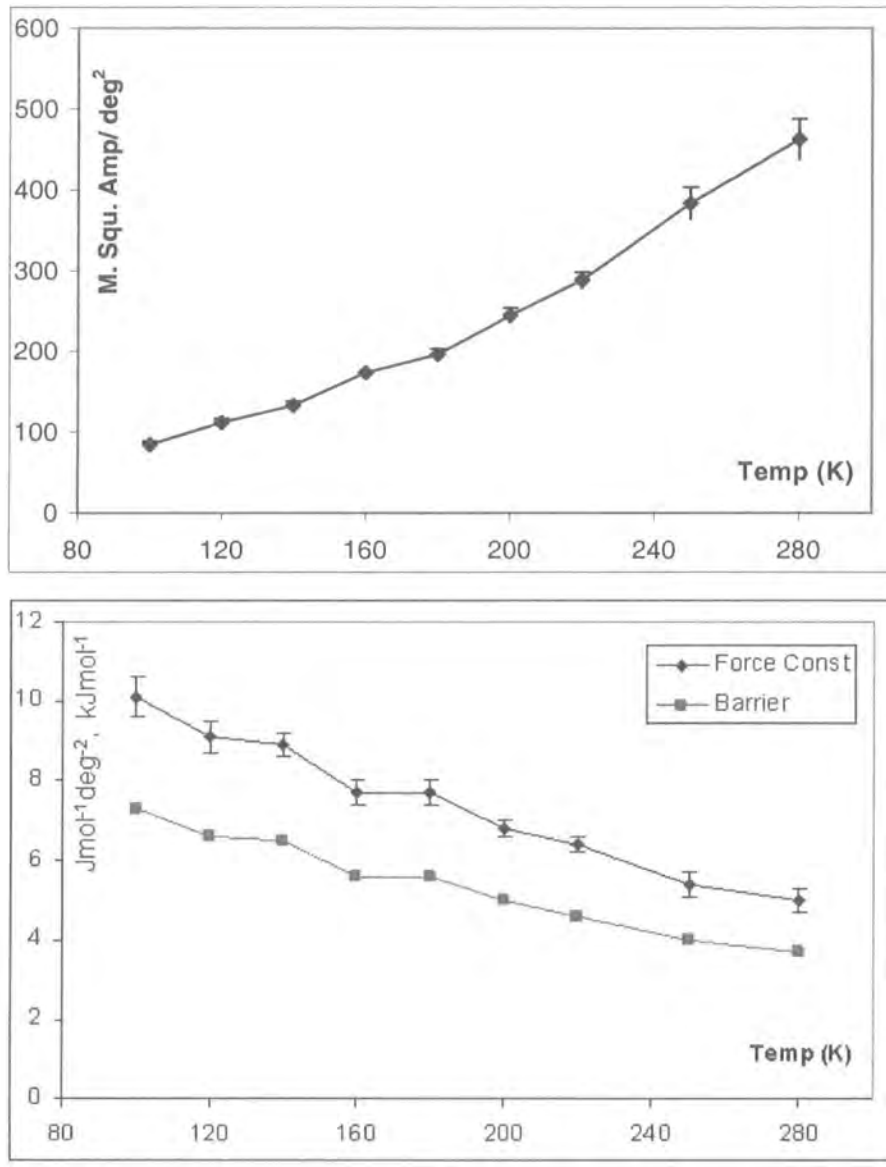

Figure 3.2-5 Plots of the mean square amplitude (top) and the corresponding force constants (bottom). Y-axis values are $Jmol^{-1}deg^{-2}$ with respect to the force constant and $kJmol^{-1}$ for the barrier to rotation. The anomalies in the unit cell volumes, and subsequently ADP sizes, are still present in these results, though in comparison with the errors, they are not hugely significant.

The procedure would appear to be remarkably robust in the values it produces. Although there are problems with the high temperature data, the mean square amplitude of the CF_3 group is approximately linear with respect to temperature. Although these were problems with the unit cell sizes at lower temperatures, this again has had minimal effect on the resulting mean squared amplitudes.

The derived physical properties once again show temperature dependence when in principle they should not. Values varying from 3.7 to 7.3 $kJmol^{-1}$ offer a factor of 2 difference from the two extreme temperatures. As before (Chapter 2.3.3) the assumptions of simple harmonic motion and constant crystal field are both questionable given the 5.2% reduction in unit cell size on going from 280 K to 100 K. Interestingly, the differences produced by the substitution of crystals and/or machine are noticeable (though within margins of error), while the poor quality of the high temperature data appear to have had a negligible effect on the results.

3.3 *Computational Chemistry*

The isolated molecular structure has been studied using plane-wave Density Functional Theory with a view to estimating the barrier to rotation of the CF_3 group. Both a rigid model for the CF_3 group and a transition state search employing LST/optimisation have been used. Due to the size of the unit cell - 2157.57 $Å^3$ at 100 K – calculations in the solid state have been omitted as the computational expense is prohibitive.

3.3.1 Geometry Optimisation of the Isolated Molecule

The molecule was placed into a unit cell of dimensions 9.50 x 10.00 x 15 Å, such that the molecule is approximately isolated, though not so large as to make the calculations impractical. A summary of the calculation input parameters are as follows:

Calculation Summary (input):

Files: 3-3-1

Exchange Functional: PW91; Plane wave cut off: 340 eV;

Energy Tolerance: $1x10^{-6}$ eV; K-point sampling: 1x1x1 (gamma point only);

Geometry Optimisation:

Energy Tolerance: 0.000010 eV/atom; Force Tolerance: 0.0300 eV/Å;

Stress Tolerance: 0.050 $eVÅ^{-3}$; Dispersion Tolerance: 0.0010 Å;

Method: BFGS

The input parameters are expected to yield results that are accurate to around a milli electron volt. For the proposes of validation, Figure 3.3-1 shows the molecular geometry of the 100 K X-ray structure and the geometry of the CASTEP calculated structure around the phenyl ring. It is immediately clear that the two structures are almost identical: the torsion angle C3-C2-C1-F1 is 24.39° in the diffraction derived structure and 22.76° in the calculated structure, and the carbon – hydrogen bond lengths are in line with those which are expected[iii]: 1.083 Å as compared with 1.082 Å calculated here.

[iii] International Tables for Crystallography; Vol C, Part 9.5 pp 691-707, IUCr - Kluwer Academic publishers (1992)

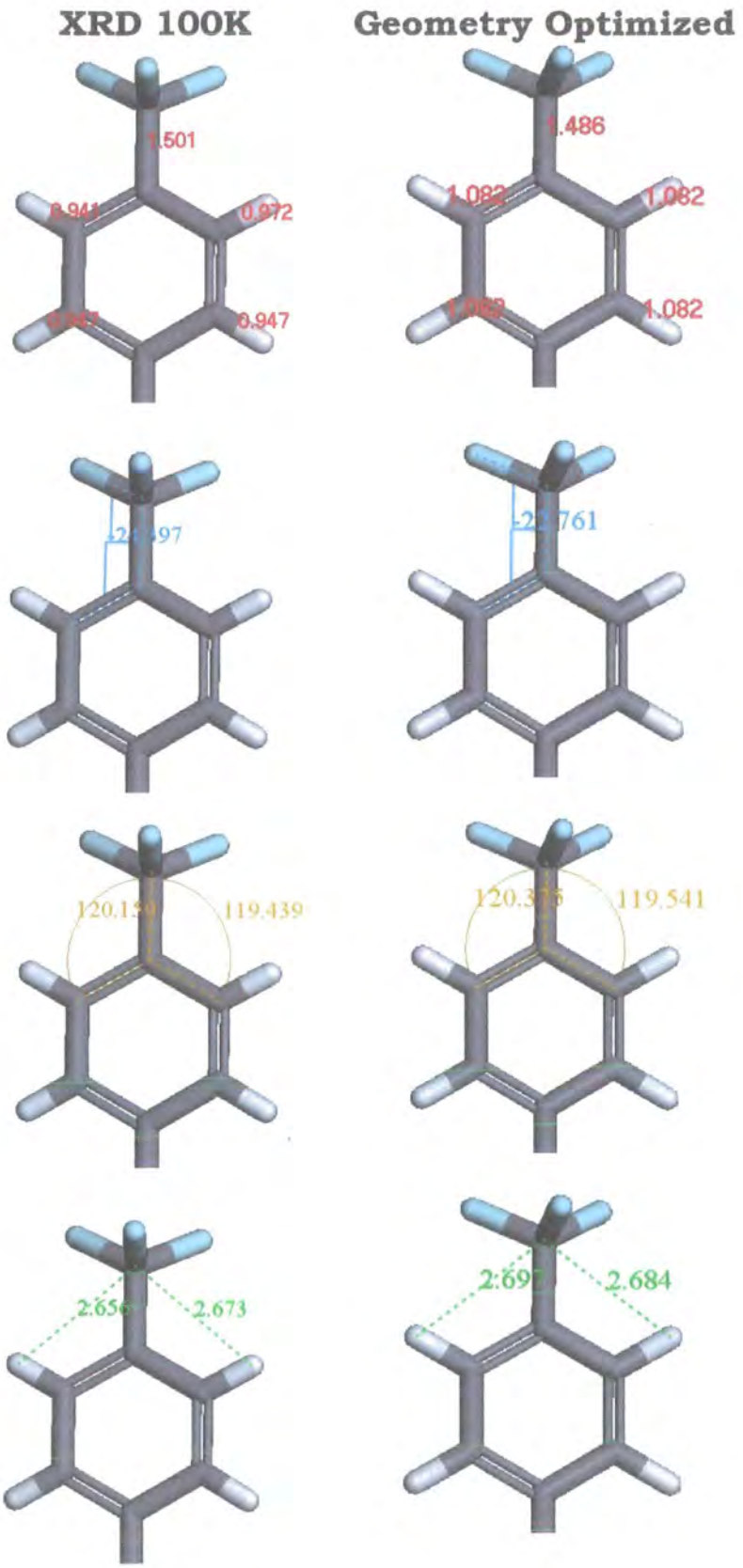

Figure 3.3-1 The molecular geometry found from the 100K X-ray data, left, and that found from the CASTEP geometry optimisation, right. The two structures are remarkably similar, even though the calculation is for the isolated structure. Note that the C1-C2 bond points straight out of the phenyl ring, and that the torsion angles of 24.4 and 22.8^{O} place none of the fluorine atoms coplanar with the hydrogen atoms of the phenyl ring.

3.3.2 Rigid CF_3 Rotation

Using the molecular structure calculated from CASTEP, the CF_3 group was rotated about the C1-C2 bond, such that the torsion angle F1-C1-C2-C3 was then varied from 0 to 354° is steps of 6°. The resulting energy profile is shown in Figure 3.3-2. The first of two things to note is that the differences in energy here are very small: it is clear that the magnitude of the effect being studied is smaller than that accessible from the computational model. Secondly, on this occasion, a plane wave basis set of 500 eV and $1x10^{-7}$ eV SCF tolerance was used after the calculation using the input parameters produced similarly unconvincing results. The difference between the two sets of data is negligible in any case.

The difference between the energy minimum (at 264°, -4887.905 eV) and maximum (at 186°, -4887.897 eV) is a mere 0.0077 eV, or 0.74 $kJmol^{-1}$. Clearly this is a small value, and far smaller than the value found from the diffraction experiment, where values in the 4-7 kJ mol^{-1} were derived. Notwithstanding that result for the isolated molecule rather than the bulk structure, it is none the less a far smaller value than its counterpart in Chapter 2.6.3.1, where a value of 2.91 $kJmol^{-1}$ was found. As discussed previously (Chapter 2.6.3.1) the results of the rigid body rotation are governed to some extent by the starting geometry. In this case there is little difference between the two 'sides' of the molecule, with the C3-C2-C1 and C7-C2-C1 bond angles being approximately equal, (see Figure 3.3-1).

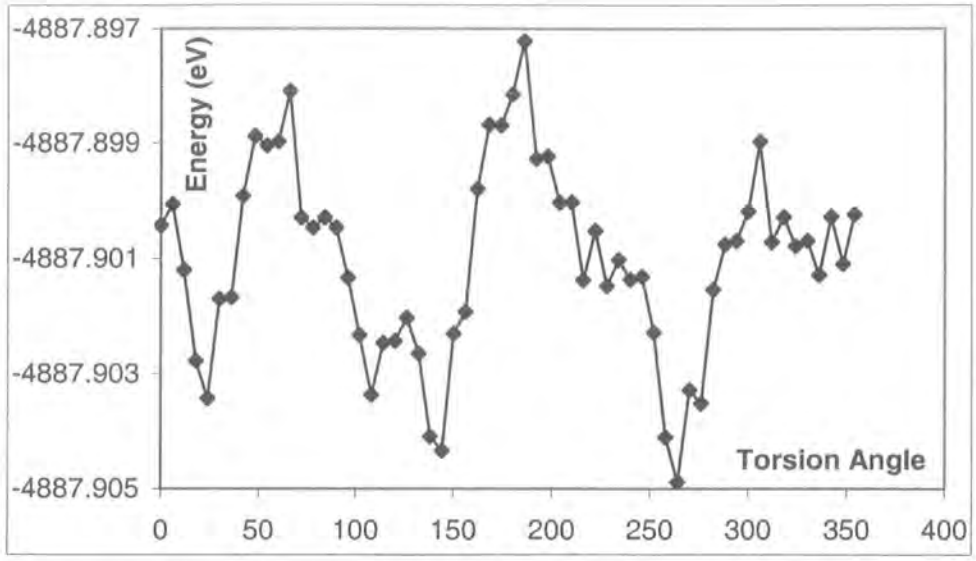

Figure 3.3-2 Energy profile of the system as the CF_3 is rotated as a rigid body about the C1-C2 bond The difference between the maximum and minimum is minimal in this case: less than a hundreth of an electron volt.

3.3.3 Barrier to Rotation via TS search

Using the LST/optimisation method, the barrier to rotation was calculated. The optimised geometry of –22.761° was used as the starting point and using end geometries of -142.761 and 97.209°, the barrier to rotation was calculated twice (i.e. the barrier to rotation in each direction, which ought to be the same). Calculation parameters from the geometry optimisation were used and a plot of the calculated energies as the calculation proceeded is found in the form of Figure 3.3-3 (going towards 97.209°), where the LST calculation is plotted in green and the optimisation is plotted in orange.

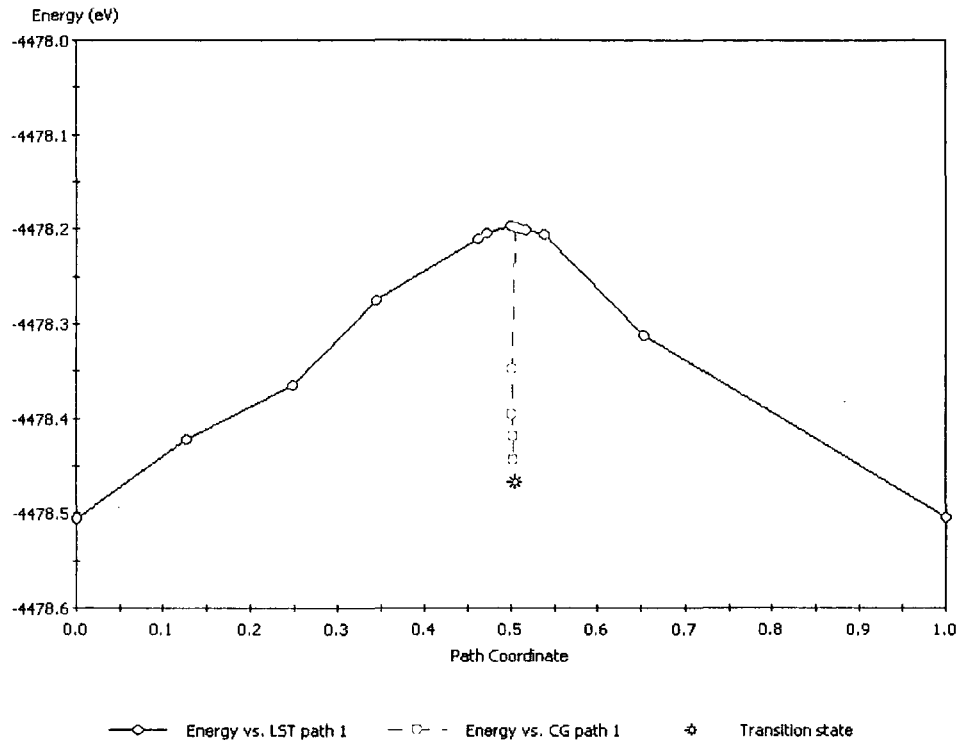

Figure 3.3-3 The energy of the LST/optimisation as the calculation proceeds. The green solid line represents the LST part of the calculation, and the orange dashed line represents the optimisation. The transition state is 3.74 kJmol^{-1} above the reactant (optimised geometry).

The results of the calculation are as follows –22.761° to 97.209° (input and output files: 3-3-2):

Energy of reactant/product: -4478.506 / -4478.505 eV

Energy of LST maximum: -4478.199 eV

Barrier from reactant/product: 0.307 / 0.306 eV

Energy of transition state: -4478.467 eV

Barrier from reactant/product: 0.039 / 0.038 eV

The values found from the calculation in the negative torsion angle direction (calculation files: 3-3-3) yielded similar results: a LST barrier of 0.309 eV and an optimised barrier of 0.039 eV. The values found here are more in line with

the values found from the diffraction experiment being 3.74/3.77 $kJmol^{-1}$ in this calculation, as against 4-7 $kJmol^{-1}$ found from the diffraction experiments. Thus while the rigid rotation method has produced essentially no barrier, the LST/Optimisation method has produced a reasonable result. The use of the isolated molecule makes definite comment difficult, though it would seem that in these systems there is only the smallest of barriers to rotation from the isolated molecule.

3.4 *Summary and Comments*

2-methyl-4-(4-trifluoromethyl-phenyl) but-3-yn-2-ol has been studied by variable temperature X-ray crystallography and plane-wave density functional theory. There is little to no disorder in the 100 K structure around the CF_3 group, though at higher temperatures this is not the case – thus the disorder is dynamic in nature. There are other problems with the data across the temperature range studied: the unit cells are not consistent and the high temperature data do not refine in a satisfactory manner. In spite of this, the segmented rigid body analysis has proven to be remarkably robust and the results derived at higher temperatures are in agreement with their low temperature counterparts, all values ranging from 3.7 to 7.3 $kJmol^{-1}$.

On the computational side, only the isolated molecule was studied, as the unit cells here are too large to make calculations on the crystal structure practical. In those calculations the barrier to rotation was found to be negligible when using the rigid motion approach, though the transition state search method produced reasonable values of 3.74 and 3.77 $kJmol^{-1}$.

4 Studies of Phenylethynyl Perfluorotoluene

The tolan phenylethynyl perfluorotoluene, formula $C_{15}F_7H_5$, "Tolan 3" hereafter, was studied by variable temperature X-ray crystallography and accompanying theoretical studies. The central consideration of this study was the disorder of the CF_3 group that is attached to a per-fluorinated phenyl ring, shown below.

4.1 *100K Crystal Structure of $C_{15}F_7H_5$*

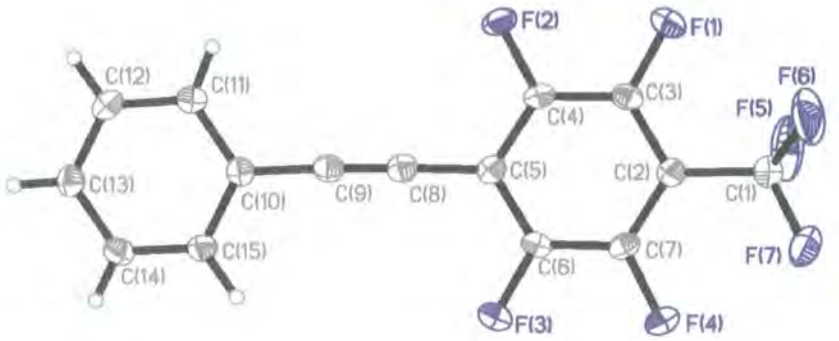

***4-1-1: $C_{16}F_{10}H_4$ at 100K**: monoclinic, $P2_1/n$ and $Z = 4$, $R_1 = 4.87\%$, $R_2 = 14.16\%$, $R_{int} = 0.0578$, $a = 5.9112(2)$ Å, $b = 28.4121(10)$ Å, $c = 7.4618(3)$ Å, $\alpha = 90°$, $\beta = 92.490°(2)$, $\gamma = 90°$, $V = 1252.02(8)$ Å^3*

Description of the crystal structure: As this is a low temperature crystal structure determination, the ADPs of all the atoms are small. However, the molecular structure shows that the terminal CF_3 fluorine atoms (F5, F6 and F7) have substantially larger ADPs than those of fluorine atoms F1 – F4. This suggests that there is disorder in the terminal CF_3 group, even at this low temperature. Other than this fact, there is little remarkable about the molecular structure of this system. The refinement statistics are good: $R_2 = 14.16\%$ and $R_1 = 4.87\%$, though there were peaks in the difference maps of 0.50 and 0.47 eÅ^{-3} around the F5-F7 group, that is, electron density which is unaccounted for in the model.

4.1.1 Crystal Packing and Intermolecular Interactions

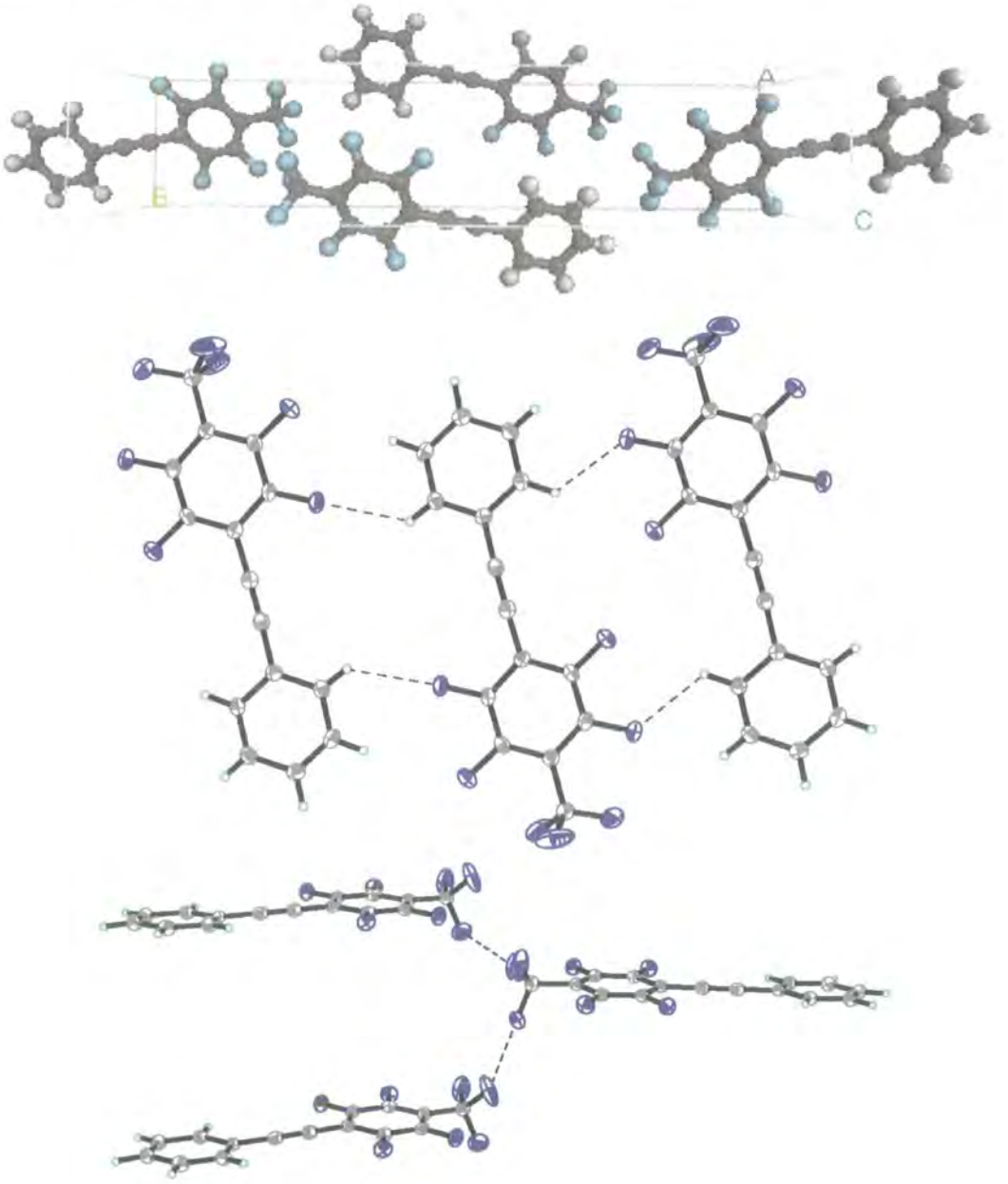

Figure 4.1-1 The unit cell viewed down the c-axis (top) showing the various 'short' F...H contacts (middle) and the packing around the CF_3 group.

There are four molecules in the unit cell. There are no intermolecular short contacts in the crystal structure, indicating that there are no strong intermolecular interactions. Figure 4.1-1 shows the molecular arrangement in the unit cell (top), and the closest contacts in the structure (middle). The carbon

– hydrogen contacts are 2.59(3) and 2.60(3) Å, and although the X-ray data will overestimate this distance somewhat, this distance is still not significant.

The packing around the CF_3 group is also devoid of close contacts that might "lock" the group into a particular conformation. The nearest intermolecular neighbours to these fluorine atoms are the fluorine atoms of other CF_3 groups, as illustrated in Figure 4.1-1 (bottom). The contacts are 2.838(3) and 2.969(3) Å, which is longer than the shortest contacts found in the crystal structures of either Tolan 1 or Tolan 2 (Section 2.2.1 and section 3.1.1 respectively).

4.2 Variable Temperature Experiments

The system was studied at eight temperatures between 100 and 280K, as outlined in Table 4.2-1. Two crystals were used for the low temperature experiments:

Crystal 1: 0.24 x 0.18 x 0.05 mm

Crystal 2: 0.30 x 0.20 x 0.05 mm

These crystals were mounted on a hair with oil and used, in back to back experiments, over a variety of temperatures. A third crystal was mounted on a glass pin with epoxy glue and used for the 280 K experiment:

Crystal 3: 0.28 x 0.20 x 0.05 mm

The crystals all had plate-like morphology and as such had only a small volume.

Temp/K	Exp No.	Machine	Crystal	Selected Diagrams:
280	4-2-7	1K	3	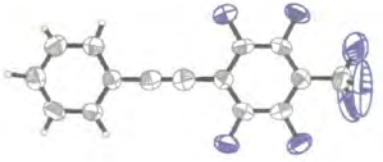
240	4-2-6	6K	1	
200	4-2-5	6K	2	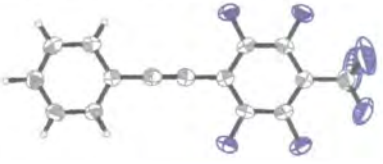
180	4-2-4	6K	2	
160	4-2-3	6K	1	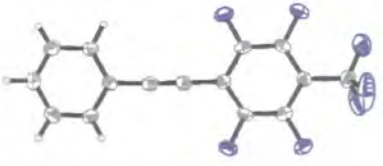
140	4-2-2	6K	2	
120	4-2-1	6K	2	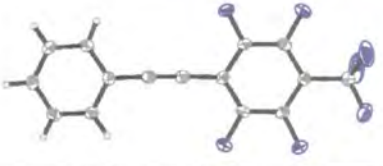
100	4-1-1	6K	1	

Table 4.2-1 A Summary of the 8 experiments undertaken. Pictures of molecular structure at 280, 200, 140, and 100 (top to bottom) included.

4.2.1 Unit Cell Parameters

Unit cell parameters for the experiments are tabulated in Table 4.2-2 and these results are plotted in Figure 4.2-1 as a percentage of the 280 K data. Over the temperature range studied, the variation in unit cell size is a little less than in the case of Tolan 1 and 2, being just short of 5%. Included in this is the fact that the 280 K data yields a slightly larger cell than might be expected from the rest of the data (assuming a linear relationship between temperature and cell volume). Note that this was the only experiment that was carried out using the Bruker SMART 1K, so this increased cell size, though unwelcome, is not unexpected (see discussion in Chapter 3.2.1).

Temp (K)	a-axis (Å)	b-axis (Å)	c-axis (Å)	Beta (°)	Volume (Å^3)
100	5.9112(2)	28.4121(4)	7.4618(3)	92.490(2)	1252.0(1)
120	5.9156(4)	28.4213(18)	7.4792(5)	92.551(3)	1256.2(1)
140	5.9236(4)	28.4508(10)	7.4991(5)	92.584(3)	1262.6(1)
160	5.9249(2)	28.4799(17)	7.5192(3)	92.604(2)	1267.5(1)
180	5.9364(3)	28.4796(13)	7.5365(3)	92.660(2)	1272.8(1)
200	5.9614(3)	28.5090(13)	7.5577(3)	92.744(2)	1279.0(1)
240	5.9614(7)	28.5924(34)	7.5915(9)	92.866(2)	1292.4(3)
280	5.9960(4)	28.6574(16)	7.6682(5)	93.153(3)	1315.6(1)

Table 4.2-2 Unit cell parameters of the 8 structure refinements.

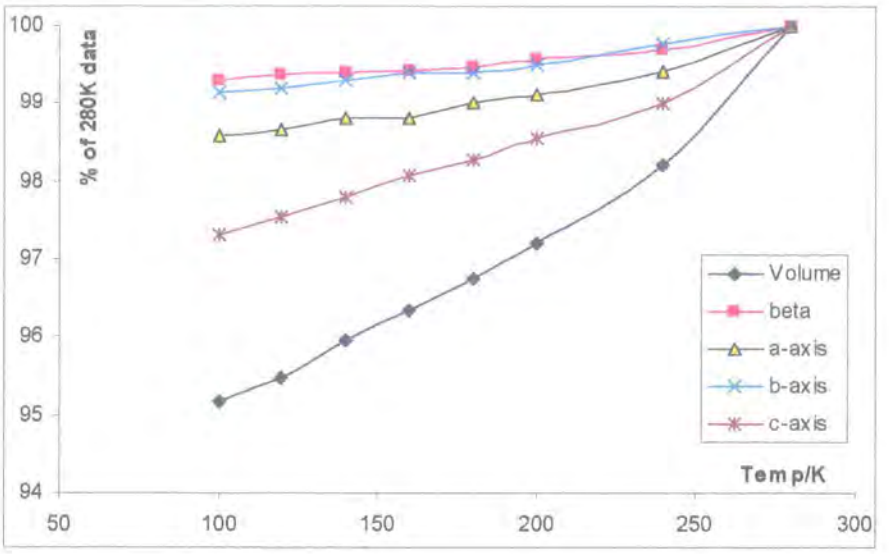

Figure 4.2-1 Plot of the cell parameters expressed as a percentage of the 280 K structure. Only the 280 K structure itself appears to be an outlier, having a larger volume than would be expected from the rest of the data.

4.2.2 Atomic Displacement Parameters (ADPs)

The mean size of the fluorine atom ADPs of the terminal CF_3 group, F5-F7, and the phenyl fluorine atoms, F1-F4, are tabulated in Table 4.2-3 and plotted in Figure 4.2-2. The linear relationship between the sizes and temperature is remarkably good, as demonstrated by R^2 (linear regression) values of over 0.99. If one extrapolates the linear relationship towards zero degrees (temperature) then one finds that the size of the ADPs of the two groups converge at 42 K – though obviously this is not entirely reasonable, as if the linear relationship were extended all the way to 0 K, the ADPs would have vanishing size. In fact, on the basis of these data, the F5-F7 ADP size at 0 K would be –0.0022: but then quantum effects close to absolute zero make such an extrapolation absurd.

Temp (K)	F1-F4 Mean	F5-F7 Mean
100	0.02806	0.06152
120	0.03404	0.07578
140	0.03913	0.09120
160	0.04174	0.10357
180	0.04760	0.12272
200	0.05290	0.14070
240	0.06143	0.17006
280	0.07426	0.20758

Table 4.2-3 The mean size of the ADPs of the atoms F1-F3 and F5-F7 over the temperature range studied.

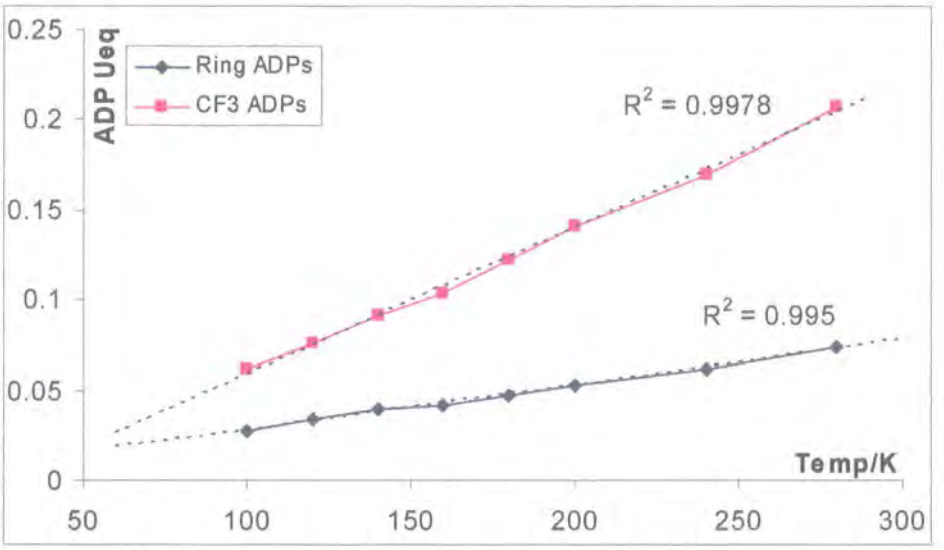

Figure 4.2-2 Plot of the mean size of the ADPs of the two groups of fluorine atoms.

The values quoted here (Table 4.2-3) and throughout the main text of this chapter refer to data that have not been corrected for absorption. On application of SADABS, the results vary only slightly from the above – a general reduction in the ADP size of 3-5% for each fluorine atom at each temperature post treatment.

4.2.3 Fourier Maps, ADPs and Modelling Disorder

Figure 4.2-3 shows the Fourier maps of the electron density in the plane of atoms F1-F3 at 280, 200 and 100 K, along with the ADPs that result from them. In all electron density diagrams, the contours are 0, 0.5 and 1 eÅ^{-3} (green); 1.5, 2.0, 2.5, 3.0, 3.5 and 4 eÅ^{-3} (blue); 5, 6, 7, 8, 9 and 10 eÅ^{-3} (brown); and 12 eÅ^{-3} (red). The 280 K experiment reveals circular smearing of the electron density, and that this smearing reduces at lower temperatures. At 280 K this disorder is so great that there is a 2 eÅ^{-3} bridge between two peaks that are themselves smaller than 5 eÅ^{-3} (Figure 4.2-3, top left). The suggestion is that the electrons are spending 2/7ths of their time in the energy maximum between the two defined atomic positions (energy minimum). There is clearly only a small difference between maxima and minima of the energy potential in which the atoms sit.

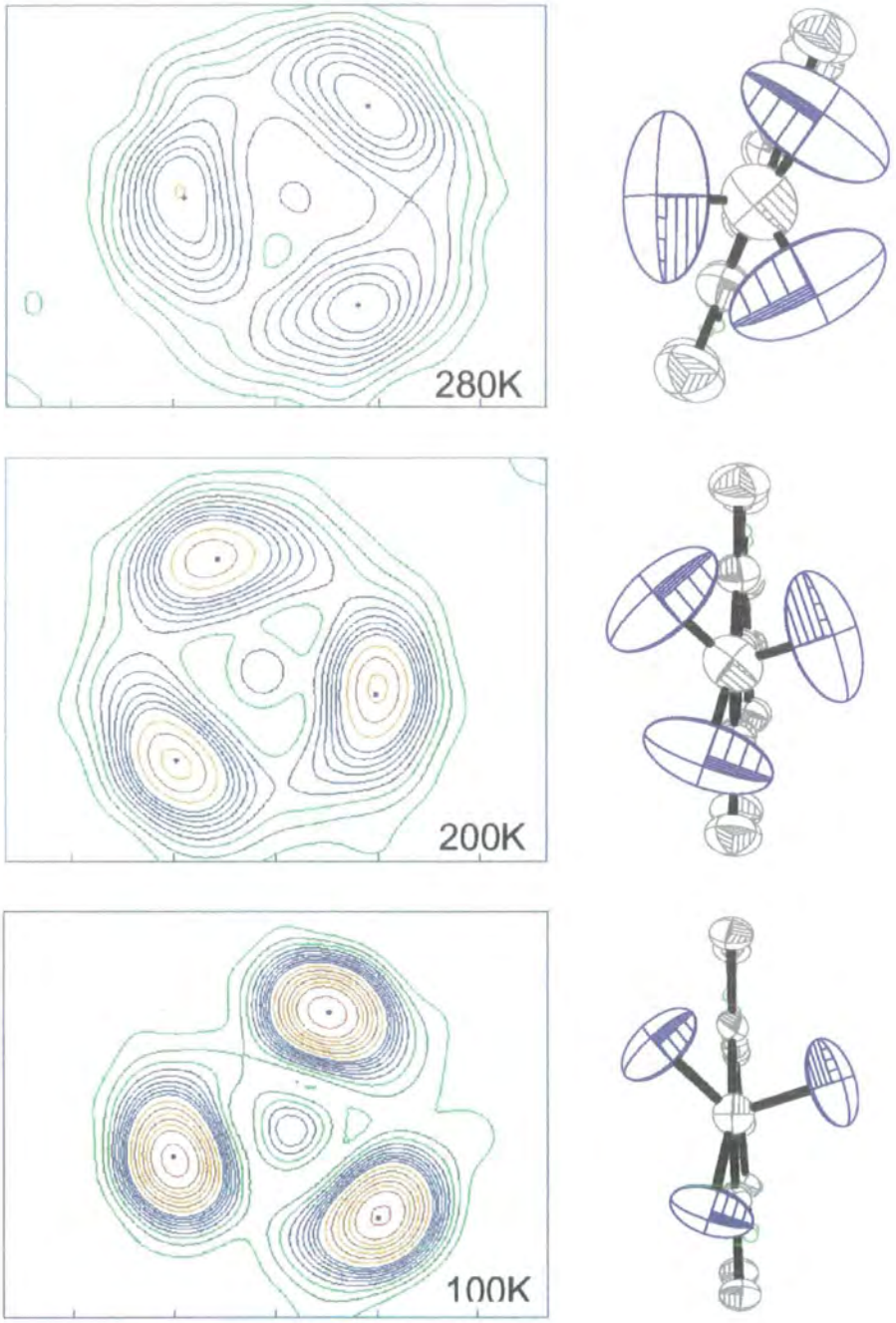

Figure 4.2-3 The Fourier maps in the plane of atoms F5-F7 at 280, 200 and 100 K, with the resulting ADPs. the contours are 0, 0.5 and 1 eÅ^{-3} (green); 1.5, 2.0, 2.5, 3.0, 3.5 and 4 eÅ^{-3} (blue); 5, 6, 7, 8, 9 and 10 eÅ^{-3} (brown); and 12 eÅ^{-3} (red). The 280 K maps are heavily disordered.

The system was refined using both an ordered and disordered model. As expected from the Fourier maps, employing a disordered model had a very large effect in the refinement statistics at the higher temperatures, though this advantage falls off at lower temperatures, where the validity of such a model is questionable. Still, it is rather reassuring to see that the two lines of best fit of the data cross at 46 K, which compares well with the 42.5 K that was the convergence point of the ADP sizes in Figure 4.2-4.

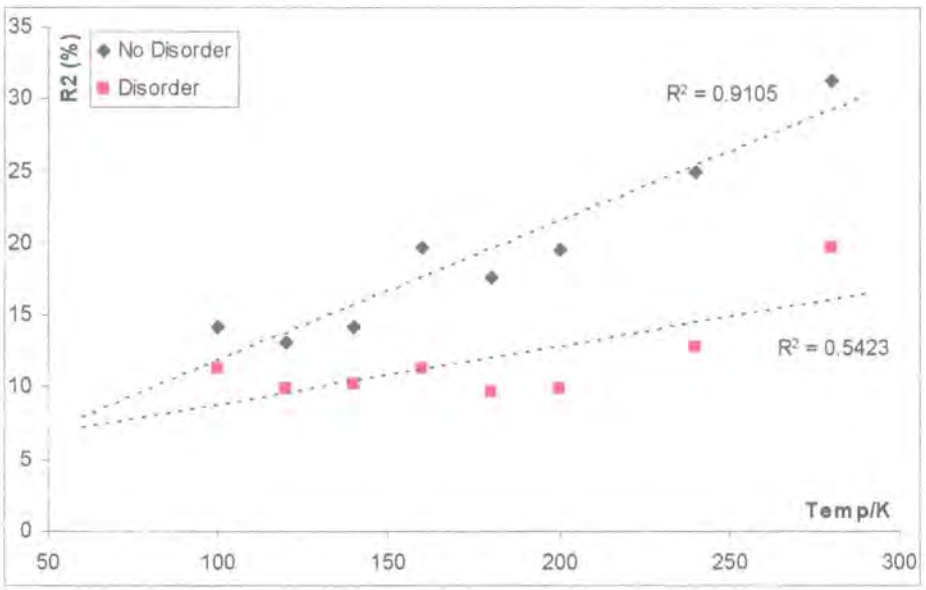

Figure 4.2-4 Plot of the R_2 values for each of the structure refinements, using a ordered model (blue) and a disordered model (pink). The refinement becomes better at lower temperatures and the difference between the ordered and disordered model also becomes less. The line of best fit through each set of data and the regression, R^2, are also plotted.

4.2.4 TLS Analysis

Segmented rigid body analysis was carried out on all structure refinements using THMA11 version 20-04-91, within the WinGX software suite[i]. In each case the molecule was divided such that the terminal CF_3 group was considered

[i] L.J. Farrugia (1991) *J. Appl. Cryst.* **32** 837-838

as a separate rigid segment with an axis of rotation about the carbon – carbon bond that attaches the CF_3 group to the phenyl ring (i.e. C1-C2). A summary of the results is given in Table 4.2-4. These include the mean squared amplitude (MSA), force constant (FC) assuming harmonic motion, and a barrier to rotation (Barrier) assuming that the CF_3 group is sitting in a three fold potential[ii]. These values are plotted in Figure 4.2-5.

F5 - F7			
Temp	**MSA** Deg^2	**FC** $J\ mol^{-1}\ deg^{-2}$	**Barrier** $kJ\ mol^{-1}$
100	194.8(5.4)	4.3(0.1)	3.1
120	246.8(7.1)	4.1(0.1)	3
140	308.5(8.2)	3.8(0.1)	2.8
160	368.7(8.8)	3.6(0.1)	2.6
180	463.9(10.0)	3.2(0.1)	2.4
200	543.0(11.9)	3.1(0.1)	2.2
240	689.8(14.3)	2.9(0.1)	2.1
280	887.6(47.1)	2.6(0.1)	1.9

Table 4.2-4 Summary of the segmented-rigid body analysis: mean squre amplitude (MSA), force constant (FC) and barrier to rotation assuming a 3-fold potential (Barrier).

[ii] The values for the barrier to rotation derived from the absorption corrected data were identical for the 120, 140, 160, 180, 200 K data, 0.1 $kJmol^{-1}$ larger for the 100 and 240 K data and 0.2 $kJmol^{-1}$ larger for the 280 K data.

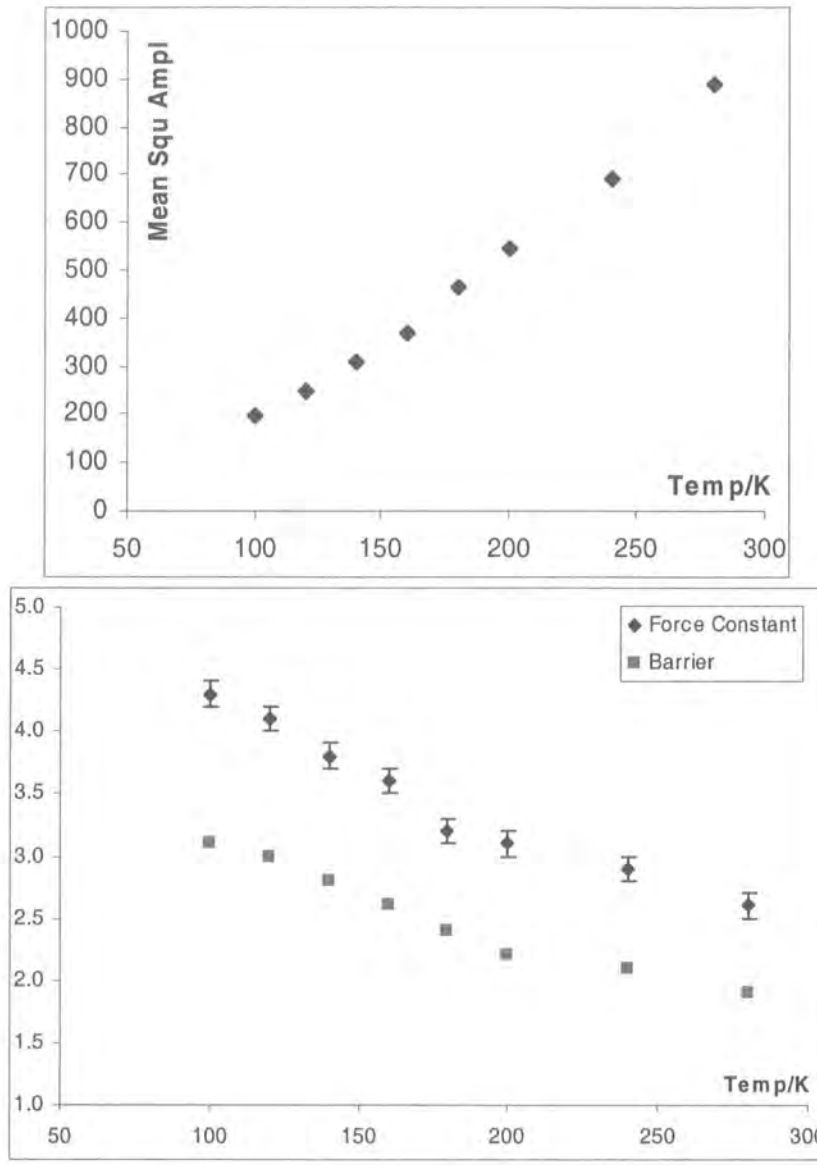

Figure 4.2-5 Plots of the mean square amplitude (top) and the corresponding force constants (bottom). Y-axis values are $Jmol^{-1}deg^{-2}$ for the force constant and $kJmol^{-1}$ for the barrier to rotation.

Once again we see that the estimate for the force constant and barrier to rotation is temperature dependant, such that at higher temperatures the values are lower than at low temperatures. The range of values derived across the various temperatures is a little less than in the previous cases (Chapters 2.3.3 and 3.2.4), being 3.1 – 1.9 $kJmol^{-1}$ for the barrier to rotation. This may well be related to the smaller variation in the unit cell volumes over the same temperature range providing a less variant crystal environment for each experiment. Additionally, as the disorder becomes greater, the use of a six

component ADP as a model for the p.d.f. of the electron density becomes less appropriate. For example, from the Fourier map of the 280 K structure (Figure 4.2-3) one should consider whether 3 ellipsoids are likely to describe the electron density well.

4.3 *Computational Chemistry*

Both the isolated molecule and bulk crystal structure have been probed via plane wave density functional theory. As before, (Chapter 2.6.3) the barrier to rotation of the CF_3 group has been estimated using both a rigid model for the CF_3 group and a transition state search employing the LST/optimisation protocol.

4.3.1 Geometry Optimisations

The geometry of the isolated molecule was optimised in a supercell of size 11.5 x 19.0 x 10.0 Å. A summary of the calculation input parameters, with expected convergence to around 1 milli electron volt, is as follows:

Calculation Summary (input):

Files: 4-3-1

Exchange Functional: PW91; Plane wave cut off: 330 eV;

Energy Tolerance: $1x10^{-6}$ eV; K-point sampling: 1x1x1 (gamma point only);

Geometry Optimisation:

Energy Tolerance: 0.000020 eV/atom; Force Tolerance: 0.0500 eV/Å;

Stress Tolerance: 0.10 $eVÅ^{-3}$; Dispersion Tolerance: 0.0020 Å;

Method: BFGS

The key geometric features of the resulting structure can be found in Table 4.3-1, along with similar features derived from the 100 K X-ray diffraction data. The calculation produced the expected carbon – hydrogen bond lengths, all between 1.081 and 1.083 Å, and the geometry around the CF_3 group is similar to that found from the X-ray data.

For the optimisation of the crystal structure, the calculation quality was reduced somewhat as the starting cell volume used (from the 100K XRD data) is 1252 $Å^3$, and as such, the calculation is on the large side of what is accessible using technology presently available. A summary of the input parameters is as follows:

Calculation Summary (input):

Files: 4-3-2

Exchange Functional: PW91; Plane wave cut off: 280 eV;

Energy Tolerance: $1x10^{-5}$ eV; K-point sampling: 2x1x2 ($P2_1/n$);

Geometry Optimisation:

Energy Tolerance: 0.000020 eV/atom; Force Tolerance: 0.0500 eV/Å;

Stress Tolerance: 0.10 $eVÅ^{-3}$; Dispersion Tolerance: 0.0020 Å;

Method: BFGS

This basis set ought to produce resulting energies that are converged to better than a hundredth of an electron volt, though not necessarily as good as a milli electron volt.

Feature	Structure from:		
	100K XRD	CASTEP: Bulk	CASTEP
 C-H Bond Length	0.908, 0.984, 0.969, 0.919, 0.970 Å	1.082 - 1.083 Å	1.081 - 1.083 Å
 Torsion Angle	14.709°	16.65°	15.783°
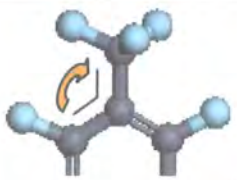 Angle	119.594, 122.803°	120.52, 122.517°	119.412, 124.06°
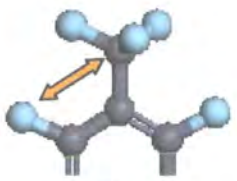 F-C distance	2.826, 2.898 Å	2.832, 2.893 Å	2.802, 2.935 Å
 F...H contact	2.593, 2.624 Å	2.542, 2.602 Å	---
 F...F Contact	2.839 Å	2.909 Å	---

Table 4.3-1 A selection of geometrical features taken from the 100 K X-ray data, geometry optimised crystal structure, and geometry optimised isolated molecule. There is very good agreement between the three structures.

The unit cell parameters post optimisation are remarkably similar to those which were input. The optimised cell size is a = 5.995 Å, b = 28.596 Å, c = 7.591 Å, β = 92.533°, Volume = 1300.01 Å^3, a marginally larger cell than that which was found at the lowest X-ray temperature studied. This is in stark contrast to the geometry optimisation of Chapter 2.6.1, where the unit cell reduced in size significantly. As a result, the intermolecular contacts found from the optimisation are in line with those found from the X-ray experiment: The shortest calculated F...H contacts are 2.542 and 2.602 Å, as compared with 2.59(2) and 2.62(2) Å from the X-ray experiment (see Table 4.3-1). Given that the carbon - hydrogen bond length is underestimated when using X-rays, these values are in excellent agreement. Other structural features are also reproduced well: the calculated C7-C2-C1-F7 torsion angle being 16.65° as against 14.71°.

4.3.2 Energy Barrier to Rotation: Isolated Molecule

Using the molecular structure calculated from CASTEP, the CF_3 group was rotated about the C1-C2 bond such that the torsion angle C7-C2-C1-F7 was varied from 0 to 354° in steps of 6 degrees. The calculation quality used was exactly as that for the optimisation of the isolated molecule in the previous section. The resulting energy profile is shown in Figure 4.3-1. The maximum and minimum energies are -7064.623 and -7064.752 eV respectively, and thus the energy barrier is approximately 0.129 eV or 12.45 kJmol^{-1}.

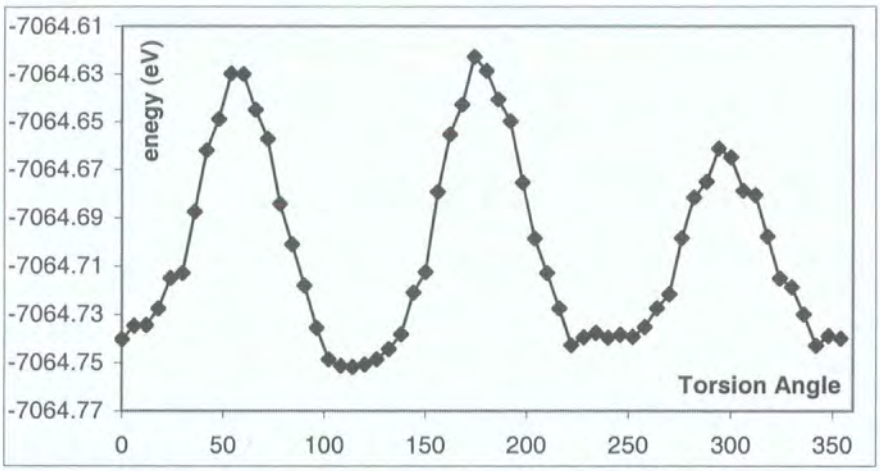

Figure 4.3-1 Energy profile generated by rotating the CF_3 group about the C1-C2 bond. An energy barrier to rotation of around 0.13 eV is found.

The LST/optimisation method has also been successfully utilised to calculate the barrier to rotation, starting at –15.783° and finishing at –135.783 and 104.217° (ie ± 120°) and using the same calculation quality as before. A plot of the calculated energies as the calculation proceeded is found for the first case (i) in Figure 4.3-2. The results of these two calculations are summarised as follows:

(i) -15.783 => -135.783°; Files: 4-3-3

Energy of reactant/product: -7064.749 / -7064.740 eV

Energy of LST maximum: -7064.304 eV

Barrier from reactant/product: 0.446 / 0.436 eV

Energy of transition state: -7064.688 eV

Barrier from reactant/product: 0.061 eV / 0.052 eV

(ii) –15.783 => 104.217°; Files: 4-3-4

Energy of reactant/ product: -7064.749 / -7064.738 eV

Energy of LST maximum: -7064.294 eV

Barrier from reactant/product: 0.455 / 0.444 eV

Energy of transition state: -7064.669 eV

Barrier from reactant/product: 0.081 eV / 0.070 eV

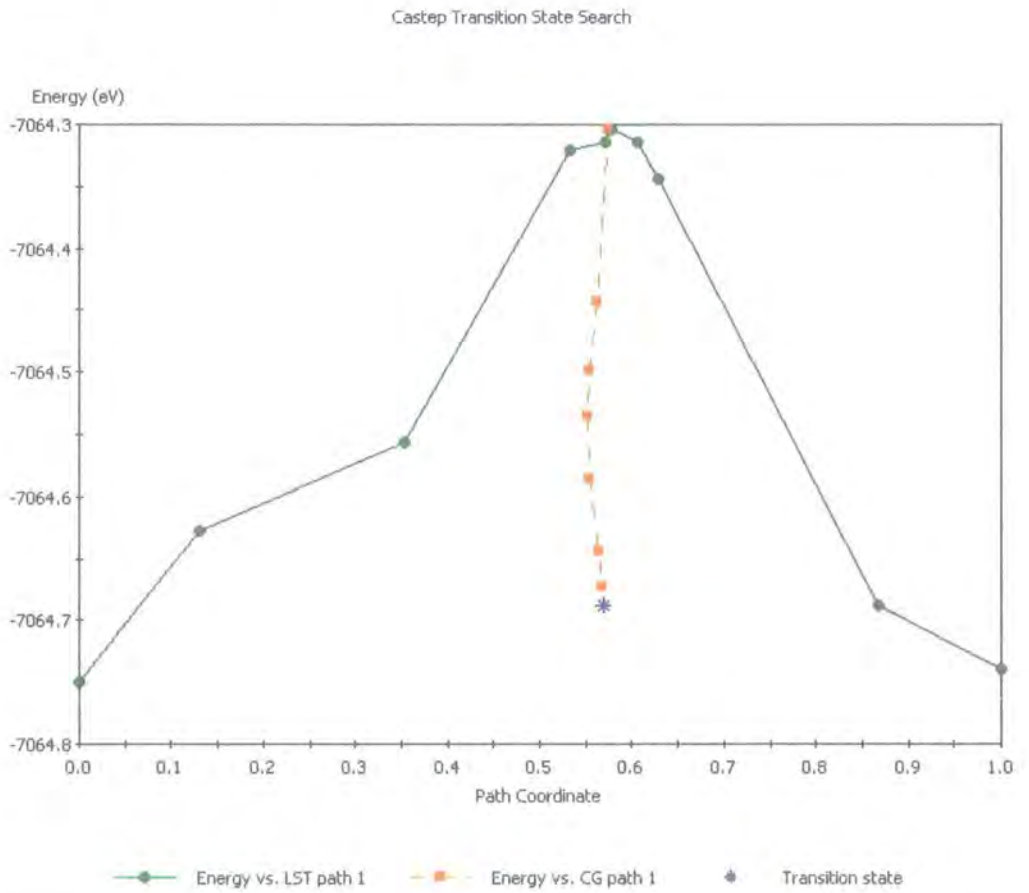

Figure 4.3-2 The energy of the LST/optimisation as the calculation proceeds from –15.78 to –135.78°. The green solid line represents the LST part of the calculation, and the orange dashed line represents the optimisation. The transition state is 5.86 kJmol^{-1} above the reactant (optimised geometry).

The energy barriers of 5.86 and 7.77 kJmol^{-1} are lower then those estimated from the rigid model, though still larger that the values estimated from the X-ray data, where barriers in the range 1.9 and 3.1 kJmol^{-1} were derived. This is rather surprising as one would expect the isolated molecule to produce lower

barriers to rotation: clearly in this case the molecular geometry of the system is having a major effect on the estimated barrier, at least with regards to the models used in these calculations.

4.3.3 Energy Barrier to Rotation: Bulk Crystal Structures

Using both the geometry optimized structure and the structure derived from 100 K X-ray data, the energy barrier to rotation has been probed utilising the two methods in the previous section. Throughout, the calculation quality is the same as that used for the geometry optimization of the full crystal structure: 280 eV cutoff, $1x10^{-5}$ eV SCF and a 2x1x2 k-point sample.

The energy profile generated by the two crystal geometries as the CF_3 group is rotated about the C1-C2 bond is shown in Figure 4.3-3. As these calculations are computationally expensive only a partial segment of the full rotation has been considered, such that only one energy minimum is covered. In the case of the XRD structure this involved steps of 5 degrees from 90° to –60° and for the calculated structure, steps of 5 degrees from 95° to –20° are considered. Energy barriers of 0.154 and 0.166 eV (14.83 and 16.03 $kJmol^{-1}$) are found from the observed X-ray geometry, while 0.146 eV (14.08 $kJmol^{-1}$) is found from the calculated structure.

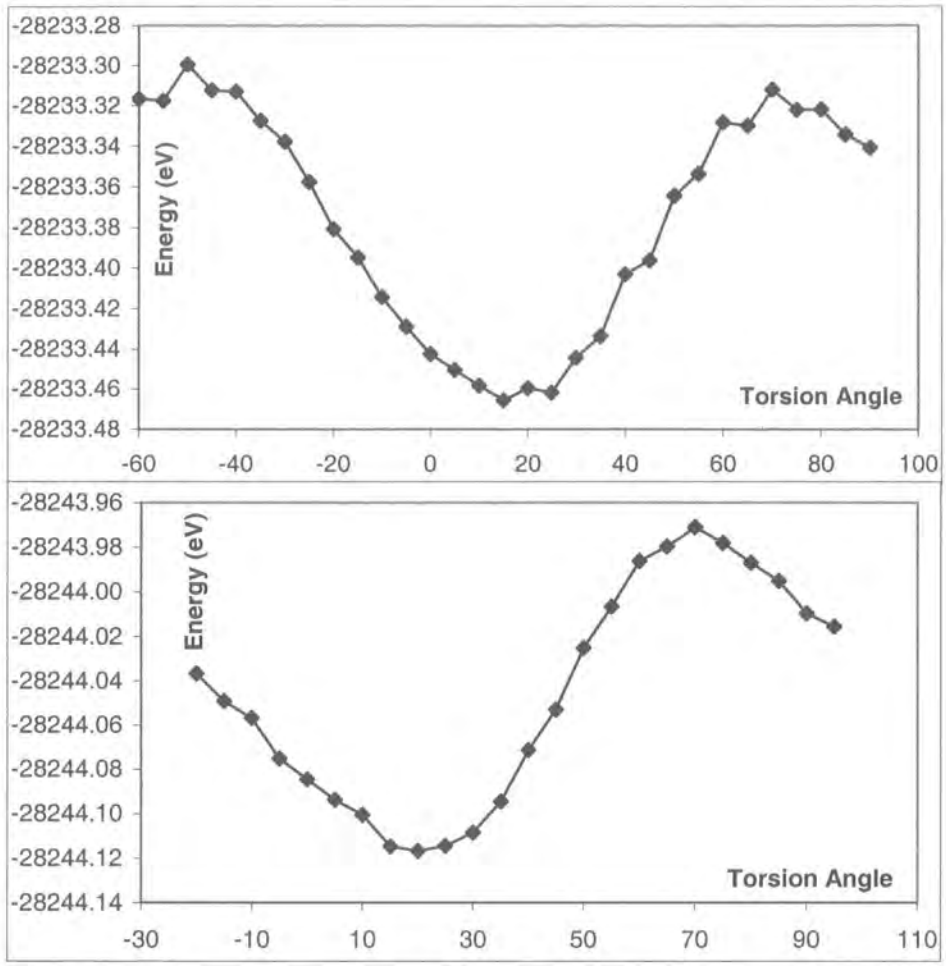

Figure 4.3-3 Energy profile generated by rotating the CF_3 group about the C1-C2 bond using the crystal geometry from the 100K XRD data, top, and the geometry optimised structure, bottom. The two profiles are similar in shape and both produce energy barriers in the region of 0.15 eV.

Using the LST/optimization protocol and starting/ending geometries of 16.65/136.65° the energy barrier was successfully calculated via a transition state search. A plot of the calculated energies as the calculation proceeded is found in Figure 4.3-4. The key results from the calculation are as follows (input and output files 4-3-5):

Energy of reactant/product: -28244.119 eV / -28244.100 eV

Energy of LST maximum: -28242.184 eV

Barrier from reactant/product: 1.935 eV / 1.916 eV

Energy of transition state: -28243.950 eV

Barrier from reactant/product: 0.169 eV / 0.149 eV

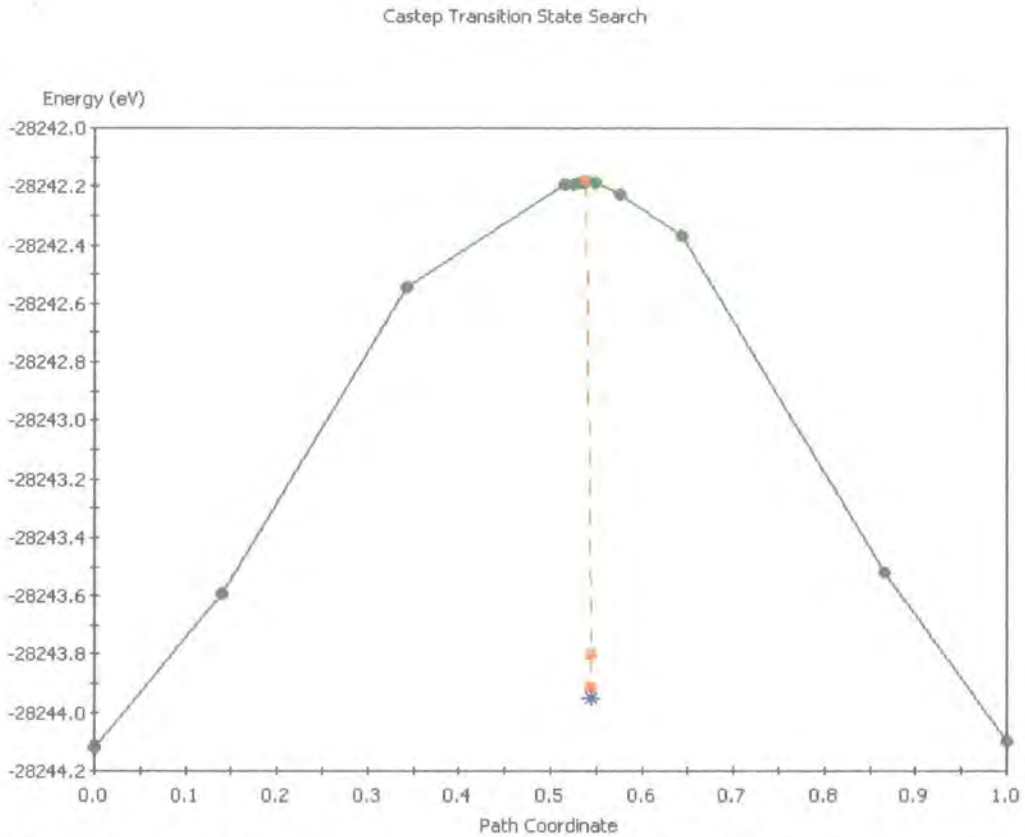

Figure 4.3-4 The energy of the LST/optimisation as the calculation proceeds from CF_3 torsion angles 16.65 to 136.65°. The green solid line represents the LST part of the calculation, and the orange dashed line represents the optimisation.

The barrier to rotation of 16.33 $kJmol^{-1}$ is similar to the values found from the rigid model. As such, all the calculated values found here are far greater then those derived from the X-ray data, where barriers of 1.9-3.1 $kJmol^{-1}$ were obtained. What is interesting here is that the computationally derived values for the crystal structure and isolated molecule are surprisingly similar. The implication, is that the molecular geometry rather than the crystal geometry is the central factor in generating the barrier to rotation.

This result can be emphasised by plotting the energy profiles of the three rigid motion profiles close to the energy minimum, on the same chart – Figure 4.3-5. While the isolated molecule does produce a shallower energy potential the differences are not huge. In fact, all these energy profiles are actually rather shallow: if one looks at the expected occupancies of the calculated energies at various temperatures (via statistical thermodynamics, see Chapter 2.6.3.1), one would expect there to be a great deal of disorder at ambient temperatures, and this in fact is the case in the 280 K XRD data.

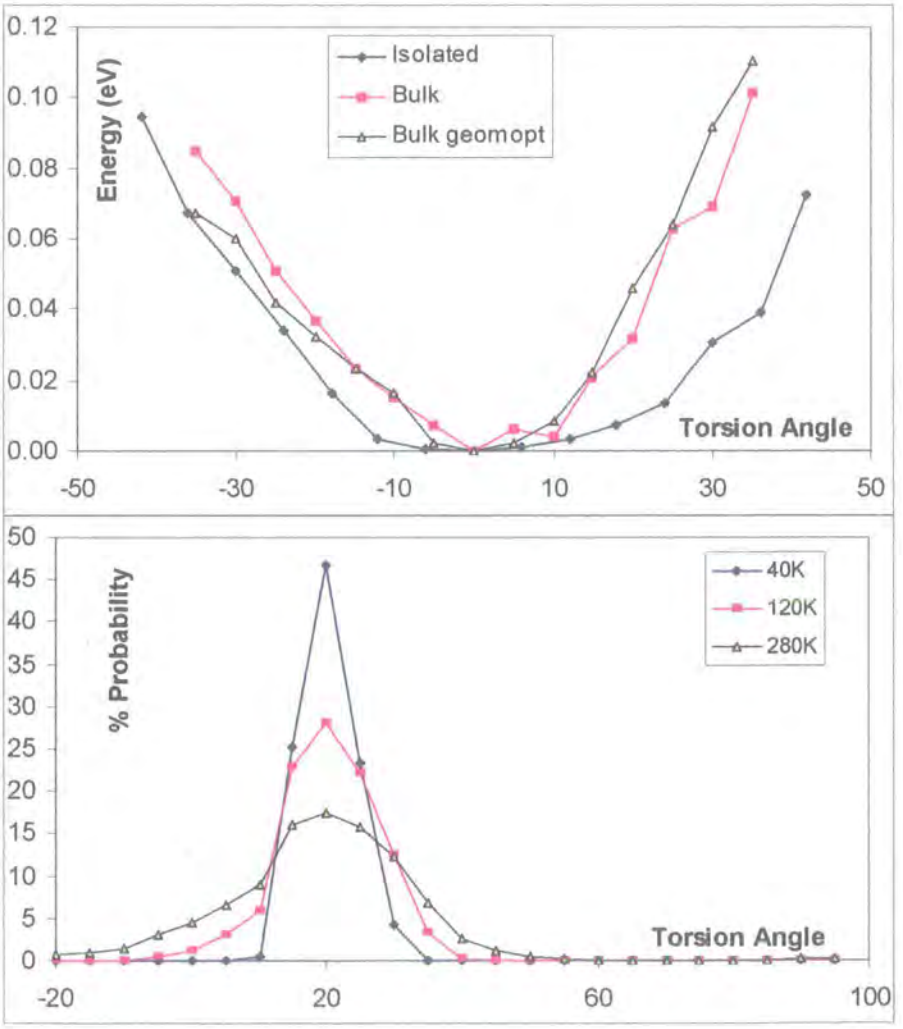

Figure 4.3-5 The various energy profiles close to the energy minimum (defined as: energy minimum = zero degrees, top). The expected populations of the various calculated energies for the geometry optimised structure (bottom). At 280 K the results lead to the expectation that there will be significant disorder around the CF_3 group.

4.4 Summary and Comments

Phenylethynyl perfluorotoluene has been studied by variable temperature X-ray crystallography and plane-wave density functional theory. Having shown that the disorder about the CF_3 group is dynamic in nature, segmented rigid body analysis was carried out and a barrier to rotation for the CF_3 group in the region of 2 to 3 $kJmol^{-1}$ so found. On the computational side, the barrier to rotation for the CF_3 group is calculated in the 12 to 14 $kJmol^{-1}$ region using a rigid model and 7.8 or 16.3 $kJmol^{-1}$ using the LST/optimisation method for the isolated molecule and crystal structure respectively. Clearly, the computational model is producing values that are significantly larger than the values found from X-ray diffraction experiments.

5 Zinc Pyromellitate

A variable temperature experiment was carried out on a sample of Zinc Pyromellitate by Dr. Roy Copley some time prior to the genesis of this work. As this work was never published prior to Dr. Copley's leaving the Durham crystallography laboratory, the author was asked to re-look at the data and carry out some re-determinations. The initial purpose of the work, from a crystallographic point of view, was to test the capabilities of the Fddd diffractometer.[i] As such, the criteria for the original experiments was that the crystals should *diffract well.* The original synthesis was carried out by Gavin Walker as a PhD student under the supervision of Professor Kenneth Wade. Details of the synthesis, along with discussion of the crystal structure can be found in chapter 5 of his PhD thesis,[ii] most pertinently, pages 129-131 for the preparation and 136-137, 152-155 for crystallographic details and discussion.

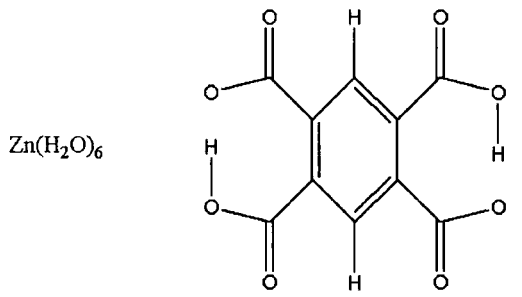

Figure 5.1-1a Chemical formula of Zinc Pyromellitate

[i] Copley RCB, Goeta AE, Lehmann CW, Cole JC, Yufit DS, Howard JAK, Archer JM *J. Appl. Crystallogr.* (1997) **30** 413-417

[ii] PhD Thesis; G.S. Walker (1995) University of Durham.

On inspection of the data previously collected, there appeared to be one aspect of the initial work that was particularly interesting: there appeared to be temperature dependent proton migration across the intramolecular hydrogen bond on the pyromellitate part of the system. That this might be a short strong hydrogen bond is not altogether surprising – the O...O distance is ca. 2.43 Å and the symmetry of the fragment is conducive to orbital mixing of the donor / acceptor oxygen atoms. The shortcomings of the X-ray method when it comes to locating hydrogen atoms, make definite statements on this score difficult to justify, so beam time on SXD at ISIS was requested, to determine accurately the position and ADPs of the proton via single crystal neutron diffraction. In addition, computational methods have been employed to provide direct information about the potential well in which the proton sites.

5.1 *Summary of Original Data*

Dr. Roy Copley collected datasets at 5 temperatures – 9, 50, 120, 210 and 296K on one crystal using the Fddd diffractometer. Figure 5.1-1b shows the molecular structure and the naming scheme for the system. The naming scheme has been retained for all diffraction experiments. A summary of the unit cell parameters for each temperature is given in Table 5.1-1. This data reveals that the unit cell volume varies by 29.11 $Å^{-3}$ over the temperature range studied; interestingly the 9 K cell is only 1.9% smaller than the 296 K cell and most of this cell volume variation is due to changes in the length of the c-axis.

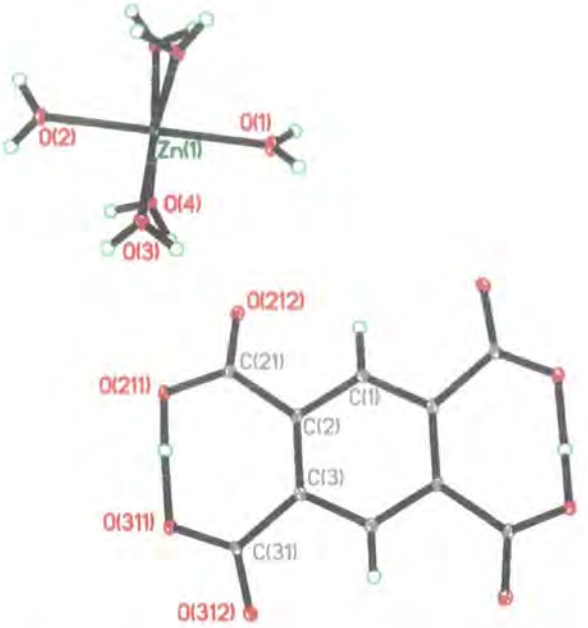

Figure 5.1-1b The molecular structure taken from the 9K X-ray diffraction experiment, with the naming scheme used in all diffraction experiments.

Temp/K	a-axis/Å	b-axis/Å	c-axis/Å	b-angle/Å	Volume/Å^3
9	21.911(4)	9.773(4)	7.158(5)	104.74(3)	1482.34
50	21.916(4)	9.772(4)	7.165(4)	104.78(3)	1483.71
120	21.928(3)	9.768(3)	7.193(4)	104.96(2)	1488.47
210	21.951(3)	9.768(3)	7.241(4)	105.22(2)	1498.14
296	21.993(4)	9.774(4)	7.296(4)	105.48(3)	1511.45

Table 5.1-1 Unit cell parameters for the five initial experiments – variation of the unit cell as a function of temperature is most pronounced in the direction of the c-axis, which translates to the variation observed in the cell volume.

As has already been noted, the position of the hydrogen atom apparently varies with temperature. At the lowest temperature the refinement places it 1.07Å from atom O211 and 1.365 Å from atom O311. At 296 K the situation is reversed: the proton is now placed 1.318 Å from O211 and 1.106 Å from O311 (See Figure 5.2-1). Were this apparent movement real, this would be rather interesting – certainly the O...O distance of c.a. 2.42 Å is short enough to constitute a Short Strong Hydrogen Bond (SSHB), or a Low Barrier Hydrogen Bond (LBHB). However, that the proton might migrate past the centre of the

hydrogen bond would be highly unexpected. Naturally, not trusting proton positioning that is derived from X-ray data alone, time was requested on SXD with a view to carrying out variable temperature single crystal neutron diffraction. Pending the neutron beam time, variable temperature X-ray data were re-collected.

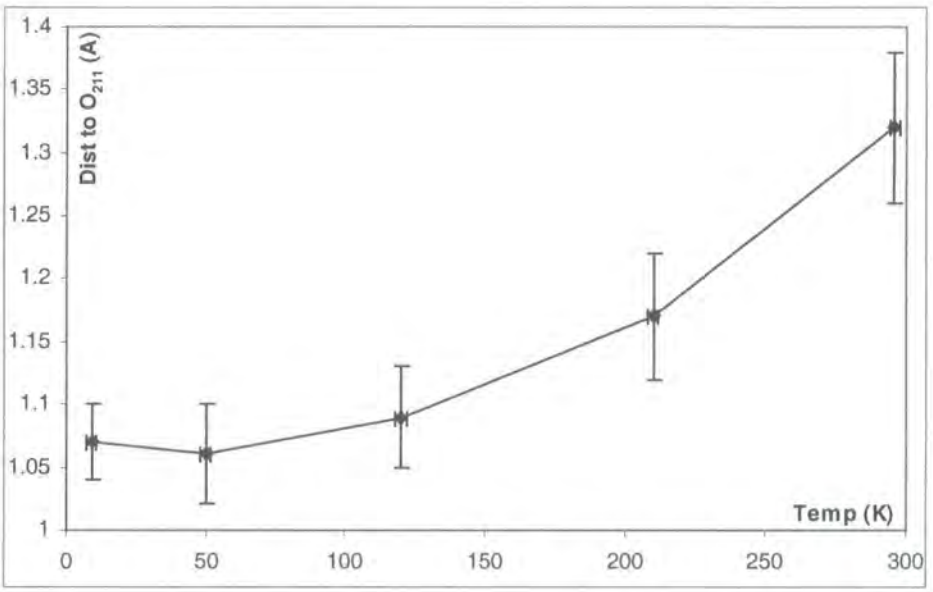

Figure 5.1-2 Across the temperature range studied there is an apparent change in the proton position, such that there appears to be migration across the hydrogen bond. Naturally, as this is an X-ray experiment the errors in the hydrogen atom positions are large and the results cannot be conclusive.

5.2 *New X-ray Data*

New data were collected at 9 temperatures ranging from 100 to 290 K, using both the 1K and 6K diffractometers using 2 different crystals. A summary of the temperatures at which data sets have been collected and the cell parameters recorded for these experiments can be found in Table 5.2-1. The cell volumes are plotted in Figure 5.2-1, along with the previously collected data from the Fddd diffractometer, expressed as a percentage of the 296 K Fddd diffractometer data. The data from the SMART 1000 yield significantly larger unit cells than the Fddd and SMART 6K diffractometers. This difference is due

to machine errors and is an excellent illustration of the 'hidden' errors in any crystallographic experiment. The 250K SMART 6K experiment showed far larger experimental error than the other experiments: this has been attributed to the fact that the crystal was mounted on a hair using oil. It would seem that the oil was not entirely solid at this temperature and thus this experiment is not reliable – data are included as a rough guide rather then as a true representation of the crystal structure at that temperature.

Temp/K	a-axis/Å	b-axis/Å	c-axis/Å	b-angle/Å	Volume/Å^3	Exp No.
100	21.892(1)	9.7652(4)	7.1819(3)	104.913(1)	1483.64	5-2-1
140	21.906(1)	9.7649(4)	7.2035(3)	105.031(1)	1488.17	5-2-2
150	21.938(1)	9.7806(5)	7.2206(4)	105.040(3)	1496.22	5-2-3
180	21.9029(7)	9.7650(3)	7.2246(2)	105.156(1)	1491.46	5-2-4
220	21.963(2)	9.7931(4)	7.2668(5)	105.358(7)	1507.17	5-2-5
220	21.972(4)	9.771(1)	7.244(1)	105.18(1)	1500.93	5-2-6
250	21.990(2)	9.791(1)	7.2810(6)	105.359(4)	1511.73	5-2-7
250	21.98(3)	9.79(1)	7.250(9)	105.25(4)	1504.13	5-2-8
290	21.997(4)	9.793(2)	7.307(2)	105.490(4)	1516.87	5-2-9

Table 5.2-1 Unit cell parameters of the 9 new X-ray diffraction experiments carried out.

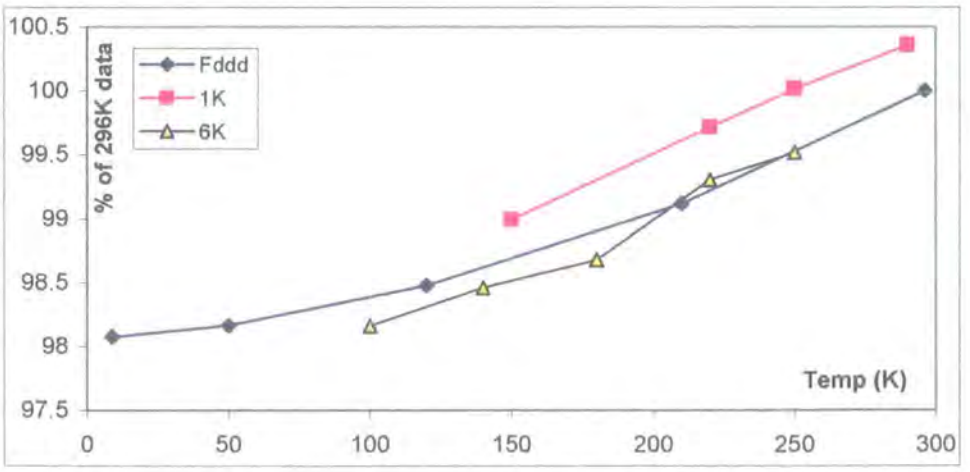

Figure 5.2-1 Plot of the unit cell volumes for the 3 experimental data sets, expressed as a percentage of the 296K Fddd diffractometer data. The SMART 1K produced systematically larger unit cells that the SMART 6K or Fddd diffractometer.

As the position of the proton in the intramolecular hydrogen bond is of central interest in this system, the length of the O211-H211 bond at all 9 new temperatures is plotted in Figure 5.2-2. Immediately seen from the plot is the fact that there is no suggestion of proton migration as was suggested by the earlier X-ray work. Obviously the short comings of the X-ray technique make the results somewhat ambiguous; however, some effort was spent to find out which of the two possibilities is more likely. The Fourier maps in the region of the hydrogen bond were plotted at 9, 210 and 296 K from the original data, along with those for 100 and 180 K (SMART 1K experiment) and 290 K (SMART 6K experiment).

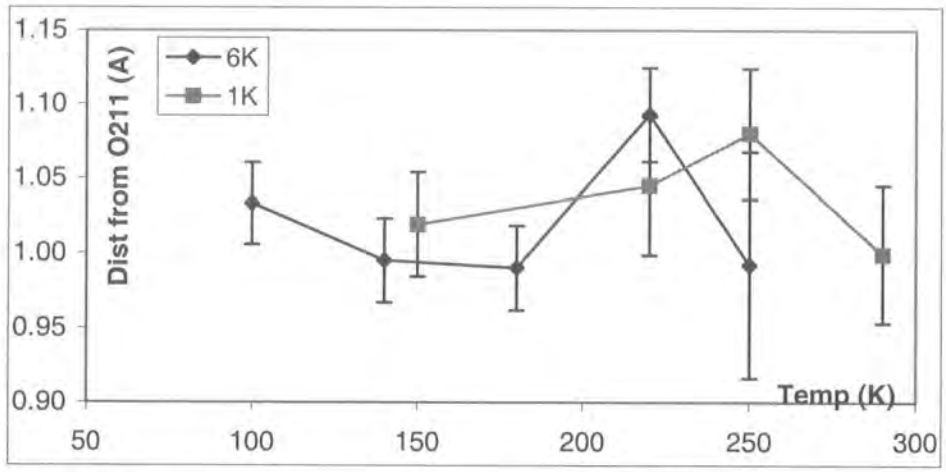

Figure 5.2-2 Plot of the hydrogen atom position across the temperature range studied. In contrast to the initial experiments (Figure 5.1-2), there is no apparent change in the proton position found in these experiments.

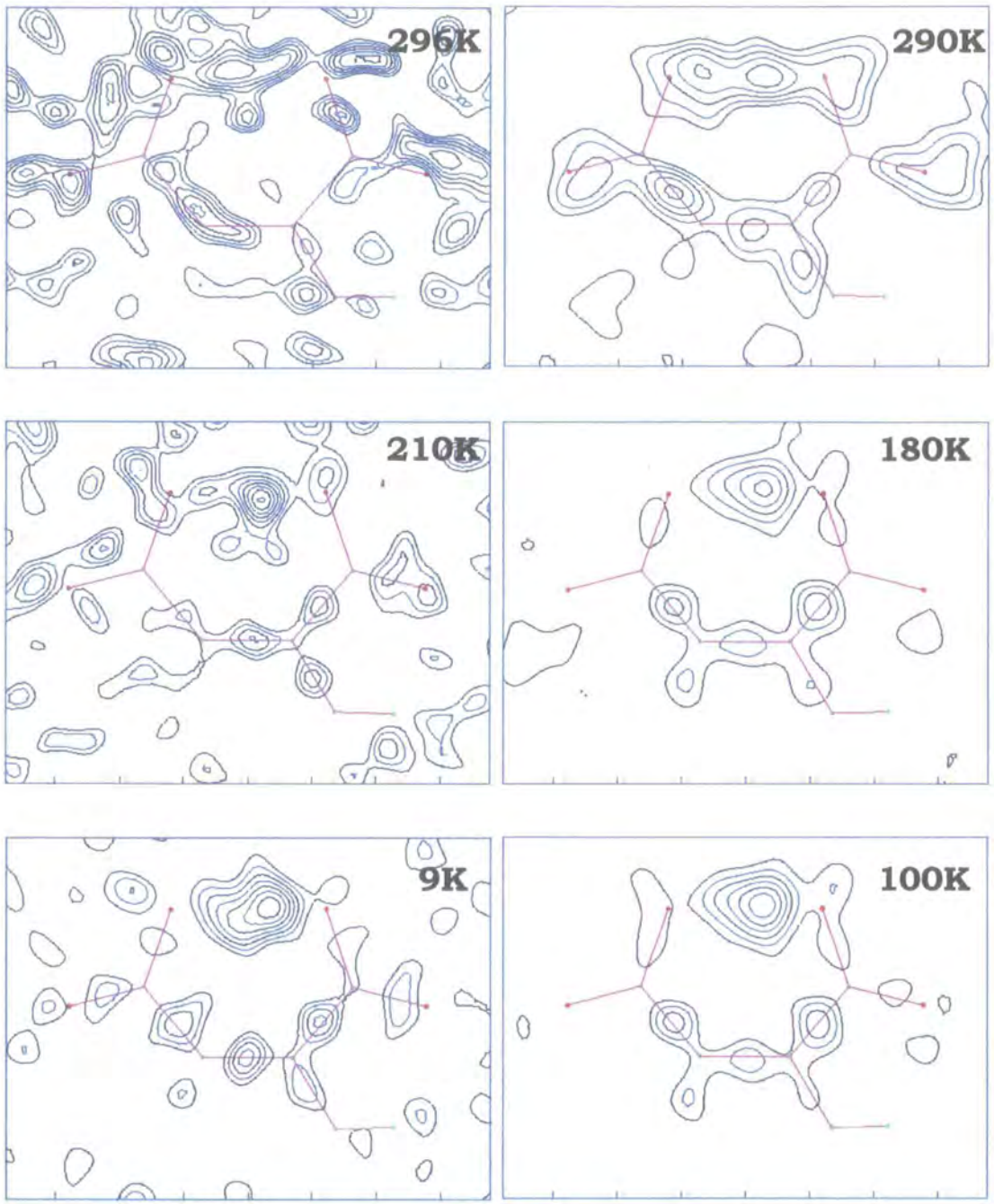

Figure 5.2-3 Plots of the Fourier maps at 9, 210 and 296 K from the original work, left, and 100, 180 and 290 K from the more recent experiments, right. In each case the proton has been removed and the structure refined. The contours are 0.1, 0.2, 0.3... $eÅ^{-3}$ throughout. The Fourier maps of the original experiments support the result that there is a shift in the position of the hydrogen atom. The maps of the newer experiments suggest that, while the ambient temperature position is rather disordered, there is no significant change in the position of the peak in the electron density.

To create each of the maps, the hydrogen atom had been removed, the structure re-refined (one least squares cycle), and then the mean plane through the atoms O211, O311, C21 and C31 used to calculate the Fourier map. In Figure 5.2-3,

the plots on the left are from the original work, where there was apparent movement of the proton, while those on the right were from the more recent work. The Fourier maps support what is seen in the refinements at all temperatures, although at the higher temperatures, the maps are rather disordered and it is unclear where the proton actually is. Given this ambiguity, the neutron diffraction experiment is clearly necessary.

5.3 *Neutron Data*

The sample was taken to ISIS and studied using single crystal neutron diffraction on SXD. Data were collected at 6 temperatures between 50 and 296 K, using the multi-crystal technique[iii], by Professor C. C. Wilson. The temperatures and unit cells of these experiments, as found from SXD, are given in Table 5.3-1. The experiments consisted of longer data sets at 296 and 100 K with somewhat shorter data sets at the other four temperatures. As there are 187 parameters in the refinement, this leads to data to parameter ratios of around 8 for the longer data sets but only around 5 for the shortest data sets. Clearly in the latter case this is not ideal, though given the time constraints, this is unavoidable and acceptable.

[iii] C.C. Wilson; *J. Appl. Crystallogr.* (1997) **30** p. 184-189

Temp/K	a-axis/Å	b-axis/Å	c-axis/Å	b-angle/Å	Volume/Å^3	Data	Exp No.
50	21.765	9.767	7.172	105.16	1471.56	1116	5-3-1
100	21.835	9.772	7.200	105.08	1483.37	1498	5-3-2
150	21.804	9.758	7.228	105.26	1483.63	956	5-3-3
200	21.849	9.758	7.251	105.48	1489.85	1157	5-3-4
250	21.806	9.769	7.274	105.40	1493.89	900	5-3-5
296	21.830	9.762	7.308	105.64	1499.70	1323	5-3-6

Table 5.3-1 Unit cells taken from the neutron diffraction experiments on SXD. The last column refers to the number of data collected at each temperature. Note that there are 187 refinement parameters and as such, the 150 and 250K data sets are rather small.

On the advice of Professor Wilson, the unit cell dimensions for the neutron data refinements were taken from the X-ray experiments (estimated where necessary). This is due to the weakness of this particular experimental method in finding accurate unit cell parameters. It is instructive is the plot of the unit cell volumes against those from the X-ray experiment parameters, which can be found in Figure 5.3-1. The cell volumes found from SXD are in the region of 11 Å^3 smaller than those found on the Fddd diffractometer, which in turn are around 5 Å^3 smaller than those than those found on the SMART 1K. The cell dimensions used for the neutron data refinements were therefore those from the Fddd experiment.

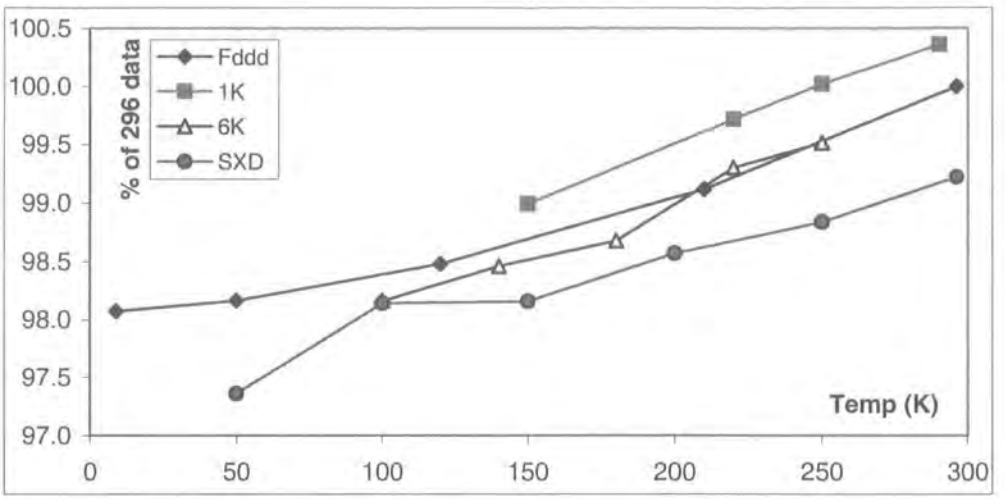

Figure 5.3-1 A plot of the unit cell parameters for all four sets of data. The neutron diffraction experiments have produced smaller unit cells than those from the X-ray experiments.

The key questions to answer from the experiment are: (i) does the proton vary in position as a function of temperature? and (ii) what are the shape and size of the ADPs that represent the nuclear positional disorder? The answer to the first question, is no – there is no significant movement of proton across the temperature range studied. Table 5.3-2 gives the O211-H211 bond length at each temperature, all values are between 1.120 and 1.103 Å, with an experimental error of approximately 0.01 Å. The O...O distance remains constant at 2.42(1) Å, and the O311...H211 distances mirror the O211-H211 values. This is a *very* convincing null result.

Temp/K	O...O	O...H	O-H	O-H esd
50	2.424	1.320	1.114	0.0106
100	2.422	1.311	1.119	0.0097
150	2.424	1.327	1.104	0.0119
200	2.415	1.314	1.112	0.0095
250	2.419	1.323	1.103	0.0138
296	2.423	1.315	1.120	0.0093

Table 5.3-2 A summary of the molecular geometry around the hydrogen bond of interest. Clearly the proton position in invariant across the temperature range studied.

As for to the second question: over the temperature range, does the positional disorder about the mean position vary to a greater extent here than might otherwise be expected. That is to ask: is there evidence in the form of an abnormally large ADP for H211 that suggests that the potential well in which it sits in is shallow? This can be answered simply by plotting the size of ADPs for various atoms and comparing the variation in size as a function of temperature. Should the variation be greater in the case of H211 then there would be direct evidence that the atom was exploring a greater proportion of the potential well, and thus that this potential well was shallower. If the answer to this question is negative then the variation in shape will also be irrelevant. Figure 5.3-2 is such a plot of the Ueq's of the zinc, O211, H211 and H1 atoms. Clearly there is nothing unusual about the H211 atom in this respect: while it is a little larger than that of H1, the difference in size is more or less constant across the temperature range.

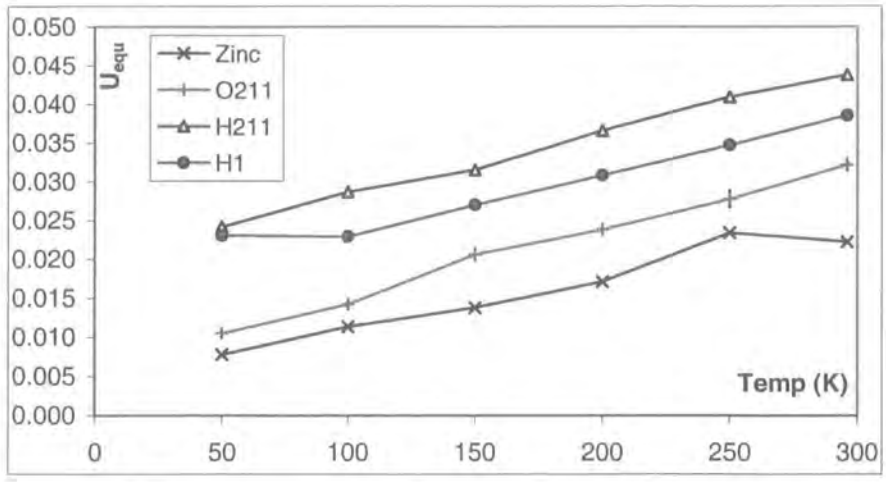

Figure 5.3-2 Plot of the size of the ADPs of atoms Zn, O211, H211 and H1. The rate of change of the size of the ADPs with respect to temperature is similar for all four atoms. This implies that there is no additional motion at higher temperatures in H211 as against the other atoms.

For completeness a close inspection of the Fourier maps of the system in the O211 – O311 – C21 – C31 plane has been carried out and is presented in Figure 5.3-3, together with the ADP diagram of the atoms in the near vicinity. In this case, the contours in the Fourier map plot are *negative*, in increments of –2, the maximum being -20.05, -13.24 and –12.87 for the 50, 200 and 296 K refinements respectively. In each of the plots, there is some evidence that there is positional disorder in the direction of the O311 atom. This is especially true of the 296 K map where the –2 contour is clearly elongated in this direction. There is thus some evidence that the proton sits in a shallow energy potential which is explored at higher temperatures. However, this doesn't translate into a measurable movement of the proton in the temperature evolution of the structure.

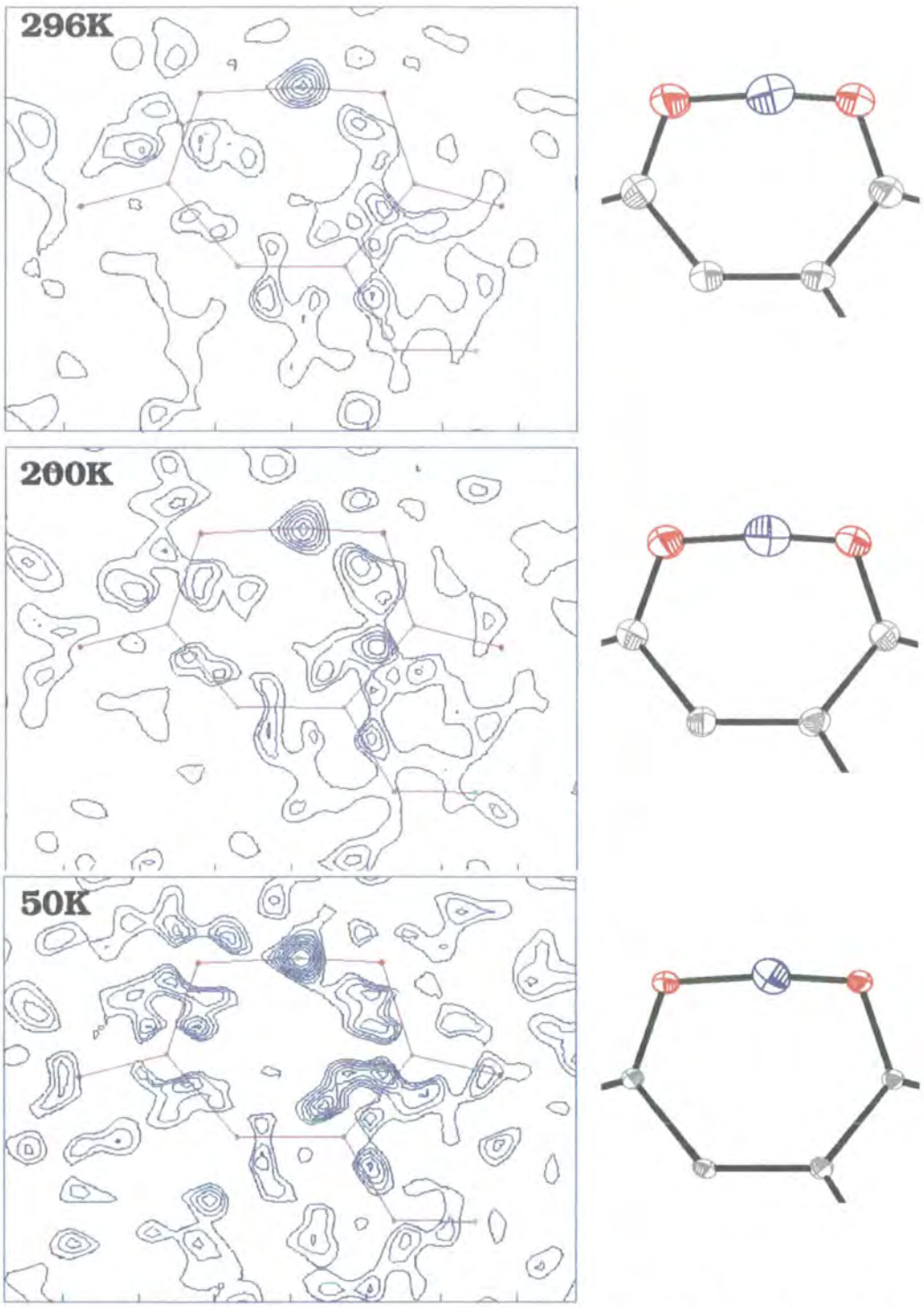

Figure 5.3-3 Plots of the Fourier maps at 50, 200 and 296 K, left, with the resulting ADPs, right. In each case the proton has been removed and the structure re-refined, and O211 is on the right side of each diagram. The contours are -2, -4, -6 barns and so on, throughout. Although there is some evidence of elongation in the O211-O311 direction, there in no significant movement in the position of the proton.

5.4 *Computational Chemistry*

The zinc pyromellitate system was studied using plane wave DFT calculations via the CASTEP package[iv]. A direct probe into the energy of the hydrogen bond is provided by moving the proton position around in the plane of the O211-O311-C21-C21 atoms and in the direction of the O211-O311 vector. Two situations were considered: the isolated pyromellitate fragment and the bulk crystal structure. For each of the two cases, both the geometry optimised structure within the chosen basis set and the results from the diffraction experiment are probed. Given the size of the unit cell – volume 1482 $Å^3$ – the quality of the calculation in the case of the bulk structure is lower than for that of the isolated fragment, computational expediency being the reason for this.

CASTEP input and selected output files can be found on the accompanying CD in the relevant section folders. The individual names for these files are given in the main text, below.

5.4.1 Geometry Optimisation of Isolated Pyromellitate

A CASTEP calculation was set up in Materials Studio to geometry optimise the pyromellitate part of the system ($C_{10}O_8H_4$) as an isolated molecule. The starting co-ordinates for the optimisation were taken from the 9 K X-ray diffraction experiment and unit cell size of 12 x 14 x 8 Å; $\alpha = \beta = \gamma = 90$ was used, such that the molecule could be constructed to be effectively isolated.

[iv] M.D. Segall, P.L.D. Lindan, M.J. Probert, C.J. Pickard, P.J. Hasnip, S.J. Clark, M.C. Payne; *J. Phys.: Cond. Matt.* **14**(11) pp.2717-2743 (2002)

Calculation Summary (input):

Files: 5-4-1

Exchange Functional: PW91; Plane wave cut off: 380 eV;

Energy Tolerance: $5x10^{-7}$ eV; k-point sampling: Gamma

Geometry Optimisation Method: BFGS

Energy Tolerance: 0.00002 eV/atom; Force Tolerance: 0.050 eV/Å;

Stress Tolerance: 0.100 eVÅ^{-3}; Dispersion Tolerance: 0.0020 Å;

Overall this represents a high quality calculation, that should be converged to the meV level. Figure 5.4-1 shows the molecular structure at the start and end of the calculation. Full details of how the calculation proceeded can be found in the file CAZN_geomopt.castep.

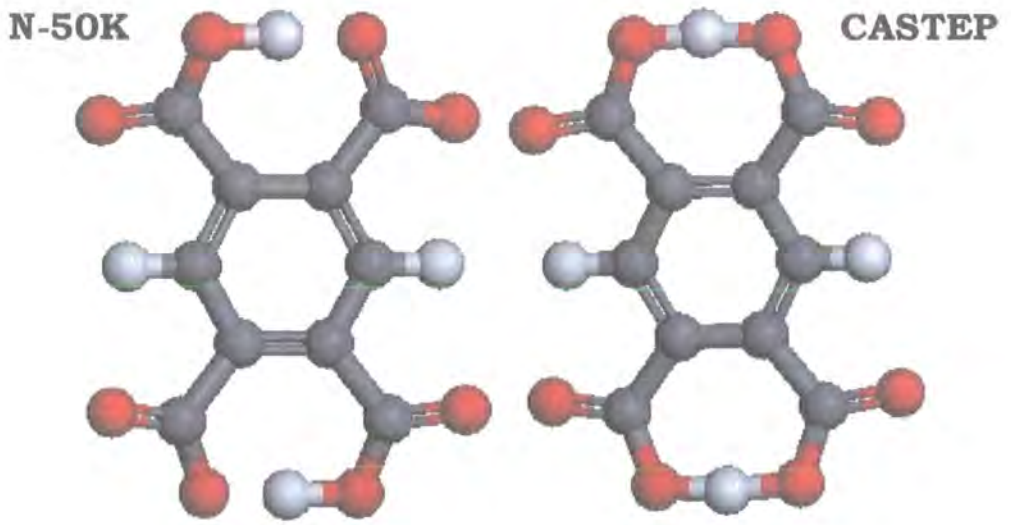

Figure 5.4-1 Diagram of the molecular structure of both the geometry optimised and the structure refined against the 50K neutron diffraction data (right and left, respectively). In the former case, the hydrogen atom is approximately centred between the two oxygen atoms while the neutron data places it closer to O211. The O...O separation is significantly shorter in the calculated structure.

The differences between the neutron diffraction structure and the calculated structure are fairly subtle, apart from the position of the proton which is

considerably more centred in the calculated (optimised) structure than in the diffraction study. While this is in part due to the oxygen - hydrogen bond being longer in the calculated structure, the oxygen – oxygen distance is also significantly shorter in this case: 2.355 Å rather than the 2.424 Å from the X-ray experiment. These features, with the C21-O211 and C31-O311 bond lengths for the 50 K neutron, 9 K X-ray and calculated structure, are in Table 5.4-1.

Structure	O...O/Å	O-H/Å	O...H/Å	C21-O/Å	C31-O/Å
CASTEP	2.355	1.167	1.194	1.287	1.285
50K Neutron	2.424	1.114	1.320	1.303	1.281
9K X-ray	2.424	1.069	1.365	1.292	1.282

Table 5.4-1 Geometry around the hydrogen bond in three refinements of the molecular structure. The calculated structure (CASTEP) produced a hydrogen bond that is 0.069Å shorter than those found from diffraction.

5.4.2 Energy Probe of the Hydrogen Bond: Diffraction Geometry

The shape of the potential well in which H211 sits is of interest as the extent to which this hydrogen bond can be considered a short strong hydrogen bonds will depend on the shallowness of this well. In this section the molecular geometry of the pyromellitate found from the 50 K neutron diffraction experiment has been used to probe this intramolecular hydrogen bond[v]. As noted, the method of probing was simply to move the proton around the hydrogen bond and calculate the energy at numerous points thus creating a potential energy map.

[v] This was a preliminary refinement of the data where the O...O and C21-O211 and C31-O311 distances were 2.420, 1.292 and 1.286 respectively. These values differ by less than 0.005 Å from the final neutron data (and fit the 9 K X-ray data even better) and so should be a perfectly reasonable representation of the diffraction structure.

15 points were taken along the O211-O311 vector in increments of 0.02 of the vector length, starting at 0.36 along the vector and ending at 0.64. The position of atom O311 has been used as the origin, that is:

Atom	x	y	z	Length
O211	4.4811	6.1257	8.0231	-
0311	2.1506	5.7903	7.4635	-
Difference	2.3305	0.3354	0.5596	2.4201

The direction of vector O311->0211 is:

$$\underline{\mathbf{O}} = 2.331x + 0.335y + 0.560z \quad \text{Equation 5.4-1}$$

and the points along this line considered are then:

$$\text{positions} = (0.36+q)\underline{\mathbf{O}} + (2.1506x, 5.7903y, 7.4635z)$$

where q takes values 0, 0.02, 0.04...0.28. This results in energy points being calculated every 0.0484 Å starting at 0.8712 Å from O311 and ending at 0.8712 Å from O211. The results of this procedure can be found in Table 5.4-2 and are plotted in Figure 5.4-2.

Dist form O211	Energy /eV	Dist from O311	Energy /eV
1.5488	-5125.44564	1.1616	-5126.15089
1.5004	-5125.80345	1.1132	-5126.15577
1.452	-5126.00107	1.0648	-5126.15062
1.4036	-5126.09795	1.0164	-5126.11614
1.3552	-5126.13625	0.968	-5126.02215
1.3068	-5126.14562	0.9196	-5125.82602
1.2584	-5126.14600	0.8712	-5125.46857
1.21	-5126.14637		

Table 5.4-2 Energy values as the proton is moved along the O211-O311 line in steps of 0.0484 Å.

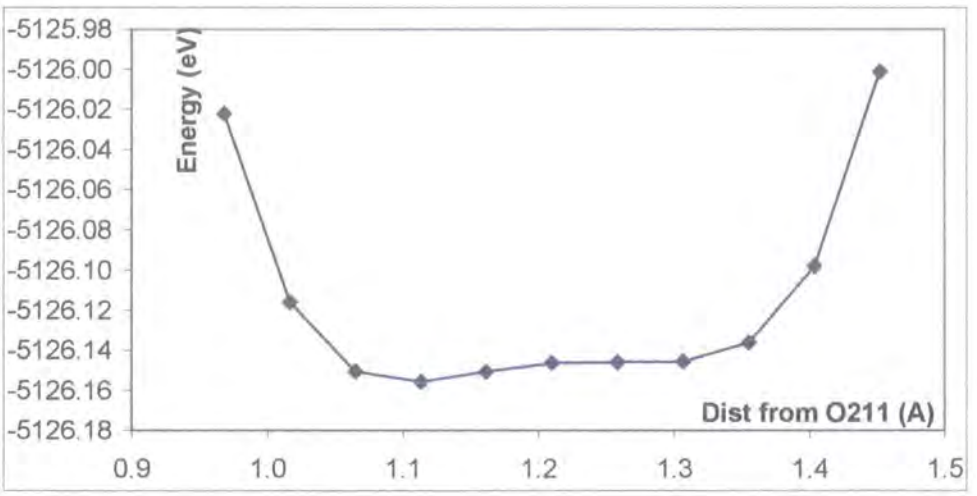

Figure 5.4-2 Plot of the energy profile of the energy potential well along the O211-O311 vector. While there is a minima around 1.1 Å from atom O211, the well is shallow with 6 energy calculations – spanning 0.242 Å – producing results within 0.01 eV of the energy minimum.

According to this calculation, the energy minimum is at 1.1132 Å from O211 and 1.3068 Å from O311. The energy potential is very shallow, however, with 6 entries having energies of less than 0.012 eV above the minimum. If one considers these data from a statistical thermodynamics point of view (see chapter 2.6.3.1) then it is expected that all 6 of these energy states will be significantly populated even at 50 K (Figure 5.4-3), resulting in significant

positional disorder over 0.242 Å. At room temperature there is little to choose between the expected occupation of these 6 sites, and so one would expect a diffuse proton occupation across this hydrogen bond.

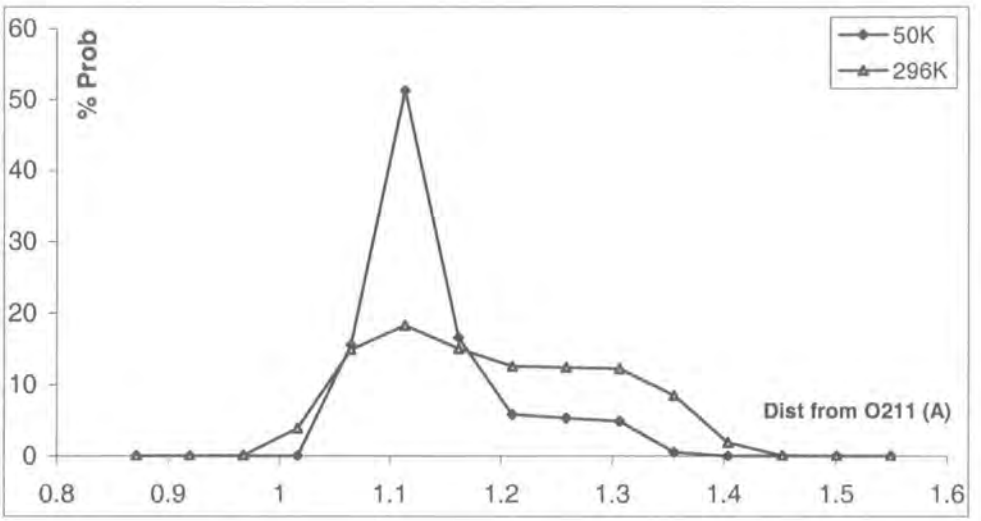

Figure 5.4-3 Resulting expected populations of the various energy levels shown in Figure 5.4-2. With such a shallow potential well, even at the lowest temperatures, there is the expectation of significant population of higher energy levels. Under ambient conditions this is accentuated to the point that there is little difference between the energy minimum and any one of 6 other energy levels.

The diffraction experiments and the calculated structure, show the proton position lying slightly off the O311->O211 line. To find the minimum energy position of this system, that is, the expected proton position given diffraction based co-ordinates for the rest of the molecule, the proton was moved in the plane of the O211-O311-C21-C31 atoms and perpendicular to vector **O**. The plane generated by those four atoms was found using XP to be:

$-0.242x + 0.140y + 0.960z = -3.191$ Equation 5.4-2

expressed in orthogonal co-ordinates, having a mean deviation 0.009Å (the atoms are not exactly co-planar). The cross product of this vector with **O**, above, gives a line in the plane and perpendicular to **O**. This yields:

$$-0.244x + 2.373y - 0.407z = \mathbf{P}$$

As the vector in equation 5.4-3 has unitary length, the resultant vector has length 2.420, thus we may once again use (0.02q).**P** as a multiplier to generate a spacing of 0.0484 Å between the data points in this direction. For the energy map, q has taken values of between -0.04 and 0.12, where the positive direction of the generated vector points away from atoms C21 and C31. An energy profile of dimensions 0.387 by 0.678 Å consisting of 9 x 15 data points has been constructed. The graphical representation of these data is found in Figure 5.4-4

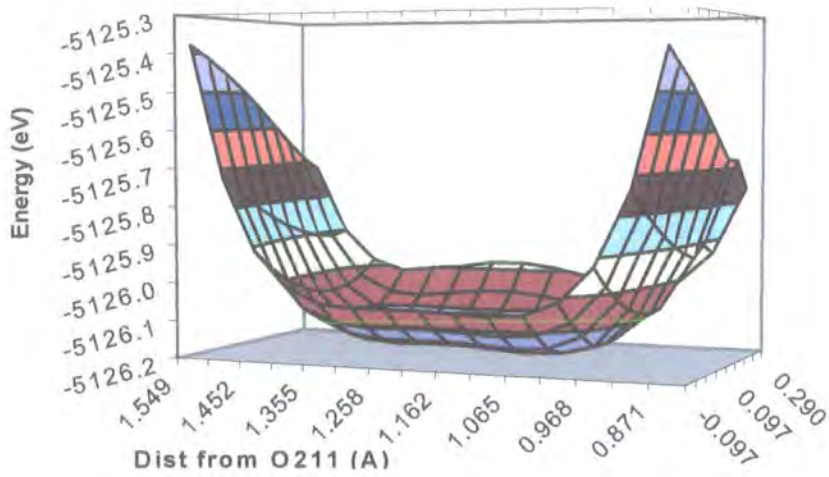

Figure 5.4-4 Energy potential well in the plane of atoms O211-O311-C21-C31 and in the direction of the O211-O311 vector. Values on the third (unlabelled) axis are quoted in (Å) and refer to distance along vector **P**, negative values being towards the molecule. The shape of the plot in the O211-O311 direction is similar to that found in Figure 5.4-2.

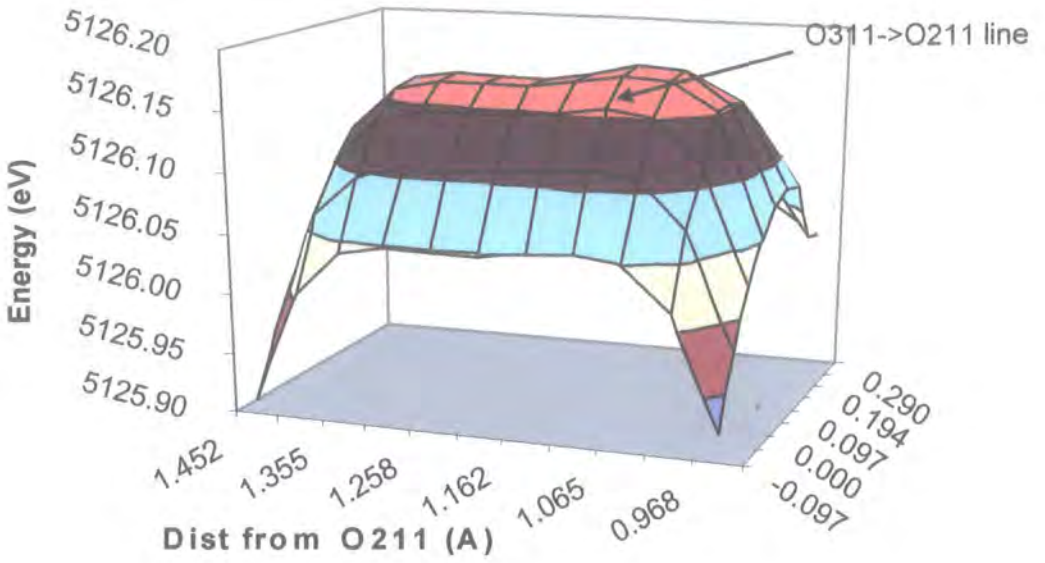

Figure 5.4-5 For clarity the results plotted in Figure 5.4-4 have been turned upside down, and the highest energy values omitted. It is clear that the energy map is far shallower in the direction of the O211-O311 vector than perpendicular to it.

This calculation places the energy minimum (expected proton position) at 1.113 Å along vector **O** starting from O211 and 0.0968 Å along **P** away from the rest of the molecule, with a O-H bond length of 1.117 Å. The neutron diffraction data placed the proton 0.1065 Å from **O** with a O-H bond length of 1.114 Å, which is in good agreement. From the calculated energy potential, the expected occupation of the various energy levels have been found for temperatures 50 and 296 K, Figure 5.4-6. What is interesting here, is that while at 50 K we would expect the proton to be well defined in its ground state geometry, at 296 K the results suggest massive smearing out of the proton position in the hydrogen bond direction Figure 5.4-6, though not in the direction perpendicular to it. It would appear that the probability of finding the proton 1.307 Å from O211 (and hence 1.113 Å from O311) is more than half of the probability of finding the proton at the energy minimum. Were this actually the case, we would expect to see a corresponding 2:1 ratio in the Fourier maps of the diffraction experiment. In addition, one would expect to see a shift in the

apparent position of the proton towards the centre of the hydrogen bond, as the diffraction experiment 'sees' the time averaged position. This is not the case, however, as there is only a slight indication of additional displacement in the said Fourier maps. Certainly there is no evidence of 'proton migration' with temperature in the neutron diffraction experiment.

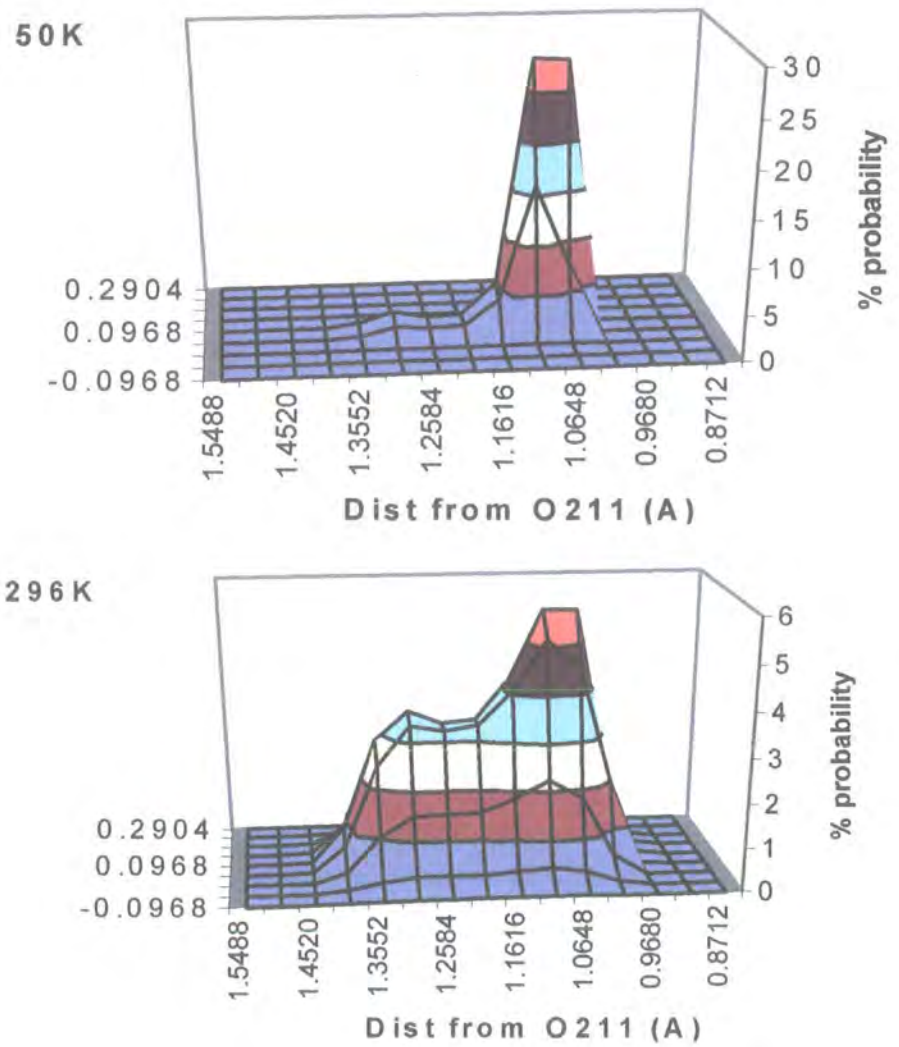

Figure 5.4-6 Expected populations of the various energy levels shown in Figure 5.4-4 at 50 K (top), and 296 K (bottom). Again, values on the third (unlabeled) axis are quoted in (Å) and refer to distance perpendicular along vector **P**, negative values being towards the molecule. The results predict that, at 296 K, the positional preference for the energy minimum position should be minimal.

5.4.3 Energy Probe of the Hydrogen Bond: Geometry Optimisation

The procedure outlined in Section 5.4.2 was repeated for the geometry optimised isolated pyromellitate molecule. The same CASTEP parameters (basis sets & tolerances) were used here as in section 5.4.1 and section 5.4.2. The major difference between the molecular structure here, and that found from the diffraction experiments, is that the O211 - O311 distance is 2.355 Å, substantially shorter than the 2.42 Å value used in the previous section. A priori, this would suggest that this was an even stronger hydrogen bond: this is a very short distance even in the context of short strong hydrogen bonds.

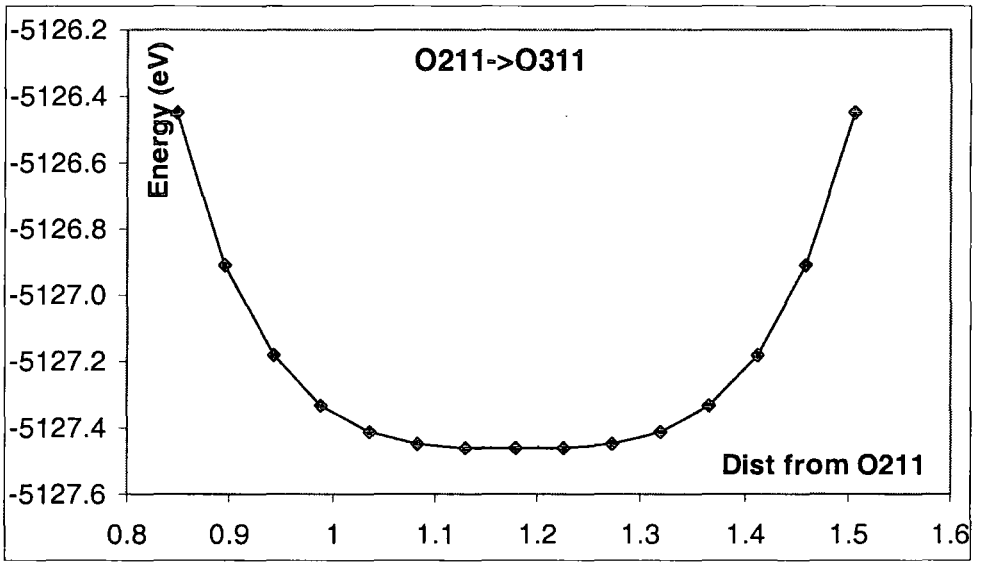

Figure 5.4-7 Energy profile of the hydrogen bond potential well along the O211-O311 line. This approximately symmetrical well is less shallow than that calculated when using the molecular geometry derived from the diffraction data (see Figure 5.4-2).

Again, points were taken every 0.02 along the O211->O311 vector from 0.36 to 0.64, though due to the O...O position being slightly shorter, this translates to calculation point separation of 0.0471 Å. As in section 5.4.2, an energy grid was found by generating a vector with direction in the plane of the O211-O311-C21-C31 and perpendicular to the direction of the O211->O311 vector. For

consistency, the spacing in these plots is also 0.0471 Å. A grid of 7 x 15 energy points was so generated covering an area of 0.330 x 0.707 Å^2.

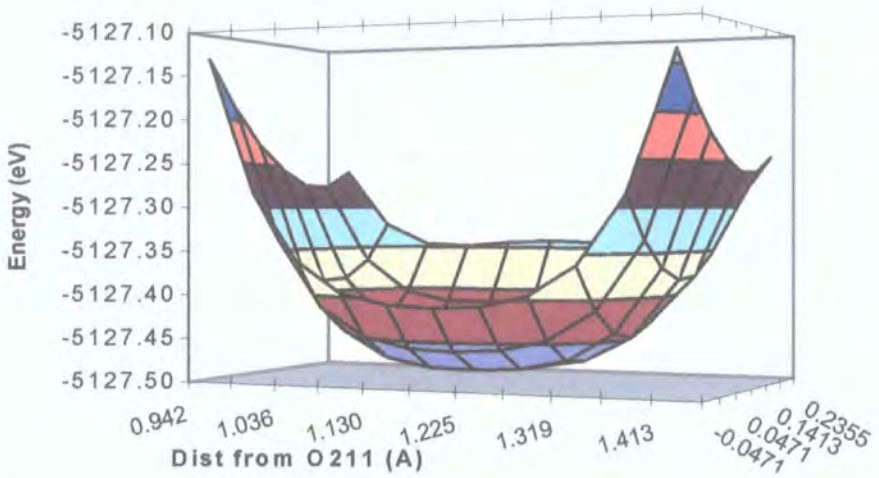

Figure 5.4-8 Energy potential well in the plane of atoms O211-O311-C21-C31 and in the direction of the O211-O311 vector. Values on the third (unlabelled) axis are quoted in (Å) and refer to distance perpendicular to the O211-O311 vector, negative values being towards the molecule. Again, the potential is far shallower in the O211-O311 direction than perpendicular to it.

From Figure 5.4-7 one can see that the well is approximately symmetrical and shallow. The energy minimum places the proton at an equidistant point between the two oxygen atoms and there are 5 energy points within 0.016 eV of the energy minimum (from 1.083 to 1.272 Å along the O211->O311 line). Interestingly this is less shallow than the case in section 5.4.2 where 6 points were within 0.012 eV of the minimum. Figure 5.4-8 shows the corresponding energy grid and it places the proton between 0.0471 and 0.0942 Å from the O211->O311 line (the difference in energy of these two points is less than 0.0001 eV). The effect on the expected occupation of the various energy points at 50 and 296 K can be seen in Figure 5.4-9. In the O211-O311 direction, a significant number of energy levels are highly populated at 296 K – this is to a far greater extent than perpendicular to the hydrogen bond direction, where only the two lowest energy points produce significant expected populations.

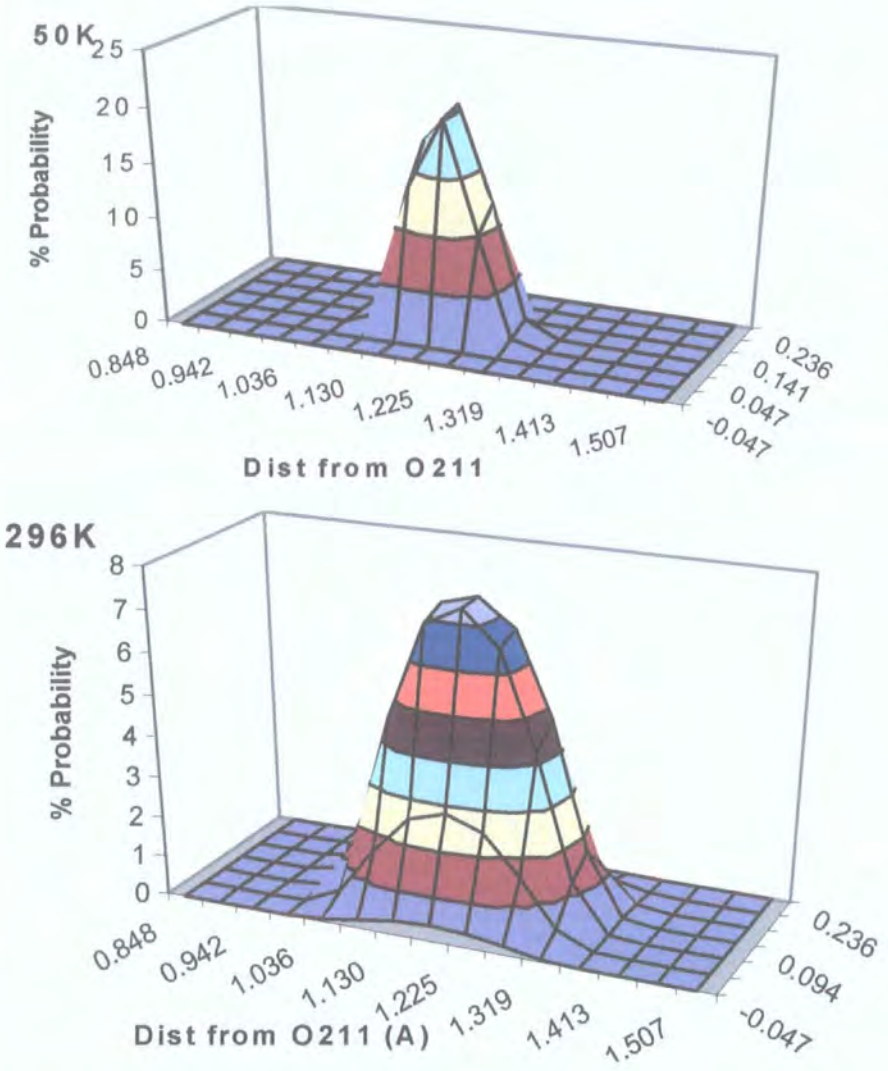

Figure 5.4-9 Expected populations of the various energy levels shown in Figure 5.4-8 at 50 K (top), and 296 K (bottom). Again, values on the third (unlabeled) axis are quoted in (Å) and refer to distance perpendicular to the O211-O311 vector, negative values being towards the molecule. The shape of the two plots is similar in that they are both wide in the O211-O311 direction and narrow in the perpendicular direction.

5.4.4 Crystal Structure Calculations

A geometry optimisation of the crystal structure was carried out in CASTEP to obtain a calculated (optimised) crystal structure. The calculation quality was lower in this case as the input unit cell volume was 1496 $Å^{-3}$ (the starting geometry has been taken from the 150 K X-ray data), with 608 electrons – a large calculation that required 127 hours to complete using the following input parameters:

Files: 5-4-2; Space Group: P1

Exchange Functional: PW91; Plane wave cut off: 280 eV;

Energy Tolerance: $5x10^{-6}$ eV; K-point sampling: Gamma

Geometry Optimisation Method: BFGS

Energy Tolerance: 0.00005 eV/atom; Force Tolerance: 0.060 eV/Å;

Stress Tolerance: 0.150 GPa; Dispersion Tolerance: 0.0020 Å;

Calculation Summary (output):

Unit Cell: a = 20.597 Å, b = 9.351 Å, c = 6.680 Å, α = 90.00°, β = 103.76°, γ = 90.00°, Volume = 1249.46 Å³ Energy = -38711.46569 eV, Enthalpy = -3.8711x10⁴ eV

Due to computational expense the basis set chosen was not as good as might has been used when studying the isolated molecule. The values chosen are expected to be reliable to a hundredth of an electron volt. The unit cell, as calculated here, is a great deal smaller than the unit cells found from the diffraction data – the volume in this case is just 84.3% of that of the 9 K X-ray data. While this smaller cell size has a large impact on the intermolecular contact distances, the calculation does reproduce bond lengths and angles well. For comparison, a selection of structural features from the CASTEP optimised structure and the 50 K neutron diffraction and 9 K X-ray crystal structures is presented in Table 5.4-3.

Feature	CASTEP	50K Neutron	9K XRD
O...O	2.396	2.424	2.424
O - H	1.0852	1.114	1.069
O...H	1.328	1.320	1.365
O211-C21	1.284	1.303	1.292
O211-C21-O212	120.01	120.45	121.189
O311-C31	1.2742	1.2815	1.1823
O311-C31-O312	122.61	122.40	122.88^{O}
O212...O4	2.509	2.676	2.679

Table 5.4-3 Geometry around the hydrogen bond [O-H...O] in three refinements of the bulk crystal structures; units are Å for lengths and degrees for angles. While the calculation reproduces the molecular bonds and angles reasonably well, the intermolecular distances – represented here by O212...O4 – are significantly shorter than the values derived from the diffraction data.

Note that CASTEP inputs yield a sequential numbering scheme, and the optimisation was carried out in P1 symmetry rather than C2/c, so there are eight intramolecular O...O contacts that could be used. The values quoted here are for the atoms O33, O35, C28, C29 and H48 in the CASTEP calculation, replacing O211, O311, C21, C31 and H311 respectively. These values are representative of the structure as a whole.

The energy of the hydrogen bond has been probed again by moving the proton along the straight line from O211 to O311, with the energy calculated at a series of points along the vector, in order to create an energy profile of the hydrogen bond. On this occasion, there have not been any calculations carried out in the plane of the O211-O311-C21-C31 atoms and perpendicular to the O211-O311 line on the grounds on computational expense. As a result, the minimum found in these calculations is not the expected minimum for the hydrogen bond, as

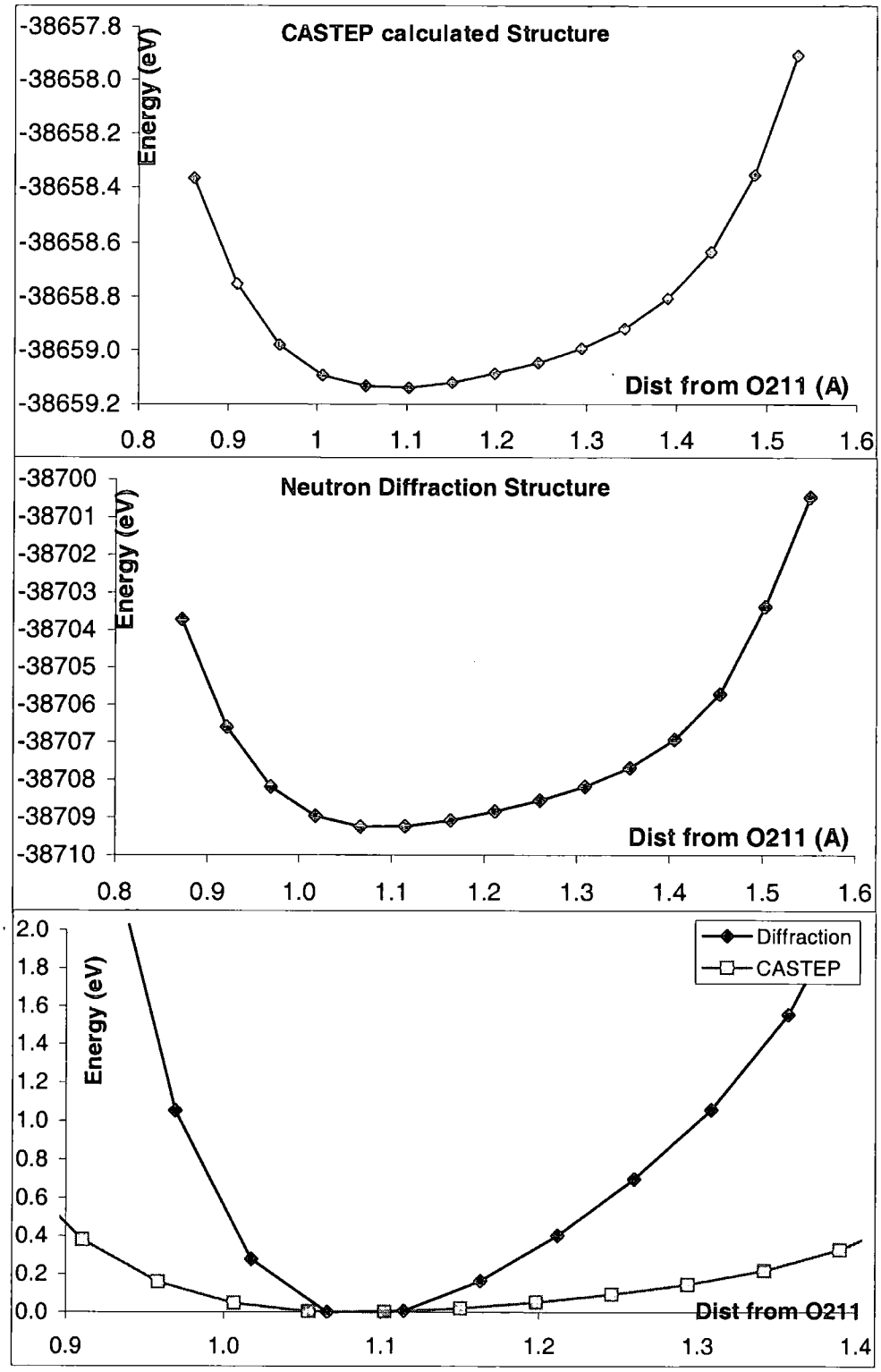

Figure 5.4-10 Plot of the energy profile of the energy potential well along the O211-O311 line when using the crystal structure found from the CASTEP geometry optimisation (top) and that found from the 50K neutron diffraction data (middle). Taking the minimum of each as zero energy, the two sets of data have been superimposed (bottom). While the shape of the two plots is similar – with a minimum around 1.1Å from O211 – the calculated structure has a far shallower potential well.

both the geometry optimisation and the neutron diffraction experiments placed the proton a little off the O211-O311 line. The profile should give a good indication of the general shape on the potential well in which the proton sits, for comparison with those found for the isolated fragments, sections 5.4.2 and 5.4.3.

For both the diffraction based crystal structure and the structure found by geometry optimisation within CASTEP, the energy minimum is in the region of 1.05 and 1.12 Å from atom O211. When using the crystal structure geometry found from diffraction data the lowest energy states are at 1.067 and 1.115 Å from O211 and have approximately the same energy, the latter of these positions being 0.0053 eV higher in energy than the minimum. For the crystal structure generated from the geometry optimisation, the lowest energy states are at 1.102 and 1.054 Å from O211 (in that order) and again the energy difference is minimal: 0.0038 eV. The calculation, therefore, places the proton closer to atom O211 when using the diffraction data than when using the calculated structure; the difference between the two in this respect is, however, not great. Given that the 50 K neutron diffraction structure placed the proton at 1.114 Å from O211 (though not directly on the O211=>O311 vector) this feature of the calculation is not unexpected.

The potential well in which the proton sits is clearly more shallow when using the calculated crystal structure rather than the diffraction data. Again, as the O...O separation is smaller in the former case this follows. It should be stressed, however, that the potential energy well for the diffraction data is in no way shallow. Apart from the lowest two energy levels, one would not expect any significant population of any of the other energy levels. From the statistical thermodynamics point of view, 99.9% of the time the proton is expected to be in

one of these two energy states when the system is at 296 K (Figure 5.4-11, top). This is certainly consistent with the variable temperature neutron diffraction data, where the position of the atom and the size of its ADP showed no unexpected behaviour across the temperature range. The energy profile of the calculated structure is shallower and leads to some of the higher energy levels being populated at higher temperatures (Figure 5.4-11, bottom).

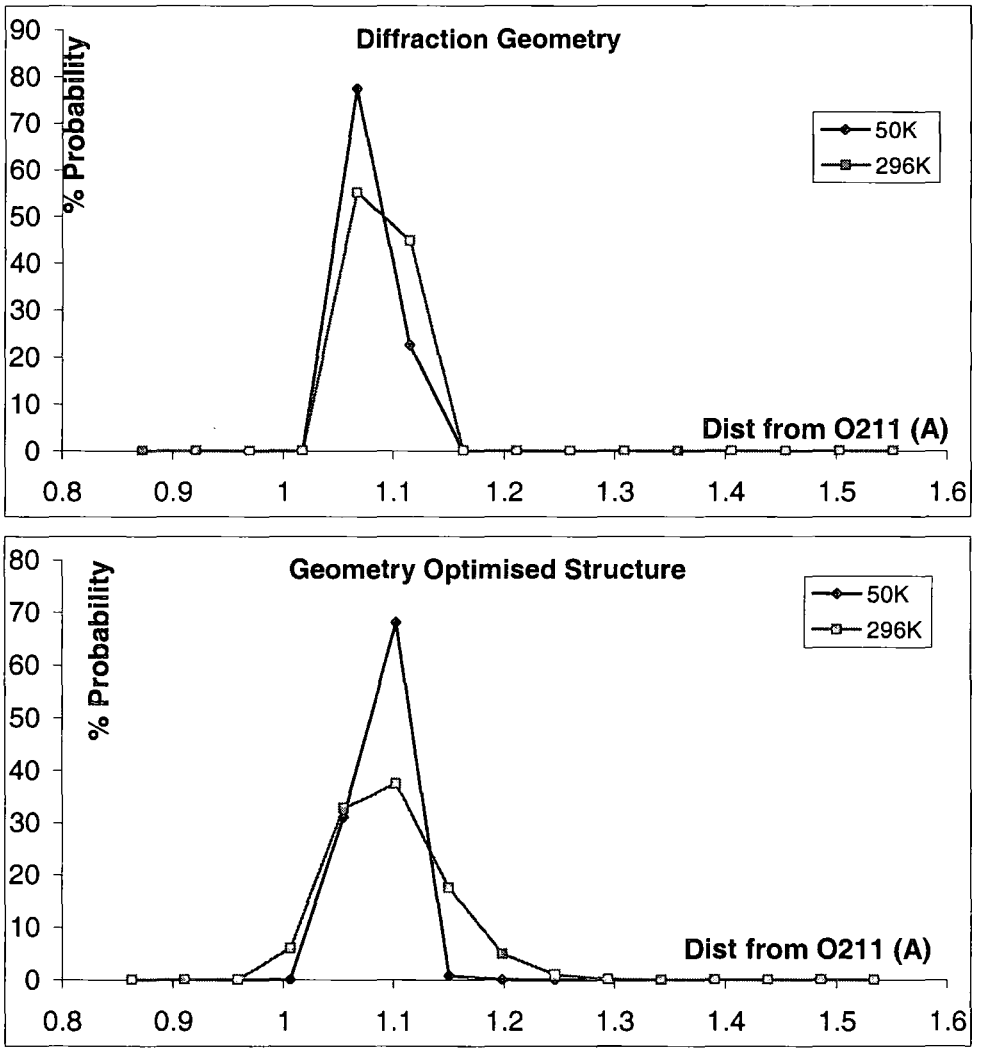

Figure 5.4-11 Expected populations of the various energy levels at 50 and 296 K for the diffraction based geometry (top) and the geometry optimised structure (bottom). Even at room temperature, the proton is expected to be localised to the lowest two energy states in the diffraction-based calculations.

5.5 *Summary and Comments*

The story of this study is as follows: a variable temperature X-ray diffraction study was carried out, initially to test new experimental equipment. Subsequent inspection of the structure revealed a short hydrogen bond, whose proton was difficult to position accurately, so a variable temperature neutron diffraction experiment was carried out. This showed that the position of the proton was constant throughout the experimental range, and that the variance of the atomic position about its mean varied as a function of temperature in only a comparable way with the other atoms in the system. Subsequent PW-DFT calculations showed that while one would expect a SSHB to exist were the pyromellitate part of the system isolated, in the bulk structure, the hydrogen bond energy potential well was not shallow, nor does it have a double minimum. The implication of this is that the hydrogen bonding is disrupted by the crystal structure environment. That is to say that the matching of the energies of the HOMO and LUMO of the proton donor and acceptor has been disrupted when including the crystal structure. The isolated pyromellitate fragment is symmetrical and thus the orbital matching is automatic – a symmetrical potential well is the outcome. Clearly this is disrupted when the crystal structure as a whole is considered.

6 Miscellaneous Studies

This chapter contains individual structure analysis, including studies on weak hydrogen bonding and crystal structure anticipation, short variable temperature studies into thermal expansion.

6.1 *Supramolecular Chemistry of Selected Homologated Aminophenols*

As part of a longstanding collaboration between the Durham XRD laboratory and the chemists in Hyderabad, India, led by Prof. G.R. Desiraju, a series of molecular systems were studied via single crystal X-ray diffraction with a view to furthering our understanding in the field of crystal structure anticipation ("Crystal Engineering"). This particular study was based around molecules similar to 4-(4-aminophenenyl)phenol. Systematic alterations in the spacer group between the two phenyl rings were correlated and rationalised with their observed resulting crystal packing (see Figure 6.1-1). The study as a whole is published in ["publication 1"]:

Vangala VR, Bhogala BR, Dey A, Desiraju GR, Broder CK, Smith PS, Mondal R, Howard JAK, Wilson CC; *J. AM. CHEM. SOC.* (2003) **125**, 14495-14509

Interesting aspects of the structures solved by this author, and the context of the work with respect to crystal engineering follow.

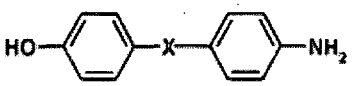

X =						
CH_2	1	S	1a	CH=CH	2d
$(CH_2)_2$	2	S-CH_2	2a	O	1b
$(CH_2)_3$	3	CH_2-S	2b		
$(CH_2)_4$	4	S-S	2c		
$(CH_2)_5$	5	S-$(CH_2)_2$	3a		

Figure 6.1-1 Diagram of the series of molecules studied taken from publication 1. The diagram is taken from there.

The compound 4-(4-aminophenenyl)phenol (4APP) forms a β-As type structure – a sheet structure in which the N(H)O hydrogen bonds are arranged in a hexagonal manner similar to the chair form of cyclohexane. But how does changing the spacer effect the resulting structure? CH_2 groups were added such that n=0, 1...5; 4APP effectively has spacer n=0, see Figure 6.1-2. Our results show that when n is even, the β-As structure is reproduced, while when n is odd there is a varying series: when n=1 a square, non-saturated hydrogen bonding motif is observed, while n=3 results in an infinite chain motif with C-H...π bridges.

CH_2 spacer units can be substituted by sulphur with the expectation that not a great deal will change in the crystal structure: sulfur is a similar size to CH_2[1]. This substitution was carried out for a number of the compounds and on the whole the substitution did result in isostructural crystal packing. However, for the n=1 compound there was found to be significant differences between the CH_2 and S spacer structures. While both this 'sulfur' structure and that of its 'CH_2' counterpart are built up of square motifs of N(H)O hydrogen bonds, the

---

[1] (a) Kitaigorodskii, A. I. *Molecular Crystals and Molecules*; Academic: New York, 1973.

(b) Kitaigorodskii, A. I. *Mixed Crystals*; Springer: New York, 1984.

difference in the sulfur case is that the four linked molecules spiral out from the square motif (see Figure 6.1-2). The two independent molecules in the unit cell form sheets that that stack alternately, with the X-H...Y bonds pointing clockwise and anti-clockwise in each sheet. Figure 6.1-2 shows the clockwise configuration that has been labelled 'type B' in publication 1. The reason for these spirals appears to be the exchange of an N-H...π interaction for a N-H...S interaction.

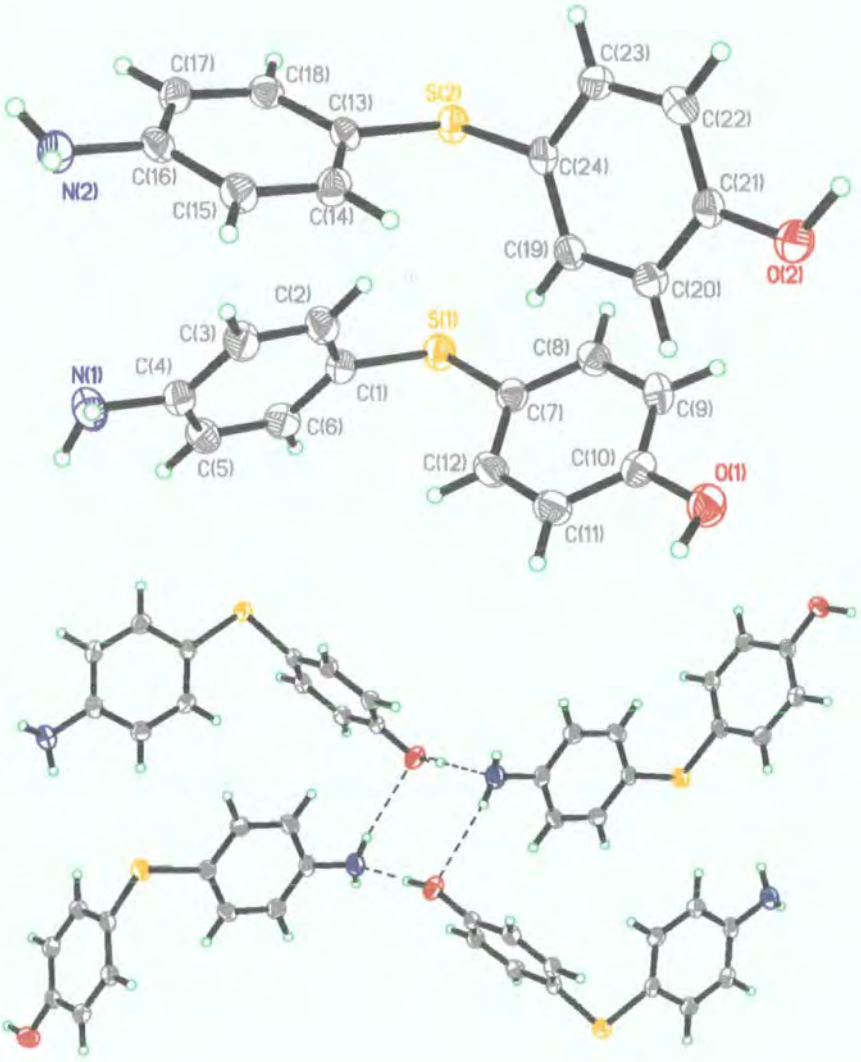

***6-1-1: $C_{12}H_{11}NOS$ at 120K**: Monoclinic, $P2_1/n$ and $Z = 8$, $R_1 = 4.37\%$, $R_2 = 12.71\%$, $R_{int} = 0.0435$, $a = 9.8597(3)$ Å, $b = 10.0879(3)$ Å, $c = 21.8081(7)$ Å, $\beta = 102.809°(2)$, $V = 2115.13(11)$ Å^3;*

Figure 6.1-2 Labelled diagram of the two unique molecules in the asymmetric unit (top) and a diagram of the crystal packing (bottom). A sheet consisting of molecule 'type B', S2 O2 N2 C13-24, is shown. A type molecules form similar sheets pointing in the opposite direction.

Substituting oxygen for a CH_2 group (or sulphur atom) is not necessarily expected to produce a similar crystal structure, as oxygen is far smaller than either sulfur or a CH_3 group. The resulting crystal structure motif was more than a little surprising, however: a β-As sheet structure rather than that of a square motif or infinite chain. A close study of the system, rationalised the result as follows:

(i) The molecule is bent out of shape to produce a large angle between the C-O and C-N vectors.

(ii) The small size of the oxygen atom allows closer packing of the molecules.

(iii) The greater electronegativity of the O-atom promotes C-H...O hydrogen bonds that pull adjacent molecules closer together.

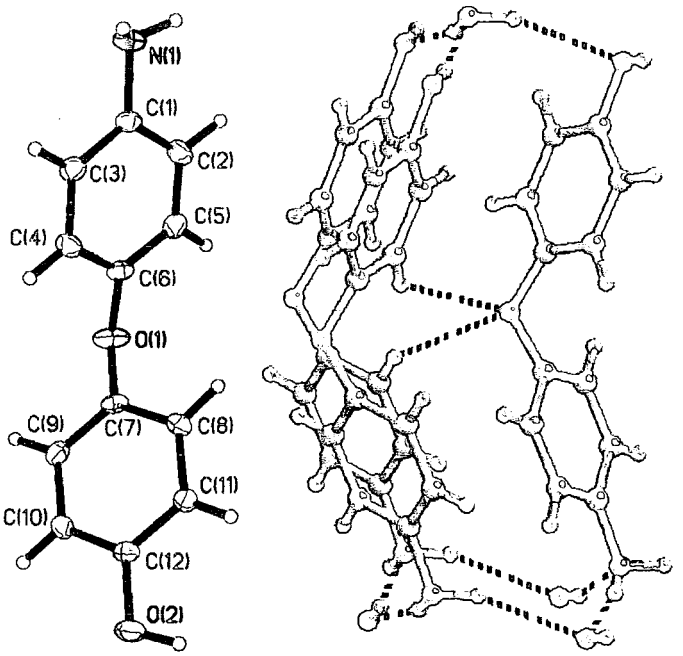

***6-1-2: $C_{12}H_{11}NO_2$ at 120K**: monoclinic, Cc and Z = 4, R_1 = 3.29%, R_2 = 8.63%, R_{int} = 0.0435, a = 22.491(1) Å, b = 5.4647(2) Å, c = 8.0466(4) Å, β = 95.674(2)°, V = 984.14(8) Å^3*

Figure 6.1-3 β-As sheet structure of 4-(4-aminophenoxy) phenol, right taken from publication 1, (ref P. 176) and the labelled molecular diagram, left.

In contrast to the surprising results of the previous structure, when CH=CH replaced CH_2CH_2, the resulting crystal structure was almost exactly equivalent. Once again we see the β-As sheet structure. As this is only a subtle chemical change, it was possible to predict the packing of this system *a priori*.

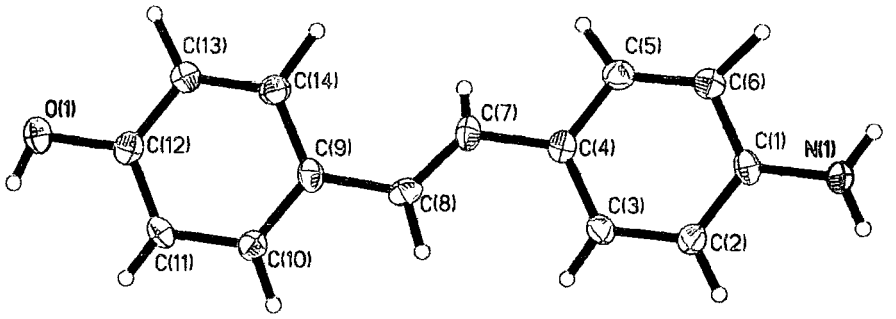

6-1-3: ***$C_{14}H_{13}NO$ at 120K****: Monoclinic, Pc and Z = 2, R_1 = 3.74%, R_2 = 10.12%, R_{int} = 0.0401, a = 12.951(8) Å, b = 5.226(3) Å, c = 8.046(3) Å, β = 98.12°(2), V = 539.2(5) Å^3*

One of the great challenges of crystal engineering results from the fact that apparently small changes in molecular structure can translate into huge (and apparently random) changes in the crystal structure. For the next subtle alteration in molecular structure, the above structure was modified such that the OH group is at the meta position of the phenyl ring. Its CH_2CH_2 analogue has also been studied and the two resulting structures form the basis of a paper that has been submitted to "Crystal Growth and Design" as a communication (April 2004).

As there is a 120° difference between the C-N and C-O vectors in each of these molecules, it might be expected that an infinite N(H)O chain would dominate the structures. This is not the case, and neither do their structures fit into any of the groups that defined the aminophenols' packing. Rather the molecules form centrosymmetric O-H...N dimers which are further connected through N-

H...O bridges. These sheets stack along the a-axis so that adjacent N(H)O infinite chains are cross-linked with N-H...O bridges, Figure 6.1-4. The two structures are essentially identical and can be considered as a narrow ribbon of the β-As sheet that has been rolled up to form a tube.

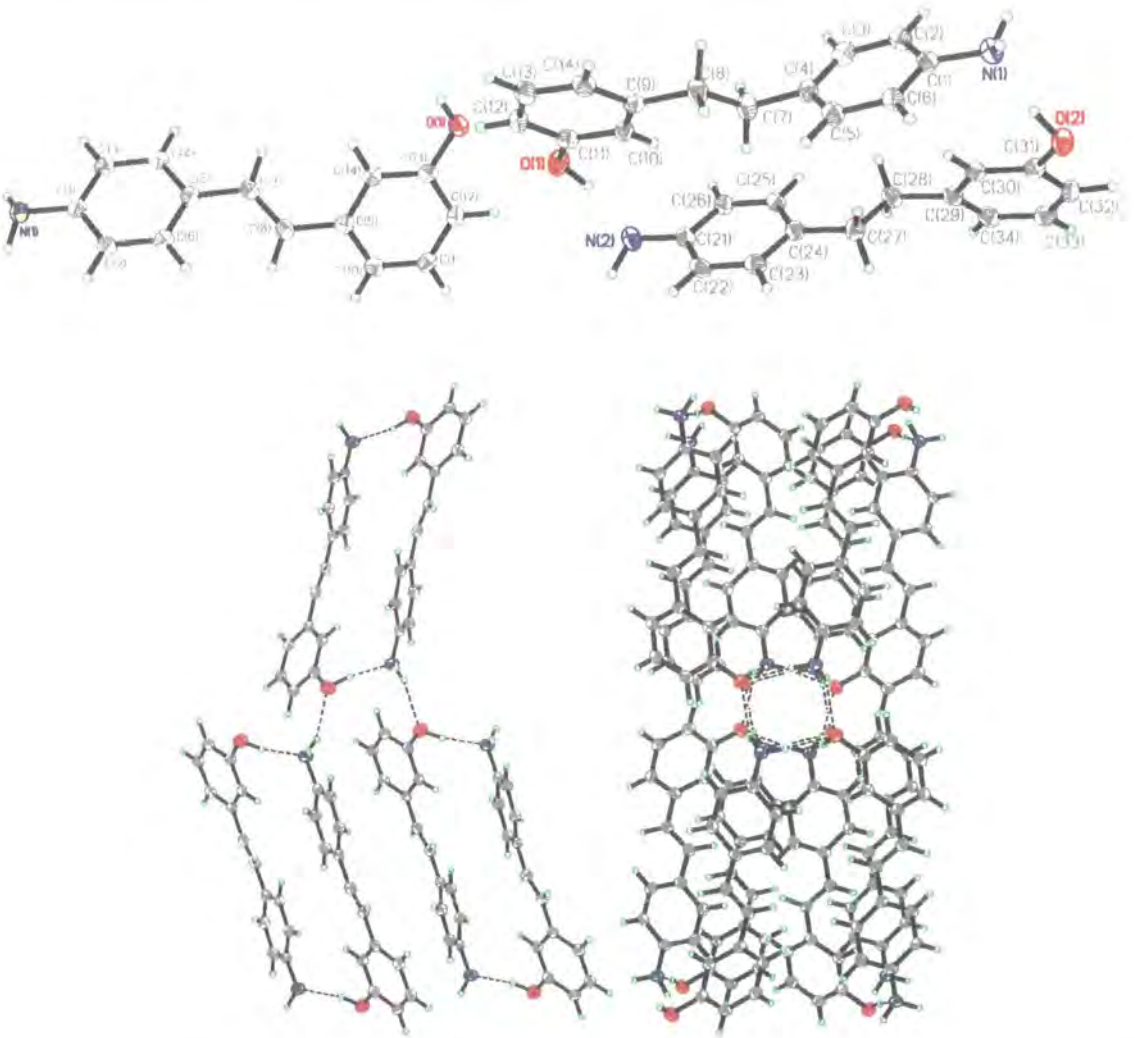

***6-1-4: $C_{14}H_{13}NO$ at 120K**: Orthorhombic, Pccn and Z = 8, R_1 = 4.16%, R_2 = 8.38%, R_{int} = 0.0703, a = 11.4815(5) Å, b = 29.053(2) Å, c = 7.1885(4) Å, V = 2150.3(2) Å^3*

***6-1-5: $C_{14}H_{15}NO$ at 120K**: Orthorhombic, $Pna2_1$ and Z = 8, R_1 = 3.71%, R_2 = 8.21%, Rint = 0.0885, a = 7.6679(2) Å, b = 26.1975(6) Å, c = 11.1698(2) Å, V = 2243.79(9) Å^3*

Figure 6.1-4 Molecular diagram of 3-[(E)-2-(4-aminophenyl)-1-etheny]phenol (top, left) and 3-(4-aminophenethyl)phenol (top left) along with the packing diagrams showing the O-H...N dimers with N-H...O bridges (bottom, left) and the packing viewed down the c-axis that shows the molecules radiate out from the β-As sheet 'tube'.

Related to these structures are 3-[3-(4-aminophenethyl) propyl]phenol and 3-[3-(4-aminophenethyl) cyclopropyl]phenol. These systems have the NH_2 group at the meta position of the phenyl ring and a spacer group of $(CH_2)_3$ and $CH(CH_2)CH$ respectively. In the former case the central feature of the packing is the β-As sheet (Figure 6.1-5). This is in direct contrast with 3-[3-(4-aminophenethyl) propyl]phenol where the crystal structure is defined as an infinite chain.

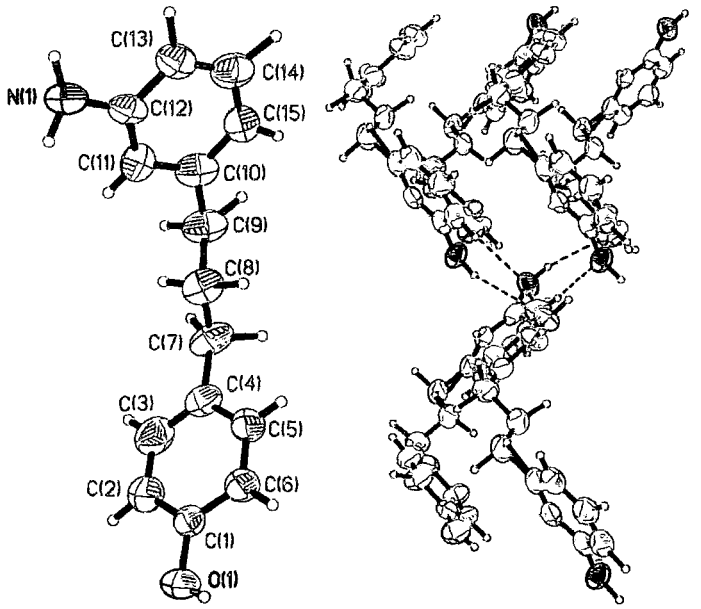

***6-1-6: $C_{15}H_{17}NO$ at 120K**: Monoclinic, P2(1) and Z = 4, R_1 = 6.43%, R_2 = 17.17%, R_{int} = 0.1108, a = 11.3868(6) Å, b = 4.8626(3) Å, c = 11.5550(6) Å, β = 103.040(2)°, V = 623.30(6) Å^3*

Figure 6.1-5 Molecular diagram and packing of 3-[3-(4-aminophenethyl) propyl]phenol.

The structure of 3-[3-(4-aminophenethyl) cyclopropyl] phenol is not comparable with the other aminols as there is solvent water included in the crystal. This has the result of creating a packing motif that involves this water, such that the H_2O acts as both a donor and acceptor. The water protons are involved in hydrogen bonds with the NH_2 groups while two O-H groups also hydrogen bond with the oxygen atom of the water molecule.

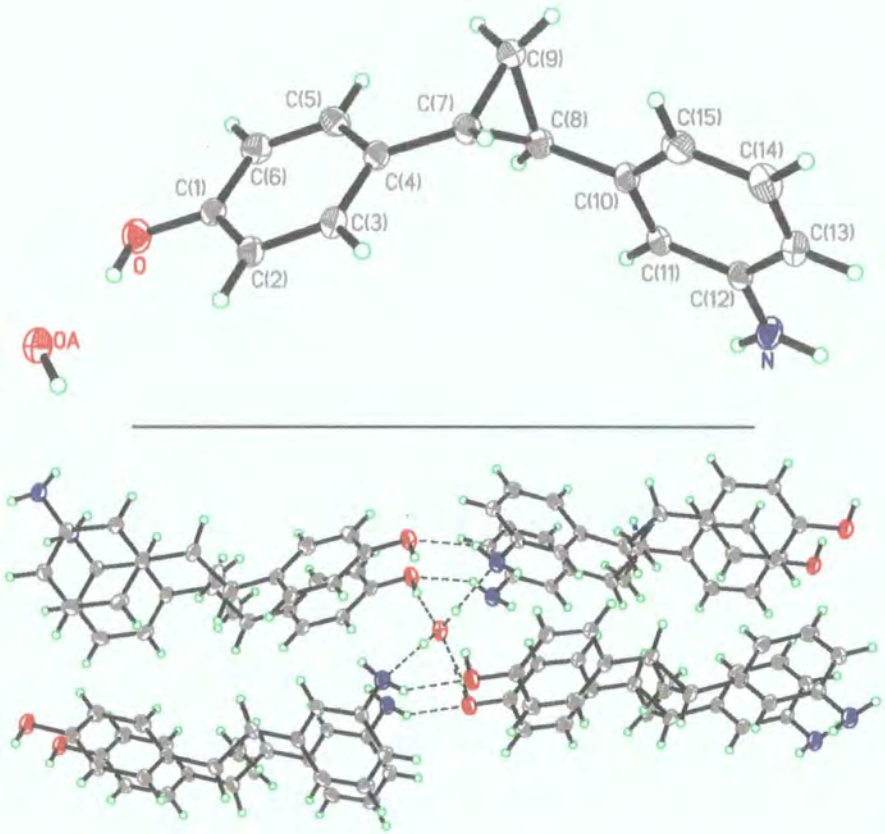

***6-1-7: $C_{15}H_{18}NO_{1.5}$ at 120K**: Orthorhombic, Pnn2 and Z = 4, R_1 = 3.92%, R_2 = 9.96%, R_{int} = 0.1086, a = 9.7427(13) Å, b = 25.403(3) Å, c = 4.9679(6) Å, V = 1229.5(3) Å^3*

Figure 6.1-6 Molecular structure and packing of 3-[3-(4-aminophenethyl) cyclopropyl]phenol.

6.2 Weak Interactions and Crystal Structure

Furthering our investigations into weak intermolecular interactions such as C-F...π and halogen – halogen interactions, a couple "of halogen substituted diphenyl pyridyl type" systems were studied using low temperature single crystal X-ray diffraction. The structures of (4-chlorophenyl)-(4-fluorophenyl)-(4-pyridyl) methanol and bis-(4-fluorophenyl)-(4-pyridyl) methanol were then compared with the structure of diphenyl-(4-pyridyl) found in the literature[ii]. In this way the effect of halogen substitution on crystal structure has been directly evaluated. The results of this study are published in [publication 2]:

Choudhury AR, Urs UK, Smith PS, Goddard R, Howard JAK, Row TNG;

J. Molecular Structure; **641**: 225-232 (2002)

[ii] C. Glidewell, G. Ferguson; *Acta. Crystallogr.* **C 50** (1994) 924

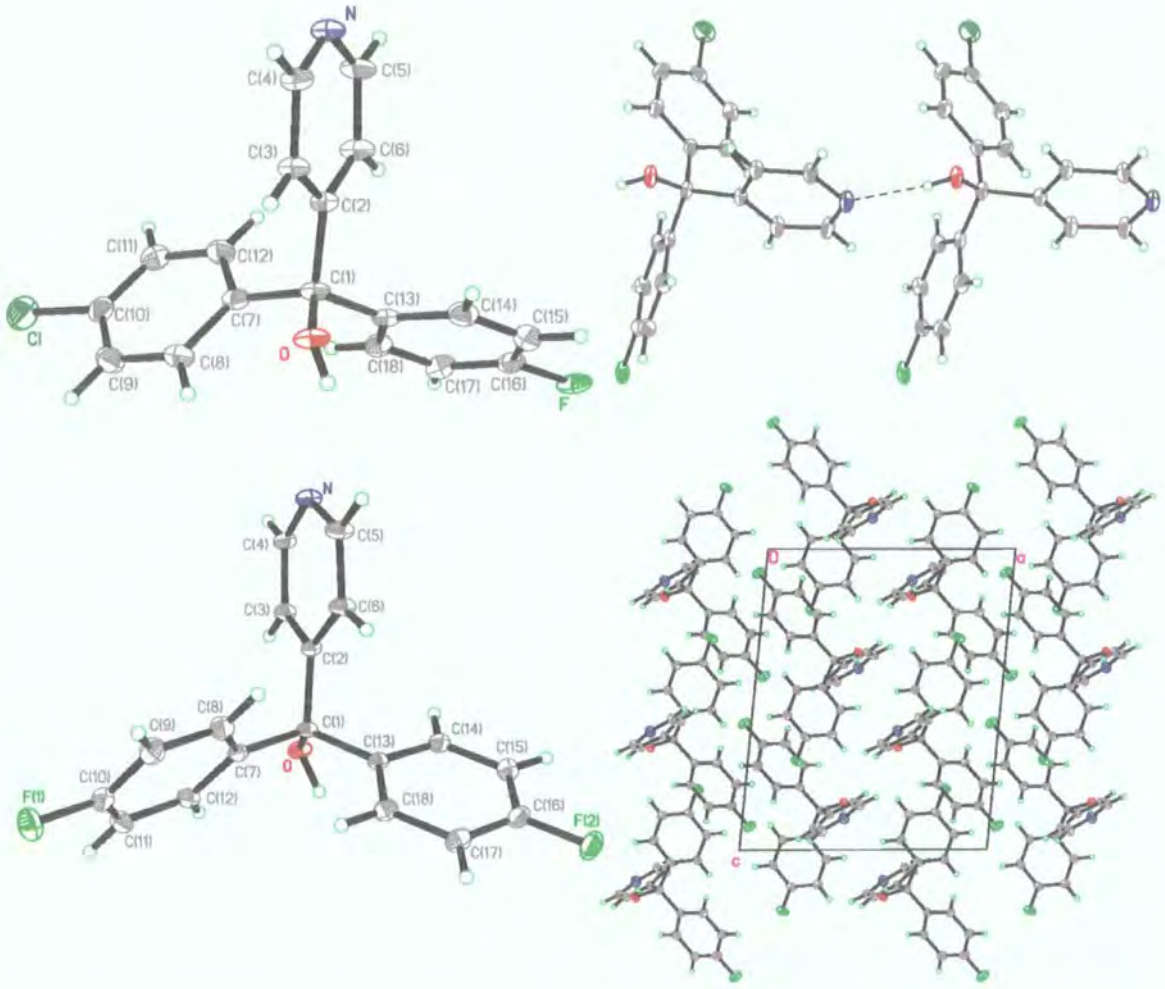

***6-2-1: $C_{18}H_{13}NOFCl$ at 100K**: Monoclinic, $P2_1/c$ and $Z = 4$, $R_1 = 6.10\%$, $R_2 = 15.70\%$, $R_{int} = 0.0999$, $a = 12.2718(2)$ Å, $b = 7.6822(1)$ Å, $c = 15.1089(3)$ Å, $\beta = 90.879(1)°$, $V = 1424.22(4)$ Å^3*

***6-2-2: $C_{18}H_{13}NOF_2$ at 100K**: Monoclinic, $P2_1/c$ and $Z = 4$, $R_1 = 4.89\%$, $R_2 = 12.69\%$, $R_{int} = 0.0568$, $a = 12.0639(3)$ Å, $b = 7.6328(2)$ Å, $c = 14.7945(3)$ Å, $\beta = 95.565(1)°$, $V = 1355.88(6)$ Å^3*

Figure 6.2-1 Molecular diagram of (4-chlorophenyl)-(4-fluorophenyl)-(4-pyridyl) methanol (top, left) bis-(4-fluorophenyl)-(4-pyridyl) (bottom, left) with a diagram of the O-H...N hydrogen bond (top, right) and the packing diagram viewed down the b axis (bottom, right).

The two systems are essentially isostructural, both containing O-H...N hydrogen bonds and apparent C-F...π interactions. The overall effect is the formation of anti-parallel chains along the b-axis (Figure 6.2-1). The two structures only differ in so far as the chlorine substituted system (6-2-1) has a significantly

short Cl...Cl contact of 3.4213(9) Å, while there is no correspondingly short contact in the purely fluorine substituted system.

When these structures are compared with the non-substituted diphenyl-(4-pyridyl) system, what is most striking is the fact that this system is also essentially isostructural with its halogen substituted counter parts. The unit cell of diphenyl-(4-pyridyl) is reported as a = 7.7221(8) Å, b = 14.9146(20) Å, c = 11.8191(14) Å, β = 95.351(9)°. The orientation, therefore, of the chain is now along the a-axis and the axis have been swapped round, such that this still represents an anti-parallel chain along the shortest axis. Other than this subtle difference, there is very little to distinguish these structures: in fact, the O-H...N hydrogen bond chain is almost identical in every way in each case. The obvious conclusion is that the O-H...N hydrogen bonding is controlling the structures in all three cases, over-riding any effect that the halogen atoms might have had. In view of this it is likely that the short Cl...Cl contact is co-incidental.

Also studied, though not included in this paper [publication 2] were 1-(3,5-trifluoromethyl)-4-methylthiosemicarbazide and di-((1H-1,2,4-triazol-1-yl)methyl)-(2,4-difluorophenyl)- methanol monohydrate, and their packing assessed. The compound 1-(3,5-trifluoromethyl)-4-methylthiosemicarbazide, shown in Figure 6.2-2, contains two CF_3, three NH groups and a sulphur. The packing is dominated by a pair of N-H...S hydrogen bonds of N...S separation 3.330(2) Å that result in the formation of molecular dimers, right in Figure 6.2-2. All other short contacts are between fluorine atoms and not thought to be bonding interactions.

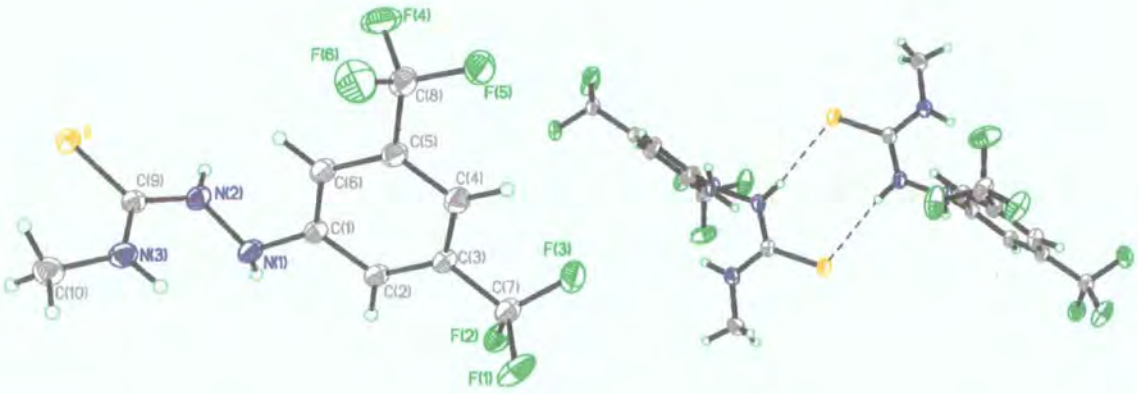

***6-2-3: $C_{10}H_9F_6N_3S$ at 100K**: Monoclinic, $C2_1/c$ and $Z = 8$, $R_1 = 4.62\%$, $R_2 = 10.64\%$, $R_{int} = 0.0718$, $a = 17.8915(8)$ Å, $b = 16.9624(10)$ Å, $c = 9.3787(5)$ Å, $\beta = 118.204(3)°$, $V = 2508.3(2)$ Å^3*

Figure 6.2-2 Molecular diagram of 1-(3,5-trifluoromethyl)-4-methylthiosemicarbazide, left, and the molecular dimers mediated by N-H...S hydrogen bonds.

Di-((1H-1,2,4-triazol-1-yl)methyl)-(2,4-difluorophenyl)- methanol monohydrate is in some respects similar to bis-(4-fluorophenyl)-(4-pyridyl) in that it contains an O-H group and possible hydrogen bond acceptors in the form of nitrogen. The differences are stark, however: two of the rings are now triazol-1-yl and, far more importantly from the point of view of crystal packing, there is water present in the structure. Both the water protons are involved in O-H...N hydrogen bonds, while the water also acts as a hydrogen bond acceptor from the O-H in the main part of the molecule. The O...H separations are 1.97(3) and 1.92(3) Å in the former case and 1.84(3) Å in the latter. There is also a C-H...F short contact: 2.54(3) Å, though whether this is a bonding interaction or simply co-incidental of the structure as a whole, is unclear.

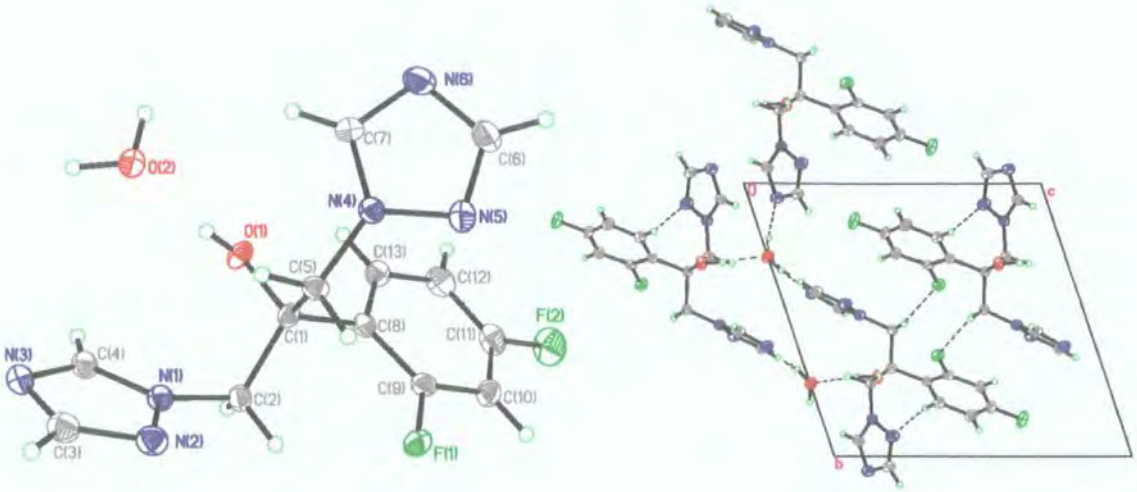

***6-2-4: $C_{13}H_{14}F_2N_6O_2$ at 100K**: Triclinic, P-1 and Z = 2, R_1 = 5.07%, R_2 = 10.80%, R_{int} = 0.0402, a = 5.5812(4) Å, b = 11.6831(8) Å, c = 12.1602(8) Å, α = 70.995(2)°, β = 78.888(3)°, γ = 84.431(2)°, V = 735.1(9) Å^3*

Figure 6.2-3 Molecular diagram of di-((1H-1,2,4-triazol-1-yl)methyl)-(2,4-difluorophenyl)-methanol monohydrate, left, with the packing viewed down the a-axis.

6.3 *Variable temperature studies of 4-amino-4'-hydroxydiphenyldisulfide (1) and 4-amino-4'hydroxybenzylsulphide (2)*

Following from the above study, two short variable temperature studies of 4-amino-4'-hydroxydiphenyldisulfide and 4-amino-4'hydroxybenzylsulphide were carried out. As these two systems are similar in terms of their molecular structure, although they differ in their packing and hydrogen bond networks, it was hoped that they would afford a good opportunity of studying the effect of crystal packing on the behaviour of unit cell parameters at variable temperatures.

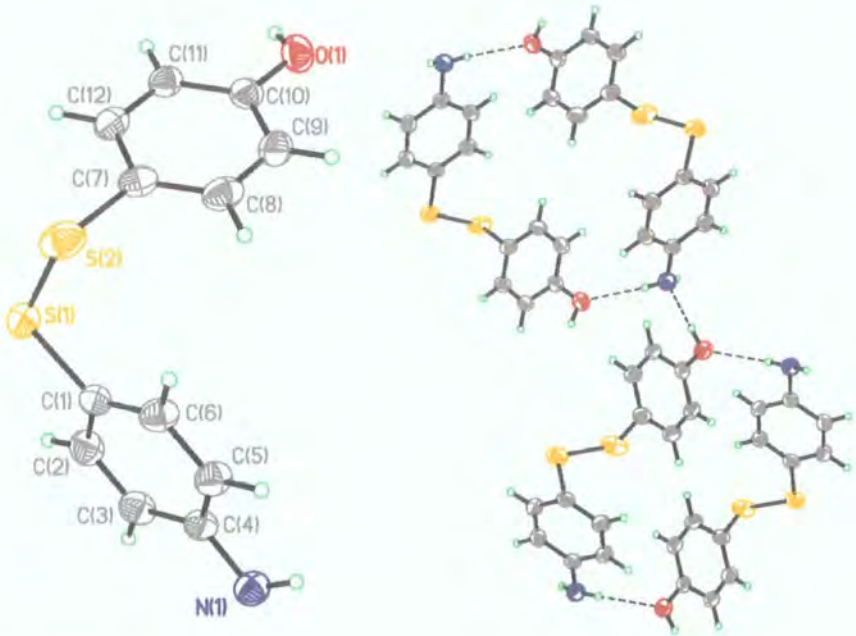

***6-3-1: $C_{12}H_{11}NOS_2$ at 200K**: Monoclinic, $P2_1/c$ and $Z = 4$, $R_1 = 3.66\%$, $R_2 = 9.54\%$, $R_{int} = 0.0556$, $a = 10.4454(8)$ Å, $b = 8.1147(6)$ Å, $c = 14.9206(11)$ Å, $\beta = 110.077(3)°$, $V = 1187.84(15)$ Å^3*

Figure 6.3-1 The molecular diagram of 4-amino-4'-hydroxydiphenyldisulfide, left, with the infinite N(H)O chain, shown on the right.

6.3.1 4-amino-4'-hydroxydiphenyldisulfide - Results

This molecule and its crystal packing are shown in Figure 6.3-1. It was studied over the 20-290K temperature range and at all temperatures was found to be monoclinic, space group $P2_1/c$. Full structural determinations were carried out at 20, 50, 200 and 290 K, and considered with the 100 K data collected previously by C.K. Broder. In addition, unit cell determinations were carried out at 135, 165, 230 and 260 K. All but the 20 and 50 K data sets were collected on a Bruker SMART CCD 1K area detector in conjunction with an Oxford Cryosystems cryostream. The 20 and 50 K data were collected on the F*ddd* four-circle diffractometer. The central feature of this structure is an infinite N(H)O chain, generating oxygen – nitrogen separation distances of 3.046(2) and 2.764(2) Å for N-H...O and O-H...N respectively.

Temp/K	A-axis/Å	B-axis/Å	C-axis/Å	Beta/°	Volume/Å^3	Structure
20	10.376(2)	8.084(2)	14.640(3)	109.56(3)	1157.1(4)	6-3-4
50	10.379(2)	8.085(2)	14.661(3)	109.61(3)	1158.9(4)	6-3-3
100	10.424(1)	8.106(1)	14.751(2)	109.79(1)	1172.8(3)	6-3-5
135	10.430(3)	8.120(3)	14.831(5)	109.82(4)	1181.7(7)	
165	10.439(3)	8.122(3)	14.882(5)	109.90(4)	1186.4(7)	
200	10.452(1)	8.126(1)	14.930(1)	110.00(1)	1191.7(1)	6-3-1
230	10.462(4)	8.133(3)	14.988(5)	110.10(4)	1197.6(7)	
260	10.469(4)	8.140(4)	15.035(5)	110.17(4)	1202.7(7)	
290	10.488(1)	8.138(1)	15.082(1)	110.30(1)	1206.3(1)	6-3-2

Table 6.3-1 The cell parameters of 4-amino-4'-hydroxydiphenyldisulfide at temperatures ranging from 20 to 290 K

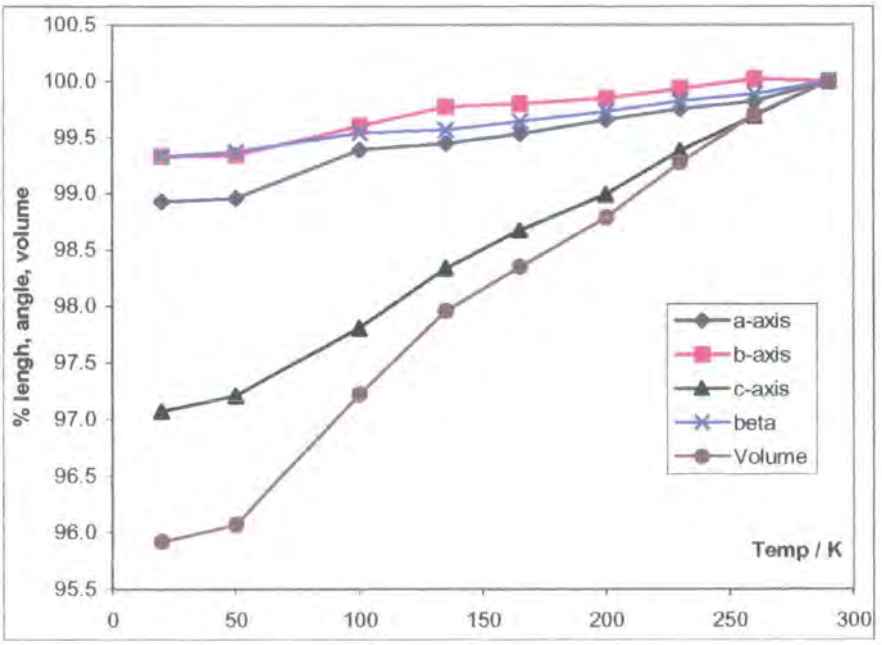

Figure 6.3-2 Unit cell parameters expressed as a percentage of the 290K data. The overall variation of the unit cell volume is largely due to variation in the length of the c-axis.

Unit cell parameters for all temperatures measured are listed in Table 6.3-1. File names for the new full structure determinations are also presented. These

values are plotted in Figure 6.3-2 as a percentage of the 290 K values. As can be seen from Figure 6.3-2, the thermal expansion is anisotropic. While the c-axis contracts by almost 3% over the temperature range, the other axes show a far more modest change. The expectation of such an experiment is that there will be a linear change in each of the cell parameters until the zero point energy is approached, where one would expect a levelling off in the cell parameters. The results are only moderately convincing, however, while the cell parameters do fall off, and there does seem to be a tail-off in the rate of change at the lowest temperatures, the parameter changes are only approximately linear with temperature, and a shortage in the number of data sets collected at the lowest temperatures makes it difficult to assess the extent to which the changes cease at the lowest temperatures.

	S1	**S2**	**N**	**O**
Temp/K	ADP/Å^2	ADP/Å^2	ADP/Å^2	ADP/Å^2
20	0.0169(2)	0.0165(2)	0.0150(4)	0.0173(4)
50	0.0169(2)	0.0166(2)	0.0149(4)	0.0175(4)
100	0.0277(1)	0.0266(1)	0.0224(1)	0.0211(3)
200	0.0465(2)	0.0444(2)	0.0357(3)	0.0431(3)
290	0.0664(3)	0.0635(3)	0.0503(5)	0.0605(6)

Table 6.3-2 Atomic displacement parameters for sulphur, nitrogen and oxygen over the temperature range.

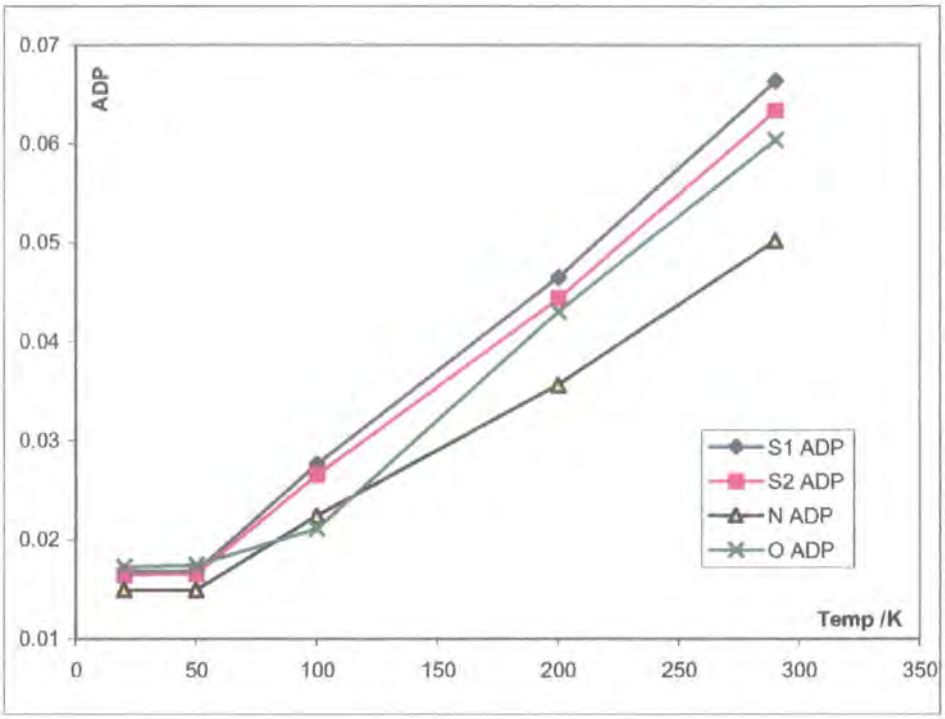

Figure 6.3-3 A plot of the ADP sizes at various temperatures. The size of the ADPs decreases almost linearly as temperature falls until we reach 50 K, when there is an abrupt end to the shrinking effect.

The atomic displacement parameters (ADPs) of the heaviest atoms in the system (sulphur, oxygen and nitrogen) have been tabulated in Table 6.3-2, and these data are plotted in Figure 6.3-3. The ADP value quoted is the isotropic equivalent of the anisotropic ADP. As can be seen clearly in Figure 6.3-3, the size of the ADPs falls linearly until, at 50 K, there is no further change observed in the ADP. The physical interpretation of this is that thermal motion decreases as temperature decreases until zero point motion is reached, when further cooling has no effect on the atomic thermal motion.

6.3.2 4-amino-4'hydroxybenzylsulphide - Results

This molecule and its crystal packing are shown in Figure 6.3-4. It was studied over the 100-290 K temperature range and at all temperatures was found to crystallise in the monoclinic space group Pc. The central feature of the packing

is the β-As sheet that runs perpendicular to the a-axis. The close contacts within this sheet (at 200K) are: N1-H11A... O1 3.168(2) Å; N1-H11B...O1 3.226(2) Å; and O1-H4...N1 2.807(2) Å, for the oxygen to nitrogen distances. There is an apparent close contact between the sulfur and H7a of 2.88(3) Å.

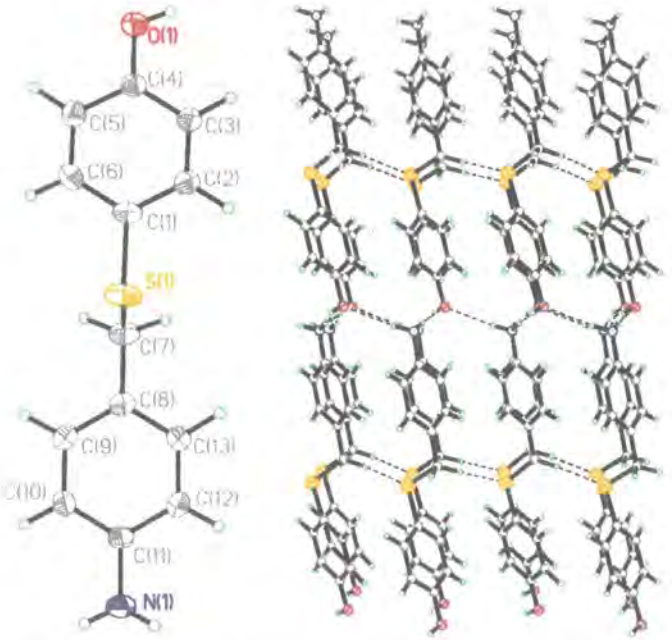

***6-3-6: $C_{12}F_3H_{11}O$ at 200K**: Monoclinic, Pc and Z = 2, R_1 = 3.26%, R_2 = 8.40%, R_{int} = 0.0401, a = 13.8819(8) Å, b = 5.1965(3) Å, c = 8.3463(5) Å, β = 106.932(3)°. V = 575.98(6) Å^{-3}*

Figure 6.3-4 Molecular diagram of 4-amino-4'hydroxybenzylsulphide, left, with the packing diagram, right.

Full structural determinations were carried out at 100, 200 and 290 K, and unit cells were determined at 135, 165, 230, 260 K. All data sets were collected on a Bruker SMART CCD 1K area detector in conjunction with an Oxford Cryosystems cryostream. The cell parameters at the temperatures measured are listed in Table 6.3-3. These data are plotted as a percentage of the 290 K data in Figure 6.3-5.

Temp/K	a-axis/Å	b-axis/Å	c-axis/Å	Beta/°	Volume/Å^3	Structure
100	8.294(1)	5.184(1)	13.881(1)	107.166(2)	570.26(3)	6-3-8
135	8.309(3)	5.194(2)	13.904(4)	107.321(5)	572.8(3)	
165	8.320(3)	5.195(2)	13.893(4)	107.226(5)	573.5(3)	
200	8.352(1)	5.187(1)	13.886(1)	107.087(3)	574.94(6)	6-3-6
230	8.376(3)	5.196(3)	13.872(5)	106.981(4)	577.5(4)	
260	8.406(4)	5.201(3)	13.867(5)	106.850(5)	580.2(4)	
290	8.459(1)	5.194(1)	13.848(1)	106.682(2)	582.80(6)	6-3-7

Table 6.3-3: The unit cell parameters of 4-amino-4'hydroxybenzylsulphide at temperatures ranging from 100 to 290 K

Again, anisotropic thermal expansion is observed – the length of the a-axis shows significant temperature dependence, mirrored by the cell volume, while there is no great variation in the other parameters over the temperature range studied. Interestingly, there seems to be a small increase in the c-axis length over the temperature range. The 100 K data would appear to be an outlier: these are the data collected by C.K. Broder on the Rigaku 4-circle diffractometer.

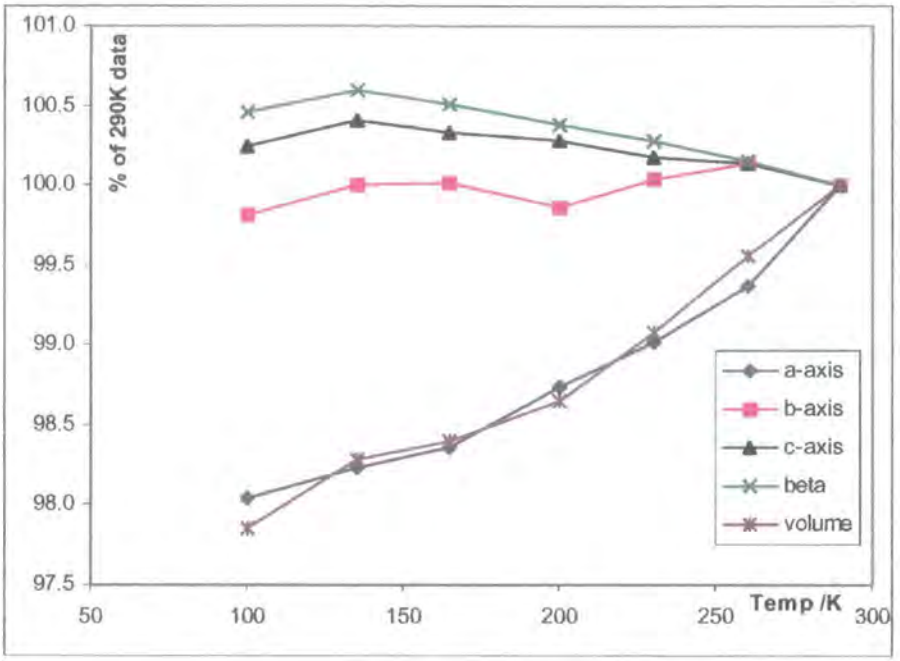

Figure 6.3-5 Unit cell parameters expressed as a percentage of the 290K data. In this case the unit cell volume, mirrors the variation in the a-axis.

Isotropic ADPs for the sulfur, nitrogen, oxygen and carbon 7 (the carbon that has replaced the sulfur in 4-amino-4'-hydroxydiphenyldisulfide) are tabulated in Table 6.3-4, and plotted in Figure 6.3-6. The contrast with the values found for 4-amino-4'-hydroxydiphenyldisulfide is obvious, however, whereas in the former case the 100-290 K data showed a linear fall in the ADP size as temperature falls, this does not seem to be the case this system. Clearly with only three data points, it is difficult to comment on any trend that this figure reveals; however, it would appear that these data do not lie on a straight line as might have been expected.

	O	N	S	C7
Temp/K	ADP/Å^2	ADP/Å^2	ADP/Å^2	ADP/Å^2
100	0.0268(3)	0.0249(3)	0.0280(1)	0.0257(4)
200	0.0350(3)	0.0329(3)	0.0368(1)	0.0332(4)
290	0.0572(9)	0.056(1)	0.0631(4)	0.056(1)

Table 6.3-4: Atomic displacement parameters for sulphur, nitrogen and oxygen and the C7 (the central carbon that has replaced sulphur in the previous section.

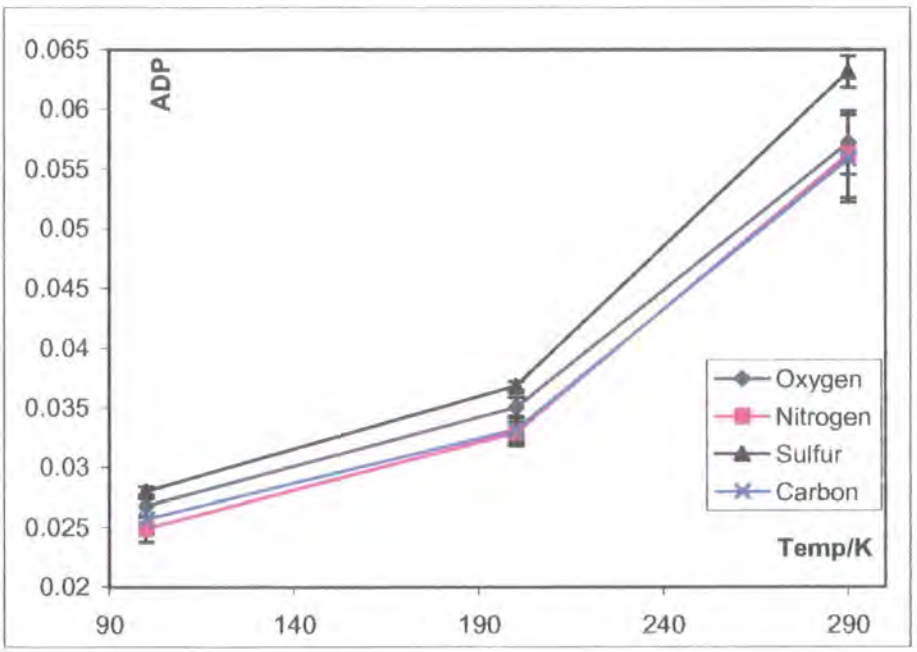

Figure 6.3-6 plot of the ADP sizes at various temperatures.

6.3.3 Discussion

There is possibly a correlation in these systems between crystal structure type and thermal expansion, though what that correlation may be is unclear. In these two systems there is anisotropic variation of the cell axis lengths as a function of temperature. In the latter case, 4-amino-4'hydroxybenzylsulphide, the packing is easily defined as a β-As sheet that runs perpendicular to the a-axis of the unit cell, and the principal component of the unit cell's thermal expansion is parallel to the same axis. Whether this is a general feature of β-As

sheet structures is not known as there are no data available on this point. In the case of 4-amino-4'-hydroxydiphenyldisulfide, the packing is harder to define as, although the infinite chains run in the direction of the b-axis, the hydrogen bonds themselves align in the direction of both the b and c-axis. The principal component of the thermal expansion is in the direction of the c-axis. It should be noted that the contact distances at 200 K and 20 K for this experiment vary by less that 1% - 3.046(2) and 2.764(2) Å at 200 K vs. 3.016(3) and 2.748(3) Å at 20 K. As such the effect of the cell variation does not affect the close contacts to any great extent.

The behaviour of the ADPs is in line with what might be expected – there is a linear relationship in the classical temperature region, while at the lowest temperatures there is a levelling off in their magnitude as quantum mechanical effects take over. With both sets of experiments, there are underlying problems when the sample is measured on different diffractometers. The Bruker SMART 1K produces unit cells that are larger then the Fddd diffractometer in the case of 4-amino-4'-hydroxydiphenyldisulfide or the Rigaku 4-circle diffractometer in the case of 4-amino-4'hydroxybenzylsulfide. This change of cell size does not have any obvious bearing on the size of the ADPs in the more extensive study of 4-amino-4'-hydroxydiphenyldisulfide, where there is sufficient data to make such a comparison.

6.4 *Dimesitylborane*

The information in this section has, in part, been published in [publication 3]:

Entwistle CD, Marder TB, Smith PS, Howard JAK, Fox MA, Mason SA;

J. ORGANOMETALLIC CHEM. (2003) **680** 165-172

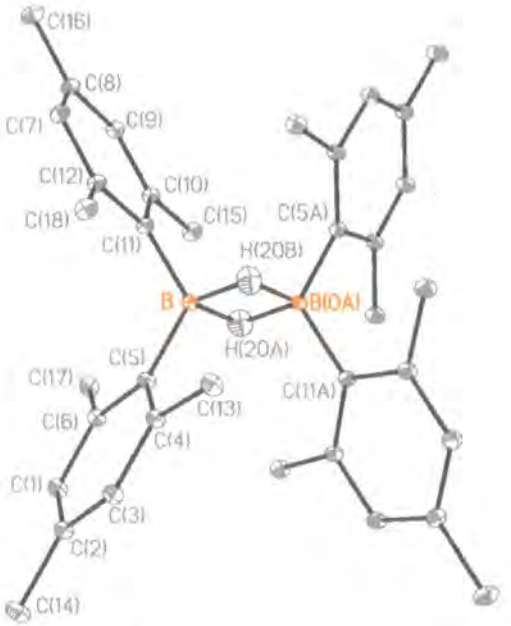

***6-4-2: $C_{36}H_{46}B_2$ at 20K (neutron structure)**: Monoclinic, P2/n and Z = 2, R_1 = 3.54%, R_2 = 8.10%, R_{int} = 0.0391, a = 12.2778(8) Å, b = 7.7353(6) Å, c = 16.5979(12) Å, β = 109.836(3)°, V = 1482.81(18) Å^3*

From a chemical point of view, dimesitylborane is interesting as it exists as a dimer in the solid state, although in solution it has been found that it exists in equilibrium with dimesitylborane monomer (see publication 3). In spite of this, dimesitylborane exhibits relatively low reactivity. Both features can be attributed to steric bulk which can (i) stabilise the monomer by relieving congestion around the 4 coordinate dimer to the 3 coordinate monomer and (ii) inhibit the formation of a π-complex with unsaturated substrates thus reducing reactivity.

From a crystallographic point of view this is interesting primarily as studies of boron B_2H_2 bridges have not been carried out using neutron diffraction. A search of the Cambridge Crystallographic Database [Conquest v. 1.6, (2003)] revealed that there were no neutron diffraction data deposited for B_2H_2 bridges, and only a total of 13 structures that contained a BH_2 group studied by neutron diffraction. This in itself makes the study interesting, if only to benchmark this structural feature accurately.

Feature	X-ray	Neutron	CASTEP
B–H (Å)	1.280(15) 1.288(16)	1.340(2) 1.342(2)	1.323 1.330
B...B (Å)	1.856(3)	1.855(2)	1.839
B–C (Å)	1.596(2) 1.577(2)	1.596(1) 1.600(1)	1.577 1.580
B–H–B (°)	93.0(10)	87.7(1)	88.0 87.5
H–B–H (°)	87.5(10)	92.46(14)	92.2
C–B–C (°)	123.4(1)	123.7(1)	123.7

Table 6.4-1 Structural features around the B_2H_2 bridge from the X-ray and neutron diffraction experiments, left columns, and the same data from a CASTEP geometry optimisation on the isolated molecule.

A geometry optimisation was carried out using plane-wave DFT via the CASTEP code. In this calculation the dimesitylborane dimer was placed in an arbitrarily large unit cell, and optimisation carried out using the following parameters:

Files: 6-4-3

Exchange Functional: PW91; Plane wave cut off: 280 eV;

Energy Tolerance: $2x10^{-6}$ eV; K-point sampling: 1x1x1 (gamma point only);

Geometry Optimisation:

Energy Tolerance: 0.00030 eV/atom; Force Tolerance: 0.100 eV/Å;

Stress Tolerance: 0.20 GPa; Dispersion Tolerance: 0.0040 Å;

Method: BFGS

This represents a medium quality calculation, and is as good as can be expected for such a large molecule – certainly CASTEP calculations on the bulk crystal structure are out of the question. Is should be noted that there is no symmetry constraint in this optimisation and thus there are two B–H–B angles rather than the one that results from the symmetry constraint about the B–H–B in the diffraction derived structure.

The common features of the three (independently determined) structures - X-ray, neutron and computational – around the B_2H_2 bridge can be found in Table 6.4-1. The X-ray structure [6-4-1] produces slightly shorter B – H bond distances than the neutron structure and as the boron – boron separation distance is the same in both structures, there is a compensating increase in the B – H – B bond angle (see Table 6.4-1). The calculated structure reproduces the neutron structure very well: although the boron – hydrogen bond lengths are slightly shorter in the calculated structure, to be precise: 0.017 and 0.012 Å shorter, this is a significant improvement on the X-ray derived structure.

6.5 *Rigid-Rod Molecules*

As part of ongoing investigations into rigid-rod molecules which contain perfluorinated and non-perfluorinated phenyl rings, data on various crystals were collected. The origins of these crystals lie with Prof. Todd Marder and co-workers. Such systems are interesting for a variety of reasons. Arene and perfluoroarenes can co-crystallise in molecular complexes, with a 1:1 composition and the packing in these is a mixed stack of alternating components: the pure arene and perfluoroarenes pack in a herringbone motif. This control of packing is of interest as starting materials for solid-state reactions (e.g. topological photopolymerisation). Additionally they may also be promising as molecular electronic and optical materials, a combination of individual properties of the molecules themselves and the interactions between these molecules in the bulk sample. Lastly, the rod like systems have prospects for liquid crystal phases. Some partially fluorinated systems display LC phases while their fully fluorinated and non-fluorinated analogues show none[iii].

[iii] CE Smith, PS Smith, RL Thomas, EG Robins, JC Collings, CY Dai, AJ Scott, S Borwick, AS Batsanov, SW Watt, SJ Clark, C Viney, JAK Howard, W Clegg, TB Marder; J. Mater. Chem., (2004) 14, 413-420; and references therein.

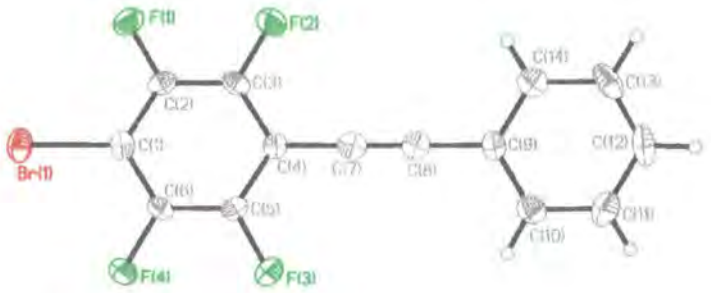

***6-5-1: $C_{14}H_5F_4Br$ at 120K**: Monoclinic, $P2_1/n$ and $Z = 4$, $R_1 = 3.74\%$, $R_2 = 7.04\%$, $R_{int} = 0.0893$, $a = 12.7523(9)$ Å, $b = 4.9660(4)$ Å, $c = 18.3674(14)$ Å, $\beta = 93.231(2)°$, $V = 1161.32(15)$ Å^3*

In this system ($C_{14}H_5F_4Br$), the para position of the phenyl ring has been replaced with bromine. The effect on the crystal structure is startling: Without the bromine, the packing motif is an infinite stack of alternating fluorinated and non-fluorinated phenyl rings (see [iii]). In the present crystal structure the packing is edgeways on, similar to the herringbone motif (see Figure 6.5-1). There is an apparent close contact between the bromine and a phenyl hydrogen atom: 3.04(3) Å, though this is almost certainly incidental to the crystal structure. It would seem that the steric bulk of the bromine disrupts the expected infinite stacking of the aromatic rings.

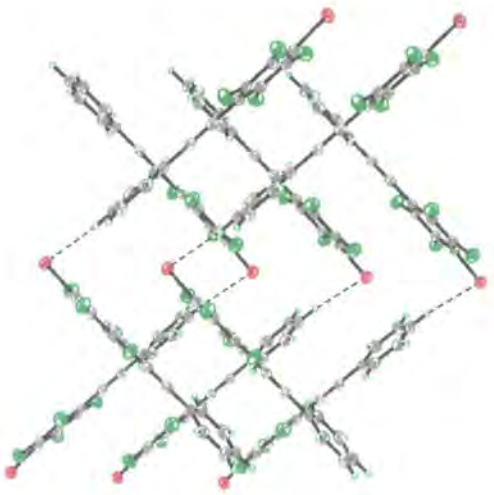

Figure 6.5-1 Packing of 6-5-1.

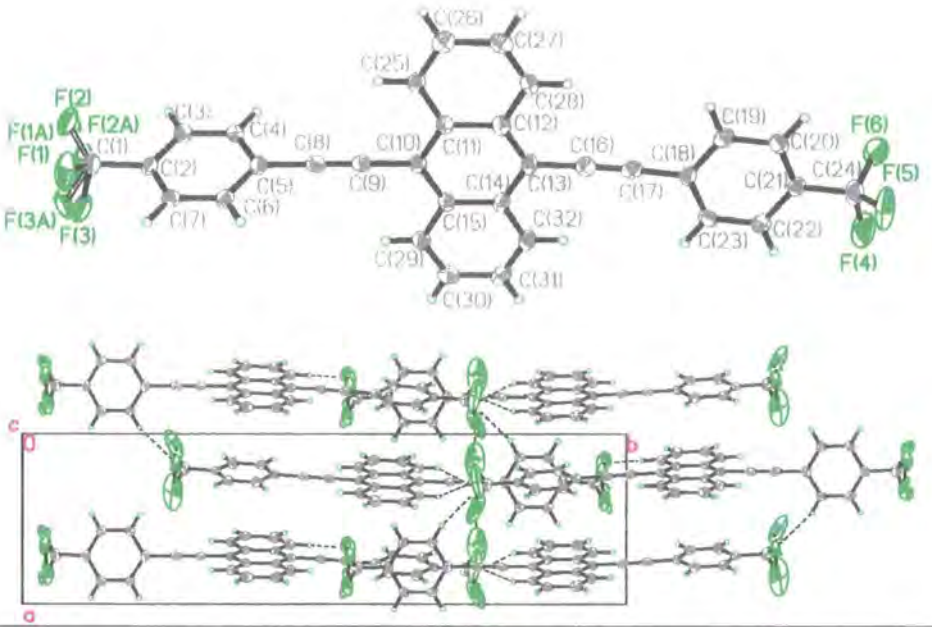

***6-5-2: $C_{32}H_{16}F_6$ at 270K**: Monoclinic, $P2_1/n$ and $Z = 4$, $R_1 = 8.04\%$, $R_2 = 19.75\%$, $R_{int} = 0.0786$, $a = 9.042(4)$ Å, $b = 28.893(12)$ Å, $c = 10.136(4)$ Å, $\beta = 114.164(2)°$, $V = 2416.1(17)$ Å^3*

9-10 bis[4'-triflouromethyl phenyl ethynyl] anthracene, above, is an example of a surprise structure to some extent: the sample submission sheet suggested that there was simply another phenyl group in the centre of this molecule, rather than the more elaborate aromatic group shown above. The phenyl ring (C2 – C7) is at right angles to the other aromatic groups. The resultant crystal structure is shown in Figure 6.5-2. Close contacts to the disordered CF_3 group are an artefact of the disordered model used. Otherwise the molecules close pack in pairs such that the C1 – C2 bonds align in opposite directions and equivalent phenyl groups are parallel.

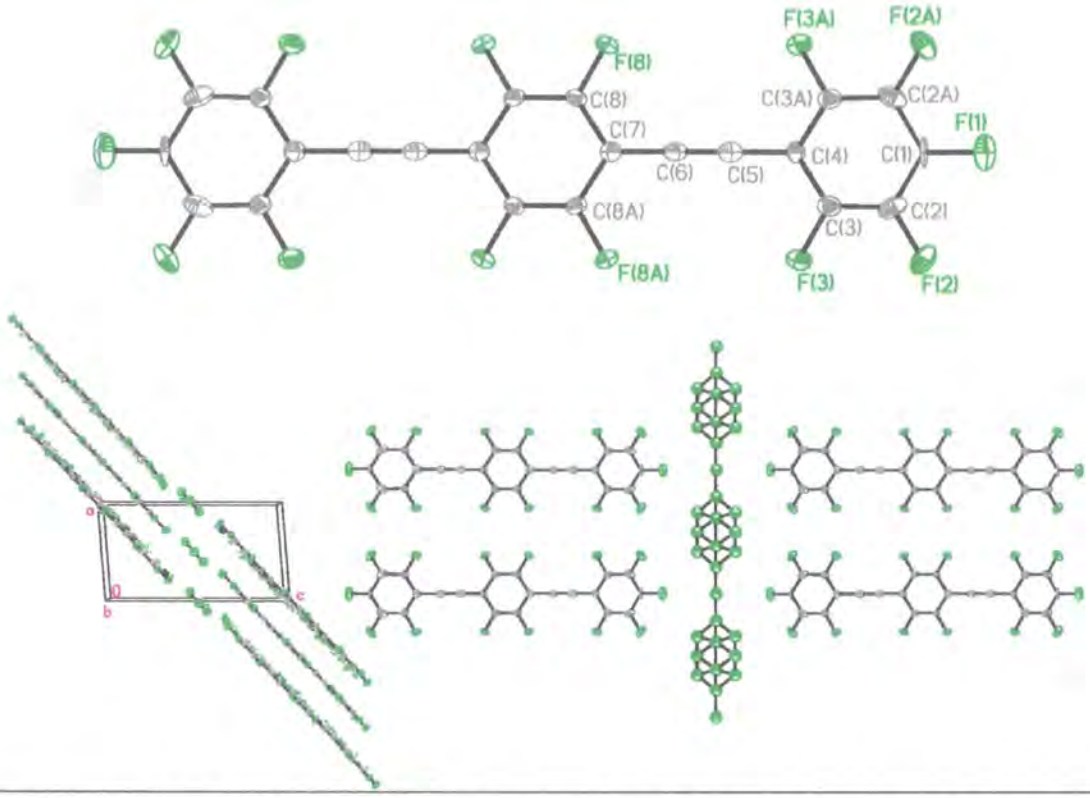

***6-5-3a: $C_{22}H_{11}$ at 120K**: Monoclinic, $P2_1/n$ and $Z = 2$, $R_1 = 22.30\%$, $R_2 = 60.96\%$, $R_{int} = 0.0172$, $a = 9.0960(5)$ Å, $b = 7.6491(4)$ Å, $c = 16.8648(9)$ Å, $\beta = 94.665(1)°$, $V = 1169.5(1)$ Å^3*

Figure 6.5-2 The 1-4 bis[pentafluoro phenylethynyl] tetrafluorobenzene molecule, top, with a diagram of the packing, bottom left, and the disordered channel, bottom right.

Here we have a problem structure involving solvent disorder. The known part of the structure is 1-4 bis[pentafluoro phenylethynyl] tetrafluorobenzene, however there is a void within this close packed structure. Herein lies 'solvent' that looks suspiciously as though it contains phenyl rings that are slipped into a number of positions in order to fill the void in the crystal structure. The refinement statistics quoted in Figure 6.5-2 do not include any attempt to model the disorder and this is the reason for the huge R1/R2 values. An attempt was made to produce such a model, based on placing two sets of discrete atom positions in the disordered void area. While this massively improved the refinement statistics (R1= 5.06 R2=16.11, structure 6-5-3b) the refinement

failed to produce chemically realistic bond distances or angles. Inspection of the Fourier map of the void shows why (Figure 6.5-3).

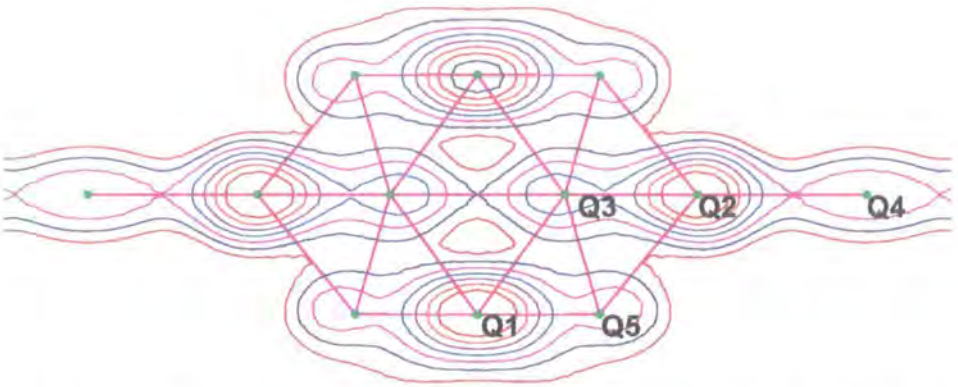

Figure 6.5-3 Fourier map (Fobs) of the structure void, contours being 0, 0.5, 1.0...4.0 eÅ^{-3}. The 5 Q-peaks labelled cover the whole space of the diagram, above, by symmetry.

The five Q-peaks have magnitude of 4.30, 4.17, 2.68, 2.61 and 2.02 eÅ^{-3} for Q1 to Q5 respectively. The separation distances are (approximately) 1.45 and 1.20 Å between Q1 and Q3 and Q5 respectively and 1.30, 1.67 and 1.52 Å between Q2 and Q3, Q4 & Q5. These values do not provide an obvious model for the disorder and lengthy attempts to created a plausible model failed. Squeeze was applied as an alternative to producing a definite model for the disorder[iv]. Unsurprisingly, the application of this technique produced even better refinement statistics: R1 = 4.71, R2 = 14.37% (structure 6-5-3c). However, the said procedure also produced a missing electron count of 50. Needless to say this isn't a terribly promising number as none of the probable 'solvent' fragments have an electron count 50: C≡C-C_6H_4 has 52 electrons associated with it. The structure remains unfinished.

[iv] A.L. Spek, Acta Crystallogr. (1990) A46, C-34

6.6 *Other Structures*

6.6.1 $[Gd_5(\mu_4\text{-}OH)(\mu_3\text{-}OH)_4(\mu_2\text{-}dbmH)_4(dbmH)_6]$

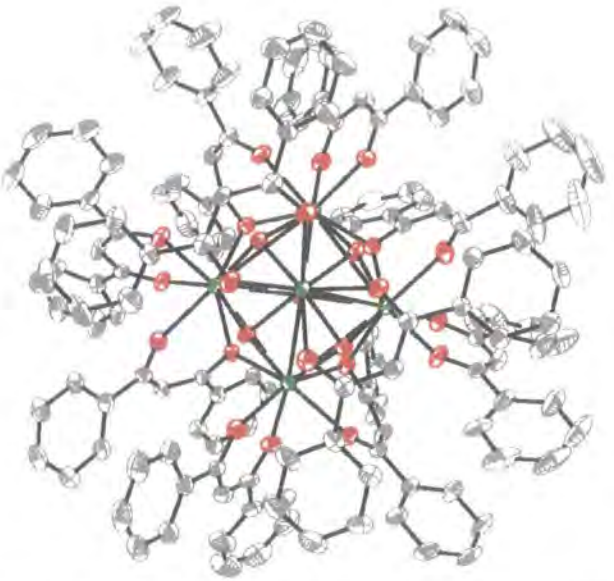

***6-6-1: $Gd_5C_{150}H_{110}O25.CCl_2H_2$ at 120K**: Monoclinic, $P2_1/c$ and $Z = 4$, $R_1 = 3.83\%$, $R_2 = 7.74\%$, $R_{int} = 0.0966$, $a = 21.879(4)$ Å, $b = 17.326(4)$ Å, $c = 36.056(8)$ Å, $\beta = 100.772(8)°$, $V = 13427(5)$ Å^3*

Figure 6.6-1 Diagram of the Gadolinium cluster. Hydrogen and solvent atoms have been omitted for clarity.

This structure was synthesised by Katie Gatenby under the supervision of Dr. Paul Low as an attempt to synthesise unusual gadolinium complexes of β-diketolates that may have applications in chemical vapour deposition (CVD). The result of this synthesis was this (entirely unexpected) cluster, which features a square pyramidal arrangement of five gadolinium atoms with chelating dibenzyl methane ligands (dbmH - Figure 6.6-1). Such a configuration is extremely rare and, to our knowledge, only one other example of a similar complex is known: a Europium complex[v]. This structure suggests that such

[v] R.G. Xiong, J.L. Zuo, Z. Yu, X.Z. You, W. Chen; *Inorg. Chem. Comm.* **2** (1999) 490-494

square pyramidal motifs of Lanthanides may be more common than previously believed.

Refinement notes:

The solvent, dichloromethane, is disordered within a void of 274Å^3. Although this disorder has been modelled by placing the chlorine atoms in two distinct sites with an ordered carbon atom in the centre, this model is somewhat arbitrary: no good definition of atomic sites is found and the carbon – chlorine bond lengths have been restrained to produce sensible results. The hydrogen atoms in this group have not been included in the model at all because there is no sensible way of including them. There are some problems with the ADPs of the carbon atoms at the periphery of the cluster that cause some serious alerts in cif check (level A and B). Unfortunately these are unavoidable artefacts of the experiment: scattering of the gadolinium atoms dominates the diffraction pattern and there are also a large number of non-hydrogen atoms in this particular structure.

Description of structure

The gadolinium atoms form a square planar pyramid with the Gd – Gd sides of the pyramid ranging from 3.5943(7) to 3.6840(8) Å in the square plane and 3.8768(8) to 3.8982(7) Å from the base to the apical gadolinium, Gd5 Figure 6.6-1. The Gd – O bonds fall into 4 classes: (i) O17, 19, 23, 24 bridge between the triangular faces of the pyramid between Gd5 and two of the other gadolinium atoms in each case (μ_3-O). (ii) O18 lies in the middle of the base of the Gd1-Gd4 square. (iii) Between each pair of Gd atoms on the base of the pyramid are bridging oxygen atoms O8, 12, 14, and 20: these are provided by the dibenzoylmethide ligands. (iv) Finally there are 3 oxygen atoms attached to

each of Gd1-4 and 4 to the axial Gd5. Table 6.6-1 contains all these bond lengths.

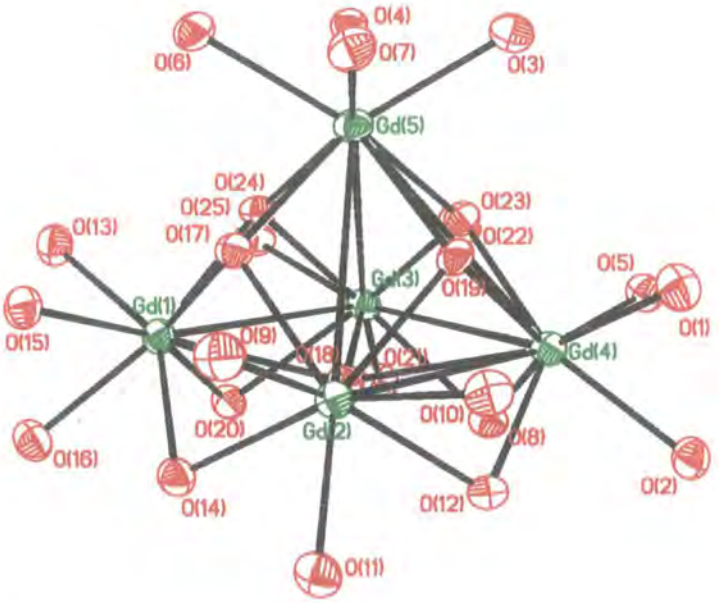

Figure 6.6-2 The core of the cluster, comprising of just the oxygen and gadolinium atoms.

In case (i) the μ_3 oxygen atom position is approximately equidistant from the three Gd atoms. In case (iii), the oxygen atoms is not equidistant between the two bound gadolinium atoms: for example, O(14) is 2.432(3)Å from Gd(1) and 2.471(3) away from Gd(2).

Table 6.6-1 Interatomic distances for all atoms within the core of the cluster

Distances (Å) of gadolinium separation

Gd(1)-Gd(3)	3.5943(7)	Gd(1)-Gd(5)	3.8768(8)
Gd(1)-Gd(2)	3.6503(8)	Gd(2)-Gd(5)	3.9484(8)
Gd(2)-Gd(4)	3.6217(7)	Gd(3)-Gd(5)	3.9023(6)
Gd(3)-Gd(4)	3.6840(8)	Gd(4)-Gd(5)	3.8982(7)

Distances (Å) for bridging oxygen

Gd(1)-O(14)	2.432(3)	Gd(3)-O(8)	2.492(3)
Gd(1)-O(20)	2.500(3)	Gd(3)-O(20)	2.391(3)
Gd(2)-O(14)	2.471(3)	Gd(4)-O(8)	2.383(3)
Gd(2)-O(12)	2.395(3)	Gd(4)-O(12)	2.433(3)
Gd(1)-O(17)	2.390(3)	Gd(3)-O(23)	2.359(3)
Gd(1)-O(24)	2.350(3)	Gd(3)-O(24)	2.370(3)
Gd(2)-O(19)	2.390(3)	Gd(4)-O(19)	2.348(3)
Gd(2)-O(17)	2.390(3)	Gd(4)-O(23)	2.379(3)
Gd(1)-O(18)	2.558(3)	Gd(3)-O(18)	2.624(3)
Gd(2)-O(18)	2.572(3)	Gd(4)-O(18)	2.722(3)
Gd(5)-O(17)	2.432(3)	Gd(5)-O(23)	2.460(3)
Gd(5)-O(19)	2.451(3)	Gd(5)-O(24)	2.444(3)

Other gadolinium – oxygen distances (Å)

Gd(1)-O(16)	2.311(3)	Gd(3)-O(25)	2.397(4)
Gd(1)-O(13)	2.350(3)	Gd(4)-O(2)	2.338(3)
Gd(1)-O(15)	2.345(3)	Gd(4)-O(1)	2.338(4)
Gd(2)-O(9)	2.289(3)	Gd(4)-O(5)	2.394(3)
Gd(2)-O(11)	2.360(3)	Gd(5)-O(7)	2.347(3)
Gd(2)-O(10)	2.410(3)	Gd(5)-O(4)	2.364(3)
Gd(3)-O(22)	2.299(3)	Gd(5)-O(3)	2.373(3)
Gd(3)-O(21)	2.331(3)	Gd(5)-O(6)	2.381(3)

6.6.2 $C_{18}H_{14}S_3$

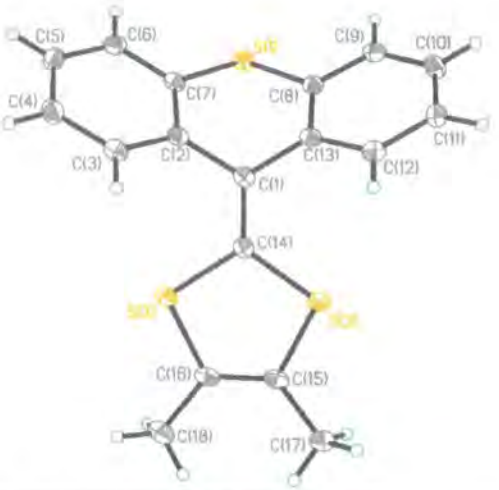

***6-6-2: $C_{18}H_{14}S_3$ at 100K**: Monoclinic, $P2_1/n$ and $Z = 4$, $R_1 = 3.39\%$, $R_2 = 7.86\%$, $R_{int} = 0.0572$, $a = 9.997(2)$ Å, $b = 7.812(1)$ Å, $c = 19.468(3)$ Å, $\beta = 91.866(4)°$, $V = 1519.8(4)$ Å^{-3}*

Synthesised by Nicholas Godbert under the supervision of Prof. Martin Bryce, this small organic with 3 sulphur atoms within is perhaps most interesting to this author as being the first crystal structure solved during the PhD tenure. It is an unremarkable small organic molecule that is reported here for completeness and closure. On a lighter note: I believe the molecule has the resemblance of a bird standing on its legs with wings fully spread.

7 Conclusions

The work presented here principally concerns 4 combined variable temperature and computational studies, of which, three discuss dynamic disorder of the terminal CF_3 groups, and the fourth relates to short, strong hydrogen bonding. In relation to the studies of CF_3 group motion, it has been found that: (i) the diffraction derived barrier to rotation, in practice, is partially dependant on the temperature used - lower temperatures yielding higher barriers; (ii) the barrier is not necessarily correlated to the molecular geometry of the system: e.g. the substitution of fluorine for hydrogen in the ortho position of the phenyl ring did not produce consistently higher barriers to rotation. It is thus the crystal structure environment that is the likely culprit for the changes in barrier height.

On the computational side, two methods of calculating the barrier to rotation were used on both isolated molecules and, where practical, the condensed matter phase. Where the isolated molecule is concerned, the barrier heights did mirror the molecular structure, though that is hardly surprising. When using the crystal structure for the calculation, it is found that the relative molecular environments play a huge role in the derived barrier to rotation: Tolan 1 (F5-7) produces far larger barriers than that of Tolan 3, in spite of the similar molecular geometry. It is gratifying to note that this trend is also observed in the diffraction derived data. For easy comparison, all of the barriers to rotation found in this work are tabulated below. In this table, 'rigid' and 'LST/opt' refer to the method of calculation used within CASTEP. The 'X-struct.' column refers to calculations carried out via CASTEP using the X-ray diffraction geometry.

Barriers to Rotation. All values expressed in $kJmol^{-1}$.

System	Diffraction Data	Crystal Structure			Isolated Molecule	
		Rigid	LST/opt	X-Struct.	Rigid	LST/opt
Tolan 1: F5-F7	5.4 - 9.1	55.46	69.43	20.63[a]	17.77	4.74
Tolan 1: F8-F10	1.9 - 4.3	22.57	n/a	n/a	2.91	0.15
Tolan 2	3.7 - 7.3	n/a	n/a	n/a	0.74	3.76
Tolan 3	1.9 - 3.1	14.08	16.33	15.43[b]	12.45	6.82

a. 240K X-ray diffraction structure used for starting geometry
b. 100K X-ray diffraction structure used for starting geometry

Zinc pyromellitate has an intramolecular hydrogen bond whose O...O separation suggests a short, strong hydrogen bond (SSHB) will exist. The neutron diffraction experiment showed none of the expected proton migration that often accompanies SSHBs. The computational study of the system sheds a great deal of light into why this result is observed. While the isolated pyromellitate fragment does have a single, shallow, energy potential well, when one carries out calculations on the crystal structure, this ceases to be the case. Again we see the huge importance of the crystal structure environment in these experiments: while molecular structure is of obvious importance, the interaction of molecules in the condensed matter phase is hugely important and not entirely predictable.

Future Work

With regard to the CF_3 motion, all three systems have been passed on to the solid state NMR group in Durham University with the aim of estimating the barrier to rotation with this method of experimentation. The agreement, or otherwise, of these independent experiments should prove interesting in itself, and will hopefully shed further light on the accuracy of barrier height estimation from both X-ray diffraction and computational methods.

As for investigations into short strong hydrogen bonding, it would be interesting to carry out similar computational studies into a system that *does* display proton migration in variable temperature neutron diffraction experiments, by comparing and contrasting the potential wells in which the protons sit, with the results from variable temperature diffraction experiments. Given the advances in computing power over recent years, combined with the direct access to this kind of information a first-principles simulation provides, it would seem reasonable to expect such studies to be highly profitable.

Appendix A: Tables for Selected Structures

Tables for Structure 2-2-1

Table 1. Crystal data and structure refinement.

Identification code	2-2-1	
Empirical formula	C16 H4 F10	
Formula weight	386.19	
Temperature	280(2) K	
Wavelength	0.71073 Å	
Crystal system	Monoclinic	
Space group	P2(1)/n	
Unit cell dimensions	a = 5.5687(3) Å	α= 90°.
	b = 14.6960(7) Å	β= 91.999(2)°.
	c = 18.5503(9) Å	γ = 90°.
Volume	1517.19(13) $Å^3$	
Z	4	
Density (calculated)	1.691 Mg/m^3	
Absorption coefficient	0.185 mm^{-1}	
F(000)	760	
Crystal size	0.30 x 0.26 x 0.16 mm^3	
Theta range for data collection	1.77 to 28.49°.	
Index ranges	-7<=h<=7, -19<=k<=19, -24<=l<=24	
Reflections collected	17417	
Independent reflections	3848 [R(int) = 0.0478]	
Completeness to theta = 28.49°	99.9 %	
Absorption correction	None	
Refinement method	Full-matrix least-squares on F^2	
Data / restraints / parameters	3848 / 6 / 263	
Goodness-of-fit on F^2	0.991	
Final R indices [I>2sigma(I)]	R1 = 0.0558, wR2 = 0.1377	
R indices (all data)	R1 = 0.1502, wR2 = 0.1837	
Largest diff. peak and hole	0.446 and -0.270 $e.Å^{-3}$	

Table 2. Atomic coordinates (x 10^4) and equivalent isotropic displacement parameters ($Å^2$x 10^3) for 2-2-1. U(eq) is defined as one third of the trace of the orthogonalized U^{ij} tensor.

	x	y	z	U(eq)
F(4)	9334(3)	4457(1)	757(1)	90(1)
F(1)	3270(4)	3850(1)	2921(1)	96(1)
F(2)	10147(4)	3070(1)	1634(1)	91(1)
F(3)	2482(4)	5247(1)	2041(1)	97(1)
C(4)	8222(5)	3597(2)	1746(2)	65(1)
C(3)	4792(6)	3989(2)	2389(2)	67(1)
C(10)	4478(6)	7109(2)	118(2)	63(1)
C(2)	6741(5)	3411(2)	2310(2)	62(1)
C(7)	5880(6)	4897(2)	1367(2)	63(1)
C(5)	4386(6)	4710(2)	1935(2)	68(1)
C(6)	7808(6)	4320(2)	1293(2)	64(1)
C(9)	5006(6)	6301(2)	533(2)	70(1)
C(8)	5428(6)	5655(2)	898(2)	73(1)
C(11)	2505(7)	7639(3)	269(2)	87(1)
C(12)	5912(6)	7381(2)	-434(2)	73(1)
C(15)	3467(6)	8687(2)	-658(2)	72(1)
C(14)	5417(6)	8167(2)	-817(2)	78(1)
C(13)	2011(7)	8425(3)	-116(2)	90(1)
C(1)	7150(8)	2645(3)	2831(2)	87(1)
C(16)	2932(10)	9545(3)	-1068(3)	103(1)
F(5)	8989(6)	2143(2)	2702(2)	162(1)
F(6)	7404(6)	2932(2)	3495(1)	144(1)
F(7)	5317(6)	2091(2)	2843(2)	148(1)
F(8)	2430(40)	10214(8)	-643(7)	149(6)
F(10)	456(40)	9816(13)	-1475(16)	183(9)
F(9)	960(30)	9421(12)	-1473(9)	162(8)
F(8A)	3590(60)	9544(14)	-1719(7)	164(11)
F(9A)	610(30)	9750(20)	-1090(30)	217(14)
F(10A)	3950(100)	10252(10)	-792(16)	216(14)

Table 3. Bond lengths [Å] and angles [°] for 2-2-1.

F(4)-C(6)	1.346(3)	C(11)-H(11)	0.9300
F(1)-C(3)	1.339(3)	C(12)-C(14)	1.379(4)
F(2)-C(4)	1.345(3)	C(12)-H(12)	0.9300
F(3)-C(5)	1.341(3)	C(15)-C(13)	1.368(5)
C(4)-C(6)	1.370(4)	C(15)-C(14)	1.368(4)
C(4)-C(2)	1.383(4)	C(15)-C(16)	1.498(5)
C(3)-C(5)	1.367(4)	C(14)-H(14)	0.9300
C(3)-C(2)	1.391(4)	C(13)-H(13)	0.9300
C(10)-C(12)	1.379(4)	C(1)-F(5)	1.291(4)
C(10)-C(11)	1.384(4)	C(1)-F(6)	1.305(4)
C(10)-C(9)	1.439(5)	C(1)-F(7)	1.307(4)
C(2)-C(1)	1.495(5)	C(16)-F(10)	1.264(11)
C(7)-C(6)	1.379(4)	C(16)-F(8A)	1.274(13)
C(7)-C(5)	1.392(4)	C(16)-F(10A)	1.281(13)
C(7)-C(8)	1.431(5)	C(16)-F(8)	1.298(11)
C(9)-C(8)	1.185(4)	C(16)-F(9)	1.320(12)
C(11)-C(13)	1.381(5)	C(16)-F(9A)	1.326(14)

F(2)-C(4)-C(6)	118.0(3)	C(8)-C(9)-C(10)	177.5(4)
F(2)-C(4)-C(2)	120.2(3)	C(9)-C(8)-C(7)	177.1(4)
C(6)-C(4)-C(2)	121.8(3)	C(13)-C(11)-C(10)	120.8(3)
F(1)-C(3)-C(5)	118.5(3)	C(13)-C(11)-H(11)	119.6
F(1)-C(3)-C(2)	120.0(3)	C(10)-C(11)-H(11)	119.6
C(5)-C(3)-C(2)	121.5(3)	C(10)-C(12)-C(14)	121.0(3)
C(12)-C(10)-C(11)	118.1(3)	C(10)-C(12)-H(12)	119.5
C(12)-C(10)-C(9)	121.5(3)	C(14)-C(12)-H(12)	119.5
C(11)-C(10)-C(9)	120.4(3)	C(13)-C(15)-C(14)	119.8(3)
C(4)-C(2)-C(3)	116.5(3)	C(13)-C(15)-C(16)	119.8(4)
C(4)-C(2)-C(1)	123.9(3)	C(14)-C(15)-C(16)	120.4(4)
C(3)-C(2)-C(1)	119.6(3)	C(15)-C(14)-C(12)	120.1(3)
C(6)-C(7)-C(5)	116.3(3)	C(15)-C(14)-H(14)	119.9
C(6)-C(7)-C(8)	122.6(3)	C(12)-C(14)-H(14)	119.9
C(5)-C(7)-C(8)	121.2(3)	C(15)-C(13)-C(11)	120.1(3)
F(3)-C(5)-C(3)	118.7(3)	C(15)-C(13)-H(13)	119.9
F(3)-C(5)-C(7)	119.4(3)	C(11)-C(13)-H(13)	119.9
C(3)-C(5)-C(7)	121.9(3)	F(5)-C(1)-F(6)	107.4(4)
F(4)-C(6)-C(4)	118.2(3)	F(5)-C(1)-F(7)	105.8(4)
F(4)-C(6)-C(7)	119.8(3)	F(6)-C(1)-F(7)	104.1(3)
C(4)-C(6)-C(7)	122.0(3)	F(5)-C(1)-C(2)	114.5(3)

F(6)-C(1)-C(2)	112.1(3)	F(10)-C(16)-F(9A)	128.6(12)
F(7)-C(1)-C(2)	112.2(3)	F(8A)-C(16)-F(9A)	106.2(15)
F(10)-C(16)-F(10A)	70.6(13)	F(10A)-C(16)-F(9A)	104.0(15)
F(8A)-C(16)-F(10A)	104.0(15)	F(8)-C(16)-F(9A)	67.5(15)
F(10)-C(16)-F(8)	107.4(11)	F(10)-C(16)-C(15)	115.7(7)
F(8A)-C(16)-F(8)	130.8(10)	F(8A)-C(16)-C(15)	114.9(9)
F(10)-C(16)-F(9)	107.7(13)	F(10A)-C(16)-C(15)	113.8(8)
F(8A)-C(16)-F(9)	73.9(11)	F(8)-C(16)-C(15)	111.9(7)
F(10A)-C(16)-F(9)	133.3(13)	F(9)-C(16)-C(15)	108.6(7)
F(8)-C(16)-F(9)	104.9(10)	F(9A)-C(16)-C(15)	112.9(10

Symmetry transformations used to generate equivalent atoms:

Table 4. Anisotropic displacement parameters ($Å^2 x\ 10^3$) for 2-2-1. The anisotropic displacement factor exponent takes the form: $-2\pi^2[\ h^2\ a^{*2}U^{11} + ... + 2\ h\ k\ a^*\ b^*\ U^{12}\ ]$

	U^{11}	U^{22}	U^{33}	U^{23}	U^{13}	U^{12}
F(4)	93(1)	105(2)	72(1)	11(1)	25(1)	-4(1)
F(1)	95(2)	106(2)	88(1)	5(1)	37(1)	-3(1)
F(2)	86(1)	100(1)	89(1)	8(1)	21(1)	22(1)
F(3)	87(1)	100(2)	106(2)	-2(1)	14(1)	21(1)
C(4)	61(2)	72(2)	62(2)	-8(2)	5(2)	2(2)
C(3)	68(2)	76(2)	58(2)	-6(2)	13(2)	-9(2)
C(10)	71(2)	64(2)	54(2)	-7(2)	-3(2)	-1(2)
C(2)	67(2)	64(2)	56(2)	-3(2)	4(2)	-8(2)
C(7)	73(2)	60(2)	56(2)	-4(2)	-6(2)	-9(2)
C(5)	65(2)	66(2)	72(2)	-9(2)	4(2)	2(2)
C(6)	67(2)	69(2)	55(2)	1(2)	8(2)	-9(2)
C(9)	81(2)	69(2)	61(2)	-6(2)	-8(2)	-4(2)
C(8)	89(2)	67(2)	61(2)	-5(2)	-9(2)	-6(2)
C(11)	88(3)	95(3)	78(2)	10(2)	26(2)	9(2)
C(12)	73(2)	72(2)	75(2)	0(2)	12(2)	9(2)
C(15)	77(2)	70(2)	68(2)	1(2)	2(2)	5(2)
C(14)	82(2)	80(2)	73(2)	6(2)	17(2)	0(2)
C(13)	89(3)	88(3)	94(3)	4(2)	17(2)	27(2)
C(1)	114(3)	73(2)	74(3)	9(2)	17(2)	-5(2)
C(16)	117(4)	84(3)	106(4)	10(3)	-2(3)	11(3)
F(5)	186(3)	141(2)	164(3)	77(2)	73(2)	78(2)

F(6)	241(3)	115(2)	74(2)	14(1)	-19(2)	14(2)
F(7)	172(3)	104(2)	168(3)	50(2)	-2(2)	-47(2)
F(8)	200(13)	76(6)	174(8)	10(5)	49(9)	44(7)
F(10)	176(10)	116(10)	260(20)	93(12)	118(12)	35(8)
F(9)	175(17)	143(9)	164(10)	77(7)	-65(10)	-11(7)
F(8A)	290(30)	115(10)	88(7)	48(5)	14(9)	26(11)
F(9A)	127(13)	180(20)	340(30)	120(20)	14(17)	63(14)
F(10A)	380(30)	76(8)	186(19)	26(10)	-112(19)	-47(14)

Table 5. Hydrogen coordinates (x 10^4) and isotropic displacement parameters ($Å^2$x 10^3) for 2-2-1.

	x	y	z	U(eq)
H(11)	1499	7464	634	104
H(12)	7233	7029	-549	88
H(14)	6411	8343	-1185	94
H(13)	685	8778	-7	108

Tables for Structure 2-3-9

Table 1. Crystal data and structure refinement.

Identification code	2-3-9	
Empirical formula	C16 H4 F10	
Formula weight	386.19	
Temperature	40(2) K	
Wavelength	0.71073 Å	
Crystal system	Monoclinic	
Space group	P2(1)/n	
Unit cell dimensions	a = 5.4397(2) Å	α= 90°.
	b = 14.4418(4) Å	β= 92.894(2)°.
	c = 18.2014(4) Å	γ = 90°.
Volume	1428.06(7) $Å^3$	
Z	4	

Density (calculated)	1.796 Mg/m^3
Absorption coefficient	0.196 mm^{-1}
F(000)	760
Crystal size	0.15 x 0.15 x 0.10 mm^3
Theta range for data collection	2.65 to 27.48°.
Index ranges	-6<=h<=6, -16<=k<=18, -23<=l<=23
Reflections collected	7543
Independent reflections	3040 [R(int) = 0.0472]
Completeness to theta = 27.48°	93.3 %
Absorption correction	None
Refinement method	Full-matrix least-squares on F^2
Data / restraints / parameters	3040 / 0 / 251
Goodness-of-fit on F^2	1.039
Final R indices [I>2sigma(I)]	R1 = 0.0425, wR2 = 0.1125
R indices (all data)	R1 = 0.0499, wR2 = 0.1186
Largest diff. peak and hole	0.371 and -0.331 $e.Å^{-3}$

Table 2. Atomic coordinates (x 10^4) and equivalent isotropic displacement parameters ($Å^2$x 10^3) for 2-3-9. U(eq) is defined as one third of the trace of the orthogonalized U^{ij} tensor.

	x	y	z	U(eq)
F(2)	-148(2)	7018(1)	8398(1)	15(1)
F(5)	1172(2)	8055(1)	7363(1)	20(1)
F(6)	5056(2)	8026(1)	7185(1)	20(1)
F(3)	7709(2)	4792(1)	7963(1)	16(1)
F(4)	648(2)	5562(1)	9256(1)	15(1)
F(7)	2553(2)	7197(1)	6503(1)	18(1)
F(1)	6945(2)	6269(1)	7096(1)	15(1)
F(10)	9619(2)	330(1)	11354(1)	24(1)
F(9)	6844(2)	-393(1)	10692(1)	23(1)
F(8)	5896(2)	258(1)	11707(1)	22(1)
C(7)	4217(3)	5131(1)	8643(1)	13(1)
C(10)	5634(3)	2840(1)	9886(1)	13(1)
C(9)	5107(3)	3665(1)	9468(1)	14(1)
C(1)	3025(3)	7503(1)	7195(1)	14(1)

C(2)	3385(3)	6692(1)	7716(1)	12(1)
C(3)	5373(3)	6101(1)	7628(1)	12(1)
C(6)	2224(3)	5723(1)	8726(1)	13(1)
C(11)	7680(3)	2294(1)	9733(1)	15(1)
C(14)	4598(3)	1772(1)	10849(1)	13(1)
C(5)	5782(3)	5338(1)	8075(1)	13(1)
C(4)	1812(3)	6484(1)	8274(1)	13(1)
C(12)	4089(3)	2571(1)	10443(1)	14(1)
C(15)	6638(3)	1241(1)	10696(1)	14(1)
C(16)	7226(3)	365(1)	11113(1)	14(1)
C(13)	8182(3)	1495(1)	10136(1)	15(1)
C(8)	4668(3)	4344(1)	9105(1)	14(1)

Table 3. Bond lengths [Å] and angles [°] for 2-3-9.

F(2)-C(4)	1.344(2)	C(9)-C(8)	1.200(3)
F(5)-C(1)	1.333(2)	C(1)-C(2)	1.514(2)
F(6)-C(1)	1.339(2)	C(2)-C(3)	1.393(2)
F(3)-C(5)	1.336(2)	C(2)-C(4)	1.393(2)
F(4)-C(6)	1.3430(19)	C(3)-C(5)	1.382(2)
F(7)-C(1)	1.3475(19)	C(6)-C(4)	1.385(2)
F(1)-C(3)	1.3447(19)	C(11)-C(13)	1.386(2)
F(10)-C(16)	1.353(2)	C(11)-H(11)	0.92(2)
F(9)-C(16)	1.346(2)	C(14)-C(15)	1.389(3)
F(8)-C(16)	1.339(2)	C(14)-C(12)	1.391(2)
C(7)-C(6)	1.395(2)	C(14)-H(14)	0.94(3)
C(7)-C(5)	1.404(2)	C(12)-H(12)	0.96(2)
C(7)-C(8)	1.428(2)	C(15)-C(13)	1.401(2)
C(10)-C(11)	1.403(3)	C(15)-C(16)	1.502(2)
C(10)-C(12)	1.404(2)	C(13)-H(13)	0.97(2)
C(10)-C(9)	1.435(2)		

C(6)-C(7)-C(5)	116.94(15)	C(12)-C(10)-C(9)	120.06(16)
C(6)-C(7)-C(8)	122.32(16)	C(8)-C(9)-C(10)	178.54(17)
C(5)-C(7)-C(8)	120.73(16)	F(5)-C(1)-F(6)	107.43(13)
C(11)-C(10)-C(12)	119.83(15)	F(5)-C(1)-F(7)	107.50(14)
C(11)-C(10)-C(9)	120.11(16)	F(6)-C(1)-F(7)	106.87(13)

F(5)-C(1)-C(2)	113.20(14)	C(3)-C(5)-C(7)	121.21(16)
F(6)-C(1)-C(2)	111.40(14)	F(2)-C(4)-C(6)	117.45(15)
F(7)-C(1)-C(2)	110.16(13)	F(2)-C(4)-C(2)	121.39(15)
C(3)-C(2)-C(4)	117.46(15)	C(6)-C(4)-C(2)	121.15(16)
C(3)-C(2)-C(1)	118.55(15)	C(14)-C(12)-C(10)	120.19(16)
C(4)-C(2)-C(1)	123.97(15)	C(14)-C(12)-H(12)	119.4(13)
F(1)-C(3)-C(5)	118.56(15)	C(10)-C(12)-H(12)	120.4(13)
F(1)-C(3)-C(2)	119.89(15)	C(14)-C(15)-C(13)	121.02(16)
C(5)-C(3)-C(2)	121.55(16)	C(14)-C(15)-C(16)	121.03(15)
F(4)-C(6)-C(4)	118.31(15)	C(13)-C(15)-C(16)	117.93(16)
F(4)-C(6)-C(7)	120.02(15)	F(8)-C(16)-F(9)	106.97(14)
C(4)-C(6)-C(7)	121.67(16)	F(8)-C(16)-F(10)	106.56(14)
C(13)-C(11)-C(10)	119.97(16)	F(9)-C(16)-F(10)	105.83(14)
C(13)-C(11)-H(11)	122.6(14)	F(8)-C(16)-C(15)	113.28(14)
C(10)-C(11)-H(11)	117.4(14)	F(9)-C(16)-C(15)	111.95(14)
C(15)-C(14)-C(12)	119.40(16)	F(10)-C(16)-C(15)	111.79(14)
C(15)-C(14)-H(14)	119.1(16)	C(11)-C(13)-C(15)	119.59(16)
C(12)-C(14)-H(14)	121.5(15)	C(11)-C(13)-H(13)	119.4(14)
F(3)-C(5)-C(3)	119.03(15)	C(15)-C(13)-H(13)	121.0(14)
F(3)-C(5)-C(7)	119.76(15)	C(9)-C(8)-C(7)	176.95(18)

Symmetry transformations used to generate equivalent atoms:

Table 4. Anisotropic displacement parameters ($Å^2 x\ 10^3$) for 2-3-9. The anisotropic displacement factor exponent takes the form: $-2\pi^2[\ h^2\ a^{*2}U^{11} + ... + 2\ h\ k\ a^*\ b^*\ U^{12}\ ]$

	U^{11}	U^{22}	U^{33}	U^{23}	U^{13}	U^{12}
F(2)	14(1)	14(1)	19(1)	0(1)	3(1)	4(1)
F(5)	24(1)	14(1)	22(1)	4(1)	6(1)	7(1)
F(6)	23(1)	12(1)	24(1)	3(1)	2(1)	-5(1)
F(3)	16(1)	13(1)	20(1)	0(1)	3(1)	4(1)
F(4)	17(1)	15(1)	15(1)	2(1)	5(1)	-2(1)
F(7)	27(1)	14(1)	13(1)	1(1)	0(1)	2(1)
F(1)	16(1)	14(1)	16(1)	1(1)	6(1)	-1(1)
F(10)	17(1)	22(1)	32(1)	12(1)	-4(1)	0(1)
F(9)	34(1)	9(1)	24(1)	-1(1)	-1(1)	1(1)
F(8)	27(1)	18(1)	21(1)	8(1)	10(1)	4(1)

C(7)	15(1)	10(1)	13(1)	-2(1)	-1(1)	-3(1)
C(10)	16(1)	9(1)	13(1)	-1(1)	-1(1)	-2(1)
C(9)	14(1)	13(1)	14(1)	-3(1)	1(1)	-2(1)
C(1)	16(1)	10(1)	15(1)	-1(1)	3(1)	1(1)
C(2)	14(1)	8(1)	14(1)	-2(1)	0(1)	-2(1)
C(3)	14(1)	11(1)	12(1)	-2(1)	3(1)	-3(1)
C(6)	14(1)	13(1)	12(1)	-1(1)	3(1)	-4(1)
C(11)	16(1)	15(1)	15(1)	1(1)	3(1)	-2(1)
C(14)	13(1)	13(1)	14(1)	0(1)	2(1)	-2(1)
C(5)	12(1)	10(1)	17(1)	-3(1)	0(1)	0(1)
C(4)	12(1)	11(1)	15(1)	-3(1)	1(1)	0(1)
C(12)	15(1)	11(1)	15(1)	-2(1)	1(1)	0(1)
C(15)	17(1)	9(1)	14(1)	-1(1)	-1(1)	-2(1)
C(16)	15(1)	11(1)	17(1)	0(1)	2(1)	1(1)
C(13)	15(1)	13(1)	17(1)	0(1)	2(1)	2(1)
C(8)	15(1)	12(1)	14(1)	-2(1)	2(1)	0(1)

Table 5. Hydrogen coordinates (x 10^4) and isotropic displacement parameters ($Å^2$x 10^3) for 2-3-9.

	x	y	z	U(eq)
H(12)	2720(40)	2950(14)	10562(11)	13(5)
H(13)	9580(50)	1118(16)	10022(12)	24(6)
H(14)	3610(50)	1586(17)	11228(14)	29(6)
H(11)	8640(40)	2487(15)	9360(13)	22(6)

Tables for Structure 2-4-1

Table 1. Crystal data and structure refinement.

Identification code	2-4-1
Empirical formula	C16 H4 F10
Formula weight	386.00
Temperature	40(2) K

Wavelength	1.32190 Å	
Crystal system	Monoclinic	
Space group	P2(1)/n	
Unit cell dimensions	a = 5.4452(2) Å	α= 90°.
	b = 14.4926(4) Å	β= 92.9193(10)°.
	c = 18.2226(6) Å	γ = 90°.
Volume	1436.17(8) $Å^3$	
Z	4	
Density (calculated)	1.785 Mg/m^3	
Absorption coefficient	0.504 mm^{-1}	
F(000)	592	
Crystal size	5.00 x 1.72 x 1.56 mm^3	
Theta range for data collection	3.34 to 65.43°.	
Index ranges	-2<=h<=6, -18<=k<=18, -24<=l<=22	
Reflections collected	9767	
Independent reflections	3002 [R(int) = 0.0197]	
Completeness to theta = 65.43°	76.8 %	
Absorption correction	Gaussian	
Max. and min. transmission	0.939 and 0.851	
Refinement method	Full-matrix least-squares on F^2	
Data / restraints / parameters	3002 / 0 / 272	
Goodness-of-fit on F^2	1.456	
Final R indices [I>2sigma(I)]	R1 = 0.0264, wR2 = 0.0513	
R indices (all data)	R1 = 0.0282, wR2 = 0.0516	
Extinction coefficient	0.00214(7)	
Largest diff. peak and hole	0.325 and -0.358 $e.Å^{-3}$	

Table 2. Atomic coordinates (x 10^4) and equivalent isotropic displacement parameters ($Å^2$x 10^3) for 2-4-1. U(eq) is defined as one third of the trace of the orthogonalized U^{ij} tensor.

	x	y	z	U(eq)
F(3)	-143(2)	-2014(1)	8396(1)	13(1)
F(4)	656(2)	-563(1)	9255(1)	13(1)
F(1)	6941(2)	-1262(1)	7097(1)	13(1)
F(6)	1171(2)	-3047(1)	7362(1)	19(1)
F(2)	7702(2)	211(1)	7963(1)	13(1)
F(5)	5056(2)	-3019(1)	7183(1)	18(1)

F(7)	2556(2)	-2190(1)	6503(1)	16(1)
C(4)	5381(1)	-1097(1)	7624(1)	9(1)
C(7)	4217(1)	-128(1)	8643(1)	9(1)
C(10)	5629(1)	2158(1)	9886(1)	9(1)
C(6)	5784(1)	-334(1)	8075(1)	9(1)
C(3)	1809(1)	-1484(1)	8273(1)	9(1)
C(2)	3384(1)	-1690(1)	7714(1)	9(1)
C(11)	4086(1)	2424(1)	10443(1)	10(1)
C(9)	5108(1)	1338(1)	9470(1)	11(1)
C(1)	3021(1)	-2496(1)	7192(1)	11(1)
C(8)	4663(1)	652(1)	9103(1)	11(1)
C(5)	2216(1)	-721(1)	8728(1)	9(1)
C(15)	6643(1)	3758(1)	10695(1)	9(1)
C(13)	4593(1)	3226(1)	10851(1)	10(1)
C(12)	7682(1)	2704(1)	9730(1)	12(1)
C(14)	8181(1)	3505(1)	10135(1)	12(1)
C(16)	7228(1)	4634(1)	11115(1)	12(1)
F(9)	6851(2)	5386(1)	10692(1)	23(1)
F(8)	9613(2)	4665(1)	11353(1)	24(1)
F(10)	5897(2)	4738(1)	11704(1)	21(1)

Table 3. Bond lengths [Å] and angles [°] for 2-4-1.

F(3)-C(3)	1.3402(11)	C(10)-C(12)	1.4102(10)
F(4)-C(5)	1.3341(11)	C(10)-C(9)	1.4296(10)
F(1)-C(4)	1.3366(11)	C(3)-C(5)	1.3931(10)
F(6)-C(1)	1.3345(12)	C(3)-C(2)	1.3967(10)
F(2)-C(6)	1.3333(11)	C(2)-C(1)	1.5136(9)
F(5)-C(1)	1.3434(12)	C(11)-C(13)	1.3990(10)
F(7)-C(1)	1.3435(11)	C(11)-H(7)	1.0864(17)
C(4)-C(6)	1.3892(10)	C(9)-C(8)	1.2158(11)
C(4)-C(2)	1.4017(10)	C(15)-C(13)	1.3985(10)
C(7)-C(5)	1.4025(10)	C(15)-C(14)	1.4015(10)
C(7)-C(6)	1.4058(10)	C(15)-C(16)	1.5075(10)
C(7)-C(8)	1.4204(10)	C(13)-H(4)	1.0884(16)
C(10)-C(11)	1.4048(10)	C(12)-C(14)	1.3941(10)

C(12)-H(5)	1.0879(17)	F(6)-C(1)-F(5)	107.32(8)
C(14)-H(3)	1.0880(18)	F(6)-C(1)-F(7)	107.85(8)
C(16)-F(10)	1.3335(12)	F(5)-C(1)-F(7)	106.98(8)
C(16)-F(9)	1.3450(13)	F(6)-C(1)-C(2)	113.08(7)
C(16)-F(8)	1.3487(13)	F(5)-C(1)-C(2)	111.18(7)
		F(7)-C(1)-C(2)	110.18(7)
F(1)-C(4)-C(6)	118.78(7)	C(9)-C(8)-C(7)	176.83(8)
F(1)-C(4)-C(2)	119.95(7)	F(4)-C(5)-C(3)	118.49(7)
C(6)-C(4)-C(2)	121.27(6)	F(4)-C(5)-C(7)	120.07(7)
C(5)-C(7)-C(6)	117.06(6)	C(3)-C(5)-C(7)	121.44(7)
C(5)-C(7)-C(8)	122.18(7)	C(13)-C(15)-C(14)	121.03(6)
C(6)-C(7)-C(8)	120.76(7)	C(13)-C(15)-C(16)	120.79(6)
C(11)-C(10)-C(12)	120.05(6)	C(14)-C(15)-C(16)	118.16(6)
C(11)-C(10)-C(9)	120.07(7)	C(15)-C(13)-C(11)	119.29(6)
C(12)-C(10)-C(9)	119.88(7)	C(15)-C(13)-H(4)	120.51(11)
F(2)-C(6)-C(4)	118.82(7)	C(11)-C(13)-H(4)	120.21(12)
F(2)-C(6)-C(7)	119.76(7)	C(14)-C(12)-C(10)	119.75(7)
C(4)-C(6)-C(7)	121.41(7)	C(14)-C(12)-H(5)	120.35(12)
F(3)-C(3)-C(5)	117.30(7)	C(10)-C(12)-H(5)	119.90(12)
F(3)-C(3)-C(2)	121.43(7)	C(12)-C(14)-C(15)	119.73(7)
C(5)-C(3)-C(2)	121.27(7)	C(12)-C(14)-H(3)	119.60(12)
C(3)-C(2)-C(4)	117.55(6)	C(15)-C(14)-H(3)	120.67(12)
C(3)-C(2)-C(1)	123.93(6)	F(10)-C(16)-F(9)	107.19(8)
C(4)-C(2)-C(1)	118.50(6)	F(10)-C(16)-F(8)	106.93(8)
C(13)-C(11)-C(10)	120.15(7)	F(9)-C(16)-F(8)	105.89(9)
C(13)-C(11)-H(7)	120.42(11)	F(10)-C(16)-C(15)	113.23(7)
C(10)-C(11)-H(7)	119.43(11)	F(9)-C(16)-C(15)	111.66(7)
C(8)-C(9)-C(10)	178.62(8)	F(8)-C(16)-C(15)	111.51(7)

Symmetry transformations used to generate equivalent atoms:

Table 4. Anisotropic displacement parameters ($Å^2 x\ 10^3$) for 2-4-1. The anisotropic displacement factor exponent takes the form: $-2\pi^2[\ h^2\ a^{*2}U^{11} + ... + 2\ h\ k\ a^*\ b^*\ U^{12}\ ]$

	U^{11}	U^{22}	U^{33}	U^{23}	U^{13}	U^{12}
F(3)	11(1)	14(1)	13(1)	-1(1)	3(1)	-3(1)
F(4)	13(1)	14(1)	11(1)	-2(1)	4(1)	1(1)
F(1)	13(1)	13(1)	12(1)	-1(1)	4(1)	0(1)
F(6)	24(1)	15(1)	17(1)	-5(1)	7(1)	-9(1)
F(2)	12(1)	13(1)	15(1)	0(1)	2(1)	-4(1)
F(5)	20(1)	13(1)	21(1)	-4(1)	1(1)	6(1)
F(7)	23(1)	15(1)	10(1)	-1(1)	-1(1)	-2(1)
C(4)	9(1)	9(1)	9(1)	0(1)	2(1)	1(1)
C(7)	10(1)	8(1)	9(1)	-1(1)	1(1)	0(1)
C(10)	10(1)	9(1)	8(1)	-1(1)	0(1)	0(1)
C(6)	9(1)	9(1)	10(1)	0(1)	1(1)	-1(1)
C(3)	9(1)	9(1)	8(1)	0(1)	1(1)	0(1)
C(2)	9(1)	8(1)	8(1)	-1(1)	1(1)	0(1)
C(11)	10(1)	10(1)	10(1)	-1(1)	2(1)	-1(1)
C(9)	13(1)	9(1)	10(1)	-2(1)	0(1)	0(1)
C(1)	14(1)	8(1)	10(1)	-2(1)	1(1)	0(1)
C(8)	14(1)	9(1)	10(1)	-2(1)	-1(1)	0(1)
C(5)	9(1)	10(1)	8(1)	-1(1)	1(1)	1(1)
C(15)	10(1)	9(1)	10(1)	-1(1)	1(1)	0(1)
C(13)	11(1)	11(1)	10(1)	-2(1)	3(1)	0(1)
C(12)	11(1)	13(1)	12(1)	-3(1)	4(1)	-2(1)
C(14)	11(1)	13(1)	13(1)	-3(1)	4(1)	-2(1)
C(16)	13(1)	11(1)	12(1)	-3(1)	1(1)	-1(1)
F(9)	36(1)	11(1)	21(1)	0(1)	-2(1)	-3(1)
F(8)	15(1)	25(1)	30(1)	-15(1)	-5(1)	0(1)
F(10)	26(1)	18(1)	20(1)	-9(1)	10(1)	-5(1)
H(3)	27(1)	31(1)	36(1)	-7(1)	13(1)	-12(1)
H(7)	25(1)	28(1)	32(1)	-5(1)	10(1)	-11(1)
H(4)	27(1)	30(1)	27(1)	-9(1)	14(1)	-2(1)
H(5)	30(1)	36(1)	30(1)	-12(1)	16(1)	-6(1)

Table 5. Hydrogen coordinates (x 10^4) and isotropic displacement parameters ($Å^2$x 10^3) for 2-4-1.

	x	y	z	U(eq)
H(3)	9766(3)	3925(1)	10014(1)	31(1)
H(7)	2503(3)	2000(1)	10556(1)	28(1)
H(4)	3401(3)	3431(1)	11283(1)	28(1)
H(5)	8863(3)	2501(1)	9295(1)	31(1)

Tables for Structure 2-5-1

Table 1. Crystal data and structure refinement for 2-5-1.

Identification code	2-5-1	
Empirical formula	C16 H4 F10	
Formula weight	386.19	
Temperature	280(2) K	
Wavelength	0.71073 Å	
Crystal system	Triclinic	
Space group	P-1	
Unit cell dimensions	a = 8.6672(3) Å	α= 90.6140(10)°.
	b = 8.8327(3) Å	β= 96.0440(10)°.
	c = 10.2460(4) Å	γ = 105.556(2)°.
Volume	750.83(5) $Å^3$	
Z	2	
Density (calculated)	1.708 Mg/m^3	
Absorption coefficient	0.187 mm^{-1}	
F(000)	380	
Crystal size	0.20 x 0.15 x 0.12 mm^3	
Theta range for data collection	2.40 to 27.01°.	
Index ranges	-11<=h<=11, -11<=k<=11, -13<=l<=13	
Reflections collected	8367	
Independent reflections	3274 [R(int) = 0.0486]	
Completeness to theta = 27.01°	99.9 %	
Absorption correction	None	

Refinement method	Full-matrix least-squares on F^2
Data / restraints / parameters	3274 / 6 / 279
Goodness-of-fit on F^2	1.055
Final R indices [I>2sigma(I)]	R1 = 0.0557, wR2 = 0.1746
R indices (all data)	R1 = 0.0902, wR2 = 0.1994
Largest diff. peak and hole	0.529 and -0.224 e.$Å^{-3}$

Table 2. Atomic coordinates (x 10^4) and equivalent isotropic displacement parameters ($Å^2$x 10^3) for 2-5-1. U(eq) is defined as one third of the trace of the orthogonalized U^{ij} tensor.

	x	y	z	U(eq)
F(3)	3938(2)	4424(2)	5959(2)	98(1)
F(2)	-620(2)	1329(2)	2137(2)	109(1)
F(4)	926(2)	-252(2)	3705(2)	98(1)
C(7)	2502(3)	2035(3)	4864(2)	65(1)
F(1)	2414(3)	6047(2)	4373(2)	111(1)
C(2)	852(3)	3743(3)	3178(2)	71(1)
C(5)	2833(3)	3650(3)	4991(2)	71(1)
C(4)	513(3)	2151(3)	3055(2)	73(1)
C(8)	3353(3)	1190(3)	5712(2)	72(1)
C(6)	1316(3)	1304(3)	3869(2)	68(1)
C(3)	2035(3)	4493(3)	4180(2)	75(1)
C(10)	4915(3)	-265(3)	7362(2)	64(1)
C(12)	4519(3)	-1881(3)	7350(3)	76(1)
C(9)	4073(3)	525(3)	6444(2)	70(1)
C(14)	5285(3)	-2656(3)	8255(3)	77(1)
C(11)	6112(3)	585(3)	8300(3)	82(1)
C(15)	6467(3)	-1794(3)	9186(2)	70(1)
C(1)	27(4)	4737(4)	2330(3)	88(1)
C(13)	6892(3)	-191(4)	9206(3)	84(1)
C(16)	7281(4)	-2634(4)	10189(3)	90(1)
F(10)	6240(15)	-3247(15)	11074(12)	127(3)
F(8)	7550(30)	-3840(20)	9689(13)	164(7)
F(9)	8520(30)	-1752(11)	10910(20)	174(7)
F(8A)	6920(30)	-2520(30)	11331(8)	147(6)
F(9A)	7040(20)	-4127(12)	9938(16)	141(5)
F(10A)	8853(10)	-2150(20)	10203(18)	146(5)

F(5)	1023(2)	5812(2)	1765(2)	123(1)
F(7)	-961(3)	3904(3)	1339(2)	137(1)
F(6)	-877(3)	5340(4)	2967(2)	166(1)

Table 3. Bond lengths [Å] and angles [°] for 2-5-1.

F(3)-C(5)	1.343(3)	C(12)-H(2)	0.90(3)
F(2)-C(4)	1.336(3)	C(14)-C(15)	1.379(4)
F(4)-C(6)	1.329(3)	C(14)-H(4)	0.93(3)
C(7)-C(5)	1.379(3)	C(11)-C(13)	1.385(4)
C(7)-C(6)	1.386(3)	C(11)-H(1)	0.87(3)
C(7)-C(8)	1.425(3)	C(15)-C(13)	1.364(4)
F(1)-C(3)	1.330(3)	C(15)-C(16)	1.500(3)
C(2)-C(4)	1.359(4)	C(1)-F(6)	1.283(3)
C(2)-C(3)	1.394(4)	C(1)-F(5)	1.288(3)
C(2)-C(1)	1.503(3)	C(1)-F(7)	1.330(4)
C(5)-C(3)	1.375(3)	C(13)-H(3)	0.95(3)
C(4)-C(6)	1.382(3)	C(16)-F(8A)	1.252(7)
C(8)-C(9)	1.185(3)	C(16)-F(8)	1.264(10)
C(10)-C(12)	1.376(3)	C(16)-F(9A)	1.297(10)
C(10)-C(11)	1.386(4)	C(16)-F(9)	1.298(8)
C(10)-C(9)	1.430(3)	C(16)-F(10A)	1.313(9)
C(12)-C(14)	1.377(3)	C(16)-F(10)	1.360(9)

C(5)-C(7)-C(6)	116.2(2)	C(9)-C(8)-C(7)	178.1(3)
C(5)-C(7)-C(8)	121.0(2)	F(4)-C(6)-C(4)	119.2(2)
C(6)-C(7)-C(8)	122.8(2)	F(4)-C(6)-C(7)	119.2(2)
C(4)-C(2)-C(3)	117.0(2)	C(4)-C(6)-C(7)	121.7(2)
C(4)-C(2)-C(1)	124.7(3)	F(1)-C(3)-C(5)	118.5(2)
C(3)-C(2)-C(1)	118.2(3)	F(1)-C(3)-C(2)	120.4(2)
F(3)-C(5)-C(3)	118.7(2)	C(5)-C(3)-C(2)	121.0(2)
F(3)-C(5)-C(7)	119.1(2)	C(12)-C(10)-C(11)	118.9(2)
C(3)-C(5)-C(7)	122.1(2)	C(12)-C(10)-C(9)	120.5(2)
F(2)-C(4)-C(2)	121.3(2)	C(11)-C(10)-C(9)	120.5(2)
F(2)-C(4)-C(6)	116.8(2)	C(10)-C(12)-C(14)	121.1(3)
C(2)-C(4)-C(6)	121.9(2)	C(10)-C(12)-H(2)	121.0(18)

C(14)-C(12)-H(2)	118.0(19)	C(11)-C(13)-H(3)	117(2)
C(8)-C(9)-C(10)	178.1(2)	F(8A)-C(16)-F(8)	125.0(8)
C(12)-C(14)-C(15)	119.3(3)	F(8A)-C(16)-F(9A)	105.8(9)
C(12)-C(14)-H(4)	119.6(16)	F(8A)-C(16)-F(9)	71.3(6)
C(15)-C(14)-H(4)	120.9(16)	F(8)-C(16)-F(9)	113.3(10)
C(13)-C(11)-C(10)	120.1(3)	F(9A)-C(16)-F(9)	124.7(8)
C(13)-C(11)-H(1)	123.1(18)	F(8A)-C(16)-F(10A)	109.2(7)
C(10)-C(11)-H(1)	116.6(18)	F(8)-C(16)-F(10A)	79.9(9)
C(13)-C(15)-C(14)	120.6(2)	F(9A)-C(16)-F(10A)	100.3(8)
C(13)-C(15)-C(16)	120.0(3)	F(8)-C(16)-F(10)	102.8(9)
C(14)-C(15)-C(16)	119.4(3)	F(9A)-C(16)-F(10)	79.4(8)
F(6)-C(1)-F(5)	110.6(3)	F(9)-C(16)-F(10)	103.7(9)
F(6)-C(1)-F(7)	104.6(3)	F(10A)-C(16)-F(10)	135.8(5)
F(5)-C(1)-F(7)	104.0(2)	F(8A)-C(16)-C(15)	114.5(4)
F(6)-C(1)-C(2)	112.0(2)	F(8)-C(16)-C(15)	111.5(7)
F(5)-C(1)-C(2)	112.7(2)	F(9A)-C(16)-C(15)	115.2(6)
F(7)-C(1)-C(2)	112.3(3)	F(9)-C(16)-C(15)	115.4(4)
C(15)-C(13)-C(11)	120.0(2)	F(10A)-C(16)-C(15)	110.7(5)
C(15)-C(13)-H(3)	122.4(19)	F(10)-C(16)-C(15)	109.0(5)

Symmetry transformations used to generate equivalent atoms:

Table 4. Anisotropic displacement parameters ($Å^2 x\ 10^3$) for 2-5-1. The anisotropic displacement factor exponent takes the form: $-2\pi^2[\ h^2\ a^{*2}U^{11} + ... + 2\ h\ k\ a^*\ b^*\ U^{12}\ ]$

	U^{11}	U^{22}	U^{33}	U^{23}	U^{13}	U^{12}
F(3)	117(1)	98(1)	72(1)	-8(1)	-22(1)	30(1)
F(2)	98(1)	119(1)	89(1)	6(1)	-30(1)	11(1)
F(4)	117(1)	74(1)	97(1)	8(1)	-3(1)	19(1)
C(7)	69(1)	77(2)	55(1)	12(1)	10(1)	30(1)
F(1)	158(2)	77(1)	102(1)	3(1)	-10(1)	48(1)
C(2)	71(1)	94(2)	56(1)	17(1)	10(1)	34(1)
C(5)	80(2)	78(2)	56(1)	3(1)	-2(1)	27(1)
C(4)	66(1)	90(2)	58(1)	12(1)	-1(1)	18(1)
C(8)	80(2)	84(2)	59(1)	13(1)	11(1)	33(1)
C(6)	74(1)	71(2)	61(1)	8(1)	10(1)	19(1)

C(3)	92(2)	71(2)	67(1)	6(1)	6(1)	33(1)
C(10)	69(1)	74(2)	56(1)	12(1)	8(1)	28(1)
C(12)	84(2)	73(2)	67(1)	1(1)	-13(1)	20(1)
C(9)	76(1)	78(2)	61(1)	11(1)	6(1)	30(1)
C(14)	93(2)	65(2)	73(2)	6(1)	-3(1)	25(1)
C(11)	92(2)	62(2)	88(2)	11(1)	-9(2)	20(1)
C(15)	77(2)	80(2)	60(1)	11(1)	4(1)	34(1)
C(1)	93(2)	112(2)	73(2)	26(2)	11(2)	47(2)
C(13)	83(2)	82(2)	81(2)	1(1)	-19(1)	20(1)
C(16)	108(2)	100(2)	73(2)	20(2)	0(2)	51(2)
F(10)	167(6)	137(5)	87(5)	48(4)	3(4)	58(5)
F(8)	269(14)	212(14)	94(4)	31(6)	32(7)	202(13)
F(9)	189(11)	134(5)	163(11)	28(6)	-112(9)	30(6)
F(8A)	207(11)	240(14)	55(3)	27(6)	22(6)	161(11)
F(9A)	195(8)	102(5)	130(9)	18(5)	-42(7)	68(5)
F(10A)	88(4)	219(11)	142(8)	70(7)	-7(4)	68(5)
F(5)	129(2)	124(2)	123(2)	63(1)	15(1)	46(1)
F(7)	139(2)	159(2)	113(2)	33(1)	-35(1)	58(1)
F(6)	209(2)	251(3)	119(2)	68(2)	58(2)	183(2)

Table 5. Hydrogen coordinates (x 10^4) and isotropic displacement parameters ($Å^2$x 10^3) for 2-5-1.

	x	y	z	U(eq)
H(4)	4930(30)	-3740(30)	8280(20)	82(8)
H(1)	6380(30)	1610(40)	8240(30)	86(8)
H(2)	3750(40)	-2470(30)	6740(30)	101(9)
H(3)	7580(40)	430(40)	9910(30)	104(9)

Tables for Structure 3-1-1

Table 1. Crystal data and structure refinement.

Identification code	3-1-1	
Empirical formula	C12 H11 F3 O	
Formula weight	228.21	
Temperature	100(2) K	
Wavelength	0.71073 Å	
Crystal system	Orthorhombic	
Space group	Pbca	
Unit cell dimensions	a = 16.4745(6) Å	α= 90°.
	b = 5.6043(2) Å	β= 90°.
	c = 23.3685(9) Å	γ = 90°.
Volume	2157.57(14) $Å^3$	
Z	8	
Density (calculated)	1.405 Mg/m^3	
Absorption coefficient	0.123 mm^{-1}	
F(000)	944	
Crystal size	0.30 x 0.14 x 0.10 mm^3	
Theta range for data collection	1.74 to 26.98°.	
Index ranges	-21<=h<=21, -7<=k<=7, -29<=l<=28	
Reflections collected	13899	
Independent reflections	2346 [R(int) = 0.1032]	
Completeness to theta = 26.98°	100.0 %	
Absorption correction	None	
Refinement method	Full-matrix least-squares on F^2	
Data / restraints / parameters	2346 / 0 / 189	
Goodness-of-fit on F^2	1.025	
Final R indices [I>2sigma(I)]	R1 = 0.0407, wR2 = 0.1014	
R indices (all data)	R1 = 0.0644, wR2 = 0.1124	
Largest diff. peak and hole	0.294 and -0.284 $e.Å^{-3}$	

Table 2. Atomic coordinates (x 10^4) and equivalent isotropic displacement parameters ($Å^2$x 10^3) for 3-1-1. U(eq) is defined as one third of the trace of the orthogonalized U^{ij} tensor.

	x	y	z	U(eq)
F(2)	4321(1)	10523(2)	6233(1)	38(1)
F(1)	3029(1)	10485(2)	6262(1)	46(1)

C(9)	3776(1)	2695(2)	8832(1)	19(1)
C(5)	3794(1)	5241(3)	7884(1)	19(1)
C(8)	3799(1)	3872(3)	8404(1)	20(1)
F(3)	3670(1)	7641(2)	5851(1)	48(1)
C(4)	4203(1)	4412(3)	7400(1)	23(1)
C(10)	3680(1)	1220(3)	9353(1)	19(1)
C(3)	4161(1)	5664(3)	6890(1)	23(1)
C(1)	3677(1)	9094(3)	6304(1)	25(1)
C(2)	3715(1)	7749(3)	6859(1)	21(1)
C(6)	3357(1)	7374(3)	7852(1)	22(1)
C(7)	3317(1)	8620(3)	7340(1)	23(1)
O(1)	2877(1)	188(2)	9337(1)	28(1)
C(11)	3781(1)	2712(3)	9894(1)	25(1)
C(12)	4266(1)	-864(3)	9351(1)	23(1)

Table 3. Bond lengths [Å] and angles [°] for 3-1-1.

F(2)-C(1)	1.3403(19)	C(3)-H(1)	0.972(17)
F(1)-C(1)	1.3250(18)	C(1)-C(2)	1.501(2)
C(9)-C(8)	1.198(2)	C(2)-C(7)	1.389(2)
C(9)-C(10)	1.480(2)	C(6)-C(7)	1.386(2)
C(5)-C(4)	1.396(2)	C(6)-H(3)	0.947(17)
C(5)-C(6)	1.398(2)	C(7)-H(4)	0.941(17)
C(5)-C(8)	1.438(2)	O(1)-H(8)	0.87(2)
F(3)-C(1)	1.3357(18)	C(11)-H(6)	0.964(17)
C(4)-C(3)	1.384(2)	C(11)-H(5)	1.006(19)
C(4)-H(2)	0.947(17)	C(11)-H(7)	0.99(2)
C(10)-O(1)	1.4435(17)	C(12)-H(10)	0.940(19)
C(10)-C(12)	1.516(2)	C(12)-H(9)	0.975(19)
C(10)-C(11)	1.524(2)	C(12)-H(11)	0.992(17)
C(3)-C(2)	1.383(2)		

C(8)-C(9)-C(10)	175.54(15)	C(3)-C(4)-C(5)	120.32(14)
C(4)-C(5)-C(6)	119.29(13)	C(3)-C(4)-H(2)	120.8(10)
C(4)-C(5)-C(8)	120.36(13)	C(5)-C(4)-H(2)	118.9(10)
C(6)-C(5)-C(8)	120.32(13)	O(1)-C(10)-C(9)	107.51(11)
C(9)-C(8)-C(5)	177.61(16)	O(1)-C(10)-C(12)	105.94(12)

C(9)-C(10)-C(12)	111.06(12)	C(5)-C(6)-H(3)	119.6(10)
O(1)-C(10)-C(11)	110.02(12)	C(6)-C(7)-C(2)	119.86(14)
C(9)-C(10)-C(11)	111.30(13)	C(6)-C(7)-H(4)	120.3(10)
C(12)-C(10)-C(11)	110.82(12)	C(2)-C(7)-H(4)	119.8(10)
C(2)-C(3)-C(4)	119.96(14)	C(10)-O(1)-H(8)	108.7(16)
C(2)-C(3)-H(1)	121.6(10)	C(10)-C(11)-H(6)	109.7(10)
C(4)-C(3)-H(1)	118.5(10)	C(10)-C(11)-H(5)	111.9(11)
F(1)-C(1)-F(3)	106.99(13)	H(6)-C(11)-H(5)	107.3(14)
F(1)-C(1)-F(2)	106.09(13)	C(10)-C(11)-H(7)	113.8(11)
F(3)-C(1)-F(2)	105.76(12)	H(6)-C(11)-H(7)	107.5(15)
F(1)-C(1)-C(2)	113.21(13)	H(5)-C(11)-H(7)	106.4(16)
F(3)-C(1)-C(2)	112.27(13)	C(10)-C(12)-H(10)	112.0(11)
F(2)-C(1)-C(2)	112.00(13)	C(10)-C(12)-H(9)	108.7(10)
C(3)-C(2)-C(7)	120.40(14)	H(10)-C(12)-H(9)	107.8(15)
C(3)-C(2)-C(1)	119.44(13)	C(10)-C(12)-H(11)	110.5(10)
C(7)-C(2)-C(1)	120.15(14)	H(10)-C(12)-H(11)	108.4(14)
C(7)-C(6)-C(5)	120.15(14)	H(9)-C(12)-H(11)	109.4(14)
C(7)-C(6)-H(3)	120.2(10)		

Symmetry transformations used to generate equivalent atoms:

Table 4. Anisotropic displacement parameters ($Å^2 x\ 10^3$) for 3-1-1. The anisotropic displacement factor exponent takes the form: $-2\pi^2[\ h^2\ a^{*2}U^{11} + ... + 2\ h\ k\ a^*\ b^*\ U^{12}\ ]$

	U^{11}	U^{22}	U^{33}	U^{23}	U^{13}	U^{12}
F(2)	39(1)	41(1)	35(1)	17(1)	1(1)	-11(1)
F(1)	39(1)	66(1)	34(1)	25(1)	5(1)	21(1)
C(9)	18(1)	20(1)	19(1)	-1(1)	-1(1)	-1(1)
C(5)	20(1)	22(1)	17(1)	1(1)	-1(1)	-4(1)
C(8)	20(1)	21(1)	20(1)	-1(1)	0(1)	-1(1)
F(3)	90(1)	36(1)	18(1)	1(1)	-4(1)	-3(1)
C(4)	24(1)	21(1)	24(1)	2(1)	2(1)	3(1)
C(10)	17(1)	23(1)	16(1)	2(1)	-1(1)	-3(1)
C(3)	26(1)	24(1)	20(1)	-1(1)	5(1)	0(1)
C(1)	28(1)	27(1)	21(1)	3(1)	3(1)	2(1)
C(2)	23(1)	23(1)	18(1)	2(1)	-1(1)	-4(1)

C(6)	22(1)	25(1)	19(1)	-1(1)	3(1)	0(1)
C(7)	24(1)	21(1)	24(1)	2(1)	0(1)	2(1)
O(1)	19(1)	34(1)	30(1)	9(1)	-2(1)	-6(1)
C(11)	32(1)	26(1)	18(1)	0(1)	-3(1)	6(1)
C(12)	26(1)	23(1)	21(1)	1(1)	-2(1)	1(1)

Table 5. Hydrogen coordinates (x 10^4) and isotropic displacement parameters ($Å^2$x 10^3) for 3-1-1.

	x	y	z	U(eq)
H(6)	3716(9)	1710(30)	10226(7)	22(4)
H(4)	3010(10)	10030(30)	7314(7)	25(4)
H(10)	4211(11)	-1810(30)	9021(8)	35(5)
H(9)	4152(10)	-1870(30)	9682(8)	33(5)
H(3)	3068(10)	7920(30)	8176(7)	27(4)
H(2)	4509(10)	2990(30)	7427(7)	28(4)
H(5)	4337(12)	3460(30)	9917(8)	41(5)
H(11)	4834(11)	-290(30)	9372(7)	25(4)
H(1)	4456(10)	5050(30)	6561(7)	29(4)
H(7)	3386(11)	4040(40)	9926(8)	44(5)
H(8)	2521(16)	1330(40)	9349(9)	64(7)

Tables for Structure 4-1-1

Table 1. Crystal data and structure refinement.

Identification code	4-1-1
Empirical formula	C15 H5 F7
Formula weight	318.19
Temperature	100(2) K
Wavelength	0.71073 Å
Crystal system	Monoclinic
Space group	P2(1)/n

Unit cell dimensions	a = 5.9112(2) Å	α= 90°.
	b = 28.4121(10) Å	β= 92.490(2)°.
	c = 7.4618(3) Å	γ = 90°.
Volume	1252.02(8) $Å^3$	
Z	4	
Density (calculated)	1.688 Mg/m^3	
Absorption coefficient	0.171 mm^{-1}	
F(000)	632	
Crystal size	0.24 x 0.18 x 0.05 mm^3	
Theta range for data collection	1.43 to 27.00°.	
Index ranges	-7<=h<=7, -33<=k<=36, -9<=l<=9	
Reflections collected	9419	
Independent reflections	2744 [R(int) = 0.0587]	
Completeness to theta = 27.00°	100.0 %	
Absorption correction	None	
Refinement method	Full-matrix least-squares on F^2	
Data / restraints / parameters	2744 / 0 / 219	
Goodness-of-fit on F^2	0.984	
Final R indices [I>2sigma(I)]	R1 = 0.0487, wR2 = 0.1256	
R indices (all data)	R1 = 0.0853, wR2 = 0.1416	
Largest diff. peak and hole	0.503 and -0.410 e.$Å^{-3}$	

Table 2. Atomic coordinates (x 10^4) and equivalent isotropic displacement parameters ($Å^2$x 10^3) for 4-1-1. U(eq) is defined as one third of the trace of the orthogonalized U^{ij} tensor.

	x	y	z	U(eq)
F(3)	869(2)	510(1)	5812(2)	28(1)
F(4)	-157(2)	1411(1)	5457(2)	28(1)
F(1)	6928(2)	1819(1)	8253(2)	30(1)
F(2)	7921(2)	910(1)	8614(2)	27(1)
F(7)	1123(3)	2258(1)	5531(3)	57(1)
F(5)	2392(4)	2350(1)	8194(2)	63(1)
C(10)	5754(4)	-713(1)	7815(3)	20(1)
F(6)	4581(3)	2403(1)	6036(3)	65(1)
C(7)	1866(4)	1299(1)	6218(3)	21(1)
C(1)	2851(4)	2166(1)	6630(3)	26(1)
C(5)	4430(4)	679(1)	7215(3)	20(1)

C(8)	4957(4)	193(1)	7441(3)	23(1)
C(3)	5408(4)	1504(1)	7624(3)	21(1)
C(4)	5923(4)	1031(1)	7816(3)	20(1)
C(14)	4429(4)	-1510(1)	7423(3)	24(1)
C(2)	3373(4)	1647(1)	6807(3)	20(1)
C(6)	2386(4)	829(1)	6414(3)	21(1)
C(13)	6486(4)	-1678(1)	8128(3)	25(1)
C(15)	4056(4)	-1031(1)	7258(3)	22(1)
C(9)	5355(4)	-216(1)	7625(3)	22(1)
C(12)	8173(4)	-1364(1)	8682(4)	25(1)
C(11)	7827(4)	-884(1)	8528(3)	23(1)

Table 3. Bond lengths [Å] and angles [°] for 4-1-1.

F(3)-C(6)	1.338(3)	C(5)-C(4)	1.395(3)
F(4)-C(7)	1.340(3)	C(5)-C(8)	1.425(3)
F(1)-C(3)	1.339(3)	C(8)-C(9)	1.191(3)
F(2)-C(4)	1.344(3)	C(3)-C(4)	1.384(3)
F(7)-C(1)	1.308(3)	C(3)-C(2)	1.385(3)
F(5)-C(1)	1.318(3)	C(14)-C(15)	1.383(3)
C(10)-C(15)	1.400(3)	C(14)-C(13)	1.388(3)
C(10)-C(11)	1.401(3)	C(14)-H(4)	0.90(3)
C(10)-C(9)	1.439(3)	C(13)-C(12)	1.386(3)
F(6)-C(1)	1.318(3)	C(13)-H(3)	0.98(2)
C(7)-C(6)	1.377(3)	C(15)-H(5)	0.98(3)
C(7)-C(2)	1.388(3)	C(12)-C(11)	1.383(3)
C(1)-C(2)	1.512(3)	C(12)-H(2)	0.93(3)
C(5)-C(6)	1.391(3)	C(11)-H(1)	0.91(3)

C(15)-C(10)-C(11)	119.5(2)	F(6)-C(1)-F(5)	106.7(2)
C(15)-C(10)-C(9)	119.5(2)	F(7)-C(1)-C(2)	113.6(2)
C(11)-C(10)-C(9)	121.0(2)	F(6)-C(1)-C(2)	111.7(2)
F(4)-C(7)-C(6)	117.8(2)	F(5)-C(1)-C(2)	111.0(2)
F(4)-C(7)-C(2)	120.9(2)	C(6)-C(5)-C(4)	116.4(2)
C(6)-C(7)-C(2)	121.3(2)	C(6)-C(5)-C(8)	121.9(2)
F(7)-C(1)-F(6)	106.4(2)	C(4)-C(5)-C(8)	121.7(2)
F(7)-C(1)-F(5)	106.9(2)	C(9)-C(8)-C(5)	178.7(3)

F(1)-C(3)-C(4)	118.1(2)	C(7)-C(6)-C(5)	121.9(2)
F(1)-C(3)-C(2)	121.0(2)	C(12)-C(13)-C(14)	120.0(2)
C(4)-C(3)-C(2)	120.8(2)	C(12)-C(13)-H(3)	121.6(14)
F(2)-C(4)-C(3)	118.6(2)	C(14)-C(13)-H(3)	118.3(14)
F(2)-C(4)-C(5)	119.4(2)	C(14)-C(15)-C(10)	119.9(2)
C(3)-C(4)-C(5)	122.0(2)	C(14)-C(15)-H(5)	121.3(16)
C(15)-C(14)-C(13)	120.3(2)	C(10)-C(15)-H(5)	118.8(16)
C(15)-C(14)-H(4)	118.6(17)	C(8)-C(9)-C(10)	177.8(3)
C(13)-C(14)-H(4)	121.1(17)	C(11)-C(12)-C(13)	120.4(2)
C(3)-C(2)-C(7)	117.6(2)	C(11)-C(12)-H(2)	121.3(16)
C(3)-C(2)-C(1)	119.6(2)	C(13)-C(12)-H(2)	118.2(16)
C(7)-C(2)-C(1)	122.7(2)	C(12)-C(11)-C(10)	119.8(2)
F(3)-C(6)-C(7)	118.5(2)	C(12)-C(11)-H(1)	115.9(17)
F(3)-C(6)-C(5)	119.6(2)	C(10)-C(11)-H(1)	124.3(17)

Symmetry transformations used to generate equivalent atoms:

Table 4. Anisotropic displacement parameters ($Å^2 x\ 10^3$) for 4-1-1. The anisotropic displacement factor exponent takes the form: $-2\pi^2[\ h^2\ a^{*2}U^{11} + ... + 2\ h\ k\ a^*\ b^*\ U^{12}\ ]$

	U^{11}	U^{22}	U^{33}	U^{23}	U^{13}	U^{12}
F(3)	25(1)	27(1)	32(1)	-4(1)	-4(1)	-6(1)
F(4)	21(1)	33(1)	29(1)	2(1)	-5(1)	4(1)
F(1)	29(1)	27(1)	33(1)	-5(1)	-3(1)	-8(1)
F(2)	21(1)	33(1)	27(1)	-1(1)	-6(1)	3(1)
F(7)	69(1)	29(1)	70(1)	3(1)	-37(1)	11(1)
F(5)	121(2)	31(1)	37(1)	-2(1)	18(1)	24(1)
C(10)	23(1)	20(1)	17(1)	0(1)	2(1)	0(1)
F(6)	48(1)	30(1)	119(2)	25(1)	25(1)	-2(1)
C(7)	17(1)	27(1)	19(1)	1(1)	1(1)	3(1)
C(1)	27(1)	23(1)	27(1)	1(1)	1(1)	1(1)
C(5)	20(1)	22(1)	18(1)	0(1)	2(1)	3(1)
C(8)	21(1)	26(1)	21(1)	-1(1)	2(1)	1(1)
C(3)	22(1)	25(1)	17(1)	-2(1)	-1(1)	-5(1)
C(4)	16(1)	27(1)	18(1)	0(1)	-1(1)	1(1)
C(14)	24(1)	24(1)	26(1)	-1(1)	-1(1)	-4(1)

C(2)	21(1)	21(1)	19(1)	-1(1)	2(1)	2(1)
C(6)	19(1)	23(1)	19(1)	-2(1)	0(1)	-5(1)
C(13)	29(1)	22(1)	24(1)	1(1)	2(1)	2(1)
C(15)	20(1)	25(1)	20(1)	-1(1)	0(1)	0(1)
C(9)	22(1)	26(1)	19(1)	-1(1)	0(1)	-1(1)
C(12)	22(1)	29(1)	26(1)	3(1)	0(1)	6(1)
C(11)	21(1)	25(1)	23(1)	0(1)	0(1)	-2(1)

Table 5. Hydrogen coordinates (x 10^4) and isotropic displacement parameters ($Å^2$x 10^3) for 4-1-1.

	x	y	z	U(eq)
H(4)	3310(40)	-1710(10)	7060(40)	29(7)
H(2)	9520(50)	-1486(9)	9170(40)	27(7)
H(1)	9010(50)	-698(10)	8910(40)	35(8)
H(5)	2620(50)	-908(10)	6760(40)	38(8)
H(3)	6670(40)	-2020(9)	8290(30)	20(6)

Tables for Structure 5-2-1

Table 1. Crystal data and structure refinement for 5-2-1.

Identification code	5-2-1	
Empirical formula	C10 H16 O14 Zn	
Formula weight	425.60	
Temperature	100(2) K	
Wavelength	0.71073 Å	
Crystal system	Monoclinic	
Space group	C2/c	
Unit cell dimensions	a = 21.8921(10) Å	α= 90°.
	b = 9.7652(4) Å	β= 104.9130(10)°.
	c = 7.1819(3) Å	γ = 90°.
Volume	1483.64(11) $Å^3$	
Z	4	

Density (calculated)	1.905 Mg/m^3
Absorption coefficient	1.736 mm^{-1}
F(000)	872
Crystal size	0.32 x 0.20 x 0.16 mm^3
Theta range for data collection	1.93 to 27.00°.
Index ranges	-26<=h<=27, -8<=k<=12, -9<=l<=9
Reflections collected	4368
Independent reflections	1610 [R(int) = 0.0141]
Completeness to theta = 27.00°	99.0 %
Absorption correction	Semi-empirical from equivalents
Max. and min. transmission	0.76 and 0.691
Refinement method	Full-matrix least-squares on F^2
Data / restraints / parameters	1610 / 0 / 148
Goodness-of-fit on F^2	1.074
Final R indices [I>2sigma(I)]	R1 = 0.0176, wR2 = 0.0493
R indices (all data)	R1 = 0.0180, wR2 = 0.0497
Extinction coefficient	0.0069(4)
Largest diff. peak and hole	0.383 and -0.273 $e.Å^{-3}$

Table 2. Atomic coordinates (x 10^4) and equivalent isotropic displacement parameters ($Å^2$x 10^3) for 5-2-1. U(eq) is defined as one third of the trace of the orthogonalized U^{ij} tensor.

	x	y	z	U(eq)
Zn(1)	0	2995(1)	2500	9(1)
O(1)	0	5152(1)	2500	14(1)
O(2)	0	898(1)	2500	16(1)
O(3)	803(1)	2891(1)	4778(1)	13(1)
O(4)	575(1)	3137(1)	553(1)	11(1)
C(1)	1879(1)	7317(1)	4071(2)	10(1)
C(2)	2291(1)	6214(1)	4173(2)	10(1)
C(21)	1974(1)	4912(1)	3256(2)	10(1)
O(211)	2221(1)	3739(1)	3837(1)	13(1)
O(212)	1469(1)	4998(1)	2007(1)	13(1)
C(3)	2933(1)	6402(1)	5126(2)	10(1)
C(31)	3462(1)	5349(1)	5416(2)	11(1)
O(311)	3321(1)	4083(1)	5482(1)	17(1)
O(312)	4012(1)	5759(1)	5654(1)	14(1)

Table 3. Bond lengths [Å] and angles [°] for 5-2-1.

Zn(1)-O(2)	2.0482(13)	C(1)-C(3)#2	1.3942(17)
Zn(1)-O(3)#1	2.0733(10)	C(1)-C(2)	1.3946(17)
Zn(1)-O(3)	2.0733(10)	C(1)-H(1)	0.904(16)
Zn(1)-O(1)	2.1057(13)	C(2)-C(3)	1.4078(17)
Zn(1)-O(4)	2.1129(9)	C(2)-C(21)	1.5156(16)
Zn(1)-O(4)#1	2.1129(9)	C(21)-O(212)	1.2352(15)
O(1)-H(11)	0.842(18)	C(21)-O(211)	1.2894(14)
O(2)-H(21)	0.765(18)	O(211)-H(211)	1.04(3)
O(3)-H(31)	0.75(2)	C(3)-C(1)#2	1.3942(17)
O(3)-H(32)	0.84(2)	C(3)-C(31)	1.5221(16)
O(4)-H(41)	0.80(2)	C(31)-O(312)	1.2375(15)
O(4)-H(42)	0.86(2)	C(31)-O(311)	1.2789(1
O(2)-Zn(1)-O(3)#1	87.17(3)	Zn(1)-O(4)-H(41)	112.4(15)
O(2)-Zn(1)-O(3)	87.17(3)	Zn(1)-O(4)-H(42)	108.7(12)
O(3)#1-Zn(1)-O(3)	174.34(5)	H(41)-O(4)-H(42)	107(2)
O(2)-Zn(1)-O(1)	180.0	C(3)#2-C(1)-C(2)	123.62(12)
O(3)#1-Zn(1)-O(1)	92.83(3)	C(3)#2-C(1)-H(1)	118.1(9)
O(3)-Zn(1)-O(1)	92.83(3)	C(2)-C(1)-H(1)	118.3(9)
O(2)-Zn(1)-O(4)	93.75(2)	C(1)-C(2)-C(3)	118.43(11)
O(3)#1-Zn(1)-O(4)	90.56(4)	C(1)-C(2)-C(21)	114.01(11)
O(3)-Zn(1)-O(4)	89.81(4)	C(3)-C(2)-C(21)	127.54(10)
O(1)-Zn(1)-O(4)	86.25(2)	O(212)-C(21)-O(211)	121.17(11)
O(2)-Zn(1)-O(4)#1	93.75(2)	O(212)-C(21)-C(2)	118.94(10)
O(3)#1-Zn(1)-O(4)#1	89.81(4)	O(211)-C(21)-C(2)	119.84(10)
O(3)-Zn(1)-O(4)#1	90.56(4)	C(21)-O(211)-H(211)	110.0(14)
O(1)-Zn(1)-O(4)#1	86.25(2)	C(1)#2-C(3)-C(2)	117.95(11)
O(4)-Zn(1)-O(4)#1	172.51(5)	C(1)#2-C(3)-C(31)	114.65(11)
Zn(1)-O(1)-H(11)	126.4(13)	C(2)-C(3)-C(31)	127.39(11)
Zn(1)-O(2)-H(21)	124.0(15)	O(312)-C(31)-O(311)	122.93(11)
Zn(1)-O(3)-H(31)	116.4(16)	O(312)-C(31)-C(3)	118.60(10)
Zn(1)-O(3)-H(32)	125.6(14)	O(311)-C(31)-C(3)	118.41(10)
H(31)-O(3)-H(32)	107(2)	C(31)-O(311)-H(211)	111.0(10)

Symmetry transformations used to generate equivalent atoms: #1 -x,y,-z+1/2 #2 -x+1/2,-y+3/2,-z+1

Table 4. Anisotropic displacement parameters ($Å^2 x\ 10^3$) for 5-2-1. The anisotropic displacement factor exponent takes the form: $-2\pi^2[\ h^2\ a^{*2}U^{11} + ... + 2\ h\ k\ a^*\ b^*\ U^{12}\ ]$

	U^{11}	U^{22}	U^{33}	U^{23}	U^{13}	U^{12}
Zn(1)	8(1)	9(1)	10(1)	0	1(1)	0
O(1)	18(1)	10(1)	13(1)	0	-1(1)	0
O(2)	10(1)	9(1)	24(1)	0	-5(1)	0
O(3)	11(1)	11(1)	16(1)	-2(1)	-1(1)	2(1)
O(4)	10(1)	10(1)	13(1)	-2(1)	3(1)	-1(1)
C(1)	8(1)	12(1)	10(1)	1(1)	2(1)	-1(1)
C(2)	11(1)	9(1)	9(1)	0(1)	4(1)	-2(1)
C(21)	10(1)	11(1)	11(1)	-1(1)	5(1)	-1(1)
O(211)	11(1)	9(1)	18(1)	0(1)	1(1)	0(1)
O(212)	11(1)	11(1)	14(1)	-1(1)	0(1)	-1(1)
C(3)	11(1)	9(1)	9(1)	1(1)	4(1)	1(1)
C(31)	12(1)	11(1)	10(1)	0(1)	2(1)	1(1)
O(311)	11(1)	9(1)	28(1)	1(1)	2(1)	1(1)
O(312)	9(1)	12(1)	21(1)	2(1)	3(1)	1(1)

Table 5. Hydrogen coordinates (x 10^4) and isotropic displacement parameters ($Å^2 x\ 10^3$) for 5-2-1.

	x	y	z	U(eq)
H(11)	177(9)	5660(20)	3430(30)	27(5)
H(21)	280(9)	460(20)	3040(30)	28(5)
H(31)	1038(10)	2340(20)	4720(30)	27(5)
H(32)	1007(9)	3570(20)	5350(30)	33(5)
H(41)	696(10)	2400(20)	300(30)	33(5)
H(42)	905(9)	3600(20)	1080(30)	25(4)
H(1)	1467(7)	7192(14)	3470(20)	4(3)
H(211)	2679(12)	3870(20)	4690(40)	66(8)

Tables for Structure 5-3-2

Table 1. Crystal data and structure refinement.

Identification code	5-3-2	
Empirical formula	C40 H64 O56 Zn4	
Formula weight	1702.42	
Temperature	293(2) K	
Wavelength	0.25000 Å	
Crystal system	Monoclinic	
Space group	C2/c	
Unit cell dimensions	a = 21.9240(13) Å	α= 90°.
	b = 9.7690(5) Å	β= 104.905(3)°.
	c = 7.1840(4) Å	γ = 90°.
Volume	1486.87(14) $Å^3$	
Z	1	
Density (calculated)	1.901 Mg/m^3	
Absorption coefficient	0.000 mm^{-1}	
F(000)	374	
Crystal size	1.5 x 1.5 x 1.3 mm^3	
Theta range for data collection	2.98 to 17.83°.	
Index ranges	0<=h<=44, 0<=k<=21, -14<=l<=13	
Reflections collected	1498	
Independent reflections	1498 [R(int) = 0.0000]	
Completeness to theta = 17.83°	13.1 %	
Absorption correction	Empirical	
Refinement method	Full-matrix least-squares on F^2	
Data / restraints / parameters	1498 / 0 / 187	
Goodness-of-fit on F^2	1.095	
Final R indices [I>2sigma(I)]	R1 = 0.0836, wR2 = 0.2101	
R indices (all data)	R1 = 0.0836, wR2 = 0.2101	
Largest diff. peak and hole	2.128 and -1.672 $e.Å^{-3}$	

Table 2. Atomic coordinates (x 10^4) and equivalent isotropic displacement parameters ($Å^2$x 10^3) for 5-3-2. U(eq) is defined as one third of the trace of the orthogonalized U^{ij} tensor.

	x	y	z	U(eq)
Zn(1)	0	2991(5)	2500	11(1)

O(1)	0	5161(5)	2500	15(1)
O(2)	0	885(6)	2500	18(1)
O(3)	804(2)	2891(4)	4779(5)	14(1)
O(4)	576(2)	3136(4)	544(5)	13(1)
C(1)	1877(1)	7313(3)	4071(4)	11(1)
C(2)	2292(1)	6217(3)	4168(4)	10(1)
C(21)	1974(1)	4911(3)	3257(4)	11(1)
O(211)	2219(2)	3740(4)	3850(5)	14(1)
O(212)	1469(2)	4999(4)	2013(5)	14(1)
C(3)	2933(1)	6401(3)	5124(4)	11(1)
C(31)	3462(1)	5347(3)	5417(4)	11(1)
O(311)	3321(2)	4076(4)	5485(6)	17(1)
O(312)	4013(2)	5757(4)	5657(6)	15(1)

Table 3. Bond lengths [Å] and angles [°] for 5-3-2.

Zn(1)-O(2)	2.057(7)	C(1)-C(3)#2	1.401(4)
Zn(1)-O(3)#1	2.077(3)	C(1)-H(1)	1.073(7)
Zn(1)-O(3)	2.077(3)	C(2)-C(3)	1.409(4)
Zn(1)-O(1)	2.120(7)	C(2)-C(21)	1.519(4)
Zn(1)-O(4)#1	2.121(4)	C(21)-O(212)	1.234(4)
Zn(1)-O(4)	2.121(4)	C(21)-O(211)	1.289(5)
O(1)-H(11)	0.978(8)	O(211)-H(211)	1.119(10)
O(2)-H(21)	0.967(8)	C(3)-C(1)#2	1.401(4)
O(3)-H(31)	0.999(10)	C(3)-C(31)	1.524(4)
O(3)-H(32)	0.967(8)	C(31)-O(312)	1.242(4)
O(4)-H(41)	0.968(8)	C(31)-O(311)	1.283(5)
O(4)-H(42)	0.993(8)	O(311)-H(211)	1.311(10)
C(1)-C(2)	1.395(4)		

O(2)-Zn(1)-O(3)#1	87.30(17)	O(3)#1-Zn(1)-O(4)#1	89.78(14)
O(2)-Zn(1)-O(3)	87.30(17)	O(3)-Zn(1)-O(4)#1	90.58(14)
O(3)#1-Zn(1)-O(3)	174.6(3)	O(1)-Zn(1)-O(4)#1	86.19(16)
O(2)-Zn(1)-O(1)	180.000(1)	O(2)-Zn(1)-O(4)	93.81(16)
O(3)#1-Zn(1)-O(1)	92.70(17)	O(3)#1-Zn(1)-O(4)	90.58(14)
O(3)-Zn(1)-O(1)	92.70(17)	O(3)-Zn(1)-O(4)	89.78(14)
O(2)-Zn(1)-O(4)#1	93.81(16)	O(1)-Zn(1)-O(4)	86.19(16)

O(4)#1-Zn(1)-O(4)	172.4(3)	C(1)-C(2)-C(21)	113.7(2)
Zn(1)-O(1)-H(11)	126.0(6)	C(3)-C(2)-C(21)	127.4(2)
Zn(1)-O(2)-H(21)	124.8(6)	O(212)-C(21)-O(211)	121.4(3)
Zn(1)-O(3)-H(31)	115.1(5)	O(212)-C(21)-C(2)	118.7(3)
Zn(1)-O(3)-H(32)	126.6(6)	O(211)-C(21)-C(2)	119.8(3)
H(31)-O(3)-H(32)	108.0(8)	C(21)-O(211)-H(211)	111.7(5)
Zn(1)-O(4)-H(41)	114.8(7)	C(1)#2-C(3)-C(2)	117.9(2)
Zn(1)-O(4)-H(42)	107.1(6)	C(1)#2-C(3)-C(31)	114.5(2)
H(41)-O(4)-H(42)	109.1(8)	C(2)-C(3)-C(31)	127.5(2)
C(2)-C(1)-C(3)#2	123.2(2)	O(312)-C(31)-O(311)	122.8(3)
C(2)-C(1)-H(1)	119.2(5)	O(312)-C(31)-C(3)	118.6(3)
C(3)#2-C(1)-H(1)	117.6(5)	O(311)-C(31)-C(3)	118.5(3)
C(1)-C(2)-C(3)	118.8(2)	C(31)-O(311)-H(211)	112.2(4)

Symmetry transformations used to generate equivalent atoms: #1 -x,y,-z+1/2 #2 -x+1/2,-y+3/2,-z+1

Table 4. Anisotropic displacement parameters ($Å^2 x\ 10^3$) for 5-3-2. The anisotropic displacement factor exponent takes the form: $-2\pi^2[\ h^2\ a^{*2}U^{11} + ... + 2\ h\ k\ a^*\ b^*\ U^{12}\ ]$

	U^{11}	U^{22}	U^{33}	U^{23}	U^{13}	U^{12}
Zn(1)	11(1)	9(2)	13(2)	0	1(1)	0
O(1)	20(2)	11(2)	14(2)	0	2(2)	0
O(2)	13(2)	14(2)	22(2)	0	-2(2)	0
O(3)	13(1)	12(1)	15(1)	-2(1)	0(1)	1(1)
O(4)	13(1)	14(1)	12(1)	-2(1)	3(1)	-1(1)
H(11)	42(4)	22(3)	23(3)	-5(2)	1(3)	-5(3)
H(21)	21(3)	18(3)	39(4)	2(2)	-4(2)	1(3)
H(31)	28(3)	33(4)	26(4)	-2(3)	1(3)	8(3)
H(32)	29(3)	24(3)	32(4)	-12(3)	2(3)	-5(3)
H(41)	31(3)	23(3)	30(4)	-4(2)	10(3)	6(3)
H(42)	21(3)	26(3)	30(4)	-5(2)	3(2)	-2(3)
C(1)	10(1)	12(1)	10(1)	-1(1)	2(1)	1(1)
C(2)	10(1)	9(1)	10(1)	-1(1)	2(1)	1(1)
C(21)	11(1)	9(1)	11(1)	0(1)	2(1)	-1(1)
O(211)	13(1)	10(1)	18(1)	1(1)	2(1)	1(1)
O(212)	13(1)	11(1)	16(1)	-2(1)	1(1)	-1(1)
C(3)	11(1)	10(1)	10(1)	-1(1)	2(1)	1(1)

C(31)	10(1)	10(1)	14(1)	0(1)	3(1)	-1(1)
O(311)	13(1)	7(1)	30(2)	1(1)	1(1)	1(1)
O(312)	10(1)	12(1)	21(2)	3(1)	3(1)	0(1)
H(1)	14(2)	20(3)	33(3)	-6(2)	2(2)	-1(2)
H(211)	30(3)	25(3)	31(4)	8(2)	6(3)	9(3)

Table 5. Hydrogen coordinates (x 10^4) and isotropic displacement parameters ($Å^2$x 10^3) for 5-3-2.

	x	y	z	U(eq)
H(11)	206(5)	5750(8)	3581(12)	30(2)
H(21)	346(4)	320(8)	3198(13)	28(2)
H(31)	1117(4)	2175(10)	4653(12)	30(2)
H(32)	1035(4)	3656(9)	5477(13)	30(2)
H(41)	714(4)	2266(9)	150(12)	28(1)
H(42)	951(4)	3687(9)	1184(13)	26(1)
H(1)	1388(3)	7179(8)	3343(11)	23(1)
H(211)	2720(4)	3843(9)	4718(13)	29(2)

Tables for Structure 6-3-1

Table 1. Crystal data and structure refinement..

Identification code	6-3-1	
Empirical formula	C13 H13 N O S	
Formula weight	231.30	
Temperature	200(2) K	
Wavelength	0.71073 Å	
Crystal system	Monoclinic	
Space group	Pc	
Unit cell dimensions	a = 13.8819(8) Å	α= 90°.
	b = 5.1965(3) Å	β= 106.932(3)°.
	c = 8.3463(5) Å	γ = 90°.
Volume	575.98(6) $Å^3$	

Z	2
Density (calculated)	1.334 Mg/m^3
Absorption coefficient	0.258 mm^{-1}
F(000)	244
Crystal size	0.26 x 0.24 x 0.18 mm^3
Theta range for data collection	3.07 to 27.48°.
Index ranges	-17<=h<=18, -6<=k<=6, -9<=l<=10
Reflections collected	5892
Independent reflections	2428 [R(int) = 0.0401]
Completeness to theta = 27.48°	99.5 %
Absorption correction	None
Refinement method	Full-matrix least-squares on F^2
Data / restraints / parameters	2428 / 2 / 197
Goodness-of-fit on F^2	1.045
Final R indices [I>2sigma(I)]	R1 = 0.0326, wR2 = 0.0840
R indices (all data)	R1 = 0.0332, wR2 = 0.0847
Largest diff. peak and hole	0.187 and -0.288 $e.Å^{-3}$

Table 2. Atomic coordinates (x 10^4) and equivalent isotropic displacement parameters ($Å^2$x 10^3) for 6-3-1. U(eq) is defined as one third of the trace of the orthogonalized U^{ij} tensor.

	x	y	z	U(eq)
S(1)	4999(1)	3648(1)	2200(1)	37(1)
O(1)	9282(1)	1598(2)	2592(2)	35(1)
N(1)	70(1)	2799(3)	-530(2)	33(1)
C(2)	6771(1)	871(3)	3199(2)	31(1)
C(10)	1633(1)	4348(3)	-1032(2)	29(1)
C(5)	7794(1)	4117(3)	1597(2)	32(1)
C(3)	7772(1)	381(3)	3308(2)	30(1)
C(1)	6270(1)	2979(3)	2283(2)	29(1)
C(12)	1679(1)	642(3)	723(2)	31(1)
C(13)	2703(1)	376(3)	910(2)	30(1)
C(7)	4320(1)	1754(3)	367(2)	33(1)
C(6)	6794(1)	4589(3)	1495(2)	31(1)
C(11)	1135(1)	2633(3)	-260(2)	26(1)
C(9)	2655(1)	4075(3)	-832(2)	30(1)

C(4)	8290(1)	2002(3)	2509(2)	26(1)
C(8)	3206(1)	2079(3)	135(2)	27(1)

Table 3. Bond lengths [Å] and angles [°] for 6-3-1.

S(1)-C(1)	1.7804(16)	C(5)-H(5)	1.04(3)
S(1)-C(7)	1.8326(17)	C(3)-C(4)	1.396(2)
O(1)-C(4)	1.3753(19)	C(3)-H(3)	1.00(3)
O(1)-H(4)	0.80(3)	C(1)-C(6)	1.393(2)
N(1)-C(11)	1.4312(18)	C(12)-C(13)	1.391(2)
N(1)-H(11A)	0.91(3)	C(12)-C(11)	1.397(2)
N(1)-H(11B)	0.83(3)	C(12)-H(12)	0.96(2)
C(2)-C(3)	1.390(2)	C(13)-C(8)	1.398(2)
C(2)-C(1)	1.399(2)	C(13)-H(13)	1.02(3)
C(2)-H(2)	1.02(3)	C(7)-C(8)	1.511(2)
C(10)-C(9)	1.388(2)	C(7)-H(7B)	1.01(3)
C(10)-C(11)	1.395(2)	C(7)-H(7A)	1.07(3)
C(10)-H(10)	0.95(3)	C(6)-H(6)	0.93(2)
C(5)-C(6)	1.387(2)	C(9)-C(8)	1.397(2)
C(5)-C(4)	1.399(2)	C(9)-H(9)	1.00(2)

C(1)-S(1)-C(7)	100.95(8)	C(4)-C(3)-H(3)	117.2(16)
C(4)-O(1)-H(4)	108.7(19)	C(6)-C(1)-C(2)	118.90(15)
C(11)-N(1)-H(11A)	112.4(14)	C(6)-C(1)-S(1)	120.85(12)
C(11)-N(1)-H(11B)	114(2)	C(2)-C(1)-S(1)	120.21(13)
H(11A)-N(1)-H(11B)	116(3)	C(13)-C(12)-C(11)	119.93(14)
C(3)-C(2)-C(1)	120.50(16)	C(13)-C(12)-H(12)	118.1(13)
C(3)-C(2)-H(2)	120.9(14)	C(11)-C(12)-H(12)	122.0(13)
C(1)-C(2)-H(2)	118.5(14)	C(12)-C(13)-C(8)	121.18(15)
C(9)-C(10)-C(11)	120.43(14)	C(12)-C(13)-H(13)	121.5(15)
C(9)-C(10)-H(10)	118.5(18)	C(8)-C(13)-H(13)	117.2(15)
C(11)-C(10)-H(10)	120.7(18)	C(8)-C(7)-S(1)	107.73(11)
C(6)-C(5)-C(4)	119.83(15)	C(8)-C(7)-H(7B)	111.5(16)
C(6)-C(5)-H(5)	122.2(14)	S(1)-C(7)-H(7B)	104.0(15)
C(4)-C(5)-H(5)	117.9(14)	C(8)-C(7)-H(7A)	110.7(13)
C(2)-C(3)-C(4)	120.13(15)	S(1)-C(7)-H(7A)	108.7(13)
C(2)-C(3)-H(3)	122.7(16)	H(7B)-C(7)-H(7A)	114(2)

C(5)-C(6)-C(1)	121.05(14)	C(8)-C(9)-H(9)	121.5(13)
C(5)-C(6)-H(6)	119.3(16)	O(1)-C(4)-C(3)	122.09(14)
C(1)-C(6)-H(6)	119.6(16)	O(1)-C(4)-C(5)	118.32(14)
C(10)-C(11)-C(12)	119.25(13)	C(3)-C(4)-C(5)	119.59(14)
C(10)-C(11)-N(1)	121.10(14)	C(9)-C(8)-C(13)	118.29(14)
C(12)-C(11)-N(1)	119.57(14)	C(9)-C(8)-C(7)	121.65(15)
C(10)-C(9)-C(8)	120.91(14)	C(13)-C(8)-C(7)	120.07(15)
C(10)-C(9)-H(9)	117.5(13)		

Symmetry transformations used to generate equivalent atoms:

Table 4. Anisotropic displacement parameters ($Å^2 x\ 10^3$) for 6-3-1. The anisotropic displacement factor exponent takes the form: $-2\pi^2[\ h^2\ a^{*2}U^{11} + ... + 2\ h\ k\ a^*\ b^*\ U^{12}\ ]$

	U^{11}	U^{22}	U^{33}	U^{23}	U^{13}	U^{12}
S(1)	23(1)	48(1)	38(1)	-14(1)	6(1)	5(1)
O(1)	25(1)	41(1)	40(1)	9(1)	11(1)	3(1)
N(1)	23(1)	40(1)	36(1)	-1(1)	8(1)	-1(1)
C(2)	27(1)	32(1)	36(1)	2(1)	12(1)	-1(1)
C(10)	31(1)	26(1)	30(1)	2(1)	8(1)	1(1)
C(5)	32(1)	33(1)	31(1)	2(1)	10(1)	-1(1)
C(3)	26(1)	31(1)	34(1)	2(1)	10(1)	2(1)
C(1)	20(1)	35(1)	29(1)	-7(1)	6(1)	1(1)
C(12)	32(1)	31(1)	32(1)	5(1)	12(1)	-3(1)
C(13)	28(1)	31(1)	31(1)	3(1)	7(1)	2(1)
C(7)	25(1)	41(1)	34(1)	-8(1)	10(1)	0(1)
C(6)	32(1)	31(1)	27(1)	2(1)	5(1)	5(1)
C(11)	23(1)	30(1)	26(1)	-4(1)	7(1)	-2(1)
C(9)	31(1)	30(1)	32(1)	0(1)	12(1)	-4(1)
C(4)	24(1)	29(1)	24(1)	-2(1)	6(1)	-2(1)
C(8)	27(1)	31(1)	23(1)	-5(1)	7(1)	-2(1)

Table 5. Hydrogen coordinates (x 10^4) and isotropic displacement parameters ($Å^2$x 10^3) for 6-3-1.

	x	y	z	U(eq)
H(6)	6480(20)	6050(40)	940(30)	37(6)
H(9)	2976(18)	5320(50)	-1440(30)	37(5)
H(5)	8195(19)	5280(50)	1000(30)	43(6)
H(7B)	4550(20)	-80(50)	680(30)	44(6)
H(2)	6396(19)	-230(50)	3840(30)	46(6)
H(7A)	4516(18)	2460(50)	-710(30)	45(6)
H(12)	1369(17)	-550(40)	1300(30)	33(5)
H(13)	3110(20)	-1130(40)	1550(40)	47(7)
H(3)	8150(20)	-1130(50)	3930(40)	46(7)
H(10)	1300(20)	5840(50)	-1590(40)	57(8)
H(4)	9500(20)	430(50)	3230(30)	40(6)
H(11A)	-113(16)	2350(40)	400(30)	36(5)
H(11B)	-190(20)	4130(60)	-1010(40)	68(9)

Tables for Structure 6-3-6

Table 1. Crystal data and structure refinement for 6-3-6.

Identification code	6-3-6	
Empirical formula	C12 H11 N O S2	
Formula weight	249.34	
Temperature	200(2) K	
Wavelength	0.71073 Å	
Crystal system	Monoclinic	
Space group	P2(1)/c	
Unit cell dimensions	a = 10.4454(8) Å	α= 90°.
	b = 8.1147(6) Å	β= 110.077(3)°.
	c = 14.9206(11) Å	γ = 90°.
Volume	1187.84(15) $Å^3$	
Z	4	

Density (calculated)	1.394 Mg/m^3
Absorption coefficient	0.425 mm^{-1}
F(000)	520
Crystal size	0.32 x 0.28 x 0.16 mm^3
Theta range for data collection	2.08 to 27.45°.
Index ranges	-13<=h<=13, -10<=k<=10, -19<=l<=18
Reflections collected	10378
Independent reflections	2700 [R(int) = 0.0556]
Completeness to theta = 27.45°	99.6 %
Absorption correction	None
Refinement method	Full-matrix least-squares on F^2
Data / restraints / parameters	2700 / 0 / 189
Goodness-of-fit on F^2	1.062
Final R indices [I>2sigma(I)]	R1 = 0.0366, wR2 = 0.0954
R indices (all data)	R1 = 0.0428, wR2 = 0.1002
Largest diff. peak and hole	0.422 and -0.211 $e.Å^{-3}$

Table 2. Atomic coordinates (x 10^4) and equivalent isotropic displacement parameters ($Å^2$x 10^3) for 6-3-6. U(eq) is defined as one third of the trace of the orthogonalized U^{ij} tensor.

	x	y	z	U(eq)
S(1)	7847(1)	-397(1)	1245(1)	44(1)
S(2)	7155(1)	1757(1)	1635(1)	47(1)
O(1)	5685(1)	5908(2)	-1848(1)	43(1)
N(1)	13699(2)	419(2)	1577(1)	36(1)
C(4)	12310(2)	273(2)	1491(1)	31(1)
C(11)	5155(2)	3630(2)	-993(1)	33(1)
C(1)	9594(2)	-54(2)	1379(1)	32(1)
C(9)	7210(2)	5220(2)	-311(1)	40(1)
C(5)	11685(2)	1488(2)	1858(1)	35(1)
C(10)	6008(2)	4910(2)	-1066(1)	34(1)
C(7)	6726(2)	2978(2)	581(1)	34(1)
C(6)	10339(2)	1320(2)	1810(1)	36(1)
C(12)	5512(2)	2683(2)	-171(1)	35(1)
C(2)	10214(2)	-1272(2)	1010(1)	39(1)
C(3)	11560(2)	-1120(2)	1074(1)	37(1)
C(8)	7565(2)	4268(2)	508(1)	39(1)

Table 3. Bond lengths [Å] and angles [°] for 6-3-6.

S(1)-C(1)	1.7891(16)	C(1)-C(2)	1.394(2)
S(1)-S(2)	2.0502(7)	C(9)-C(8)	1.384(3)
S(2)-C(7)	1.7813(18)	C(9)-C(10)	1.392(2)
O(1)-C(10)	1.364(2)	C(9)-H(9)	0.93(2)
O(1)-H(10)	0.86(3)	C(5)-C(6)	1.390(2)
N(1)-C(4)	1.417(2)	C(5)-H(5)	0.94(2)
N(1)-H(4B)	0.81(2)	C(7)-C(8)	1.394(3)
N(1)-H(4A)	0.85(3)	C(7)-C(12)	1.395(2)
C(4)-C(5)	1.394(2)	C(6)-H(6)	0.925(19)
C(4)-C(3)	1.394(2)	C(12)-H(12)	0.947(19)
C(11)-C(12)	1.386(2)	C(2)-C(3)	1.382(3)
C(11)-C(10)	1.397(2)	C(2)-H(2)	0.93(2)
C(11)-H(11)	0.94(2)	C(3)-H(3)	0.95(2)
C(1)-C(6)	1.384(2)	C(8)-H(8)	0.97(2)
C(1)-S(1)-S(2)	106.33(6)	O(1)-C(10)-C(9)	118.33(15)
C(7)-S(2)-S(1)	103.31(6)	O(1)-C(10)-C(11)	122.11(15)
C(10)-O(1)-H(10)	111.3(17)	C(9)-C(10)-C(11)	119.53(16)
C(4)-N(1)-H(4B)	111.3(16)	C(8)-C(7)-C(12)	119.22(16)
C(4)-N(1)-H(4A)	109.9(18)	C(8)-C(7)-S(2)	120.86(13)
H(4B)-N(1)-H(4A)	111(2)	C(12)-C(7)-S(2)	119.89(13)
C(5)-C(4)-C(3)	118.83(15)	C(1)-C(6)-C(5)	120.01(16)
C(5)-C(4)-N(1)	120.53(15)	C(1)-C(6)-H(6)	120.3(12)
C(3)-C(4)-N(1)	120.60(15)	C(5)-C(6)-H(6)	119.6(12)
C(12)-C(11)-C(10)	119.81(15)	C(11)-C(12)-C(7)	120.70(16)
C(12)-C(11)-H(11)	119.0(12)	C(11)-C(12)-H(12)	118.2(11)
C(10)-C(11)-H(11)	121.2(12)	C(7)-C(12)-H(12)	121.1(11)
C(6)-C(1)-C(2)	119.42(15)	C(3)-C(2)-C(1)	120.58(16)
C(6)-C(1)-S(1)	124.47(13)	C(3)-C(2)-H(2)	116.9(15)
C(2)-C(1)-S(1)	116.11(13)	C(1)-C(2)-H(2)	122.5(15)
C(8)-C(9)-C(10)	120.50(16)	C(2)-C(3)-C(4)	120.37(16)
C(8)-C(9)-H(9)	120.6(14)	C(2)-C(3)-H(3)	119.7(13)
C(10)-C(9)-H(9)	118.9(14)	C(4)-C(3)-H(3)	119.9(13)
C(6)-C(5)-C(4)	120.76(15)	C(9)-C(8)-C(7)	120.23(16)
C(6)-C(5)-H(5)	121.6(13)	C(9)-C(8)-H(8)	120.3(13)
C(4)-C(5)-H(5)	117.7(13)	C(7)-C(8)-H(8)	119.4(13)

Table 4. Anisotropic displacement parameters ($Å^2 x\ 10^3$) for 6-3-6. The anisotropic displacement factor exponent takes the form: $-2\pi^2[\ h^2\ a^{*2}U^{11} + ... + 2\ h\ k\ a^*\ b^*\ U^{12}\ ]$

	U^{11}	U^{22}	U^{33}	U^{23}	U^{13}	U^{12}
S(1)	31(1)	45(1)	53(1)	15(1)	9(1)	-4(1)
S(2)	35(1)	72(1)	35(1)	6(1)	15(1)	7(1)
O(1)	41(1)	32(1)	48(1)	2(1)	5(1)	-7(1)
N(1)	33(1)	36(1)	39(1)	-4(1)	14(1)	1(1)
C(4)	31(1)	32(1)	28(1)	1(1)	7(1)	2(1)
C(11)	28(1)	32(1)	38(1)	-6(1)	7(1)	-2(1)
C(1)	28(1)	35(1)	30(1)	7(1)	6(1)	0(1)
C(9)	33(1)	31(1)	53(1)	-7(1)	10(1)	-5(1)
C(5)	32(1)	32(1)	38(1)	-8(1)	8(1)	-1(1)
C(10)	32(1)	27(1)	42(1)	-5(1)	11(1)	2(1)
C(7)	28(1)	40(1)	35(1)	-4(1)	12(1)	5(1)
C(6)	32(1)	38(1)	37(1)	-5(1)	10(1)	4(1)
C(12)	28(1)	37(1)	41(1)	-4(1)	13(1)	-2(1)
C(2)	41(1)	30(1)	40(1)	-2(1)	6(1)	-5(1)
C(3)	42(1)	30(1)	36(1)	-4(1)	11(1)	4(1)
C(8)	28(1)	42(1)	43(1)	-10(1)	5(1)	0(1)

Table 5. Hydrogen coordinates (x 10^4) and isotropic displacement parameters ($Å^2 x\ 10^3$) for 6-3-6.

	x	y	z	U(eq)
H(4B)	13920(20)	1370(30)	1594(16)	47(6)
H(12)	4910(20)	1840(20)	-131(13)	34(5)
H(11)	4340(20)	3400(20)	-1489(14)	38(5)
H(8)	8390(20)	4500(30)	1035(15)	51(6)
H(9)	7780(20)	6070(30)	-369(16)	59(6)
H(6)	9927(19)	2160(20)	2029(13)	35(5)
H(5)	12200(20)	2440(30)	2123(15)	49(6)
H(2)	9750(20)	-2220(30)	717(16)	57(6)
H(3)	11990(20)	-1990(30)	850(14)	45(5)

H(4A)	13840(30)	-90(30)	1122(19)	72(8)
H(10)	5050(30)	5480(30)	-2323(18)	62(7)

Tables for Structure 6-4-2

Table 1. Crystal data and structure refinement for 6-4-2 (Neutron data).

Identification code	6-4-2	
Empirical formula	C36 H46 B2	
Formula weight	500.00	
Temperature	20(2) K	
Wavelength	1.31860 Å	
Crystal system	Monoclinic	
Space group	P2/n	
Unit cell dimensions	a = 12.2778(8) Å	α= 90°.
	b = 7.7353(6) Å	β= 109.836(3)°.
	c = 16.5979(12) Å	γ = 90°.
Volume	1482.81(18) $Å^3$	
Z	2	
Density (calculated)	1.120 Mg/m^3	
Absorption coefficient	4.44 mm^{-1}	
F(000)	156	
Crystal size	5.2 x 1.4 x 0.9 mm^3	
Theta range for data collection	3.35 to 66.14°.	
Index ranges	-15<=h<=16, -3<=k<=9, -22<=l<=22	
Reflections collected	10868	
Independent reflections	3342 [R(int) = 0.0391]	
Completeness to theta = 66.14°	80.5 %	
Absorption correction	Gaussian	
Max. and min. transmission	0.6942 and 0.3258	
Refinement method	Full-matrix least-squares on F^2	
Data / restraints / parameters	3342 / 0 / 409	
Goodness-of-fit on F^2	1.134	
Final R indices [I>2sigma(I)]	R1 = 0.0354, wR2 = 0.0810	
R indices (all data)	R1 = 0.0400, wR2 = 0.0833	
Extinction coefficient	0.00013(11)	
Largest diff. peak and hole	0.694 and -1.170 $e.Å^{-3}$	

Table 2. Atomic coordinates (x 10^4) and equivalent isotropic displacement parameters ($Å^2$x 10^3) for 6-3-6. U(eq) is defined as one third of the trace of the orthogonalized U^{ij} tensor.

	x	y	z	U(eq)
C(4)	9983(1)	3623(1)	2959(1)	9(1)
C(3)	11172(1)	3415(1)	3123(1)	10(1)
C(7)	7224(1)	4119(1)	5005(1)	10(1)
C(1)	11171(1)	722(1)	3822(1)	10(1)
C(2)	11783(1)	1977(1)	3547(1)	10(1)
C(10)	6678(1)	1241(1)	3932(1)	8(1)
C(6)	9985(1)	885(1)	3671(1)	9(1)
C(12)	7723(1)	3932(1)	4371(1)	9(1)
C(11)	7453(1)	2482(1)	3810(1)	8(1)
C(9)	6184(1)	1487(1)	4571(1)	10(1)
C(15)	6333(1)	-405(1)	3419(1)	11(1)
C(5)	9360(1)	2348(1)	3231(1)	8(1)
C(14)	13063(1)	1786(1)	3719(1)	14(1)
C(8)	6439(1)	2915(1)	5114(1)	10(1)
C(13)	9450(1)	5252(1)	2484(1)	11(1)
C(16)	5899(1)	3160(1)	5797(1)	14(1)
C(17)	9388(1)	-589(1)	3949(1)	11(1)
C(18)	8492(1)	5379(1)	4275(1)	12(1)
B	8001(1)	2414(1)	3063(1)	7(1)

Table 3. Bond lengths [Å] and angles [°] for 6-3-6.

C(4)-C(3)	1.4009(12)	C(1)-H(1A)	1.089(2)
C(4)-C(5)	1.4131(12)	C(2)-C(14)	1.5059(12)
C(4)-C(13)	1.5129(13)	C(10)-C(9)	1.4019(12)
C(3)-C(2)	1.3924(13)	C(10)-C(11)	1.4138(12)
C(3)-H(3A)	1.093(2)	C(10)-C(15)	1.5103(13)
C(7)-C(12)	1.3938(12)	C(6)-C(5)	1.4224(12)
C(7)-C(8)	1.3952(13)	C(6)-C(17)	1.5099(13)
C(7)-H(7A)	1.087(2)	C(12)-C(11)	1.4235(13)
C(1)-C(2)	1.3960(13)	C(12)-C(18)	1.5071(13)
C(1)-C(6)	1.3967(12)	C(11)-B	1.6000(14)

C(9)-C(8)	1.3918(13)	C(16)-H(16B)	1.067(13)
C(9)-H(9A)	1.088(2)	C(16)-H(16C)	1.062(15)
C(15)-H(15D)	1.080(2)	C(16)-H(16D)	1.037(12)
C(15)-H(15E)	1.087(2)	C(16)-H(16E)	1.019(12)
C(15)-H(15F)	1.087(2)	C(16)-H(16F)	1.063(12)
C(5)-B	1.5959(13)	C(17)-H(17A)	1.091(2)
C(14)-H(14A)	1.065(3)	C(17)-H(17B)	1.089(2)
C(14)-H(14B)	1.076(3)	C(17)-H(17C)	1.088(2)
C(14)-H(14C)	1.073(3)	C(18)-H(18A)	1.092(2)
C(8)-C(16)	1.5071(13)	C(18)-H(18B)	1.097(2)
C(13)-H(13A)	1.081(2)	C(18)-H(18C)	1.085(2)
C(13)-H(13B)	1.083(2)	B-B#1	1.855(2)
C(13)-H(13C)	1.088(2)	B-H(20A)	1.340(2)
C(16)-H(16A)	1.039(12)	B-H(20B)	1.342(2)

C(3)-C(4)-C(5)	119.99(8)	C(11)-C(12)-C(18)	122.09(8)
C(3)-C(4)-C(13)	115.78(8)	C(10)-C(11)-C(12)	117.37(8)
C(5)-C(4)-C(13)	124.22(8)	C(10)-C(11)-B	124.74(8)
C(2)-C(3)-C(4)	122.48(9)	C(12)-C(11)-B	117.84(8)
C(2)-C(3)-H(3A)	119.26(14)	C(8)-C(9)-C(10)	122.50(8)
C(4)-C(3)-H(3A)	118.26(14)	C(8)-C(9)-H(9A)	119.40(14)
C(12)-C(7)-C(8)	121.90(9)	C(10)-C(9)-H(9A)	118.09(14)
C(12)-C(7)-H(7A)	118.55(15)	C(10)-C(15)-H(15D)	113.79(15)
C(8)-C(7)-H(7A)	119.55(15)	C(10)-C(15)-H(15E)	110.89(16)
C(2)-C(1)-C(6)	121.54(8)	H(15D)-C(15)-H(15E)	107.3(2)
C(2)-C(1)-H(1A)	119.52(14)	C(10)-C(15)-H(15F)	110.41(16)
C(6)-C(1)-H(1A)	118.94(14)	H(15D)-C(15)-H(15F)	107.0(2)
C(3)-C(2)-C(1)	117.61(8)	H(15E)-C(15)-H(15F)	107.2(2)
C(3)-C(2)-C(14)	121.48(8)	C(4)-C(5)-C(6)	117.57(8)
C(1)-C(2)-C(14)	120.90(8)	C(4)-C(5)-B	124.69(8)
C(9)-C(10)-C(11)	120.10(8)	C(6)-C(5)-B	117.72(8)
C(9)-C(10)-C(15)	115.52(8)	C(2)-C(14)-H(14A)	111.92(19)
C(11)-C(10)-C(15)	124.38(8)	C(2)-C(14)-H(14B)	110.90(18)
C(1)-C(6)-C(5)	120.80(8)	H(14A)-C(14)-H(14B)	106.6(4)
C(1)-C(6)-C(17)	117.46(8)	C(2)-C(14)-H(14C)	112.53(17)
C(5)-C(6)-C(17)	121.66(8)	H(14A)-C(14)-H(14C)	108.7(4)
C(7)-C(12)-C(11)	120.76(8)	H(14B)-C(14)-H(14C)	105.8(3)
C(7)-C(12)-C(18)	117.04(8)	C(9)-C(8)-C(7)	117.36(8)

C(9)-C(8)-C(16)	121.83(9)	H(16C)-C(16)-H(16F)	83.3(17)
C(7)-C(8)-C(16)	120.82(9)	H(16D)-C(16)-H(16F)	103.2(14)
C(4)-C(13)-H(13A)	110.70(16)	H(16E)-C(16)-H(16F)	107.7(16)
C(4)-C(13)-H(13B)	113.70(16)	C(6)-C(17)-H(17A)	110.85(15)
H(13A)-C(13)-H(13B)	106.8(2)	C(6)-C(17)-H(17B)	110.60(15)
C(4)-C(13)-H(13C)	110.83(16)	H(17A)-C(17)-H(17B)	107.3(2)
H(13A)-C(13)-H(13C)	107.5(3)	C(6)-C(17)-H(17C)	112.74(16)
H(13B)-C(13)-H(13C)	107.0(2)	H(17A)-C(17)-H(17C)	108.0(2)
C(8)-C(16)-H(16A)	113.1(8)	H(17B)-C(17)-H(17C)	107.2(2)
C(8)-C(16)-H(16B)	112.3(8)	C(12)-C(18)-H(18A)	110.86(15)
H(16A)-C(16)-H(16B)	107.8(14)	C(12)-C(18)-H(18B)	110.67(15)
C(8)-C(16)-H(16C)	113.4(10)	H(18A)-C(18)-H(18B)	107.1(2)
H(16A)-C(16)-H(16C)	105.6(15)	C(12)-C(18)-H(18C)	112.85(16)
H(16B)-C(16)-H(16C)	104.1(14)	H(18A)-C(18)-H(18C)	108.2(2)
C(8)-C(16)-H(16D)	112.3(8)	H(18B)-C(18)-H(18C)	106.8(2)
H(16A)-C(16)-H(16D)	77.7(15)	C(5)-B-C(11)	123.70(8)
H(16B)-C(16)-H(16D)	33.6(12)	C(5)-B-B#1	118.23(10)
H(16C)-C(16)-H(16D)	127.8(12)	C(11)-B-B#1	118.07(9)
C(8)-C(16)-H(16E)	112.9(10)	C(5)-B-H(20A)	107.73(8)
H(16A)-C(16)-H(16E)	125.1(13)	C(11)-B-H(20A)	110.45(8)
H(16B)-C(16)-H(16E)	80.3(17)	B#1-B-H(20A)	46.17(10)
H(16C)-C(16)-H(16E)	26.6(18)	C(5)-B-H(20B)	110.49(8)
H(16D)-C(16)-H(16E)	110.0(15)	C(11)-B-H(20B)	107.55(8)
C(8)-C(16)-H(16F)	110.2(10)	B#1-B-H(20B)	46.29(10)
H(16A)-C(16)-H(16F)	26.9(15)	H(20A)-B-H(20B)	92.46(14)
H(16B)-C(16)-H(16F)	128.9(13)		

Symmetry transformations used to generate equivalent atoms:

#1 -x+3/2,y,-z+1/2

Table 4. Anisotropic displacement parameters ($Å^2 x\ 10^3$) for 6-3-6. The anisotropic displacement factor exponent takes the form: $-2\pi^2[\ h^2\ a^{*2}U^{11} + ... + 2\ h\ k\ a^*\ b^*\ U^{12}\ ]$

	U^{11}	U^{22}	U^{33}	U^{23}	U^{13}	U^{12}
C(4)	8(1)	7(1)	11(1)	1(1)	3(1)	0(1)
C(3)	9(1)	8(1)	12(1)	1(1)	4(1)	-1(1)

H(3A)	22(1)	21(1)	33(1)	6(1)	11(1)	-2(1)
C(7)	12(1)	9(1)	11(1)	-2(1)	5(1)	-1(1)
H(7A)	33(1)	21(1)	26(1)	-9(1)	14(1)	-8(1)
C(1)	9(1)	9(1)	13(1)	1(1)	3(1)	0(1)
H(1A)	21(1)	19(1)	33(1)	10(1)	7(1)	5(1)
C(2)	8(1)	10(1)	12(1)	1(1)	4(1)	0(1)
C(10)	9(1)	6(1)	10(1)	0(1)	4(1)	-1(1)
C(6)	9(1)	7(1)	11(1)	1(1)	3(1)	0(1)
C(12)	10(1)	7(1)	11(1)	-1(1)	4(1)	-1(1)
C(11)	9(1)	6(1)	9(1)	-1(1)	4(1)	-1(1)
C(9)	10(1)	8(1)	12(1)	-1(1)	5(1)	-1(1)
H(9A)	28(1)	21(1)	33(1)	-5(1)	18(1)	-10(1)
C(15)	13(1)	8(1)	13(1)	-2(1)	5(1)	-2(1)
H(15D)	42(1)	28(1)	44(1)	-13(1)	30(1)	-10(1)
H(15E)	24(1)	35(1)	44(1)	-12(1)	-4(1)	0(1)
H(15F)	66(2)	17(1)	29(1)	3(1)	18(1)	-6(1)
C(5)	8(1)	7(1)	10(1)	1(1)	3(1)	0(1)
C(14)	9(1)	15(1)	18(1)	3(1)	5(1)	1(1)
H(14A)	30(1)	44(2)	137(4)	-41(2)	28(2)	-1(1)
H(14B)	23(1)	109(3)	30(1)	3(2)	2(1)	7(2)
H(14C)	26(1)	63(2)	78(2)	45(2)	23(1)	6(1)
C(8)	12(1)	9(1)	10(1)	0(1)	5(1)	0(1)
C(13)	12(1)	7(1)	14(1)	2(1)	4(1)	1(1)
H(13A)	28(1)	20(1)	53(2)	5(1)	-2(1)	-8(1)
H(13B)	28(1)	30(1)	55(2)	15(1)	24(1)	10(1)
H(13C)	60(2)	33(1)	19(1)	5(1)	11(1)	12(1)
C(16)	18(1)	13(1)	15(1)	-1(1)	10(1)	-1(1)
H(16A)	64(11)	128(14)	57(10)	-70(10)	44(9)	-65(11)
H(16B)	71(9)	140(20)	54(6)	48(9)	41(6)	78(10)
H(16C)	142(18)	22(5)	83(11)	1(6)	91(13)	-4(8)
H(16D)	125(18)	16(5)	89(14)	15(4)	89(15)	29(6)
H(16E)	75(9)	76(17)	71(10)	-45(10)	62(8)	-65(11)
H(16F)	42(7)	141(18)	18(5)	7(8)	5(4)	30(11)
C(17)	11(1)	8(1)	14(1)	2(1)	4(1)	-1(1)
H(17A)	26(1)	24(1)	42(1)	17(1)	10(1)	7(1)
H(17B)	36(1)	30(1)	26(1)	-3(1)	5(1)	-14(1)
H(17C)	35(1)	26(1)	41(1)	1(1)	26(1)	0(1)
C(18)	14(1)	9(1)	14(1)	-2(1)	6(1)	-3(1)
H(18A)	42(1)	27(1)	32(1)	-14(1)	19(1)	-15(1)
H(18B)	36(1)	28(1)	32(1)	12(1)	5(1)	-6(1)

H(18C)	23(1)	26(1)	48(1)	-3(1)	20(1)	-3(1)
B	7(1)	6(1)	8(1)	0(1)	3(1)	-1(1)
H(20A)	23(1)	14(1)	22(1)	0	6(1)	0
H(20B)	22(1)	16(1)	20(1)	0	4(1)	0

Table 5. Hydrogen coordinates (x 10^4) and isotropic displacement parameters ($Å^2$x 10^3) for 6-3-6.

	x	y	z	U(eq)
H(3A)	11632(2)	4429(3)	2909(2)	25(1)
H(7A)	7454(2)	5242(3)	5423(1)	26(1)
H(1A)	11623(2)	-418(3)	4158(2)	25(1)
H(9A)	5585(2)	512(3)	4643(2)	25(1)
H(15D)	6865(2)	-704(3)	3035(2)	34(1)
H(15E)	5441(2)	-335(4)	2988(2)	38(1)
H(15F)	6393(3)	-1501(3)	3842(2)	37(1)
H(14A)	13276(3)	539(5)	3544(4)	70(1)
H(14B)	13545(2)	1945(6)	4390(2)	56(1)
H(14C)	13392(2)	2746(5)	3394(3)	55(1)
H(13A)	10043(2)	6328(3)	2684(2)	38(1)
H(13B)	8656(2)	5636(3)	2582(2)	35(1)
H(13C)	9248(3)	5091(4)	1797(2)	38(1)
H(16A)	6460(17)	3720(40)	6352(12)	77(8)
H(16B)	5140(20)	3940(40)	5582(12)	84(8)
H(16C)	5620(20)	1990(20)	5994(15)	69(7)
H(16D)	5550(30)	4386(15)	5781(16)	63(7)
H(16E)	5290(20)	2250(30)	5775(17)	65(8)
H(16F)	6546(14)	3100(40)	6414(8)	68(7)
H(17A)	10018(2)	-1534(3)	4323(2)	31(1)
H(17B)	8804(2)	-1263(3)	3394(2)	32(1)
H(17C)	8877(2)	-162(3)	4334(2)	31(1)
H(18A)	8701(2)	6261(3)	4820(2)	32(1)
H(18B)	8054(2)	6141(3)	3698(2)	34(1)
H(18C)	9297(2)	4920(3)	4217(2)	30(1)
H(20A)	7500	1165(4)	2500	20(1)
H(20B)	7500	3669(4)	2500	20(1)

Appendix B Publications, Conferences and Seminars

Publications

Arene-perfluoroarene interactions in crystal engineering. Part 10. Crystal structures of 1 : 1 complexes of octafluoronaphthalene with biphenyl and biphenylene.

J.C. Collings, P.S. Smith, D.S. Yufit, A.S. Batsanov, J.A.K. Howard, T.B. Marder. *Cryst. Eng. Comm.*, (2004) **6**, 25-28

Arene-perfluoroarene interactions in crystal engineering: structural preferences in polyfluorinated tolans.

C.E. Smith, P.S. Smith, R.L. Thomas, E.G. Robins, J.C. Collings, C.Y. Dai, A.J. Scott, S. Borwick, A.S. Batsanov, S.W. Watt, S.J. Clark, C. Viney, J.A.K. Howard, W. Clegg, T.B. Marder. *J. Mater. Chem.* (2004) **14**, 413-420

Correspondence between molecular functionality and crystal structures. Supramolecular chemistry of a family of homologated aminophenols.

V.R. Vangala, B.R. Bhogala, A. Dey, G.R. Desiraju, C.K. Broder, P.S. Smith, R. Mondal, J.A.K. Howard, C.C. Wilson. *J. Am. Chem. Soc.* (2003) **125**, 14495-14509

Dimesitylborane monomer-dimer equilibrium in solution, and the solid-state structure of the dimer by single crystal neutron and X-ray diffraction.

C.D. Entwistle, T.B. Marder, P.S. Smith, J.A.K. Howard, M.A. Fox, S.A. Mason, *J. Organomet. Chem.* (2003) **680**, 165-172

Study of weak interactions in (4-chlorophenyl)-(4-fluorophenyl)-(4-pyridyl) methanol and bis-(4-fluorophenyl)-(4-pyridyl) methanol.

A.R. Choudhury, U.K. Urs, P.S. Smith, R. Goddard, J.A.K. Howard, T.N.G. Row, *J. Mol. Struct.* (2002) 641, 225-232

In Preparation:

A novel saturated hydrogen bridge architecture in supraminols.

B.R. Bhogala, V.R. Vangala,† P.S. Smith, J.A.K. Howard, G.R. Desiraju. *Cryst. Growth Des. Commun.* (Accepted April 2004)

Conferences and Poster Presentations

15th November, 2000	BCA Chemical Group Autumn Meeting, Glaxo Smith-Kline, Harlow
30th March – 7th April, 2001	BCA School, University of Durham. "Eighth Intensive Course in X-Ray Structural Analysis".
7th – 10th April, 2001	BCA Spring Meeting, University of Reading Poster Presentation: "*The Low Temerature Structures of Various Partially Fluorinated Tolan Derivatives*"
25th – 31st August, 2001	20th European Cyrstallographic Meeting, Krakow, Poland. Poster Presentation: "*The Effect of Variable Temperature on Selected Aspects of Crystal Structure*"
14th November, 2001	BCA Chemical Group Autumn Meeting, University of Aston, Birmingham
5th December, 2001	BCA Physical Group Autumn Meeting, Daresbury Laboratory
6th – 13th December, 2001	CASTEP Workshop University of Durham "The Nuts and Bolts of First-Principles Simulation"
25th – 28th March, 2002	BCA Spring Meeting, University of Nottingham Poster Presentation: "*The Effect of Variable Temperature on Selected Aspects of Crystal Structure*"
13th November, 2002	BCA Chemical Group Autumn Meeting, King's College, London.
15th – 17th April, 2003	BCA Spring Meeting, University of York Poster Presentation: "*A Variable Temperature Approach of Analysis of Motion in the Solid State*"

Departmental Seminars

Date	Title	Speaker
11th October 2000	Recent Developments in OLED Technology: Organolanthanide Phosphors	Dr. V. Christau
25th October 2000	Science, art and drug discovery	Prof. S.F. Cambell
1st November 2000	Advances in polymeric based sensor systems	Prof. M. Thompson
8th November 2000	Cosmic: A Universal DNA - Language for Communication with Aliens & Other Intelligent Lifeforms	Dr. J. P. L. Cox
29th November 2000	Life, Death and the caratenoids	Dr. T.G. Truscott
6th December 2000	Dual Activation Approaches to Electroanalysis	Prof. R. Compton
7th December 2000	Cambridge Database Study of CH3/CF3 Exchange	Prof. A. Nangia
31st January 2001	Making Space for Molecules	Dr. P. Wright
21st February 2001	Liquid Crystals of All Shapes and Sizes	Dr. N. Norman
6th June 2001	The Melting Point Alternation of n-Alkanes and Derivatives	Prof. R. Boese
1st October 2001	Asymmetric Diels-Alder Catalysis using Chiral Zirconocene Complexes	Prof S. Collins
4th October 2001	Molecular Motion from Multi-Temperature ADPs	Dr. S Capelli
17th October 2001	Towards accurate ab initio electronic structure for large molecules	Prof P. Knowles
24th October 2001	Photonic Crystals in a Flash	Prof. B. Denning
31st October 2001	benign supramolecular chemistry: synthesis - self organisation	Dr. C.L. Raston
23rd January 2002	Control over polymeric materials at the (sub)-micron level	Dr W. Huck
30th January 2002	Chemistry in a Spin – Effects of Magnetic Fields on a Chemical Reaction	Dr. P.J. Hore
31st January 2002	Some Supramolecular Chemistry of Magnets and Superconductors	Prof. P. Day

27th February 2002	Dynamic Experiments in the Environmental SEM	Dr. B. Thiel
7th May 2002	Understanding the Properties of Molecular Solids: Structure, Dynamics and Applied Aspects	Prof. K.B.M. Harris
13th June 2002	Single crystal Diffraction at the ILL: Science and Facilities	G. McIntyre
2nd October 2002	Enzymology of Glycosyl Transfer: How Enzymes Make and Degrade Polysaccharides	Dr. G. Davis
9th October 2002	New design approaches for NLO chromophores and for molecular conductive magnets	Prof. J. Qin
6th November 2002	Modelling large uncrystallisable protein structures using X-ray and neutron scattering	Prof. S. Perkins
12th February 2003	Adventures in Organometallic Polymer Chemistry.	Prof P. Raithby
5th March 2003	Redox-active Metal Alkyne and Related Complexes: Structure, Bonding and Reactivity	Prof N. Connelly

Appendix C – Supplementary Information on CD

On the accompanying CD, one can find:

- Tables and cifs for *all* crystal structures.
- CASTEP input and output files for the principle calculations (typically the geometry optimisation and LTS/optimisation).
- Input and output files for THMA11 (TLS analysis).

The CD is divided in chapter folders, and each of these folders is then sub-divided into secondary folders for each main subsection. The structure numbering scheme within this thesis also reflects this hierarchy: for example structure 3-2-1 is in chapter three, section 2 and all the tables for this structure can be found in the 3-2 sub folder of chapter 3.